Validity and Reliability of Endoprobe Ultrasound Elastography in Oil-in-Gelatin Phantoms: Implications for the Characterization of Uterine Tissue Stiffness

Catriona Czyrnyj, MASc, PhD Candidate

A doctoral thesis proposal submitted to the Faculty of Graduate and Postdoctoral Studies in partial fulfillment of the requirements for the degree of

Doctor of Philosophy

in Biomedical Engineering

Ottawa-Carleton Institute for Biomedical Engineering

University of Ottawa

Ottawa, Canada

April 23, 2022

Abstract

Uterine fibroids, endometriosis, and adenomyosis are gynecological disorders causing significant symptoms and have clinical struggles around diagnosis and treatment planning. The tissue changes associated with these disorders may support assessment via ultrasound shear wave elastography (SWE), an imaging method that estimates tissue stiffness. This dissertation examined the feasibility of gynecological SWE for the in vivo assessment of uterine tissues. Specifically, this thesis evaluated: 1) the validity and reliability of endoprobe SWE stiffness measured in tissue mimicking materials (TMMs), 2) the validity of indentation testing in TMMs, 3) the impact of indentation parameters on the agreement between indentation stiffness and stiffness parameters measured by SWE, and 4) the reliability of and confounders on in vivo SWE of the uterus.

First, to establish the reliability and validity of gynecological endoprobe SWE stiffness measures, 31 homogenous TMM phantoms were manufactured with a range of elastic moduli. SWE stiffness was measured at 1cm, 3cm, and 5cm depths using a linear, curvilinear, and endo- SWE probes. Quasi-static ramp compression stiffness was the validity benchmark. Phantom moduli ranged from 17.10 kPa to 88.12 kPa. Endoprobe SWE stiffness reliability was excellent at all depths, however endoprobe SWE validity was poorer at 1cm depths than that of both the linear and curvilinear probe. The validity of endoprobe SWE stiffness was lower at the 3cm depth compared to the 1cm depth, and outcomes were not valid at the 5cm depth.

Second, to establish the validity of indentation testing as a benchmark standard for SWE applications, indentation testing was conducted in TMM phantoms under a series of testing parameters with quasi-static ramp compression used as the benchmark. The best agreement between indentation and ramp compression outcomes was observed at low strain ranges with the lowest testing rate (0.01Hz). Higher strains required different material model and geometry parameters to improve validity. Regardless, indentation and ramp compression outcomes were highly correlated. It is recommended

that researchers match testing parameters to in vivo loading conditions, while using this work to support material model and sample geometry selection.

Third, to identify the optimal indentation testing parameters to maximize agreement between SWE and indentation stiffness, several loading strain, loading rate, sample geometry, and indentation models were evaluated in TMM phantoms. Findings showed strong relationships between indentation and SWE stiffness outcomes, regardless of testing conditions. It is recommended to match loading parameters to in vivo conditions. Small sample geometries and low indentation rates appeared to optimize agreement between indentation and SWE outcomes.

The fourth and final study of this dissertation examined the in vivo reliability of uterine SWE. Institutional research ethics board approval was obtained (20170872-01H, H-08-18-790) and data were acquired from 32 participants with no active uterine disorders. SWE reliability was good to excellent, except in the anterior myometrium, where poor reliability was attributed to difficulty standardizing SWE sites between days. Phase in the menstrual cycle did not impact SWE outcomes. Site depth exhibited significant correlations with stiffness for multiple cases and heterogeneity in uterine stiffness was observed across sites. Anecdotal observations of confounding factors require further investigation.

The findings of this thesis suggest that quasi-static flat-tip indentation testing is a suitable benchmark standard to validate SWE under a variety of parameters. However, endoprobe SWE of the uterus does not appear to be valid at target depths of 3cm and beyond. Even at depths less than 3cm, linear or curvilinear probe SWE outperformed endoprobe SWE. Results suggest that further development of endoprobe SWE for uterine applications is required prior to clinical investigation of gynecological SWE for diagnostic and treatment planning purposes.

Acknowledgements

Throughout the completion of this thesis, I have been surrounded by outstanding and enthusiastic researchers who have shared their knowledge and experience with me. First, I would like to thank my supervisors. Dr. Michel Labrosse has provided important technical and analytical insights throughout the completion of this work, while always offering a kind word. He has modelled an attentive and impressive work ethic, while offering practical insights when it comes to the non-academic side of life. I would also like to thank Dr. Linda McLean for her contributions to the conceptualization of the original project, support of all the COVID and non-COVID related changes, and contributions to all aspects of this work. She has continually supported my professional development and offered years' worth of constructive feedback that has helped me develop substantially. I would not have the skill set, experience or abilities that I have today without Linda's support and mentorship.

On the clinical side of this project, I want to thank Dr. S. Sony Singh for his pointed and thoughtful guidance. The contributions of Dr. Singh and his clinical team have ensured that this work balances technical rigor with clinical utility, at all steps of the process. Thank you to Dr. Teresa Flaxman as well, who worked tirelessly to obtain funding for this project and who has provided guidance on the clinical research side, as well as on the methods, data processing, and analysis. She has been an ardent supporter of this project and it would not have been possible without her contributions.

I would like to thank my colleagues and friends who have supported my professional and personal development throughout this degree. In particular, I want to thank Ana Brennan, Megan Vandermolen, Céline Girard, Marie-Ève Bérubé, Kaylee Brooks, Flavia Ignacio Antonio, Olena Klahsen, Claire Warren, , Kristen Beange, Matthew Mavor, and Alex Steeves. I also wanted to thank the summer co-op students who supported the completion of this work: Alexis McCreath Frangakis, Alina Danilova, Maya Salame, and all of the undergraduate engineering students and volunteers who helped. All of these researchers have supported me throughout the difficult process of completing this degree. I am confident that it

would not have been possible without the community we have built to support each other. I also wanted to thank my community outside of academia: André Sponder, James Walker, Nicki Plouin, Arwen Moore, Adriana Babineau, Chris Deraiche, Linda Gadde, Kevin Gadde.

I would also like to thank Dr. Francois Hug, Dr. Ryan Graham, Dr. Fabio Variola, and Dr. Adrian Chan for their professional, technical, and personal guidance at various points throughout the completion of this work. Despite their busy schedules, these researchers have made themselves available for technical and professional discussions to support my development as an engineering researcher.

Finally, I would like to thank my pooch and best buddy, Pops. Thank you for being the best distraction from work I could ask for, and making sure I got fresh air, exercise, and lots of fun and games. Thank you for always being ready to run away and forget about everything with me, whenever I needed a break. I could not have dreamt up a better partner in crime. Thank you for getting me through this in one piece. You may not be here to enjoy the rewards, but I will never forget how much your love and companionship meant during this time.

Contents

List of Figures

List of Tables

List of Abbreviations

95% CI – 95% confidence interval
AdjR^2 – adjusted R^2
ARFI – acoustic radiation force imaging
CC – correlation coefficient
CT – computerized tomography
HZ – Hayes [172] and Zhang et al. [111]
ICC – intraclass correlation coefficient
LFI – liver function index
MCN – maximum consistent depth for SWE imaging
MD – mean difference
MRgFUS – magnetic resonance imaging guided focused ultrasound
MRE – magnetic resonance elastography
MRI – magnetic resonance imaging
MTE – mechanical tissue testing
OP – Oliver and Pharr [109]
ROC – receiver operator characteristic
SR – strain ratio
SSI – supersonic shear imaging
STD – standard deviation
SWE – shear wave elastography
TMM – tissue mimicking material
T_s – tissue thickness
UE – ultrasound elastography
UF – uterine fibroid
USI – ultrasound imaging

1 Introduction

1.1 Overview

Uterine fibroids (UFs), endometriosis, and adenomyosis are gynecological disorders that can cause significant symptoms including excessive bleeding, gynecological pain, and infertility [1]–[7]. These disorders are highly prevalent, with prevalence estimated to be between 10% and 30% of premenopausal women, depending on the disorder [1], [2], [14], [5], [7]–[13]. UFs are benign tumors of the myometrium [8], endometriosis is the extra-uterine growth of endometriotic cysts and/or lesions [6], and adenomyosis is the growth of endometrial glands deep in the myometrium causing myometrial hypertrophy and/or hyperplasia [15]. All of these disorders are associated with clinical struggles around diagnosis and/or treatment planning [4], [6], [23]–[25], [7], [16]–[22]. Further, these three disorders can co-occur, further confounding clinical decision making [6], [7], [26].

Changes to the microscopic structure of healthy tissue (i.e. histology), such as those associated with UFs, endometriosis, or adenomyosis, can lead to different distributions of deformations under mechanical loading [27], [28], [37]–[40], [29]–[36]. This is the mechanical basis of assessment via manual palpation, which is used by physicians to identify regions of abnormal tissue stiffness that may be indicative of pathology. Similarly, ultrasound elastography (UE) is used to estimate soft tissue mechanical response (e.g. stress, strain) or mechanical properties (e.g. elastic modulus) using ultrasound imaging (USI) during quasi-static or dynamic deformations of the tissue [41]–[46]. Shear wave elastography (SWE), a particular type of UE, has been developed to non-invasively estimate the elastic modulus of soft tissues from the dynamic deformation of the tissues. SWE involves the excitation of shear waves in soft tissues; the elastic modulus is then estimated using the relationship between shear wave velocity and mechanical properties of the tissues, combined with a series of assumptions [47].

While preliminary investigations of SWE for gynecological applications show promise [48]–[56], systematic investigations of gynecological SWE lag behind other SWE applications [57], [58], [67]–[70], [59]–[66]. There have been several studies attempting to validate SWE stiffness estimates acquired using linear [71]–[76] and curvilinear [77]–[80] SWE probes. However, SWE endoprobes, which have a unique geometry, center frequency, and SWE excitation sequences, have been largely ignored in the SWE validation literature. In a systematic search of the peer reviewed SWE validation literature, only a single study was found to have investigated the validity of SWE estimates acquired using an endoprobe. In this study, Cao et al. 2013 [81] detailed the performance of an SWE endoprobe for measuring the stiffness of phantoms made of tissue mimicking materials (TMMs). However, the generalizability of the findings is limited as the sample included SWE measurements in only five targets. In fact, five TMM phantom targets appears to be the standard sample size threshold for validating UE in the literature [71]–[75], [77]–[80]. This may be due to the limited number of targets available in commercially available standardized phantoms [71]–[75], [77]–[80] and the time and expertise required for manufacturing custom phantoms in-house [82]–[87]. Regardless, these small sample sizes combined with the small stiffness ranges often investigated in the SWE validation literature provide an incomplete picture of SWE validity.

In vivo testing and phantom validation of SWE both require some type of mechanical bench testing to act as a criterion standard. There are many mechanical tests that support the estimation of material stiffness, each of which can be implemented with a variety of testing parameters (loading rate, loading amplitude, specimen geometry, material model). This can yield a wide range of possibilities for mechanical testing benchmarks used in the validation of SWE [71], [72], [88]–[94]. The flat-tip indentation test is an accessible, economical, non-destructive mechanical testing method that addresses limitations around surgical tissue sampling procedures (e.g. minimally invasive approaches in which the tissue may be cut into smaller pieces), geometrical irregularities (e.g. non-uniform tissue resection),

sample geometries (e.g. surgical restrictions), and intact state (e.g. pathology restrictions) that are particularly relevant to fresh tissue testing [88]. Yet to date, the validity of indentation testing and the confounding impacts of testing parameters have seen relatively little investigation for SWE applications [88], [95]. Further, there has been no investigation of optimal indentation testing parameters for the validation of SWE.

SWE may have the potential to realize optimized treatment planning for uterine pathologies [37], [39], [55], [96], [97]. However, the omission of gynecological endoprobe data from the SWE validation literature [71]–[80], the lack of adequate sample sizes including the relevant range of target stiffnesses [71]–[75], [77]–[80], and the lack of consideration of the impact of mechanical testing parameters on the validitation models for SWE [95] pose a problem for the valid interpretation of endoprobe SWE data. The studies described in this dissertation aim to determine if tissue stiffness, non-invasively measured by endoprobe SWE, is a feasible method for the in vivo assessment of uterine tissues. This research is an essential first step to ultimately improve our ability to apply SWE to diagnose and direct treatment for uterine pathologies, including UFs, adenomyosis and endometriosis.

2 Background

2.1 The Uterus and Uterine Fibroids

2.1.1 Uterine Anatomy and Uterine Adnexa

The uterus, fallopian tubes, ovaries, and vagina are the female internal genital organs (Figure 1). The central organ in the system is the uterus, a hollow muscular organ that generally resembles an upside-down pear shape. The nulliparous uterus measures ~7.5 cm in length, ~5 cm in width, and ~2 cm in thickness, and weighs ~90 g, while multigravida uteri increase in length and weight with increasing parity [181], [329]. Superiorly, the fallopian tubes, which are ~10 cm long, extend out bilaterally from the superior region of uterus. The fallopian tubes open into peritoneal cavity bilateral to the uterus and conduct the ovum from the ovary to the uterus each month during childbearing years. The ovaries are located adjacent to the openings of the fallopian tubes on each side of the uterus. The ovaries, which are 2-4 cm long and almond-like in shape, are the female gonads, and contain approximately 400,000 follicles (i.e. fluid filled sacs) at puberty [181], [315]. The ovarian follicles are fluid filled sacs that secrete reproductive hormones and produce the ova [181], [315]. At the inferior region of the uterus, the vagina connects the uterine ostium, superiorly, to the vulvar vestibule, inferiorly, at the introitus. The vagina is a ~7-9 cm long musculomembranous tube, which is posterior to the urethra and anterior to the rectum [181]. The internal female genital system develops from a pair of tubes which grow together during fetal development in utero and is essentially mirrored with two ovaries, two fallopian tubes, and a uterus which is somewhat symmetrical about its longitudinal axis, though mild asymmetries are more common [330].

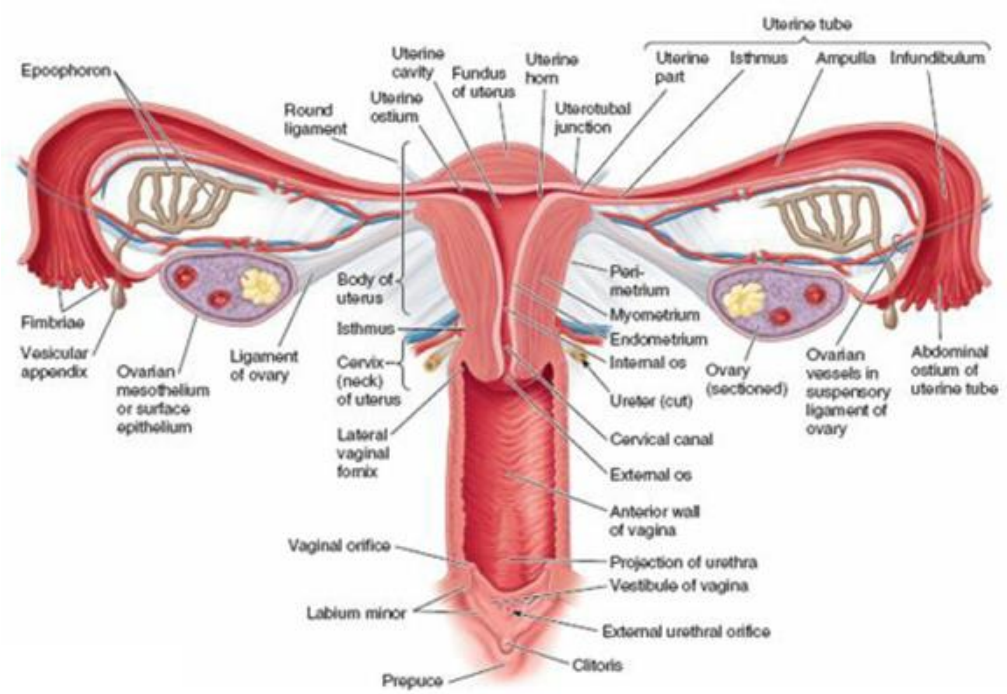

Figure 1 Mid-frontal plane diagram of the uterus, fallopian tubes, ovaries, vagina and some support ligaments. Reproduced from [181] *© 2006, with permission from Wolters Kluwer Health, Inc.*

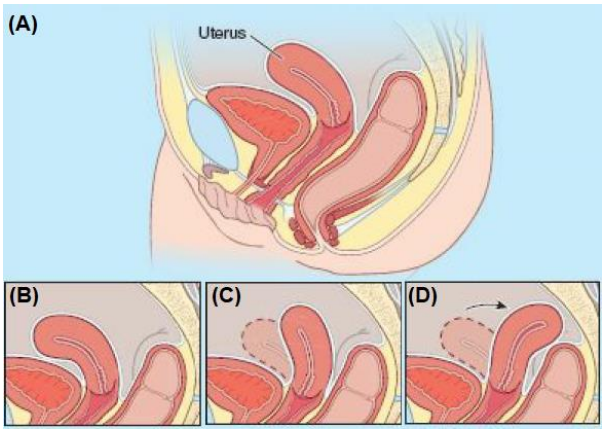

Figure 2 Mid-sagittal plane diagram showing the position of a uterus showing (A) normal anteversion and anteflexion, (B) excessive anteflexion, (C) retroversion, and (D) retroversion with retroflexion. Reproduced from [181] *© 2006, with permission from Wolters Kluwer Health, Inc.*

In nulliparous women, the uterus sits inferior to the pelvic brim and is generally anteverted and anteflexed so that its anterior surface rests on the bladder, and its posterior surface is adjacent to the sigmoid colon superiorly and the rectum inferiorly (Figure 2). Anatomically, the uterus has two main

regions. The body, or corpus, of the uterus forms the superior two thirds of the organ, while the inferior third of the uterus is the ~2.5 cm long cervix [181]. At the junction between the uterine body and cervix is a ~1 cm narrowing of the uterus, which is called the isthmus (Figure 1) [181]. The fundus of the uterus is the rounded superior region of the organ above the uterine horns (uterine ostium, proximal tube opening), where orifices of the fallopian tubes are located. The body of the uterus has a cavity, which is slit-like, measuring ~6 cm in length, and extends up from the cervix to the fundus, the superior-posterior end of the organ [181]. The cervix and cervical canal are a tubular continuation of the uterus and uterine cavity and open to the vagina at the external ostium (external os) of the uterus.

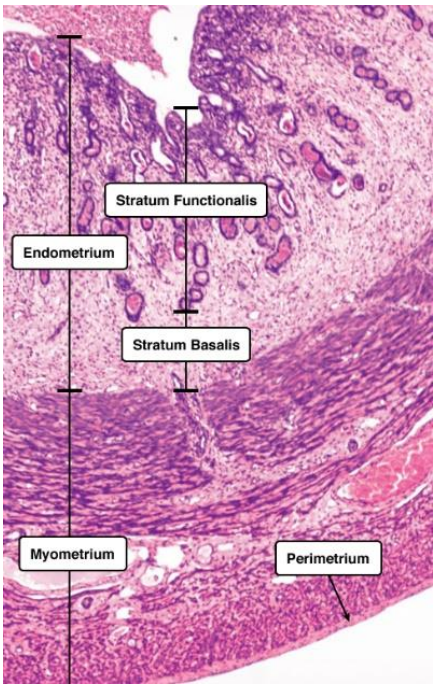

Figure 3 The body of the uterus is composed of three layers: the perimetrium, the myometrium, and the endometrium. Reproduced from [331] *with the permission of Dr. Peter Takizawa.*

The uterine body is composed of three layers: the perimetrium, the myometrium, and the endometrium (Figure 3, Figure 4). The perimetrium or uterine serosa, which is the thin outer membrane of the uterus, is composed of peritoneum supported by a thin layer of connective tissue [181]. The myometrium, which is the middle layer of the uterine body, is the location of the main blood vessels and

nerves in the uterus. Myometrial tissue is composed mainly of organized myometrial smooth muscle cells (SMCs), vascular SMCs, and fibroblasts [294], [332]. At the isthmus of the uterine body, 50-60% of the tissue is composed of concentrically organized smooth tissue, acting similar to a sphincter [329]. This ratio is supported experimentally by Wu et al. [294], who found that tissue from unspecified regions of the myometrium consisted of 61.2 ± 14.9% myometrial SMCs (n=51).

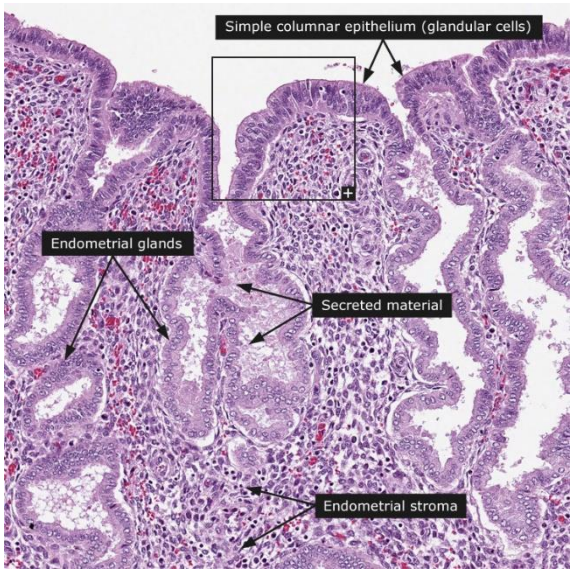

Figure 4 The endometrium is composed of two layers: the functional layer and the basal layer. Reproduced from [333], [334] *with permission from the Human Protein Atlas.*

The endometrium, the innermost layer of the uterus, is composed of two layers or stratum: the inferior basal layer and the superficial functional layer (Figure 3, Figure 4). The basal layer, which makes up the deeper one-third of the endometrium, attaches the functional layer to the myometrium and exhibits minimal morphological changes over the menstrual cycle [329]. The basal layer is composed of endometrial stroma, a layer of connective tissue, the terminal ends of glands present in the functional layer, and spiral arteries that supply the functional layer [329]. The functional layer, which makes up the superficial two-thirds of the endometrium, undergoes changes over the menstrual cycle. The functional

layer includes a single layer of columnar epithelium and contains the majority of the glands in the tissue, which respond to hormonal changes throughout the menstrual cycle [329]. In contrast to the uterine body, the cervix is made of mostly fibrous tissue and is mainly made of collagen with a small amount of smooth muscle and elastin, and the structure itself is lined by columnar and squamous epithelium [181], [329]. The cervix is composed of only ~15% smooth muscle, which is located mainly in the endocervix [329].

It should be noted, that the myometrium has been described in the literature as having an inner "junctional" zone, which is adjacent to the cervix, and an outer zone [335]. Similar to the endometrium, the structure and function of the junctional zone changes profoundly with hormonal fluctuations associated with the menstrual cycle [335]. In contrast, there are no cyclic changes in steroid receptors or structure of the outer myometrium [335]. Junctional myometrial tissue is characterized by high cell density, low cytoplasm to nucleus ratio, and differences in ECM composition with respect to the outer myometrium [335].

The uterus is supported by passive and active structures in the peritoneal cavity. Among the many ligaments and fascia supporting the internal female genital organs are the broad ligament of the uterus, the round ligament of the uterus, and the ligament of the ovary. The broad ligament of the uterus is a double layer of peritoneum (mesentery) and attaches the uterus to the lateral walls and floor of the pelvis. The round ligament of the uterus attaches the uterus, anteroinferiorly at the fallopian tube junction, to the pubis via the inguinal canal. The ligament of the ovary connects the ovary to the uterus, at a point posteroinferior to the fallopian tube junction (Figure 1). The cervix, which is the least mobile part of the uterus [181], receives additional passive support from the transverse cervical and uterosacral ligaments. The pelvic floor also provides passive and active support to the internal female genital organs. Dynamic support of the organ is provided by active contraction of the pelvic floor during tasks that increase intra-abdominal pressure, while resting tone provides passive support.

2.1.2 Uterine Fibroids

Uterine fibroids (UFs; a.k.a. myoma, leiomyoma, leiomyomata) are the most common gynecological tumors, with women exhibiting a cumulative incidence of 70% – 80% by the age of 50 [8], [9], [293], [306], [340]. Although these tumors are benign, 20% – 50% of women with UFs experience significant symptoms [1], [2], [12], including menstrual abnormalities (e.g. heavy and prolonged bleeding), iron deficiency anemia, bladder and/or bowel obstructions, abdominal protrusion, pelvic pain, and infertility [1], [2], [12], [341], [342]. Symptomatic UFs are estimated to cost the health care system $9,319 per patient, per year [343], not to mention indirect symptom-related costs, such as losses in productivity [2], [12] estimated at $2,399 – $15,549 annually per patient [344], and the well documented negative impacts UFs can have on women's quality of life [2], [12], [345], [346].

2.1.2.1 Macroscopic Characterization of Uterine Fibroids

Generally, on gross examination, typical UFs are spherical and firm, white or tan in color, and cut surfaces exhibit a heterogeneous whorled trabecular pattern [347]–[349] (Figure 5a). The "pseudocapsule", a thin fibro-neurovascular collagenous sheath, surrounds the UF and separates it from adjacent normal myometrium [350]. The vascularity of UFs supports maintenance and growth [351], [352] (Figure 5) however, these masses can easily outgrow their blood supply (more common in UFs ≥5cm in size) which leads to degenerative changes [348], [349], [353]. As the UF grows, the blood supply may become insufficient, oxygen deprivation to cells may occur, and interstitial edema (hydropic swelling), visible on medical imaging, is sometimes a precursor to degeneration [349], [354]. Edema is present in approximately 50% of all UFs [347] and if vascular insufficiency continues, more marked degenerative changes to the UF tissue may occur. Most UFs exhibit at least regions of degeneration [349] and degeneration may be visible on gross examination (Figure 5) or pockets can be so small that they are only visible microscopically [347].

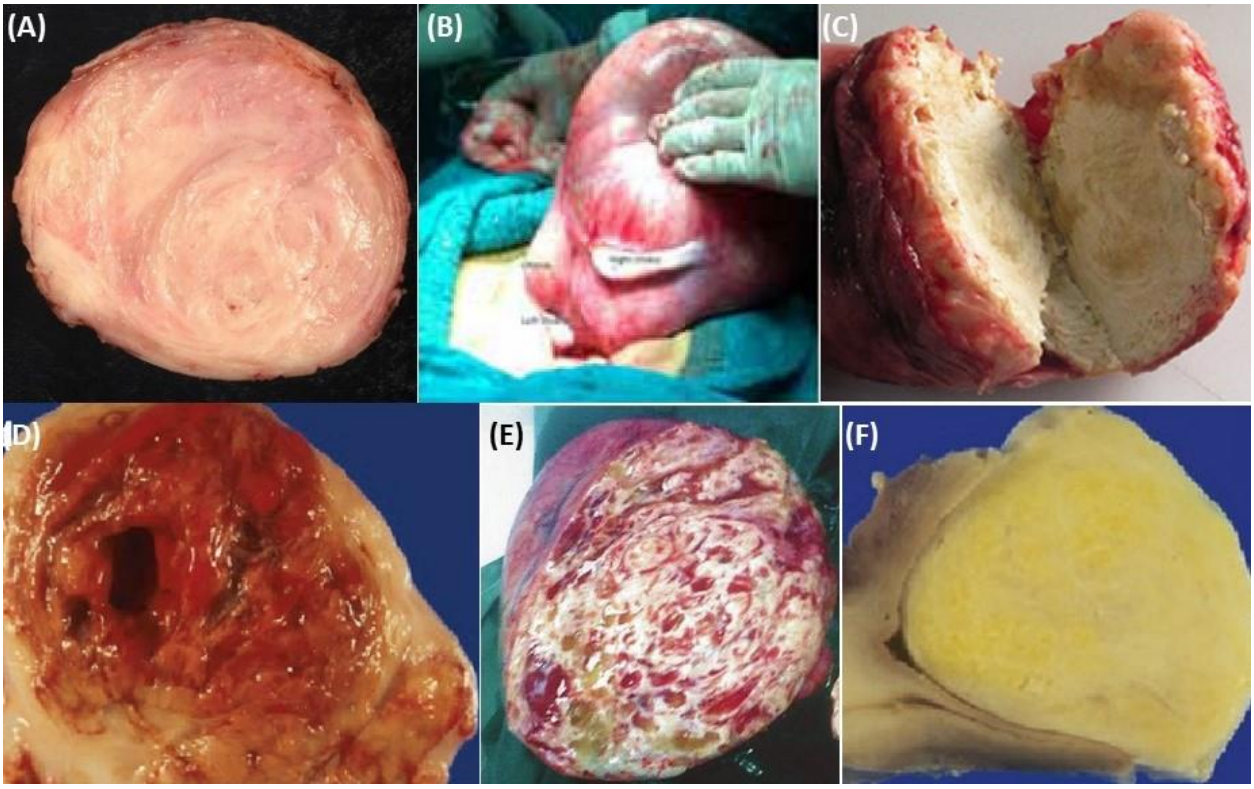

Figure 5 Images of uterine fibroids with various gross presentations A) typical, B) cystic, C) calcific, D) red (hemorrhagic, carneous, telangiectasic), E) myxoid, and F) lipoleiomyoma (i.e. fatty, adipose). Images A) [355], *B)* [356], *C)* [357], *E)* [358] *reproduced with author permission. Images (D), (F) reprinted from* [359] *©2018 with the permission of Springer Nature.*

Despite the dearth of information on UF degenerative changes in the literature, the general consensus is that UF degeneration manifests in several common types: hyaline fibrosis, cystic degeneration, myxoid degeneration, hemorrhagic degeneration, calcification, fatty deposition, and necrosis [349], [353], [354], [360], [361]. Hyaline degeneration, which is present in more than 60% of UFs [8], [347], [349], is marked by zones of amorphous translucent or white hyalinized collagenous tissue [347]. Cystic degeneration, liquefactive necrosis forming cyst cavities of varying sizes, is thought to occur in 4% of cases, perhaps as an extreme sequela of localized edema [354], [362], [363]. Myxoid degeneration, difficult to differentiate from cystic degeneration [349], [354], [360], [364], yields soft translucent lesions in which bundles of smooth muscle cells (SMCs) are separated by regions of mucoid ECM [347], [354]. Obstruction of UF drainage veins can lead to massive hemorrhagic infarction or coagulative degeneration of the UF [354], [360], and accounts for approximately 10% of cases [347], manifesting as coagulative necrosis of the lesion.

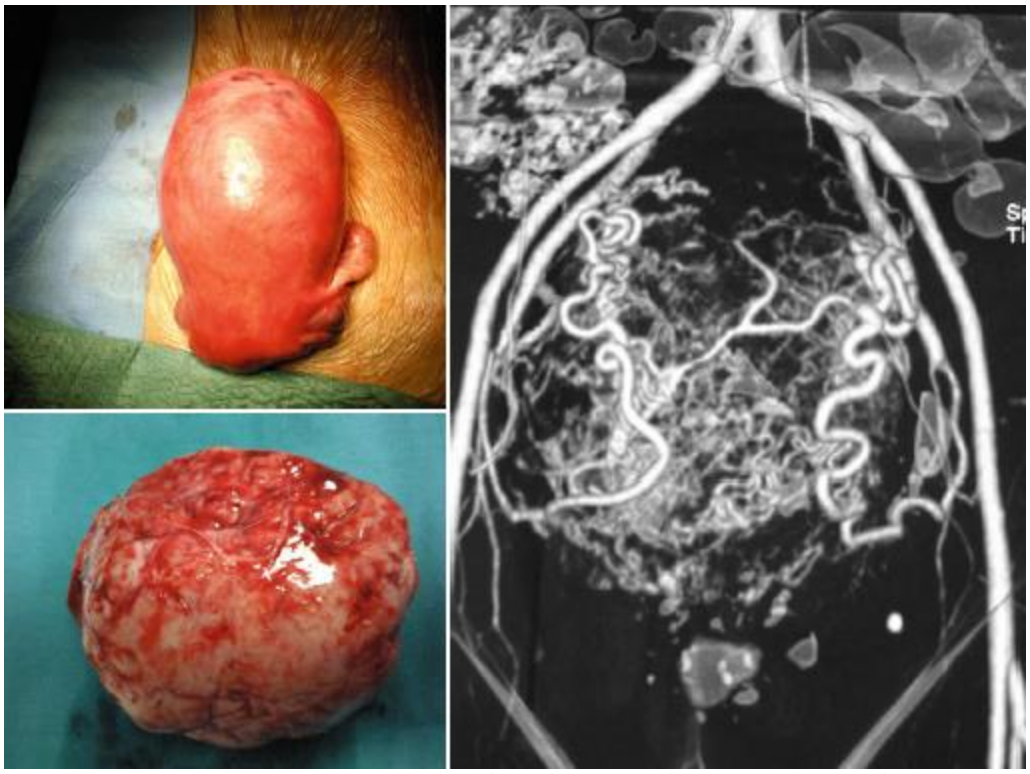

Figure 6 Abdominal hysterectomy showing the uterus with a large fundal fibroid (top left), the single enucleated fibroid (bottom left), and an angiographic image showing the hypervascularization of the fibroids with large supplying blood vessels. Reproduced from [350] *© 2015 with permission from Springer Verlag.*

Other forms of degeneration exist at much lower prevalence. Calcification, a dense amorphous degenerative change thought to be a sequela of hyaline [354] or red degeneration [354], [360], occurs in 4% of cases and is difficult to differentiate from hyaline degeneration [347], [349], [354], [360]. Lipoleiomyoma, or fatty degenerated UFs, which may in fact be neoplastic rather than degenerative [365]–[367], are composed of an admixture of smooth muscle, adipose, and fibrous tissue and have a prevalence of between 0.2% and 2% [354], [360], [366], [367]. While typical UFs often contain single scattered fat cells [347], lipoleiomyoma are a specific subclass of UFs which contain larger clusters of adipocytes [365]. Necrosis, cell death which may precede hyaline degeneration, is often found in UFs and may appear as self-contained zones of necrotic tissue surrounded by hyaline eosinophilic collagen [347]. Regardless of the variability in histological presentation, to date UFs are only classified by their location within the uterus [368] and their size (Section 9.1.1.1). Macroscopic characteristics of UFs are a

function of the microscopic organization of the UF tissues [347]–[349], which may relate to behavior of the pathology or response to treatment [369], [370]; however, there are currently no methods in place to assess the macroscopic properties of UFs until after surgical excision.

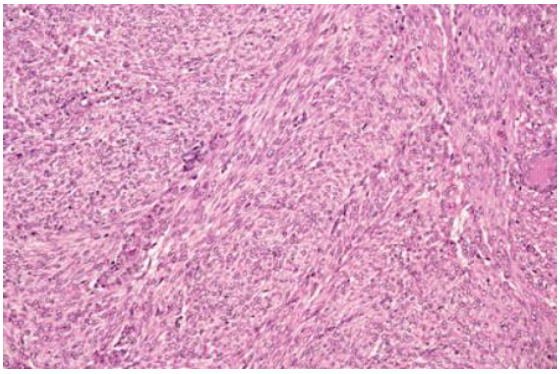

Figure 7 Hematoxylin eosin stain of a normative uterine fibroid tissue with spindle shaped cells, uniform nuclei (purple), and abundant cytoplasm (pink). Reproduced from [347] *©2004 with permission from Springer Nature.*

2.1.2.2 Microscopic Characterization of Uterine Fibroids

UF composition is generally characterized as disordered spindle-shaped myometrial SMCs embedded in abundant fibrous ECM, which is present in substantially higher amounts in UFs (~50% more) compared to adjacent myometrium [350], [371], [372] (Figure 7). While "virtually all in vitro and gene profiling studies to date have treated UF tumors as a homogeneous population consisting of an SMC phenotype" [332], UFs also contain vascular SMCs [294], [332] and populations of somatic stem cells (~1% of all cells in UFs) [373]. Further, fibroblasts also constitute a main cellular component of UFs that may contribute to ECM production and maintenance [294], [332], [374], [375]. Sparse numbers of granulocytes, monocytes, macrophages, and endothelial cells have also been identified in some UFs, though their mass appears to be negligible compared to the mass contribution of myometrial SMCs and fibroblasts [294]. Despite this heterogeneity in the cellular composition of benign UFs, evidence suggests that most UFs are still monoclonal in origin [297], [332], [376] and the primary cellular components of

UFs appear to be uterine SMCs and fibroblasts [294]. It should also be noted that UFs can exhibit unique microscopic characteristics depending on their region of origin in the myometrium (Section 9.1.1) [350].

Uterine tumors can have “normal” presentation on gross examination, yet exhibit abnormal microscopic characteristics with histological staining [377]. Microscopic findings, including differentiated cell type, necrosis, atypia, mitotic index, and cell density [347], may provide insight into a uterine tumor’s potential for malignancy [347], [377], [378], karyotype abnormalities [298], [371], or perhaps response to treatment [369]. The differentiated cell type of a uterine tumor is important: tumors composed primarily of spindle-shaped myometrial SMCs are less likely to be malignant, while tumors composed of round or polygonal-shaped epithelioid SMCs are more likely to be malignant [347]. While both tumors have eosinophilic cytoplasm (i.e. stained easily by eosin), epithelioid leiomyoma can have clear cytoplasm (Figure 8).

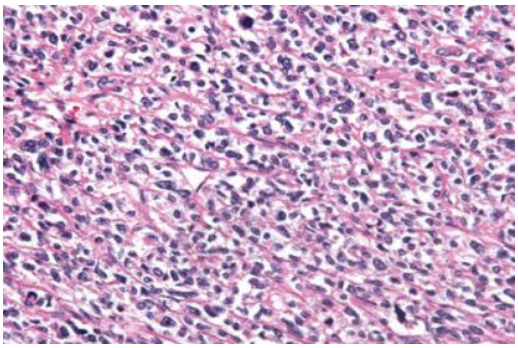

Figure 8 Hematoxylin eosin stain exhibiting clear cell variant of epithelioid leiomyoma. Reproduced from [347] *©2004 with permission from Springer Nature.*

Thresholds for necrosis, atypia, the mitotic index, and cell density, can also provide relevant insight into the behavior of a UF [347]. Necrosis, which differs from apoptosis, can be identified on gross examination as a clear region of yellow tissue, or microscopically as a central region of necrosis surrounded by hyalinized fibrosis (hyaline eosinophilic collagen) (Figure 8, Figure 9) [347]. Cytologic atypia is identified with histologic staining as a combination of pleomorphism (i.e. variable cell nuclei shape, size, staining) and hyperchromatism (i.e. cell nuclei stain dark) (Figure 10) [347]. A high mitotic

index is defined as at least 20 mitotic factors (MF) per 10 high power fields (HPF) [347]. MFs are identified as cells undergoing the process of mitosis (i.e. usually visible in metaphase, anaphase, telophase) (Figure 11) [119], [347], [379]. High cell density is simply the presence of a large number of cells per square unit with respect to some control region or tissue and is often characterized by small cells, minimal cytoplasm, and reticulin fibers that run parallel to the fascicles of cells (Figure 11) [347], [369]. Microscopic characteristics of tissues may provide insight into UF behavior or response to treatment.

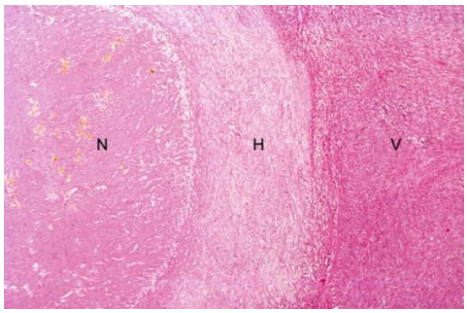

Figure 9 Hematoxylin eosin stain exhibiting a zone of necrosis (N), surrounded by hyalinised collagen (H), and finally viable spindle-shaped uterine fibroid cells. Reproduced from [347] *©2004 with permission from Springer Nature.*

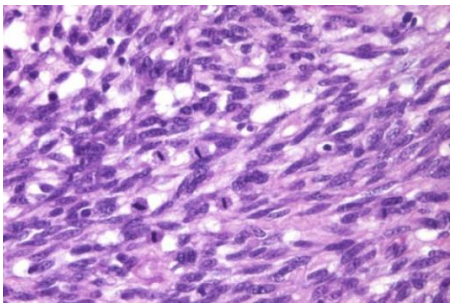

Figure 10 Hematoxylin eosin stain exhibiting atypia (irregularity), hyperchromasia (dark color), and a high mitotic index of the nuclei (purple), respectively. Reproduced from [347] *©2004 with permission from Springer Nature.*

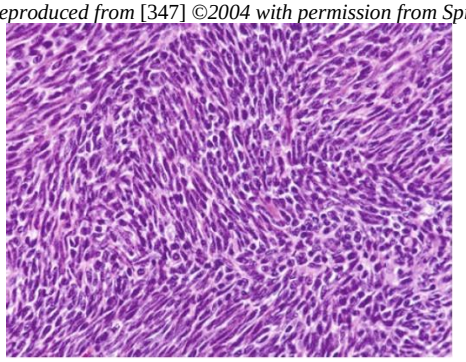

Figure 11 Hematoxylin eosin stain exhibiting leiomyoma tissue with marked hypercellularity. Reproduced from [347] *©2004 with permission from Springer Nature.*

2.2 Overview of Ultrasound Elastography

Manual palpation has been used by clinicians to detect dysfunction and pathology of human tissues since Hippocrates [122]. Through manual palpation, a skilled clinician can accurately measure the size of the uterus [123], assess cervix readiness for labor [124], [125], and clinically stage cervical carcinoma [126]. Indeed, certain prostate and breast malignancies exhibit much higher stiffness than unaffected tissues [113] and, in many cases, the mechanical properties of tissues have been linked to function, composition, and state (i.e. normal, benign, malignant) [54], [55], [106], [113], [127]. However, in most applications, palpation is limited to the assessment of superficial tissues [43], depends significantly on clinical experience [128]–[133], and exhibits low sensitivity [133]–[135]. As such, elastography, the use of biomedical imaging to provide non-invasive measures of tissue stiffness, has become a promising modality for the diagnosis and monitoring of pathologies [47], [136], [137].

The term elastography originally described the estimation of local strain induced in tissue from axial shifts in US echo arrival time after an applied quasi-static deformation [138]. Elastography involves using internal or external applied force(s) to cause local tissue deformations. Local mechanical properties are then estimated from these local tissue displacements, measured using medical images taken pre-, peri-, and/or post-deformation. Elastography may be performed using USI, magnetic resonance imaging (MRI), optical coherence tomography, X-ray computerized tomography (CT), and more [138]–[141]. This overview will specifically discuss ultrasound elastography (UE).

The different types of UE can be classified based on the elastic parameter that is being estimated or based on the type of excitation. In terms of classification by elastic parameters, UE techniques can be subdivided into three major types [43]. The first type, strain imaging, estimates strain or displacement of soft tissues in the axial direction (i.e. along the US beam) [138]. Outcomes for strain elastography are usually reported as strain ratios (SRs), a ratio of the strain in the affected and unaffected tissues [55], [56], [85], [142], [143]. Quasi-static strain imaging relies on strain arising from

compression/relaxation of the tissues. The second type, stress imaging, uses combined position-pressure sensors to measure superficial stress and strain patterns in tissues [144], [145]. The third type, modulus imaging, estimates the elastic modulus of the tissues using two possible techniques. The modulus can be calculated using estimates of tissue deformation and boundary conditions of the deformation combined with assumption of the stress distribution to solve an inverse problem. Alternatively, in shear wave elastography (SWE), acoustic radiation force (ARF) is used to create propagating shear waves in the tissues and the elastic modulus is estimated based on the relationship between the shear wave velocity and mechanical properties in the tissue, with an assumption of constant tissue density. SWE involves the use of (Equation 1) [47], where c_s, is the shear wave velocity, E is Young's modulus of the tissue, ρ is the density of the tissue, and v is Poisson's ratio of the tissue. Incompressibility is a simplifying assumption often used for soft tissues, due to their high water content, and is appropriate for characterizing macroscopic properties in cases where fluid exchange is negligible [146]. Assuming that soft tissue is incompressible ($v = 0.5$), Equation 1 becomes a simple relationship between the elastic modulus and shear wave velocity (Equation 2).

$$c_s = \sqrt{\frac{E}{2\rho(1+v)}} \quad (1)$$

$$E = 3\rho {c_s}^2 \quad (2)$$

Alternatively, the different types of UE can be classified based on the type of excitation used to elicit deformations in the tissues. UE operating by steady-state quasi-static excitation employs single or multiple quasi-static tissue deformation stages [138], [147] or steady-state quasi-static low-frequency excitation (1-10Hz) [148]–[150] to deform the tissues. UE employing harmonic steady-state excitation operates in the 10-1000Hz frequency range and excitation is applied by either an external loading source [151] or using a highly localized, low-frequency (kHz) dynamic acoustic radiation force (ARF) field [152].

Transient excitation in UE employs impulse loads, either a single impulse or repeated impulses (i.e. pulsed excitation), to deform the tissues [43]. In methods developed thus far, impulse excitation has been delivered by ARF [153], [154], while pulsed excitation has been delivered by ARF [115] or external electromagnetic vibrators [155]. Regardless of its nature, transient excitation generates shear waves: low speed waves with short wavelengths whose velocity can be related to the mechanical properties of the tissue (Equation 1). For this reason, many UE methods are grouped under the heading of shear wave elastography (SWE). Conversely, physiologic excitation in UE employs excitations of tissue deformation arising from naturally occurring (physiologic) sources (e.g. respiration [156], cardiac pulsation [157], [158], vascular pulsation [159]).

SWE is a specific type of UE which aims to improve upon other UE techniques that rely upon bulky external vibrators or manual palpation for tissue excitation [64], [115], [160], [161] and is better able to cope with heterogeneities in the focal region [64], [162]. It has been rapidly adopted for diagnosis and monitoring of liver fibrosis [57]–[62] and in the detection and differentiation of breast tumors [63]–[70]. Preliminary results suggest that SWE may have utility in the detection, diagnosis, and monitoring of gynecological conditions including uterine polyps, UFs [48]–[52], and cancers [49], [53], [54]. UE has promising potential for screening uterine masses [52], [54]–[56] and thus SWE may be useful in differentiating UF subtypes to aid in treatment planning and to improve outcomes [52], [54], [55], but further investigation is required

2.3 SuperSonic Shear Imaging

2.3.1 Overview of SuperSonic Shear Imaging

Supersonic Shear Imaging (SSI, Aixplorer, SuperSonic Imagine, Aix-en-provence, France) is a type of SWE developed by Bercoff et al. [207] to improve upon the limitations of other forms of UE. SSI employs transient pulsed ARF to create remote moving dipolar acoustic sources. Due to the motion of

these acoustic sources, constructive interference occurs to yield quasi-plane shear waves of larger amplitude (~100um in phantoms, ~40um in vivo) than other UE modalities (Figure 12). Ultrafast USI (up to 3000Hz) captures the motion of the plane shear waves in the tissue and correlation-based techniques are used to measure the speed of shear wave propagation in the tissue. Assuming incompressibility ($v = 0.5$), isotropy, and a uniformly linear elastic, infinite, homogeneous medium ($\rho = 1\frac{g}{cm^3} = 1000\frac{kg}{m^3}$), Equation 2 is applied to calculate the modulus in a specific region of interest (ROI). SSI generates a 2D map of tissue stiffness (i.e. elastic modulus) in the ROI in less than 30 ms with a comparatively rapid frame rate of 1Hz [64], [163].

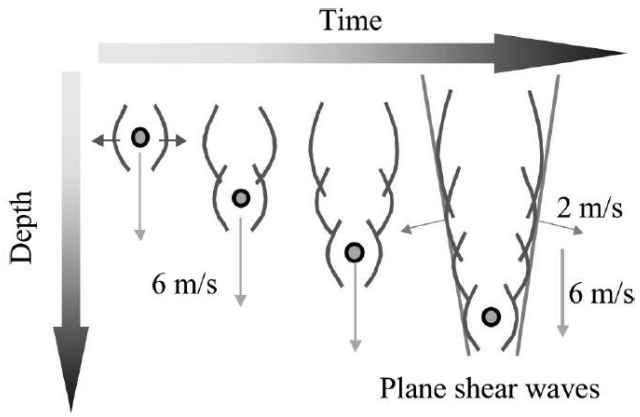

Figure 12 Supersonic Shear Imaging: the dipolar acoustic radiation force (ARF) source is sequentially moved along the ultrasound beam axis and constructive interference yields planar shear waves of larger amplitude. Reproduced, with permission, from [115]. *© 2004 IEEE*

2.3.2 Reliability of Supersonic Shear Imaging

The within- and between-day and intra- and inter-observer reliability of SSI has been reported in a variety of populations and under a variety of conditions. Reliability of SSI is often quantified using intraclass correlation coefficients (ICCs), a reliability metric computed as a ratio of variability in the outcome measure to the estimated biological variability in the population [164]. Depending on the application, reliability may be considered poor (ICC<0.40), fair (0.40<ICC<0.60), good (0.60<ICC<0.75), or excellent (0.75<ICC) [105]. Generally, SSI has been found to yield excellent within-day and within-rater reliability and good to excellent between-day and between-rater reliability. In a study of breast

phantoms, SSI measures of mean stiffness exhibited excellent intra-observer ($0.70 \leq \mathrm{ICC} \leq 0.94$) and inter-observer ($\mathrm{ICC} = 0.82$) reliability [103]. Considering a range of healthy and pathological human tissues in vivo, reliability of SSI, ranges from 0.75 to 0.95 within-day [99]–[101], [165] and 0.63 to 0.84 between-days [99], [101], [165]. Within- and between-rater reliability of SSI, quantified using ICCs, ranges from 0.75 to 0.98 [100], [101], [165], [166] and 0.65 to 0.97 [99]–[101], [165], [166], respectively. The reliability of SSI has yet to be evaluated in healthy or pathological uterine tissues, however Peralta et al. [167] found the reliability of SSI to measure cervix stiffness, using Cronbach's alpha (Cα) as an outcome, to range from 0.897 to 0.941 within-rater and 0.861 to 0.936 between-raters.

2.3.3 Validation of Supersonic Shear Imaging

2.3.3.1 Phantom Studies

SSI is quoted to have an estimation accuracy equal to the larger of ±30% or 3kPa [108]. These estimation accuracy values are derived from testing on a single rectangular polymer phantom (CIRS049 Quality Assurance Elasticity Phantom, CIRS, Norfolk, USA) with no phantom structures to simulate endocavity UE testing. Further, the CIRS phantoms for determining estimation accuracy have only four spherical targets over a limited stiffness range (29kPa background; 8.4kPa, 17.7kPa, 47.7kPa, and 80.1kPa inclusions) [108], which may not be an adequate sample size and stiffness range over which to characterize the validity of the system. Further, the units of measure (kPa vs. m/s), depth of the target ROI, angle of the imaging probe, and precompression by the imaging probe can all impact the accuracy of SSI measurements [71], [73], [81], [107], [168], [169]. While studies of SSI in phantoms, in vivo and ex vivo show promising results, specific validation of SSI for evaluating UFs is needed.

In a phantom that mimicked intra-cavitary imaging of prostate masses, Cao et al. [81] used the SSI 2D endoprobe (SE12-3, 3.0 – 12.0MHz) to measure the modulus of an agar phantom with

polyacrylamide (PAA, 2% Al_2O_3) inclusions at depths of 64.0 mm, 52.4 mm, 43.8 mm, and 36.6 mm and a silicone inclusion at 30.6 mm depth. The stiffness of these targets measured by SSI were 84.6±26.8 kPa, 93.8±4.4 kPa, 78.9±5.8 kPa, 86.2±4.5 kPa at the respective depths. The stiffness of the inclusions was also compared to quasi-static mechanical compression testing (1-2 N preload, 2 mm amplitude) for the 36.6mm deep PAA target and for the silicone target. SSI measures of these two targets' stiffnesses were 86.2±4.5 kPa and 271.5±25.7 kPa, respectively. Mechanical testing measured the targets' moduli to be 104.3±5.6 kPa and 297.3±6.7 kPa, respectively [81]. While the deepest target exhibited the largest standard deviation in SSI measures, there was good agreement in the mean stiffness measured across the four depths and good agreement between SSI and mechanical testing. This is expressly important, as the depth of penetration of the SE12-3 endoprobe is only quoted as 2.5 to 30 mm [108], however the system appears to perform well in a cavitary phantom model, as long as measures are averaged across multiple trials. Unfortunately, Cao et al. [81] did not report the number of measures taken at each depth.

Shin et al. [73] studied the effect of target depth and USI transducer on SSI measures of a 16.9 kPa ($v_{SWE} \approx 2.37$ m/s) liver fibrosis phantom (model 039, CIRS Inc., Norfolk, VA, USA) using the SC6-1 curvilinear probe (1.0 – 6.0MHz) and the SL10-2 linear probe (2.0 – 10.0MHz). Shear wave velocity was measured in the phantom using each probe at 2 cm, 3 cm, 4 cm, and 5 cm depths and 15 measurements were taken at each depth. Using the curvilinear probe, SSI measures of v_{SWE} were 2.37±0.05 m/s, 2.00±0.00 m/s, 1.90±0.00 m/s, and 1.98±0.04 m/s at the four respective depths. Using the linear probe, SSI measures of v_{SWE} were 1.80±0.00 m/s, 1.89±0.03 m/s, 1.90±0.00 m/s, and 1.99±0.05 m/s at the four respective depths. The transducers were found to yield significantly different measures at both 2 cm and 3 cm depths, but not at 4 cm or 5 cm depths. While there were significant differences in v_{SWE} between measures acquired by the different transducers at the two shallower sites and across the four sites for both probes, the coefficient of variation ($CV = \frac{\sigma}{\mu} * 100\%$) was 2% or less for all conditions. While these

results suggest that transducer type and target depth may impact v_{SWE}, low CVs suggest that SSI may still perform well in a larger study where between-patient variability exceeds depth or probe effects. The low number of trials in this study limits its applicability.

Many smaller phantom-based studies have also shown some potential for SSI to be used as a clinical and research tool. Widman et al. [170] studied six phantom models of plaques on the carotid artery (n_{soft}=3, n_{hard}=3) and compared SSI measures of shear modulus (G) to mechanical tensile testing in soft plaques (5.8±0.3 kPa and 3.3±0.5 kPa, respectively) and in hard plaques (106.2±17.2kPa and 98.3±3.4kPa, respectively). Dillman et al. [74] conducted a small phantom study of SSI at superficial depths (≤4.0cm), using the SL10-2 (2.0 – 10.0MHz) and SL15-4 (4.0 – 15.0MHz) SSI linear probes. Measures of v_{SWE} in both probes were affected by the depth of the target; however, measures were consistent across probes and there was no operator effect [74]. Franchi-Abella et al. [75] used a standardized phantom (model 049, CIRS, Norfolk, VA, USA) with targets ranging from 12 kPa to 74 kPa and found that SSI yielded CVs less than 4% at all targets [75]. However, findings from this study also showed that stiffness measures changed when the ROI position was more superficial or deep, with respect to an inclusion [75]. More recently, a study of SSI using standardized phantoms (model 049 & 049a, CIRS, Norfolk, VA, USA) found that measures of stiffer phantoms had lower precision (80 kPa target, 18.05 kPa error), while measures taken on lower stiffness targets yielded higher precision (<30kPa targets, <1kPa error) [77]. The same study found no consistent relationship in terms of accuracy or precision and target depth [77].

2.3.3.2 Tissue Studies

Ex vivo studies of human and animal tissues show strong relationships between SSI measures of tissue stiffness and various forms of mechanical testing. In a study of 8 fresh porcine patellar tendons under tensile loading of up to 10 N, multiple SSI images were captured during loading and correlations between experimental and SSI moduli ranged over $0.82 \leq \rho \leq 1.00$ ($p<0.05$ in all samples) [166]. Similarly,

another study showed significant moderate correlations between SSI measures of rabbit tendon stiffness in vivo and both the elastic modulus ($r=0.52$, $p<0.001$) and ultimate stress ($r=0.58$, $p<0.001$), measured in ex vivo tensile testing [171]. In a study of UE for breast cancer, Lee et al. [71] found that peak modulus measured in vivo by SSI correlated moderately with elastic modulus measured ex vivo by indentation testing [172]. However, Lee et al. [71] also observed that in grade III cancers, which show low fibrosis, high cellularity, and necrosis, SSI measures of tissue stiffness were significantly higher than indentation measures ($p<0.001$), compared to results found in grade I and II cancers ($p=0.268$). Further, SSI heterogeneity was correlated with heterogeneity in mechanical elasticity ($r=0.469$, $p=0.009$) and signal voids were associated with dense collagen depositions or necrosis [71]. Similarly, Ogawa et al. [173] conducted a study of liver fibrosis in twenty male rats, which included SSI, mechanical compression testing, and liver histology. Findings showed that liver SSI stiffness increased with histological inflammation ($p=0.002$), hepatic fibrosis ($p=0.029$) and ballooning ($p=0.012$), which is a type of liver parenchymal cell death [173]. In contrast, compression test measures of tissue stiffness increased only with increasing histological fibrosis ($p=0.033$) [173].

Findings from the literature continue to show that there is a moderate to strong relationship between in vivo SSI measures of tissue stiffness and ex vivo mechanical testing outcomes. In many cases, SSI is capable of measuring tissue properties reliably [99]–[101], [165], [166], however reliability appears to decrease with target depth [107]. Similarly, there appears to be a significant effect of target depth on the validity of stiffness measurements taken using linear and curvilinear probes in phantoms [73], [77], [78], [107]. Regardless, findings from the literature suggest that SSI may provide some insight into histological tissue properties (e.g. inflammation, fibrosis, malignancy [71], [173]). SSI has yet to be validated for the assessment of uterine masses and, like other clinical and research applications, reliability and validity must first be systematically established.

2.3.4 Limitations of Supersonic Shear Imaging

2.3.4.1 Assumptions

Many of the limitations of SSI are tied to the assumptions that allow the calculation of tissue stiffness from v_{SWE}. The assumption of a uniform, homogeneous, isotropic, infinite medium is regularly violated by anisotropy and heterogeneity of tissues and structures of the body. SSI also assumes incompressibility, linear elasticity, and constant density to allow for the calculation of E from v_{SWE}; however, it is clear that many soft tissues exhibit a substantial non-linear elastic response in compression and tension [54], [174]. The validity of the elasticity assumption may also be questioned in some cases, as many tissues exhibit a viscoelastic response to strain, which yields a dependency of v_{SWE} on excitation frequency and parameters [47]. The infinite medium assumption required for SSI calculation of tissue stiffness also breaks down in the case of thin tissue layers (e.g. bladder wall, blood vessels) [175]. Further, variability in excitation methods and estimation algorithms between different SWE systems may limit the translation of knowledge in the field of UE to clinical practice.

Anisotropy: While isotropy is assumed to facilitate the estimation of the tissue stiffness, anisotropy (i.e. different properties in different directions) is an inherent property of many human tissues. For example, the mechanical properties of uterine tissue may vary depending on the orientation of the muscle fibers with respect to the direction of loading [54]. An in vivo study of pig kidneys showed that SSI elasticity measures were higher when imaged perpendicular to the main pyramid axis compared to SSI measures taken parallel to the main pyramid axis [176]. In another case, the anisotropy measured by SSI, using two perpendicular imaging planes, was assessed as a potentially promising indicator of malignancy in solid breast lesions [177] and these findings were reproduced in a larger study [178]. Chatelin et al. [179] further observed the impact of muscle fiber orientation on SWE outcomes and developed a model to reproduce the experimental impact of probe orientation on SSI measures of stiffness in an anisotropic

phantom. The model was developed as a tool to enhance our understanding of elastography in anisotropic mediums. Further, spatial coherence measured during SSI has also been found to relate to anisotropy in bovine skeletal muscle and porcine myocardium [180]. Anisotropy of the tissues and structures may have particular relevance in the case of SSI imaging of uterine tissue as uterine orientation, and flexion (Figure 13), the mode of imaging (transvaginal vs. transabdominal), and the orientation of the imaging probe will all change the orientation of the fibers and borders of the uterus.

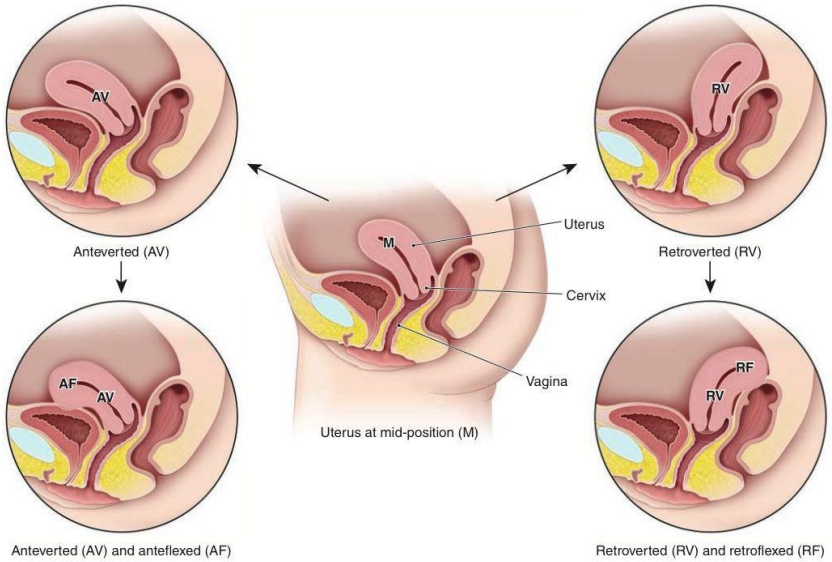

Figure 13 While anisotropy is a concern when measuring tissue stiffness by ultrasound elastography, we are also limited by the type of imaging (transabdominal, transvaginal), orientation of the uterus, and flexion of the uterus. Reproduced with permission from [181] *© 2006 Wolters Kluwer Health, Inc.*

Local and Global Heterogeneity: Similar to anisotropy, another concern for measures taken from SSI is the heterogeneity (i.e. different properties at different locations) within specific tissues or across anatomical structures in the body. Within a lesion, the presence of calcifications, which can increase tissue stiffness, or necrosis, which tends to be soft, can bias SSI elasticity estimates [161]. Alternatively, in organs adjacent to the bowels, peristalsis can impair SSI quality and limit reproducibility, while gas bubbles can cause shadows on USI, thereby decreasing the fidelity of SSI data [161]. Further, fluid and subcutaneous fat can attenuate the propagation of shear waves and invalidate measures [182], bringing the validity of SSI in obese patients or people with edema into question [183]. UFs are heterogeneous by nature, thus precluding our ability to control for this factor during SSI data acquisition.

2.3.4.2 *Tissue Precompression*

The effect of tissue compression, either static or dynamic, can further confound potentially valid measures of tissue stiffness made using SSI [54], [113], [168], [184]–[187]. In cases of non-linear elasticity, tissue precompression can shift the operating range on the stress strain curve, causing discrepancies in measures of mechanical properties, including the elastic modulus [168], [184], [187] (Figure 14). Barr and Zhang [168] developed a semi-quantitative method to assess precompression applied by the USI probe, tested using SSI (SL15-4 linear transducer, 4.0 – 15.0MHz). Pre-compression was gradually increased from 0% to 45% and measures were taken in a range of tissue types (e.g. cancer, fat, necrosis, glandular, fibrous, fibroadenoma). At 0% precompression, the stiffness of all tissue

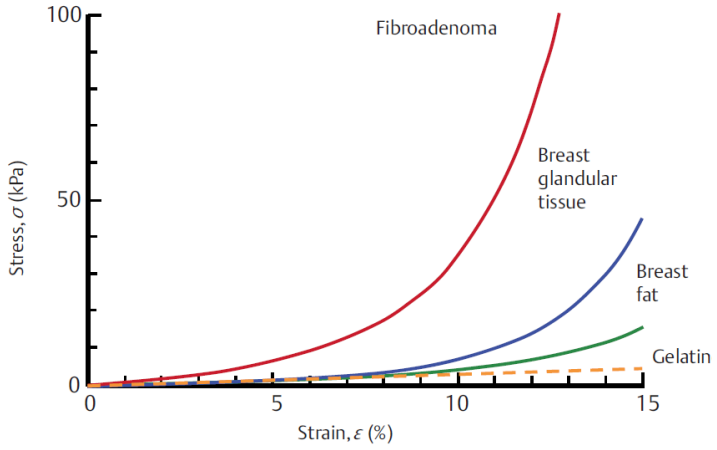

Figure 14 The linear elastic response of gelatin compared with the non-linear elastic response of various breast tissues. Reproduced with permission from [188] *© 2009 IEEE.*

types except cancer were ~0kPa, the stiffness of all tissues increased with precompression, and all tissues yielded stiffness measures of 300kPa by the 40% precompression. Barr and Zhang's [168] method for assess precompression yielded <10% variability across three raters for UE of breast lesions [168], however the sample size of the study was small (n=3), there was no quantitative validation of the methods, and the compression gradient that occurs with depth may limit the applicability of the method [168].

In the case of dynamic loading, tissue motion and compression caused by breathing during imaging is another concern. Pellot-Barakat et al. [79] investigated this phenomenon by comparing SSI measures taken in the liver during free-breathing and apnea. Findings showed that liver stiffness values taken during free-breathing and apnea were significantly correlated ($r=0.76$, $p<0.001$), however liver stiffness measured during free-breathing (range = [1.6 kPa, 27.7 kPa]) was consistently 20% to 25% lower than when measured during apnea (range = [2.0 kPa, 60.7 kPa], $p<0.001$) [79]. Further, SSI ROIs contained significantly more signal voids ($p<0.001$) and exhibited higher temporal variability ($p<0.005$) when acquired during free-breathing (mean % void pixels = 15.24%, mean temporal variability = 1.10 kPa) compared to apnea (mean % void pixels = 8.17%, mean temporal variability = 0.88 kPa) [79]. Temporal variability was quantified as the mean difference in stiffness across subsequent SWE data frames. These findings suggest that SSI stiffness measured during apnea may provide more robust outcomes than when collected during free-breathing.

2.3.4.3 Measurements in Thin Tissues

While large organs (e.g. breast, liver) are well suited to the infinite medium assumption required for the calculation of tissue stiffness from shear wave velocity (Equation 2), SSI validity appears to decrease in the case of thin tissues (e.g. bladder wall, blood vessels) [175]. Shear waves propagate in tissues only at low frequencies (<1000Hz), yielding small wavelengths (>10mm) that are larger than the thickness of many thin tissues (e.g. arterial wall <2mm [189]). These relatively large wavelengths in relatively thin tissues result in guided mode propagation [190]; the external surfaces of the thin tissue act as a wave guide and the shear waves can propagate along multiple paths [191]. Consequently, different frequency components of the shear wave packet can propagate with different phase velocities, distorting the shape of the wave packet (i.e. dispersion). This wave dispersion invalidates the standard

relationship between shear wave velocity and material properties implemented for non-invasive estimation of tissue stiffness in SWE.

To address this limitation of SWE in thin tissues, Couade et al. [191] used a guided wave model (Lamb wave model) to relate shear wave dispersion to tissue stiffness in thin phantoms and in the carotid artery. Further investigation of elastography implementing guided wave models in vascular tissue [191]–[193], the bladder [194], and on tendons [195] has also shown potential. However, shear wave dispersion is highly dependent on boundary conditions, geometry, and pre-stress in soft tissues [191], [192], [196]–[199]. Thus further development of this methods for estimating the mechanical properties of thin tissues from SWE is required [190].

As an alternative to these complex models, Mo et al. [175] proposed an empirical formula to correct SSI estimations of material properties; the corrected elastic modulus was estimated as a function of the measured elastic modulus, tissue thickness, and SWE pulse repetition frequency. Finite element simulation was used to develop the empirical model and comparison was performed against an anti-symmetric Lamb wave model. Results showed that the measured Young's modulus decreased with sample thickness in phantoms with thicknesses <15mm. Finite element modelling suggested that the empirical model gave the best agreement for a 600Hz pulse repetition frequency. When the empirical model was compared with a finite element model and a Lamb wave model, the three models showed good agreement for thicknesses below 5mm, but for thicknesses between 5mm and 15mm, the Lamb wave model appeared to underestimate tissue stiffness while the empirical model showed good agreement with the finite element simulations. The elastic moduli of the phantoms were never measured using mechanical testing, however results from this study suggest that this empirical model is a simplified and promising tool for estimating tissue stiffness in thin-walled structures.

2.3.4.4 *Variability of UE Systems*

Another limitation of SWE is the inter-system variability, which can limit meaningful comparison across different UE systems. The Radiology Society of North America (RSNA) has undertaken two multisite studies to compare current generation UE systems capable of measuring v_{SWE} [80], [200]. The first study included stiffness measures of 11 custom phantoms (CIRS, Norfolk, VA, USA) taken using five different UE systems, including SSI [200]. Measures across SWE systems were in good agreement; SSI measures were within the range of dynamic mechanical testing results, but there appeared to be more variability in SSI measures with increasing target depth (up to 7.0 cm) [200]. In a follow-up multisite study, RSNA members again investigated seven SWE systems capable of measuring v_{SWE}, including SSI, using three liver phantoms (models A1, B3, C1, E2297, CIRS, Norfolk, VA, USA) [80]. Findings showed that intersystem variability (median v_{SWE}) appeared to increase with depth (17.7% at 7 cm depth), but was consistent across all phantoms and did not relate to the stiffness of the target region in the phantoms [80].

More recently, a study comparing SSI and the Siemens UE system (ACUSON S3000™, Siemens, Erlangen, Germany) found a mean difference of 0.37±0.3 m/s (~20±16 kPa) in v_{SWE} when imaging a bovine tendon ex vivo loaded to between 0 N to 18N [201]. There were strong correlations between the tangent modulus and both the SSI ($0.827 \leq r \leq 0.954$, $p<0.001$) and the Siemens UE system ($0.877 \leq r \leq 0.915$, $p<0.001$); however, exact values for the tangent modulus were not reported. Another study comparing SSI and Siemens (ACUSON S3000™, Siemens, Erlangen, Germany) SWE systems using manufactured phantoms (CIRS, Norfolk, VA, USA) found v_{SWE} measures in a soft phantom were 0.84±0.04 m/s and 0.90±0.02 m/s ($p=0.003$), respectively [74]. In a hard phantom, the systems showed good agreement with v_{SWE} measures of 2.14±0.08 m/s and 2.07±0.03 m/s ($p>0.05$), respectively [74]. There were significant differences between the systems in terms of results acquired using the soft phantom, however CVs were low (0.5-6.8%), suggesting that the systems showed somewhat good agreement in this specific case [74]. Unfortunately, while the manufacturer of the phantoms was

reported (CIRS, Newark, VA, USA), the models and the theoretical stiffness of the material were not reported [74].

2.4 In vivo Elastography of Uterine Pathologies

Elastography has only recently begun to be used for applications in uterine pathologies. The majority of studies investigating UF and uterine tissue stiffness using UE to date have used strain imaging [48], [52], [56], [142], [143]. However, magnetic resonance elastography (MRE) [202]–[206] and SWE [207]–[209] have also been used. Few studies that applied SSI to the investigation of uterine pathologies were identified in the literature [121], [209].

2.4.1 Strain Elastography

Indeed, early results when using strain elastography to investigate endometrial pathologies have been promising. In 106 women with a thickened endometrium, Gultekin et al. [142] observed good intra-operator (ICC=0.633) and inter-operator (ICC=0.649) reliability of strain elastography for measuring endometrial tissue stiffness. Findings from this study showed significant differences ($p<0.001$) in SRs between normal endometrium (n=64, mean SR=1.06±0.11), endometrial hyperplasia (n=22, SR=0.67±0.10), and endometrial polyps (n=20, mean SR=0.28±0.08). Interestingly, Abdel Latif et al. [210] observed higher SRs in typical endometrial hyperplasia (mean SR=1.96, range = [0.90,4.00]) compared to Gultekin et al. [142], as well as drastically higher SRs in endometrial carcinoma (n=13, SR=11.40±3.05) compared to typical and atypical endometrial hyperplasia (n=32, SR=2.75±1.81). These conflicting results between two different studies may be a factor of small sample sizes combined with biological variability in material properties of these neoplasms. Alternatively, Abdel Latif et al. [210] did not explicitly define their calculation of the SR outcome and may have inverted their SR from the standard format (i.e. $SR = \frac{unaffected\ tissue\ strain}{target\ tissue\ strain}$).

Strain elastography has also shown promise for the assessment of the myometrium in cases of uterine pathologies. In a sample of 10 women, Frank et al. [143] observed excellent intra-operator (ICC=0.987) and inter-operator (ICC=0.983) reliability of strain elastography for measuring myometrium stiffness. Further, SRs were significantly different between healthy myometrium tissues (n=143, SR=1.19 [1.07,1.34]), UF tissues (n=41, SR=2.65 [2.12,3.34]), and tissues exhibiting adenomyosis (n=22, SR=0.44 [0.36,0.46]) [143]. Stoelinga et al. [51] used a qualitative assessment of strain elastography color maps from 218 women and found adenomyosis to be softer ("brighter") than myometrium and UFs to be stiffer ("darker") than myometrium. In contrast to Frank et al. [143], Liu et al. [211] found that SRs in women with confirmed adenomyosis (n=112, SR=3.90±1.00) were significantly higher than SRs in women with UFs (n=67, SR=2.68±0.66), which were in turn significantly higher than in women with no known uterine pathology (n=130, SR=1.54±0.82). In this study, the stiffness of lesions correlated positively with uterine size and fibrosis (determined by Masson Trichrome staining) and correlated negatively with PrR expression levels [211]. Lesion stiffness also correlated with the severity of dysmenorrhea and menses [211]. In a much smaller study ex vivo, Hobson et al. [212] observed that SRs were quite different between small UFs (<1.5cm diameter, n=5, SR=1.75±1.14), larger UFs (>1.5cm diameter, n=10, SR=2.5±1.15), and endometrial polyps (n=3, SR=0.40±0.05). These findings are particularly relevant to the proposed application of SWE in this document, considering that the literature suggests that the larger UFs tend to exhibit a specific subtype of genetic mutation [213].

Strain elastography has also shown promise as a tool for diagnosis and treatment monitoring. In a study of 218 women comparing qualitative strain elastography of UFs, adenomyosis, and healthy uterine tissue, Stoelinga et al. [51] found that qualitative strain elastography showed excellent agreement with MRI and substantial agreement with histology [51]. A smaller study on the qualitative assessment of strain elastography in submucosal UFs (n=18) and endometrial polyps (n=29), found significantly higher diagnostic accuracy from qualitative strain elastography (89.4%) than USI (70.2%,

p=0.0265) and power Doppler (65.9%, p=0.0153) [48]. Moreover, in a study of women undergoing MRI guided focussed ultrasound (MRgFUS) treatment, Marigiliano et al. [214] observed a significant correlation between the extent of symptom reduction and the decrease in SR post-treatment. The reduction in SR was particularly significant in UFs with >70% non-perfused volume [215], where 100% non-perfused volume is considered complete ablation of the UF [216]. A few other studies have investigated strain elastography for application in uterine pathologies [52], [217], [218], however limitations based on study designs (e.g. case reports, lack of comparator, incomplete reporting) limits the comparative value of these studies.

More recently, Sun-Wei Guo' et al. have been evaluating shear wave elastography for application in uterine pathologies [211]. In a study of 309 women, unaffected myometrium (n=130), UF (n=67), or adenomyosis (n=112) tissues were evaluated in vivo using strain elastography and ex vivo using histology. Tissue stiffness outcomes for the study were taken using a built-in outcome for elastography of the liver: liver function index (LFI; Aloka ARIETTA 70, Hitachi, Tokyo, Japan). LFI is a composite measure of several strain characteristics. Their findings showed that the LFI of AM lesions (LFI=3.66±1.02) was significantly higher ($p<0.001$) than that of UF tissues (LFI=2.79±0.69), which, in turn, was significantly higher ($p<0.001$) than that of unaffected myometrium tissue (LFI=1.42±0.59). Tissue LFI measured by UE exhibited positive correlations with fibrosis in fibroids ($r=0.85$, $p<0.001$) and moderate correlations with severity of dysmenorrhea ($0.32<r<0.48$, $p<0.001$). There was no relationship between fibroid size and LFI ($r=-0.09$, $p=0.69$). Multiple linear regression did not show any relationships among age, menstrual phase, parity, pre-operative use of hormone therapy, uterine size, or UF size and LFI, however linear regression with large numbers of predictors and small sample sizes (n=67) may be subject to overfitting and yield spurious results [219]. The clinical and mechanical relevance of the LFI outcome to uterine pathologies is unclear.

2.4.2 Magnetic Resonance Elastography

Magnetic resonance elastography (MRE) is another type of elastography imaging, which includes the addition of a phase shift of a "motion sensitive" magnetic-field gradient to standard MRI sequences for estimating voxel motion (related to strains and mechanical properties of the tissue). While a detailed overview of MRE is beyond the scope of this thesis, in vivo and ex vivo measures of the mechanical properties of the uterus are sufficiently rare in the literature and measurements taken by MRE measurements of the uterus are included here for reference purposes.

Stewart et al. [202] assessed the feasibility of MRE for use in cases of UFs and found that the mean stiffness of UFs ranged from 3.95 kPa to 6.68 kPa across six patients. A second feasibility study found that MRE was able to detect increases in mechanical stiffness of UF tissues after MRgFUS treatment, however data were not presented in the abstract [206] and a peer reviewed manuscript detailing the study has yet to be published. Another small study of 11 patients undergoing MRgFUS found that a substantial decrease in symptom severity was associated with a reduction in UF tissue stiffness [205]. A study of 102 patients by Jondal et al. [208] found that MRE was able to differentiate between UFs yielding high intensity T2W signals, signals that were isointense with the myometrium, and low intensity signals. This study confirmed prior suspicions that UFs with high intensity T2W were softer, while UFs with low T2W intensity were stiffer [208]. Moreover, the intensity of UFs on MRI has been linked to ablation efficiency of MRgFUS, measured by non-perfused volume, and long-term reductions in UF volume post-treatment [220]. While, with adequate sample sizes, MRE may have potential in treatment planning and monitoring of UFs, the high cost, limited availability, and human resource implications (time, skill) pose huge limitations in terms of translation to practice.

2.4.3 Shear Wave Elastography

To date, there have been several peer reviewed studies reporting on the potential of SWE for application in the evaluation of uterine pathologies (Table 1). Furukawa et al. [221] used SWE to

measure v_{SWE} in a case of leiomyosarcoma where histological analysis was also performed to characterize the tissue (fibrosis, necrosis, viable). Substantial heterogeneity was observed in tissue histology and in SWE measures [221]. Viable tissue was associated with high stiffness (v_{SWE}= 4.14±0.22 m/s), fibrosis was associated with intermediate stiffness (v_{SWE}= 3.71 ±0.66 m/s, v_{SWE}= 2.19±0.0 4m/s), and necrosis was associated with low tissue stiffness (v_{SWE}= 1.55±0.26 m/s) [221]. In a larger study investigating the feasibility of ARF imaging for the assessment of uterine tissues stiffness, Soliman et al. [222] measured shear wave velocity in a sample of 32 women who varied in menopausal status and hormonal contraceptive use. Repeated measures taken in the myometrium (v_{SWE}= 2.82±0.77 m/s) and endometrium (v_{SWE}= 2.05±0.77 m/s) were consistent at each site, however there was no statistical reliability assessment (Figure 15).

In an study of uterine pathologies using SSI, Zhang et al. [121] found that shear wave velocity of the myometrium in women with no pathology (n=16, v_{SWE}=4.3±1.7 m/s) was significantly lower ($p<0.001$) than shear wave velocity in women with MRI diagnosis of myometrial pathology (n=18, v_{SWE}=5.7±2.3 m/s). However, once the groups were stratified by diagnosis of adenomyosis (n=6, v_{SWE}=4.9±2.5 m/s) or UFs (n=12, v_{SWE}=5.6±2.5 m/s), the statistical difference disappeared [121]. There was no significant difference in shear wave velocity measured in UF and adenomyosis tissue (p=0.40) [121].

Similarly, in a study of 97 women with suspected adenomyosis, using SSI, Acar et al. [209] found that tissue stiffness was lower in women with no uterine pathology (n=97, E_{mean}=24.4kPa±2.3 kPa) than in women with confirmed adenomyosis (n=39, E_{mean}=72.7kPa±9.9 kPa). Interestingly, there was no difference in SSI measures of uterine tissue stiffness between healthy controls and women who were suspected of having adenomyosis on USI but had no clinical findings of adenomyosis (n=14, E_{mean}=28.3kPa±3.0 kPa). Using a receiver operating characteristics (ROC) curve, a mean stiffness cutoff of E_{mean}=34.6k Pa was found to yield a sensitivity of 89.7% and a specificity of 92.9% for the diagnosis of

adenomyosis. There have been other studies where SWE was used to differentiate UFs from other tissues or to monitor response to treatment, however incomplete reporting limits the applicability of the results. Further, the currently available studies are quite preliminary and limited by lack of data indicating reliability and validity of SWE in cases of symptomatic UFs.

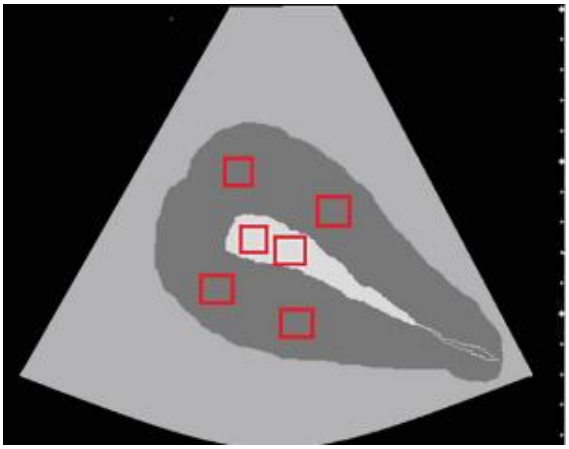

Figure 15 Soliman et al.'s [222] *ultrasound elastography imaging sites in the midsagittal endometrium and myometrium. Reproduced from* [222] *© 2015 with permission from IOS Press .*

Table 1 Summary of shear wave elastography findings in the literature measured using Supersonic Shear Imaging (SSI) and acoustic radiation force impulse imaging (ARFI) in women with no pathology (aymptomatic), adenomyosis (ADM), uterine fibroids (UFs), or other pathologies. Measurements were taken on lesions, in the myometrium, or in the cervix. Stiffness outcomes were measured using Young's Modulus (E) or shear wave velocity (c_s) and quantified as mean ± standard deviation (std) or median [range].

Authors	UE Type	Sample	n	Site	Age		Outcome & Units	Outcome		Statistical Analysis
					Median	Range		Magnitude	Variance	
Acar et al. 2016 [209]	SSI	Asymptomatic	56	Myometrium	30	[21-45]	E (kPa) median [range]	24.4	[17.9-32.4]	ADM stiffer than asymptomatic & pathology group (p<0.05)
		Pathology (no ADM)	14	Lesion	47	[32-58]		28.3	[12.7-59.5]	
		ADM	39	Lesion				72.7	[22.3-274.2]	
Furukawa et al. 2014 [221]	ARFI	Leiomyosarcoma	1	1cm deep lesion	70	NA	c_s (m/s) mean±std	4.14	±0.22	1cm vs 4cm p<0.05; 1cm vs 6cm p<0.05; 2cm vs 4cm p<0.05
				2cm deep lesion				3.71	±0.86	
				4cm deep lesion				1.55	±0.26	
				6cm deep lesion				2.19	±0.04	
		UF	1	random site 1	50	NA		4.07	±0.36	No differences.
				random site 2				3.77	±0.66	
				random site 3				4.1	±0.40	
				random site 4				3.88	±0.73	
Soliman et al. 2015 [222]	ARFI	Asymptomatic	32	Myometrium	42	[19-68]	c_s (m/s) mean±std	2.82	±0.77	Myometrium stiffer than endometrium (p<0.001)
				Endometrium				2.05	±0.77	
Zhang et al. 2019 [121]	SSI	Asymptomatic	34	Cervix	36.8	[22-52]	c_s (m/s) mean±std	5.3	±2.0	Cervix stiffer than myometrium (p=0.04)
		Asymptomatic	14	Myometrium				4.8	±1.9	p=0.34 no significant difference
		ADM	6	Lesion				4.9	±2.5	
		UF	12	Lesion				5.6	±2.5	

2.5 Mechanical Tissue Testing

In order to assess the validity and clinical relevance of UE for characterizing soft tissue properties, mechanical testing is generally regarded as the gold standard in material characterization [54], [71], [72], [89], [106], [113], [172], [186]. Mechanical testing of solid materials involves controlled deformation or loading of a material, while measuring force and displacement [127]. These data are then incorporated into a mathematical model, where the coefficients in the model may represent specific mechanical properties of the material. In order to execute mechanical tissue testing, an understanding of the material properties of interest is necessary.

2.5.1 Quantifying the Mechanical Properties of Soft Tissues

A wide range of mechanical tests and mathematical models have been employed in the literature to characterize the properties of soft tissues ex vivo. Mechanical testing may be performed to characterize the stiffness of material samples globally or locally [89], [106], [186]. In both cases, testing may be performed using dynamic or quasi-static testing conditions. Loading during mechanical testing can be applied along one axis or biaxially [223], with uniaxial testing generally used for UE applications [54], [89], [90], [106], [113], [224]–[227]. Further, a wide array of material models are available for characterizing viscoelastic material properties [127], [228]–[230].

Tissue testing for UE applications may involve loading the tissues in compression or tension. While tensile testing is most appropriate for tissues loaded under tension in vivo (i.e. muscles, tendons, blood vessels) [94], [170], [225], [231]–[233], it often requires gripping of the sample, which may result in slippage thereby complicating the boundary conditions [88]. Gripping tissues for tensile testing can also cause tissue damage, which may not be acceptable for biological specimens [88]. Compressive testing is generally used for UE applications in tissues that are not subject to primarily tensile loads in vivo, and may take on the form of global ramp compression or local indentation [54], [89], [90], [106], [113], [224]–[227]. Global ramp compression of soft tissues is generally regarded as the ideal method for

measuring tissue properties, however specimen irregularity, non-uniform surfaces, and small geometries may limit the validity of tissue characterization using this approach [88]. Indentation testing addresses many of the limitations of tensile and compression testing; a wide array of material models are currently used for characterizing material properties by indentation [88], [109], [111], [112], [114]. In the literature, several tests and models have been applied for the purposes of UE validation.

2.5.1.1 Dynamic Tissue Testing

Dynamic tissue testing allows for the characterization of both the elastic and time-dependent (i.e. viscoelastic) material properties [54], [89], [90], [106], [113], [224]–[227]. Dynamic mechanical testing can be performed locally (e.g. indentation) or globally (e.g. ramp compression). For UE applications, dynamic tissue testing usually involves cyclic (sinusoidal) loading of the tissue sample [54], [89], [106]. Generally, only small deformations are applied to respect the assumption of linearity; however, the deformation range over which linear assumptions are valid varies depending on the tissue properties [54], [89], [113].

The complex Young's modulus (E*) [127], [229], with the assumption of linear viscoelasticity and isotropy, has been used for many cases of tissue testing in UE applications [54], [83], [89], [106], [186]. Christensen's [229] formulation of the complex modulus, expressed using a Stieltjes integral, has been applied for cases of dynamic (sinusoidal) ramp compression and can be simplified to a function of the loading frequency (ω), peak-to-peak stress amplitude (σ_0), peak to peak strain amplitude (ε_0), and the phase angle (δ) between the stress and strain curves (Equation 3) [54]. This formulation of the complex modulus also allows for quantification of the *storage modulus* (E_S), a measure of the energy storage during loading, and the *loss modulus* (E_L), a measure of energy lost between loading and unloading (Equation 3) [54]. Alternatively, data may be presented in terms of the magnitude ($|E^*(\omega)|$) and phase ($\tan\delta$), referred to as the loss factor, of the complex modulus [54].

$$E^*(\omega) = \frac{\sigma_0}{\varepsilon_0}(\cos\delta + i\sin\delta) = E_S + iE_L \quad (3)$$

As an alternative, Krouskop et al. [113] performed dynamic (and quasi-static) indentation testing on breast and prostate tissues with a sinusoidal displacement control. Their work applied Timoshenko and Goodier's [114], [230] model of a uniform load acting at the surface of a semi-infinite linear elastic, nearly incompressible (ν=0.495), isotropic solid to estimate Young's modulus of breast and prostate tissue. This formulation expresses Young's modulus as a function of Poisson's ratio (ν), the load per unit area (σ; i.e. stress under the indenter tip), the indenter radius (a), and the depth of indentation (w; Equation 4). Krouskop et al. [113] applied this model to cases of quasi-static (0.1Hz) and dynamic (1Hz, 4Hz) loading rates. This study did not include any quantification of energy loss or hysteresis during mechanical tissue testing [113].

$$E = \frac{2(1-\nu^2)\sigma a}{w} \quad (4)$$

For cases of dynamic nano-indentation testing to characterize local mechanical properties of soft tissue samples, Herbert et al.'s [234] adaptation of Christensen's formulation [229] developed for viscoelastic solids, has been applied in several studies [89], [106]. This formulation draws on the expression of the storage modulus (E_S; Equation 5) and the loss modulus (E_L; Equation 6), the real and complex components of the complex modulus (Equation 3). Based on the parameters of the nano-indentation test, the storage (Equation 7) and loss modulus (Equation 8) can be expressed in terms of Poisson's ratio (ν), the amplitude of load oscillation (F_0), the amplitude of the displacement oscillation (h_0), the phase lag (δ), the projected contact area of the indenter (A), and a geometry term (β). The geometry term is equal to 1 for a circular projected contact area (flat cylinder, sphere, cone indenters) and 1.034 for a Berkovich indenter. Similar to Christensen's formulation [229], mechanical properties may be presented in terms of the magnitude ($|E^*(\omega)|$) and phase ($\tan\delta$) of the complex modulus [89], [106].

$$E_S = \frac{\sigma_0}{\varepsilon_0}\cos\delta \quad (5)$$

$$E_L = \frac{\sigma_0}{\varepsilon_0}\sin\delta \quad (6)$$

$$E_S = \frac{(1-\nu^2)\sqrt{\pi}}{2\beta\sqrt{A}}\frac{F_0}{h_0}\cos\delta \quad (7)$$

$$E_L = \frac{(1-\nu^2)\sqrt{\pi}}{2\beta\sqrt{A}}\frac{F_0}{h_0}\sin\delta \quad (8)$$

Dynamic tissue testing allows for thorough observation of a viscoelastic material's stress-strain response, which in turn allows for characterization of material stiffness and viscoelastic behavior. However, dynamic testing must be performed under a variety of conditions (e.g. preload, strain amplitude, frequency), thereby increasing testing duration, which may decrease the viability of tissue samples [127]. As an alternative, quasi-static testing, though unable to characterize viscoelastic response, can be used to characterize the mechanical properties of biological tissue with a more rapid testing procedure [71], [72], [90]–[92], [94], [172].

2.5.1.2 Quasi-static Tissue Testing

Quasi-static tissue testing is often used as an alternative to dynamic testing for quasi-static and dynamic UE applications. While quasi-static tissue testing does not simulate the high loading frequencies observed in SSI [115], it can still provide accurate, efficient, and economical means of material characterization [71], [72], [88], [89], [94], [109], [111], [113], [172]. Quasi-static tissue testing has been used to characterize global (e.g. ramp compression) [89] or local (e.g. indentation) [71], [72], [172] material properties for UE applications. Quasi-static tissue testing may involve cyclic (sinusoidal) loading [113] or loading/unloading at a constant strain rate [89]. Similar to dynamic testing, elastic modulus calculations are often made over small deformations to respect linearity assumptions [71], [72], [113], [172].

For healthy and pathological uterine tissue, Omari et al. [89] used quasi-static ramp compression testing with a constant strain rate (0.1% per second) over large deformations. Substituting these testing parameters into Boltzmann's superposition integral and simplifying yields an expression of the elastic modulus as a function of time (t), stress (σ), and strain rate ($\dot{\varepsilon}$; Equation 9). Under the assumptions of a linear elastic, isotropic material, the elastic modulus was then characterized over small strain amplitudes (2%) for comparison with other testing outcomes.

$$E(t) = \frac{1}{\dot{\varepsilon}} \frac{d\sigma}{dt} \tag{9}$$

Quasi-static indentation testing is also commonly used to characterize soft tissue properties as it requires minimal sample preparation, minimizes potential damage to the tissues, and may bypass the uniformity and larger geometric requirements of other types of material testing [88]. Zhai et al. [172] and Lee et al. [71] used quasi-static indentation testing for local characterization of phantom and soft tissue material properties for UE applications. These studies implemented the Snedden [110] model, which was popularized by Oliver and Pharr [109] and assumes quasi-static testing conditions to calculate the modulus of a homogeneous semi-infinite linear elastic medium under a cylindrical, flat indenter tip with a small strain assumption. The definition of a "small" strain was not included in this work. Using the analytic solution by Boussinesq [114], the elastic modulus (E) is expressed as a function of the applied force (P), the radius of the indenter tip (a), the Poisson's ratio (ν), and the indentation depth (δ) with no conversion factor [72], [172] (Equation 10).

$$E = \frac{(1 - \nu^2)}{2a} \frac{P}{\delta} \tag{10}$$

Similarly, Amador et al. [72] used the Hayes model [112], a common mathematical model used for indentation testing of biological tissues. The Hayes model [112] assumes a lateral infinite isotropic elastic material with a finite thickness resting on a rigid half space with only small strains applied [72]. A sample of tissue is placed on the indenter mounting plate and a plane end indenter of radius a is

brought into contact with the tissue surface, assuming adhesion at the sample-mounting plate interface, negligible shear tractions at the indenter-sample interface, infinitesimal deformation (<0.1% strain), and frictionless indenter surface [111], [112]. The shear elastic modulus (G) for indentation testing performed using a flat-end cylindrical indenter (Figure 16) is given in (Equation 11), where v is Poisson's ratio, P is the applied load, δ is the depth of the indentation (displacement), a is the radius of the indenter, h is the thickness of the tissue sample, and κ is a constant determined by the sample geometry and Poisson's ratio (v; **Error! Reference source not found.**) [112]. Alternatively, using the r elationship outlined in Equation 25, the Hayes model can be used to express the elastic modulus as a function of the same variables (Equation 12).

$$G = \frac{(1-v)}{4a\kappa(v, a/h)} \frac{P}{\delta} \tag{11}$$

$$E = \frac{(1-v^2)}{2a\kappa(v, a/h)} \frac{P}{\delta} \tag{12}$$

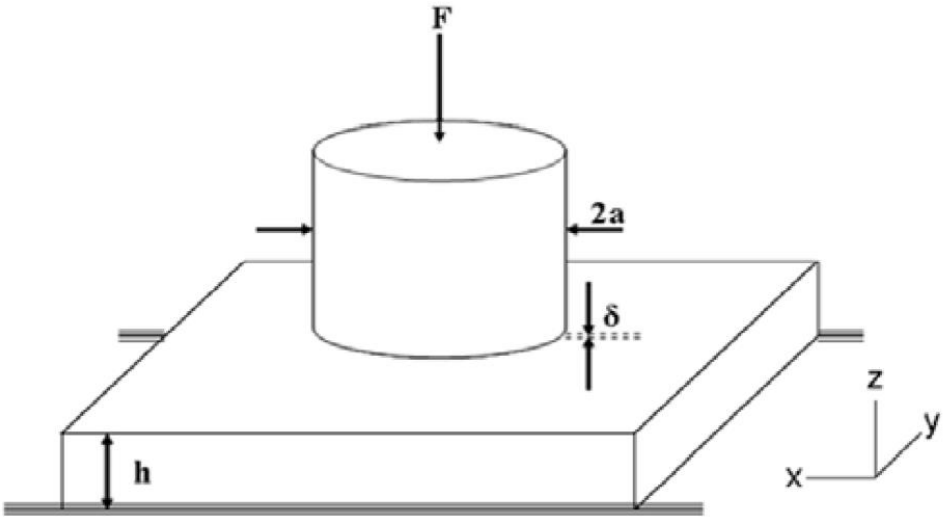

Figure 16 Experimental set up for plane-end indentation testing, where F is the force applied by the cylindrical indenter onto the tissue sample, δ is the indentation depth, a is the radius of the indenter, and h is the thickness of the material sample. Reproduced with permission from [72]. *© 2011 IEEE*

In 1997, Zhang et al. [111] addressed the limitation of Hayes' [112] small strain and frictionless contact assumptions for indentation testing in biological tissues. Using non-linear finite element modelling, a new series of constants (κ) were calculated for use in Equation 11 or Equation 12 for indentation using a flat end cylindrical indenter under large deformations. Similar to Hayes' [112] work, the constants presented in this updated model are a function of sample thickness (h), indenter radius (a), and Poisson's ratio (ν); however, Zhang et al.'s [111] constants are also a function of strain (**Error! R eference source not found.**, **Error! Reference source not found.**, **Error! Reference source not found.**). Finite element modelling showed that friction between the indenter tip and test surface increases with the ratio a/h; while this effect can be ignored at smaller a/h, friction should be considered for larger ratios (a/h >2) as it can theoretically cause substantial error in estimates of E (up to 33% for a/h =2). This refinement of the Hayes [112] constants has been found to improve calculation of the shear and elastic modulus for large strains (up to 20%) [88] and linear interpolation of the constants presented by Zhang et al. [111] can be used for estimation of the elastic modulus at these larger strains [88].

In a review of indentation testing for biological tissues, Delaine-Smith et al. [88] performed a quantitative comparison of the mathematical models presented by Hayes [112] and Zhang et al. [111], Snedden [110] and Oliver and Pharr [109], and Timoshenko and Goodier [114]. Delaine-Smith et al. [88] applied these indentation models to characterize the "reduced" or "effective" elastic modulus (E_R) as a function of the indenter tip modulus (E_i), the indenter Poisson's ratio (ν_i), the tissue sample modulus (E_s), and the tissue sample Poisson's ratio (ν_s, Equation 13) [109]. In all cases in this study, $E_i >> E_R$ and the definition of the reduced modulus was simplified (Equation 14). The reduced modulus was characterized as a function of indentation stiffness (S), where the indentation stiffness was defined as the slope of the load-displacement (P-δ) curve ($\frac{dP}{d\delta}$). Calculations of material parameters from indentation testing using

these mathematical models were compared to the same outcomes found using global bulk compression testing for hydrogel polymers, diseased human omentum, and bovine articular cartilage.

Delaine-Smith et al.'s [88] findings revealed that all indentation models showed strong correlations with global ramp compression testing when used to quantify the tangent elastic modulus from 2.5% to 7.5% strain and from 15% to 20% strain. Oliver and Pharr's [109] model showed the best agreement for sample thickness (T_s), indenter diameter (Φ_i), and sample diameter (Φ_s) for certain "ideal" geometric relationships (T_s:Φ_i>=1:1 and Φ_s:Φ_i>=4:1). When samples deviated from these "ideal" relationships (T_s:Φ_i<1:1 and/or Φ_s:Φ_i<4:1), Zhang et al.'s [111] improved Hayes [112] model showed the best agreement. A series of indentation and compression tests on hydrogels were used to develop a correction factor (G_k) to improve agreement between Zhang et al.'s [111] improved Hayes [112] indentation model for a series of specific non-ideal geometric cases. Testing on the human omentum tissue and the bovine articular tissue validated the corrections to Zhang et al.'s [111] model for non-ideal geometries.

$$\frac{1}{E_R} = \frac{1 - {v_s}^2}{E_s} + \frac{1 - {v_i}^2}{E_i} \tag{13}$$

$$E_R = \frac{E_s}{1 - {v_s}^2} \tag{14}$$

While quasi-static testing omits the time-dependent properties in the characterization of viscoelastic materials, these methods reduce the duration of testing and can be appropriate in many applications. Omari et al. [89] observed that while elastic modulus estimates from quasi-static ramp compression testing of healthy and pathological uterine tissue were larger than those obtained with dynamic testing, quasi-static testing results exhibited comparable trends to those observed with dynamic testing. Delaine-Smith et al.'s [88] findings showed strong correlations between indentation and bulk compression testing, where the best agreement for non-ideal geometries was exhibited by an updated Hayes model. Quasi-static indentation testing provides a rapid, economical, non-destructive

mechanical tissue testing alternative to dynamic tissue testing for characterizing soft tissue properties and still allows for characterizing material nonlinearity through quantification of hysteresis and stress relaxation [71], [88], [172]. Further, indentation testing can provide non-destructive, valid characterization of tissue mechanical properties for the small and irregular geometries common to soft tissue applications [88].

2.5.1.3 Quasi-static Indentation Testing of Soft Tissue for SSI Applications

Lee et al. [71] used elastography phantoms (model 049a, CIRS, Newark, VA, USA), ranging from 8 kPa to 80 kPa, to validate indentation testing, using indenters with radii of 1.0 mm and 2.4 mm, by measuring the modulus of the materials at the center and peripheries of all samples. Their findings showed that test repeatability, measured by ICCs, was above 0.99 for both radii of indenters and at all locations in the masses [71]. Further, the modulus measured by indentation was well within the bounds of estimated moduli on all phantoms tested [71].

Lee et al. [71] followed their preliminary phantom study with an evaluation of the relationship between SSI, indentation testing, and histology. Indentation measures of tissues stiffness were taken at five regions across malignant breast tumor samples from 30 masses excised from 30 women (center, superior, inferior, superficial, deep). Their findings showed significant moderate correlations between peak stiffness (kPa) measured by SSI and indentation stiffness ($r=0.530$, $p=0.003$), however no significant relationships were found between indentation stiffness and mean SSI stiffness ($r=0.163$, $p=0.390$) or minimum SSI stiffness ($r=0.191$, $p=0.312$). Indentation stiffness was positively correlated with tissue fibrosis ($r=0.505$, $p=0.004$) and negatively correlated with cellularity ($r=-0.415$, $p=0.023$) and necrosis ($r=-0.367$, $p=0.046$), while there was no significant correlation with microcalcification of the tissue ($r=-0.08$, $p=0.671$). This study also found that both SSI and indentation measures of peak stiffness were

significantly higher in breast cancer tissue excised from patients with lymph node metastases, compared to those without.

While correlations in Lee et al.'s [71] study were often moderate or non-significant, the number of indentation measurement sites was small in comparison to the SSI ROI resolution (~1 mm), and a larger number of indentation testing sites may increase the strength of the correlations. Malignant tumors, such as those tested by Lee et al. [71], are known to exhibit large amounts of heterogeneity and thus would likely benefit from averaging outcomes over a larger number of indentation testing sites [235], [236]. However, increasing the number of testing sites increases the duration of testing and can reduce the viability of the tissue. With only five testing sites being used, median stiffness may be a more appropriate mechanical tissue testing outcome for comparison with SSI measures. Further, Lee et al.'s [71] SSI data appeared to be retrieved from only a single image, while the literature suggests that averaging SSI over multiple frames and multiple trials can reduce the variability of SSI outcomes and provide more robust outcomes [76], [102], [104]. Finally, depending on the range of tissue geometries, indenter geometries, and testing parameters implemented [88], the material model used by Lee et al. [71] may not have been ideal, however the limited data from the literature requires further investigation to better understand this potential limitation.

There are many limitations of quasi-static indentation testing identified in the literature [106]. Measures are typically taken at room temperature, not body temperature, and the modulus can vary with tissue temperature [113]. Unfortunately, heating tissue samples is not feasible as it would lead to desiccation. Only a few sites can be indented per sample, as the longer the tissue is in dry air, the more quickly it desiccates. The number of testing sites is further limited by the indenter diameter, where larger indenters yield more robust measures, but less information. One strategy may be to randomize testing sites on the tissue and check for correlations between time and measures from indentation testing; however, depending on the test setup, this may limit the use of automated actuators, which

reduce the duration of the testing protocol, thus allowing for more sites to be tested. Heterogeneities in the tissues may also bias measures and ex vivo tissue testing removes all physiological loading on the tissues which may reduce the correlations between in vivo SSI and ex vivo indentation testing [71]. Despite its limitations, mechanical tissue testing is the best approximation of a gold standard to which UE can be compared, and quasi-static indentation testing appears to be an appropriate modality against which to validate SSI.

2.5.2 Ex vivo Mechanical Tissue Testing of the Uterus

Several studies in the literature have quantified the mechanical properties of healthy and pathological uterus and cervix tissue using a variety of methods. Unfortunately, all known studies to date are limited in their applicability to this work by small sample sizes of pathological uterine tissue, especially with regards to UF samples ($n \leq 6$). While more recent studies investigating gynecological applications of UE focus on compressive mechanical properties of healthy and pathological tissue ex vivo [54], [89], [94], [186], a series of older works focus on mechanical measurement of active force generation of myometrial tissue ex vivo and are beyond the scope of this thesis [237]–[239]. A subset of research completed mid-20th century investigated the tensile properties of the myometrium [240]–[244], which are different from compressive properties. Distinct tensile responses between pregnant and non-pregnant myometrium were unrelated to age, parity, phase in the menstrual cycle or tissue histology [241], [242].

2.5.2.1 Mechanical Tissue Testing of the Uterus

Kiss et al. [54] collected myometrium tissue samples from 24 patients (age 31 to 79 years, mean=50.4±10.8 years). Uterine fibroid (n=6) and unaffected myometrium (n=24) tissue samples

underwent (sinusoidal) bulk compression testing at a range of precompressions (ε=[1.5%,2.5%,3%]), strain amplitudes (ε_0=[1%,2%]), and testing frequencies (0.1 Hz to 100 Hz). Testing parameters were determined based on the observation of a non-linear response for strain amplitudes above 5% and non-uniform deformation for strain amplitudes below 1%. The order of testing parameters was randomized for each sample, though a qualitative comparison of cases tested using randomized testing frequencies compared with descending testing frequencies suggested that there was no effect of testing order on outcomes. Myometrial tissue was tested parallel or perpendicular to the muscle fibers. Christensen's [229] formulation (Equation 3) was used to characterize the global storage modulus, loss modulus, and magnitude of the complex modulus. It should be noted that although a dynamic model was applied in this case, sample dimensions (~5 mm thick) combined with the strain amplitudes, precompressions, and lower testing frequencies (0.1 Hz) yield between 0.005 mm/s and 0.01 mm/s testing speed, which many would qualify as quasi-static [71], [72], [91], [94], [172], [245].

Findings from Kiss et al.'s [54] work showed that the modulus ($|E^*(\omega)|$) of both myometrium and UF tissue increased monotonically with the testing frequency and that the loss factor decreased between the 0.1 Hz and 1 Hz, then increased with testing frequency up to 100 Hz for all tissue types. The myometrial tissue modulus ranged from 20 kPa to 115 kPa, and UF tissue modulus ranged from 40 kPa to 230 kPa, depending on the testing parameters. Myometrial tissue testing along the muscle fibers exhibited moduli between 10% and 25% higher than those measured perpendicular to the muscle fibers. At all strain amplitudes and testing frequencies, the UF moduli were substantially higher than the myometrium moduli (Figure 17a) and the loss factors for all tissue types were similar (Figure 17b).

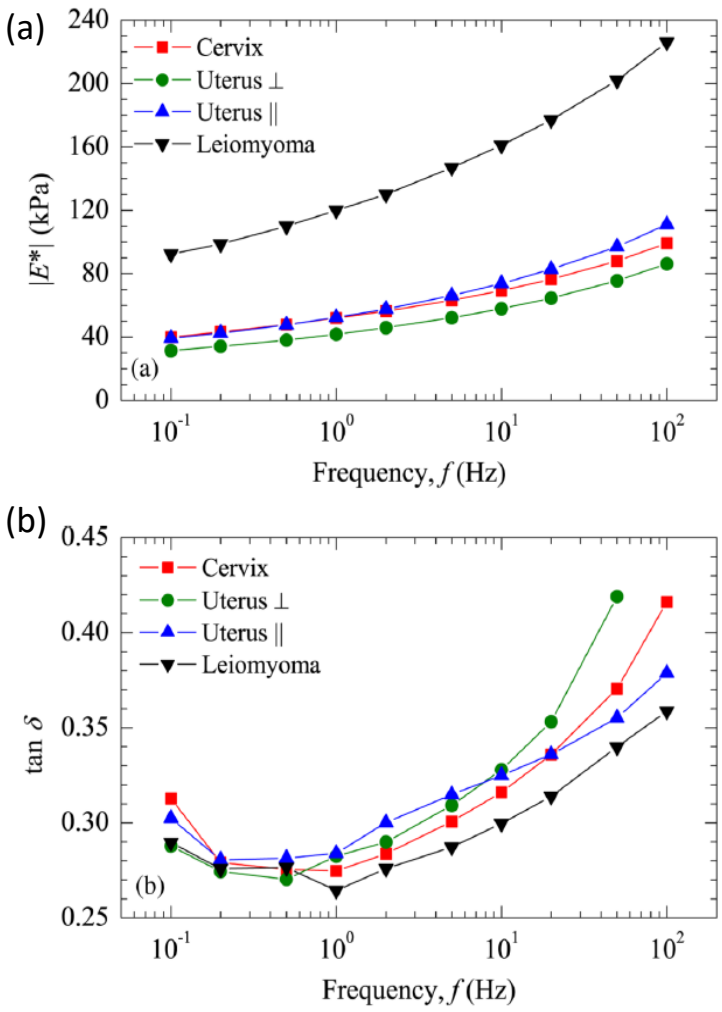

Figure 17 The frequency dependent modulus (|E|; a) and loss factor (tan δ; b) of cervix, uterus, and uterine fibroid (leiomyoma) tissue measured in compression from 2-3% strain amplitudes for a range of testing frequencies (Hertz, Hz). The uterus tissue was tested along the muscle fibers (||) and perpendicular to the muscle fibers (⊥). Reproduced from* [54] *©2007 Institute of Physics and Engineering in Medicine. Reproduced by permission of IOP Publishing. All rights reserved.*

Omari et al. [89], [246] also observed the frequency dependent nature of the complex modulus and loss factor of unaffected and pathological uterine tissues. Omari et al. [89], [246] used dynamic global ($n_{unaffected}$=18; n_{UF}=2; n_{cancer}=1), quasi-static global ($n_{unaffected}$=14; n_{UF}=4; n_{cancer}=2), and dynamic local ($n_{unaffected}$=9; n_{UF}=1; n_{cancer}=1; $n_{adenomyosis}$=1; n_{polyp}=1) testing to characterize the mechanical properties of unaffected, UF, cancer, polyp, and adenomyosis tissue from the uterus. Dynamic (sinusoidal) bulk compression tests at a range of testing frequencies (f=[1Hz, 10Hz, 20Hz, 30Hz]), precompressions

(ε=[2%,3%,4%,5%,6%]), and strain amplitudes (ε_0=[2%,3%,4%]) were used to quantify the complex modulus (Equation 3) on 20 tissue samples from 18 patients (mean age=53.8±14.2 years). Quasi-static (load/unload, constant $\dot{\varepsilon}$=0.1% per second) bulk compression from 0.1% to 15% strain was used to quantify Young's modulus (Equation 9) at a range of compression values (ε = [(1-3%), (2-4%), (3-5%), (4-6%), (5-7%), (6-8%)]) and to qualitatively assess hysteresis in 20 tissue samples from 14 patients (mean age=54.1±14.7 years). Finally, dynamic (sinusoidal) indentation testing was used to locally quantify the complex modulus (frequency = 1Hz) and build 2D stiffness maps for 9 tissue samples from 9 patients (mean age = 52.0±13.4 years).

Findings from Omari et al.'s [89], [246] dynamic and quasistatic testing expanded on the work of Kiss et al. [54]. Dynamic testing results showed that the magnitude of the complex modulus ($|E^*(\omega)|$) of unaffected uterine tissue, uterine fibroids tissue, and uterine cancer tissue ranged from 5 kPa to 30 kPa, 20 kPa to 60 kPa, and 5 kPa to 8 kPa, respectively, depending on testing parameters. The calculated modulus was the same, regardless of strain amplitude, while increasing the precompression resulted in the monotonic increase of the modulus for all tissues. This was observed at all testing frequencies except 20Hz, which appeared to yield erroneous results due to technical errors. Similar to Kiss et al. [54], the mean modulus appeared to increase with testing frequency for all tissues, although error bars for testing frequencies between 10Hz and 30Hz appeared to overlap for a majority of testing conditions. While the magnitudes of the complex modulus increased with testing frequency and precompression, trends between the tissues (cancer = soft, unaffected = midrange, UF = hard) were the same across all testing conditions (Figure 18). Interestingly, as with Kiss et al.'s [54] findings, Omari et al. [89], [246] observed that the loss factor was fairly constant for each tissue type across the testing conditions. Interestingly, the loss factor for UF and unaffected myometrium tissue were almost identical, while the loss factor of the cancerous tissue differed substantially (Figure 19).

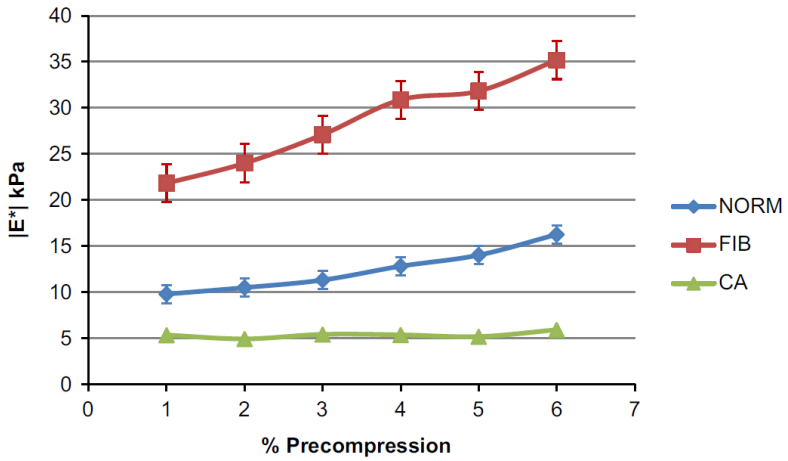

Figure 18 The magnitude of the complex modulus (|E|) as a function of the precompression (strain as a percent), tested at strain amplitude of 2% and a frequency of 1Hz, for unaffected (NORM; n=18), uterine fibroid (FIB; n=2), and uterine cancer (CA; n=1) tissue. Reproduced from* [89], [246] *© 2014 with permission from Elsevier.*

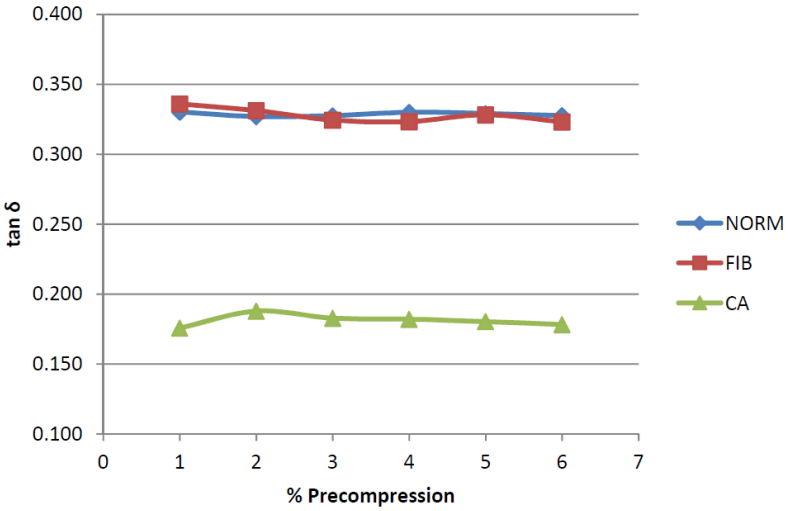

Figure 19 The loss factor (tan δ) as a function of the precompression (strain as a percent), tested at strain amplitude of 2% and a frequency of 1Hz, for unaffected (NORM; n=18), uterine fibroid (FIB; n=2), and uterine cancer (CA; n=1) tissue. Reproduced from [89], [246] *© 2014 with permission from Elsevier.*

Omari et al.'s [89], [246] findings from quasi-static ramp compression testing and dynamic nano-indentation were comparable to the dynamic testing results (Figure 20). Quasi-static testing yielded higher modulus values than dynamic testing for all tissue types, however trends were consistent across testing parameters and tissue types. Local measures of tissue stiffness were also used to quantify the modulus of unaffected myometrium tissue (|E*|=22.6±18.2 kPa), one case of uterine cancer

(|E*|=17.98±10.0Pa), one endometrial polyp (|E*|=9.98±3.7 kPa), one uterine fibroid (|E*|=36.0±11.0 kPa), and one case of a proliferative endometrium (|E*|=26.9±6.0 kPa). When data were pooled across all cases, the ranges of tissue stiffness overlapped substantially. However, two measures of myometrium stiffness (|E*|=54.6±1.1 kPa) were substantially larger than the rest of the group (|E*|=13.5±1.6 kPa). Further, in the case of each pathology, the modulus of the given pathology tended to differ from the surrounding unaffected tissue ($|E^*|_{cancer}$=17.98±10.0 kPa and $|E^*|_{unaffected}$=55.4±10 kPa; $|E^*|_{polyp}$=9.98±3.7 kPa and $|E^*|_{unaffected}$=15.5±3.9 kPa; $|E^*|_{fibroid}$=36.0±11.0 kPa and $|E^*|_{unaffected}$=15.8±7 kPa). These findings suggest the potential value of contrast ratios (similar to SRs).

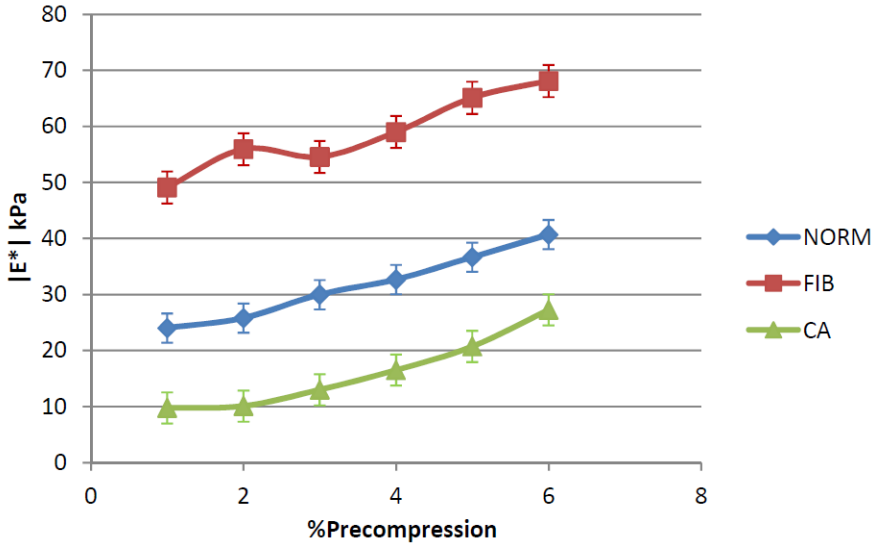

Figure 20 The complex modulus (|E|) as a function of the precompression (strain as a percent), calculated at strain amplitudes of 2% and a frequency of 0.1Hz, for unaffected (NORM; n=14), uterine fibroid (FIB; n=4), and uterine cancer (CA; n=2) tissue. Reproduced from* [89], [246] *© 2014 with permission from Elsevier.*

Pearsall and Roberts [243] performed quasi-static ramp compressive testing (speed = 0.085 mm/s) on ~23 samples of unaffected myometrium tissue taken from the anterior wall and/or the fundus of the uterus. Uterine samples were cored from the organ and relaxation was observed after coring. Stress-strain curves were calculated and then true stress ($\sigma_t = \sigma(\varepsilon + 1)$) and true strain ($\varepsilon_t = \ln(\varepsilon + 1)$), which incorporate instantaneous sample geometry, were calculated to better understand the intrinsic properties of the material. Results from this study showed a consistent nonlinear response

of the tissue and a large variation in the length of the toe region and the slope of the linear region (Figure 21a). Interestingly, when viewed on a logarithmic scale, the results showed that true stress-strain response was approximately linear above 6.9 kPa (1 Psi) and the authors presented a simple expression to characterize responses above this threshold (Equation 15; Figure 21b) in terms of two constants (C and B). Unfortunately, no information on the number of patients, demographics, or anthropometrics were reported.

$$\varepsilon_t = C \ln \sigma_t + B \qquad (15)$$

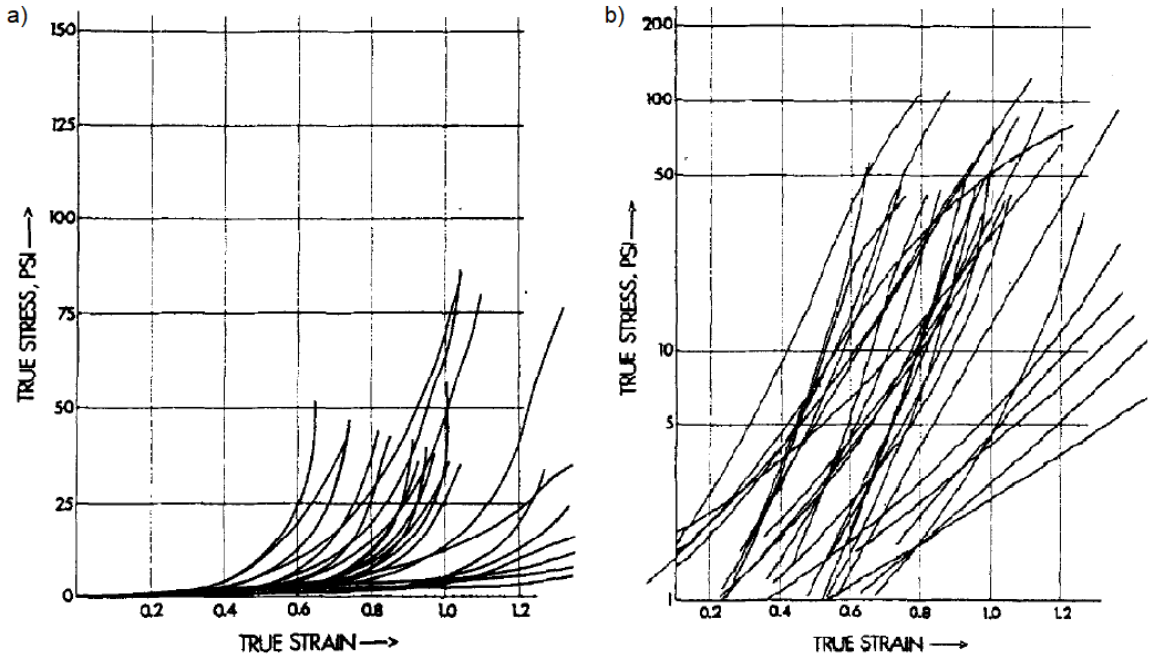

Figure 21 True stress-strain response of uterine muscle to quasistatic bulk compressive loading presented on a linear (a) and logarithmic (b) scale. Reproduced from [243] *© 1978 with permission from Elsevier.*

Although no statistical testing was documented in any of these works, qualitatively, the findings for both Kiss et al. [54], Omari et al. [89], [246], and Pearsall and Roberts [243] suggest somewhat consistent stiffness of unaffected myometrium tissue, with the potential for outliers. Findings from Kiss et al. [54] and Omari et al. [89], [246] also show that that the modulus of UF tissue may be substantially higher than that of the uterus at the available range of testing parameters. However, it should be noted

that, for the same testing conditions, the moduli of UF tissues reported by Kiss et al.'s [54] appear to be substantially higher than those reported by Omari et al. [89], [246]. Further, Kiss et al. [54] reported that one of six fibroids tested exhibited a lower modulus than the normal tissue from the same patient. While this was surprising to Kiss et al. [54], based on Omari et al.'s [89], [246] findings, this phenomena may not be as unique as originally thought. Hobson et al. [247] observed a large range in strain contrast ratios between UF and unaffected uterus tissues when performing ex vivo strain elastography of the uterus, in the absence of any signs of necrosis or hemorrhage. There is currently insufficient information in the literature on the variability of mechanical properties of UF tissues and further research is required to validate the characterization of UFs by UE and support UE as a potential tool for treatment planning in cases of symptomatic UFs.

2.6 Aims and Objectives

The goal of this dissertation was to determine if tissue stiffness, non-invasively measured by endoprobe SWE, is a feasible method for the in-vivo assessment of uterine tissue stiffness. This general goal was broken down into a series of specific aims, each of with included several objectives and associated outcomes. The dissertation is structured such that, following a review of the literature in Chapter 2, each specific aim functions as the central purpose of an individual study that is described in depth in an individual chapter of this work.

2.6.1 Aim 1: The Validity of Endoprobe SWE Estimates of Stiffness

Chapter 3 of this work describes Study 1 of this the dissertation. The aim of Study 1 was to evaluate the validity and reliability of the stiffness (i.e. the elastic modulus) estimated by endoprobe SWE in an adequately sized sample of homogeneous oil-in-gelatin tissue mimicking (TMM) phantoms, using unconfined quasi-static ramp compression testing as a criterion standard. The general omission of endoprobe SWE from the literature discussing the validity of SWE estimates of stiffness limits our ability to interpret findings from in vivo endoprobe SWE studies and the generalizability of these results. This

study quantifies the validity of endoprobe SWE measures of stiffness by (1) assessing the reliability of endoprobe SWE estimates of material stiffness in TMM phantoms at three target depths (1cm, 3cm, 5cm), (2) assessing the accuracy of endoprobe SWE measures of material stiffness in TMM phantoms, using unconfined quasi-static ramp compression testing as a criterion standard, and (3) comparing endoprobe SWE reliability and accuracy to that of linear and curvilinear SWE ultrasound probes in TMM phantoms. By quantifying the reliability and accuracy of endoprobe SWE measures of stiffness in TMM phantoms and placing this within the context of the more widely accepted linear and curvilinear SWE probes, this study delivers clear performance metrics for endoprobe SWE that will influence its clinical utility moving forwards.

2.6.2 Aim 2: The Validity of Indentation Estimates of Stiffness

The next step in validating endoprobe SWE involves evaluating in vivo SWE tissue stiffness against ex vivo mechanical testing stiffness estimates from those same resected tissues. However, the small, non-uniform tissue geometries characteristic of surgical samples require indentation stiffness as a benchmark outcome and indentation testing parameters require independent validation. Thus, the purpose of Study 2 of this thesis, which is detailed in Chapter 4, was to evaluate the validity of indentation testing with unconfined quasi-static ramp compression testing as a criterion standard, under a series of testing and model parameters, for an adequately sized sample of oil-in-gelatin TMM phantoms over a 100 kPa moduli range.

In particular, using unconfined ramp compression testing estimates of material stiffness as the criterion standard, the objectives of this study were to (1) investigate the validity of indention stiffness measured using the Oliver and Pharr indentation model [109], [110] and Zhang et al.'s [111] improved Hayes [112] indentation model, (2) investigate the impact of indentation strain, sample geometry, and quasi-static testing speed on indentation stiffness validity, (3) evaluate the correction equations

developed by Delaine-Smith et al. [88] to improve indentation model accuracy, and (4) to provide recommendations around experimental use of indentation testing in fresh tissue samples. To the author's knowledge, this study is the only work in the literature providing a systematic validation of soft tissue indentation testing parameters in an adequately sized sample targeted towards in vivo SWE validation approaches.

2.6.3 Aim 3: Optimal Indentation Parameters for the Validation of SWE

While Study 2 clearly quantifies the validity of indentation testing, there may be certain indentation parameters to optimize the agreement between mechanical testing and SWE estimates of stiffness. With this in mind, Chapter 5 of this work describes Study 3, the aim of which was to provide a systematic investigation of the impact of indentation testing parameters and material models on the agreement between indentation stiffness and SWE measures of material stiffness for an adequately sized sample of oil-in-gelatin TMM phantoms over a 100 kPa moduli range. In particular, the objectives of this study were to: (1) investigate the impact of the indentation model on agreement between indentation stiffness and SWE stiffness, (2) to investigate the impact of two sample geometries, a large (thickness > 5mm) and small (thickness < 5 mm), on the agreement of indentation and SWE measures of material stiffness, (3) investigate the impact of three quasi-static testing rates (0.01 Hz, 0.055 Hz, and 0.1 Hz) on the agreement between indentation and SWE measures of stiffness, and (4) investigate the impact of three strain ranges (toe region, 2.5%-7.5%, and 15%-20%) on the agreement of indentation and SWE measures of stiffness. Findings from this study have the potential to allow for optimization of indentation testing parameters for SWE validation applications and potentially support the pooling of SWE validation study outcomes and improve generalizability of validation data in this field.

2.6.4 Aim 4: In vivo Reliability and Confounders on SWE Measures of Uterine Tissue Stiffness

The first three studies in this thesis provide a quantitative estimate of endoprobe SWE stiffness validity in a TMM phantom model and generate data to support in vivo validation of endoprobe SWE. In the fourth study, this research takes the first step into investigating the feasibility in vivo endoprobe SWE measures of uterine tissue stiffness. Chapter 6 of this work details Study 4, the aim of which was to assess the reliability of SWE to non-invasively measure tissue stiffness of uterine tissue in vivo and to evaluate the impact of potential confounding factors, including phase in the menstrual cycle, target depth, and site in the uterus. In particular, the objectives of this study were to: (1) determine if SWE estimates of in vivo uterine tissue stiffness were reliable within-day and between-days within the same phase of the menstrual cycle, (2) assess the impact of phase in the menstrual cycle on SSI measures of uterine tissue stiffness, (3) investigate the impact of target site in the uterus and depth of target site on tissue stiffness, and (4) provide a qualitative evaluation of any potential confounders on estimates of uterine tissue stiffness made using SWE. This study is essential to determining the utility of uterine SWE and the outcomes provide the data needed to justify or nullify the complex and costly next step, which is evaluating estimation accuracy of in vivo SWE stiffness against ex vivo indentation testing.

2.7 Contributions

This dissertation serves as an initial proof-of-concept that will provide quantitative data to direct and support the currently sparse field of gynecological elastography. Data from this work bridges the gap between endoprobe SWE and more conventional and clinically acceptable forms of SWE that implement linear and curvilinear probes. The performance metrics for endoprobe SWE established here using TMM phantoms and non-pathological populations will allow clinicians and clinical researchers to make informed decisions on the potential value of endoprobe SWE and the optimal avenues for gynecological SWE research. Moreover, the study of indentation testing parameters and mathematical models for SWE applications included in this work is the first of its kind and addresses a major gap previously identified in the SWE validation literature around the use of mechanical testing and selection of mechanical testing parameters [95]. The recommendations generated through this work will support in vivo validation of endoprobe SWE and future investigations that will be needed as elastography technology develops and demonstrates a wider range of clinical utility. Finally, the in-vivo experiments systematically assessed the reliability of endoprobe SWE measures of tissue stiffness and provided insight into potential confounders that may require further investigation. Taken together, this work will form the basis for future work to inform on endoprobe SWE for the medical and surgical management of uterine pathologies.

2.8 Conclusion

The literature documents important current and potential future applications for UE the clinical diagnosis and management of many pathologies. Reports of intra- and inter-rater and intra- and inter-day repeatability are consistently high and measures within each elastography technique are somewhat consistent. However, variability in elastography techniques, inconsistency in outcomes reported, and lack of reporting of sample characteristics limit the clinical value of this modality for uterine pathology applications. Technical limitations around the elastography estimates of tissue stiffness and the validation techniques limit researchers' ability to applying UE in gynecological pathologies. Prior to exploring the utility of SSI for clinical gynecology, it is essential that we establish the validity and reliability of SSI in phantoms and establish robust mechanical testing techniques for in vivo validation. Moreover, the performance of SSI in unaffected uterine tissue must also be evaluated to characterize baseline in vivo measures of unaffected uterine tissue stiffness.

This dissertation involved the completion of four studies which, taken together, provide guidance around the feasibility of using SSI to identify mechanical tissue properties in uterine tissue, and will direct future efforts in this specialized field. The first study involved evaluating the reliability and validity of endoprobe SWE in a sample of tissue mimicking (TMM) phantoms, using quasi-static unconfined ramp compression testing at the criterion standard. The second study evaluated the validity of quasi-static indentation testing under a variety of testing parameters, using two mathematic models, using quasi-static unconfined ramp compression testing at the criterion standard. The third study systematically investigated the impact of indentation testing parameters and mathematical models on the agreement of indentation and SWE measures of material stiffness. Finally, the fourth study assessed the reliability of SWE of uterine tissue stiffness in vivo and evaluated the impact of a series of potential confounding factors. The studies from this thesis provide an initial proof-of-concept that we hope will catalyze the currently sparse field of gynecological elastography.

3 Study 1: Validity and Reliability of Endoprobe Shear Wave Elastography in Homogeneous Tissue Mimicking Phantoms

3.1 Introduction

Shear wave elastography (SWE), an ultrasound modality used for the non-invasive measurement of tissue stiffness, is gaining popularity as a diagnostic aid and monitoring tool for many pathologies [57], [58], [67]–[70], [59]–[66]. While preliminary investigations of SWE for gynecological applications show promise [48]–[56], systematic investigations of gynecological SWE lag behind other SWE applications [57], [58], [67]–[70], [59]–[66]. Further, the omission of gynecological endoprobe data from the majority of SWE validation studies presented in the literature [71]–[80] poses a problem to the valid interpretation of SWE data acquired using an endovaginal SWE probe, such as is the case for many gynecologic applications. While a series of validation studies has been performed using linear [71]–[76] and curvilinear [77]–[80] SWE probes, SWE endoprobes have a unique geometry, center frequency, and curvature with unique excitation sequences and thus require separate validation.

The small sample sizes used in the systematic validation of SWE is another area of concern. Cao et al. [81] detailed the performance of an SWE endoprobe for measuring the stiffness of phantoms made of tissue mimicking materials (TMMs). This work aimed to assess the agreement between SWE and mechanical testing measures of material stiffness but included only two different material stiffnesses, with a single target depth in the first and five target depths for the second (31 mm, 37 mm, 44 mm, 52 mm, and 64 mm). Five targets of unique stiffness and depth appears to be the standard sample size threshold for validating UE in the literature [71]–[75], [77]–[80]. This may be due to the limited number of targets available in commercially available standardized phantoms [71]–[75], [77]–[80] or the time required for manufacturing quality phantoms in-house [82]–[87]. Cao et al.'s [81] findings suggested that agreement between SWE and mechanical testing decreased at depths beyond 44 mm and variance in agreement increased at depths beyond 52 mm. The small sample size combined

with the limited range of material stiffnesses limits quantitative analysis of agreement, leaving an incomplete picture of endoprobe SWE validity.

Many statistical tests used to assess validity require a minimum sample size threshold. In the case of correlation analyses, a sample size of at least n=19 is required to detect a significant moderate correlation (α=0.05; β=0.20; r= 0.60) [248], [249]. If a regression model is used to assess validity, Babyak [219] and Peduzzi [250], [251] both showed that a sample size of at least n=10 to n=15 (per predictor) is necessary provide adequate power to detect true relations and avoid significant bias. When Bland Altman analysis is used to assess validity, sample size can similarly influence the power of the analysis. For example, if the expected mean difference (MD) between UE and a gold standard is ~4kPa, the expected standard deviation (STD) is ~2kPa [77], and the maximum allowable MD is ~10kPa, then a sample size of n=26 is required to achieve 80% power (β=0.20) with α=0.05 [252]. In this case, the typical sample size used in validation studies of SWE (n=5) yields a power of <5%, which is not adequate [252]. Thus, adequate sample sizes in SWE validation studies should lie between n=10 and n=26, depending on the statistical test and parameters used to assess validity.

In-house manufactured TMM phantoms are an economical method for validating gynecological UE, allowing for the study of an adequate sample size with appropriately tuned mechanical properties. Oil-in-gelatin dispersions [82], [84] are economical option that allow for tuning of mechanical properties across a wide range of stiffnesses (20kPa < storage modulus < 100kPa [82], [84], [253]) that align closely to those of human tissue [87]. The manufacture and storage of oil-in-gelatin dispersions have been well documented in the literature [82]–[85], [87], [254]. Acoustic and material properties (sound speed, density, attenuation) of oil-in-gelatin TMMs also lie well within the range of properties displayed by human soft tissues [82], [87]. Further, oil-in-gelatin TMMs are inexpensive, easy to manufacture, and can be tuned to the desired mechanical and acoustic properties,

making oil-in-gelatin TMM phantoms ideal for developing adequately large samples with a range of relevant mechanical properties for the validation of SWE endoprobe measurements.

In order to provide reference measures of the mechanical properties for TMM phantoms, mechanical testing (MTE) is required. Dynamic bulk compression testing has been used to determine the mechanical properties of TMM phantoms [82], [85], [253], [255], yet this requires specialized testing equipment and testing over a range of frequencies, which can increase testing duration, making desiccation a concern [106]. Quasi-static unconfined ramp compression testing, a common alternative, is often used to characterize material properties [71], [72], [90], [172]. Quasi-static unconfined ramp MTE is easy to implement and shows similar trends to dynamic testing [174], [246]. While quasi-static testing may yield qualitatively lower values than those of dynamic testing [174], [246], this has not been definitively observed for SWE applications [95].

The purpose of this study was to evaluate the validity and reliability of endoprobe SWE in homogeneous oil-in-gelatin TMM phantoms against MTE. In particular, the objectives of the study were to (1) establish the reliability of endoprobe SWE stiffness measured at three target depths (1cm, 3cm, 5cm); (2) validate the performance of endoprobe SWE in homogeneous phantoms against unconfined ramp MTE at three target depths (1cm, 3cm, and 5cm); and (3) compare SWE outcomes acquired using an endoprobe to those acquired using linear and curvilinear probes. Findings from this work will provide the necessary foundation for future systematic investigations of gynecological UE, including in vivo and ex vivo validation of SWE in healthy and pathological human gynecological tissue.

3.2 Methods

3.2.1 Preparation of Oil-in-Gelatin Phantoms

Oil-in-gelatin phantoms were manufactured according to the methods described by Madsen et al. 2006 [253]. In brief, the phantoms were composed of a solvent (water), a matrix (gelatin), and a series of additives (propylene glycol, safflower oil, liquid surfactant, formalin), which function to tune

the acoustic, mechanical, and physical properties of the phantoms. First the molten gelatin solution was mixed; water, propylene glycol (5.09% by volume, P4347, Sigma-Aldrich Canada Co., Oakville, Canada), and 200 Bloom gelatin (13.06% by volume Nitta Gelatin, Morrisville, USA) were combined in a beaker. A thermometer was placed in the beaker, the beaker was covered with plastic wrap, and then the beaker placed in a double boiler, and heated to 90^{o}C to produce clarified molten gelatin [253]. The molten gelatin was then cooled in an ice bath to 55^{o}C. At this point, the molten gelatin solution was then combined with safflower oil (Loblaws, Brampton, Canada) and stirred to produce oil droplets (<1mm diameter) [253]. The method of stirring to yield oil droplets in the gelatin matrix involve taking a standard dinner spoon and bending the spoon at 90^{o} to the handle. The spoon was then placed in the mixture in the beaker and stirred about a horizontal axis. This method encourages the dispersion of the oil droplets, while minimizing air introduction into the mixture. Following this, liquid surfactant (1.1% by volume, Liquid Ivory Ultra, Proctor and Gamble, Toronto, Canada) was added to the mixture to preserve the emulsion and stirred vigorously until the mixture because opaque. Formalin (0.735% by volume, F8775, Sigma-Aldrich Canada Co., Oakville, Canada) was then added to the oil-in-gelatin solution and the mixture was stirred to complete the manufacture of the TMM solution [253].

The oil-in-gelatin TMM solution was cast into a cylindrical mould with a height and diameter each of 7.5cm and placed under positive gauge pressure [253]. The mold included a syringe embedded in the outer was that. When the mixture was in the mold and the syringe was engaged, the material was placed under a positive gauge pressure. After 24 hours, cross-linking of the gelatin had increased the melting temperature well above room temperature. Molds were then removed to yield a cylindrical homogeneous TMM phantom (Figure 22A). Phantoms were placed in safflower oil to prevent desiccation until testing [253]. A total of n=27 phantoms were manufactured, to yield adequate statistical power for the purposes of this study. The ratio of safflower oil in the phantoms was varied between 2.5% and 67.5% in 2.5% increments to yield a uniform spread across a physiologically relevant

range of healthy and pathological tissue stiffnesses (20kPa < storage modulus < 100kPa) [82], [84], [253]. Additionally, six extra phantoms were manufactured according to the same procedures using a stiffer 220 Bloom gelatin (13.06% by volume, Sigma-Aldrich, St. Louis, USA) to extend the upper end of the range of stiffnesses over which SWE could be validated. In the end, with two manufacturing failures, the total sample of phantoms was n = 31.

It should be noted here that Madsen et al. [82], [253] observed slight variations in elastic contrasts and strain ratios measured in heterogeneous phantom made using this TMM. Their team also observed a decrease in the amplitude of the storage modulus measured over a period of 16 months [253]. Regardless, this study purely aimed to validate measures of SWE stiffness against MTE measures. SWE and MTE measures for a given phantom were obtained on the same day, thus eliminating any concerns regarding long-term temporal stability of mechanical properties.

3.2.2 Ultrasound Elastography Imaging

Endocavity, superficial linear, and curvilinear SWE ultrasound imaging probes from the Aixplorer system (SuperSonic Imagine, Aix-en-provence, France) were used in this study [108] (Table 2). All probes used proprietary excitation sequences, the overall mechanism of which is summarized in the literature [115].

Table 2 Aixplorer (SuperSonic Imagine, Aix-en-provence, France) shear wave elastography (SWE) ultrasound imaging probes used for testing and their specifications [108].

Model	Type	Imaging Frequency Range (MHz)	Nominal Centre Frequency (MHz)	SWE Penetration Range (mm)	SWE Spatial Resolution (mm)
SE12-3	Endoprobe	3.0 to 12.0	7.5	2.5 to 30	2.0
SL15-4	Linear Probe	4.0 to 15.0	8.5	2.5 to 30	2.0
SC6-1	Curved Probe	1.0 to 6.0	3.5	25 to 75	3.0

The SWE imaging procedure was executed with the phantom suspended in a safflower oil bath, in order to minimize confounding factors [175]. SWE measurements were taken in a mid-longitudinal plane of the phantom (Figure 22). The probe was inserted into the oil bath and centered to visualize a B-mode image of the target region. The SWE region of interest (ROI) was set to its minimum size and placed along the central axis of the probe. The maximum stiffness of the imaging system was set to 180kPa and the penetration mode, which appeared to act as a spatial filter, was enabled for consistency of visualization across all depths. The probe was fixed in place and three UE cineloops of at least 10 frames each wereacquired at the desired depth. This process was performed for the target region at 1cm, 3cm, and 5cm depths for the endoprobe, the linear probe, and the curvilinear probe, in a randomized order. While the linear probe and curvilinear probe did not exhibit any qualitative failures during data acquisition, the endoprobe often lost signal at 5cm depths or exhibited highly irregular data. For this reason, data were also acquired at a “maximum consistent” depth (MCN) using the endoprobe. This depth was set qualitatively as the deepest region at which complete signals, without any irregular artifact, could be acquired. The imaging system was then turned off, reset, and the same procedure was repeated for a total of two complete imaging sessions acquired on the same testing day.

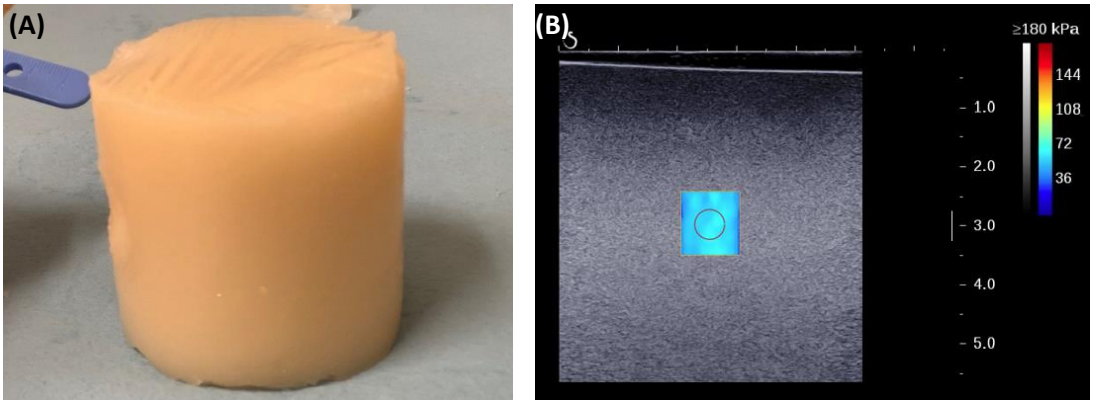

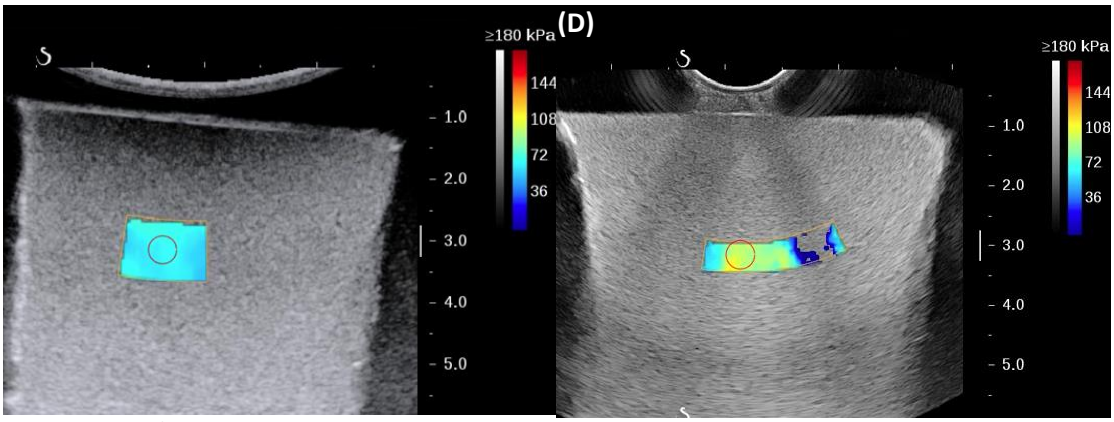

Figure 22 In-house manufactured homogeneous oil-in-gelatin tissue mimicking phantom (A), with shear wave elastography (Aixplorer, Supersonic Imagine, Aix-en-Provence, France) imaging performed at a 3cm target depth using a SL 15-4 superficial linear probe (B), SC 6-1 curvilinear probe, and the (C) SE 12-3 endoprobe.

3.2.3 Unconfined Ramp Compression Testing

In order to validate the elastography measures of material stiffness, unconfined quasi-static ramp compression MTE was used as a criterion standard. MTE of the phantoms was conducted using the BiotTester materials testing system (CellScale, Waterloo, Canada), with a 23N load cell (5.5 mN resolution, 3.5 mN noise floor) and a positional accuracy of 1um. The load cells and displacement controls on the system were calibrated on an annual basis (CellScale, Waterloo, Canada) and monitored for deviations that may impact testing. Three-dimensional printed adapters made from polyactide (PLA) with 90% infill were secured to the material testing system and MTE was conducted using a stainless steel 50mm square platen. Samples were cut (>20mm square, 5 to 8 mm thick) from the imaging plane of the phantom and were fixed to a stainless-steel support stage. The sample dimensions were taken as an average of three trials measured using a Vernier caliper. The support stage holding the sample was inserted into the MTE system. The sample thickness was calculated as an average of three trials of the measured distance between the support stage and the top of the sample when loaded to 15 mN, taken using the BioTester materials testing system (CellScale, Waterloo, Canada). The ramp compression

platen was then withdrawn from the sample surface to a distance of 500 um. The samples were compressed to a strain of 25% for 20 cycles at a rate of 0.055 Hz.

3.2.4 Data Processing

SWE stiffness measures (kPa) were calculated as the median over 10 frames and the average of 3 trials for a circular ROI of 5 mm diameter, centered at the target depth of interest in the frame. For each MTE signal, the final 10 cycles of loading were ensemble averaged and a low pass Butterworth filter (3 Hz cut-off, 2^{nd} order, dual pass) was applied to minimize noise in the data signals. Any bias in the signal was identified as an average of the unloaded period prior to contact of the ramp compression platen and the signal was zeroed. Contact was detected automatically using a 15 mN force threshold and then verified by visual inspection. In cases where residual noise confounded the algorithm, manual identification of the surface contact was used.

Due to the small strain amplitudes applied by the elastography system (~100 um in phantoms, ~40 um in vivo [115]), the toe region of the stress-strain curve was used to estimate the elastic modulus, using methods described by Zhai et al. [172]. In brief, beginning from the surface contact point (i.e. 0% strain), a data window with a length of 5% of the tip diameter was identified. A linear regression was chosen to fit a linear model to the window, in order to limit the impact of residual noise on a tangent calculation. The error between the linear model and the data window was calculated as the mean absolute difference between the linear model and the force-displacement data window. The data window was then extended one sample at a time and the procedure was repeated for each new data window. The procedure was halted when the error exceeded the 15 mN threshold and the stiffness was taken as the slope of the linear model in this data window. The elastic modulus was then calculated as the ratio of stress to strain over the linear model. See Figure 23.

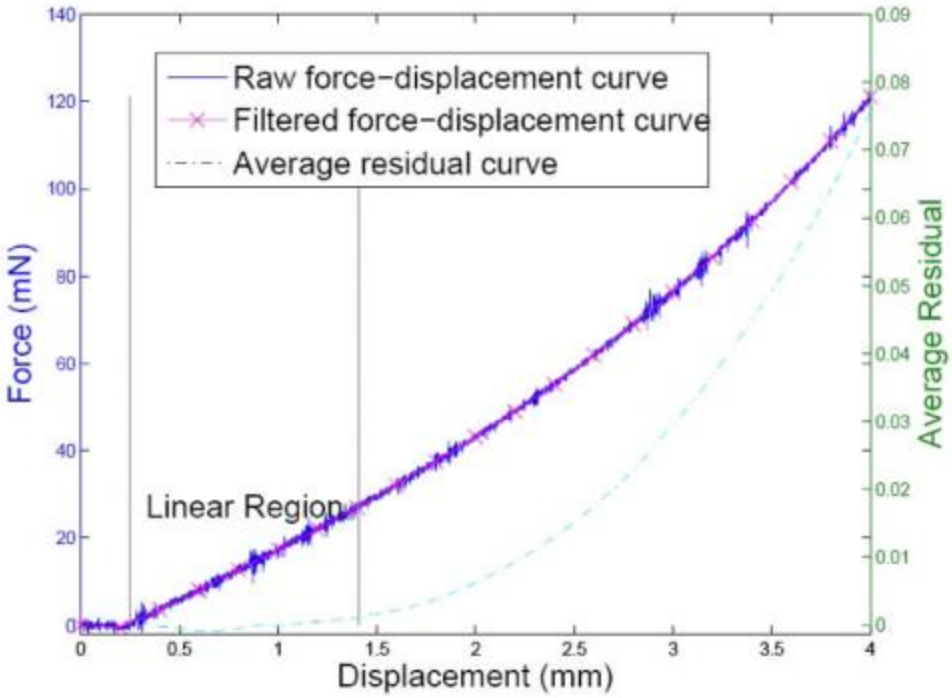

Figure 23 Indentation curve and the determination of the linear region, reproduced with permission from Zhai et al. [172]. The solid line is the raw indentation load-displacement curve with load measured in millinewtons (mN) and displacement measured in millimetres (mm). The purple line that includes X markers is the filtered indentation curve. The dashed blue line shows the average residual over the window at each point along the curve, with magnitudes indicated by the axis labels on the right-hand y-axis. The vertical black bars indicate the linear region selected for calculating the indentation stiffness and the indentation modulus.

3.2.5 Statistical Analysis

The data were checked to ensure that as the percent volume of oil increased in the phantoms, the elastic modulus measured by SWE and MTE showed a decreasing trend. Target depth across the two imaging sessions was checked using pairwise comparisons to ensure that the depths were consistent between imaging sessions. The reliability of SWE tissue stiffness outcomes was then assessed using intraclass correlation coefficients (ICCs) (two-way mixed effects, mean of multiple measurements, absolute agreement, [256]) (Matlab, Mathworks, Natick, USA). The ICC is calculated as the quotient of the variance of interest over the total variance. The following definitions given by Cicchetti et al. [105] were used: ICC≤0.40 was poor, 0.40<ICC≤0.60 was fair, 0.60<ICC≤0.75 was good, 0.75<ICC was excellent. Once adequate reliability was established, outcomes were averaged across the two imaging sessions. The relationship between elastography and MTE outcomes was initially visualized using

scatter plots. Data were checked for normality and Pearson's r correlation coefficients were used to characterize the relationship between MTE and SWE outcomes. Bland Altman analyses were used to quantify exact agreement and a two sample Kolmogorov-Smirnov test was included to test the likelihood that data were derived from the same population. Finally, linear regression models were fit using SWE modulus as the main predictor and MTE modulus as the dependent variable to examine the quantitative relationship between SWE and MTE outcomes for all conditions. The level of significance was set to $\alpha = 0.05$ for all statistical tests.

3.3 Results

The entire sample of oil-in gelatin elastography phantoms yielded elastic moduli ranging from 17.10 kPa to 88.12 kPa, as measured on quasi-static ramp compression testing, with the elastic modulus showing a general trend of decreasing as volume percent of oil increased (Table 3). Quasi-static ramp compression MTE failed in four phantoms due to testing malfunctions. As such, the resulting sample size differed between the SWE reliability assessment (n = 31) and the SWE validation against MTE (n = 27). As well, SWE data acquisition for the 5cm condition for the endoprobe failed for 8 phantoms, all with moduli below 40kPa on MTE. In contrast, complete SWE data sets were acquired with all probes at all other conditions. Pairwise comparisons revealed that target depths for each were consistent between the first and second imaging sessions (*Table 4*), supporting between session reliability assessment of the data.

Table 3 Gelatin stiffness (Bloom) and oil concentration (by vol %) for all manufactured homogeneous oil-in-gelatin tissue mimicking phantoms with the corresponding modulus (E) measured by quasi-static unconfined ramp compression mechanical testing (MTE) at a rate of 0.055Hz and E was calculated in the toe region of the stress-strain curve. Shear wave elastography (SWE) measures of E taken using a linear ultrasound probe (4 - 15 MHz) at a 1cm target depth are also included. Phantoms that failed to cure or were damaged in storage are marked as "FAIL", while MTE testing failures are marked with a "-".

ID	Gelatin Stiffness	Oil (by Volume)	MTE E (kPa)	Linear Probe @ 1cm SWE E (kPa)
PS02P5	220 Bloom	2.5%	-	60.50
PS05P0	220 Bloom	5.0%	88.12	65.78
PS07P5	220 Bloom	7.5%	74.12	62.91

PS10P0	220 Bloom	10.0%	81.47	57.77
PS12P5	220 Bloom	12.5%	77.34	55.70
PS15P0	220 Bloom	15.0%	66.87	54.01
PH02P5	200 Bloom	2.5%	95.60	52.24
PH05P0	200 Bloom	5.0%	-	51.31
PH07P5	200 Bloom	7.5%	71.22	70.53
PH10P0	200 Bloom	10.0%	83.27	54.83
PH12P5	200 Bloom	12.5%	63.78	55.07
PH15P0	200 Bloom	15.0%	79.84	55.65
PH17P5	200 Bloom	17.5%	-	50.19
PH20P0	200 Bloom	20.0%	62.77	45.96
PH22P5	200 Bloom	22.5%	64.89	43.98
PH25P0	200 Bloom	25.0%	42.21	44.15
PH27P5	200 Bloom	27.5%	48.03	41.66
PH30P0	200 Bloom	30.0%	FAIL	FAIL
PH32P5	200 Bloom	32.5%	49.29	35.82
PH35P0	200 Bloom	35.0%	48.13	37.62
PH37P5	200 Bloom	37.5%	32.14	37.66
PH40P0	200 Bloom	40.0%	53.05	41.63
PH42P5	200 Bloom	42.5%	52.53	35.96
PH45P0	200 Bloom	45.0%	30.07	28.01
PH47P5	200 Bloom	47.5%	44.39	28.28
PH50P0	200 Bloom	50.0%	43.89	27.14
PH52P5	200 Bloom	52.5%	33.14	29.11
PH55P0	200 Bloom	55.0%	32.33	24.74
PH57P5	200 Bloom	57.5%	17.10	20.47
PH60P0	200 Bloom	60.0%	35.01	23.32
PH62P5	200 Bloom	62.5%	FAIL	FAIL
PH65P0	200 Bloom	65.0%	-	19.34
PH67P5	200 Bloom	67.5%	17.46	18.11

Table 4 Depth of shear wave elastography (SWE) targets for acquisition of the elastic modulus (E) data in oil-in-gelatin homogeneous tissue mimicking phantoms. SWE data was collected using a linear, curvilinear, and endocavity probe at target depths of 1cm, 3cm, and 5cm. In the case of the endoprobe only, a maximum consistent depth (MCN) at which signal appeared to be present and consistent with shallower depths was also collected for comparison. SWE data was collection was repeated at two separate imaging sessions (Session 1 and Session 2). Target depth is given as a mean ± standard deviation (STD). There was no significant difference between depths at session 1 and session 2 for any of the conditions considered.

Probe	Depth	Sample Size	Session 1		Session 2	
			Mean Depth (mm)	STD (mm)	Mean Depth (mm)	STD (mm)
Linear Probe	1cm	31	10.5	1.2	10.3	1.8
	3cm	31	29.7	1.6	29.6	1.4
	5cm	30	46.2	4.7	46.0	4.6
Curved Probe	1cm	31	14.2	1.9	13.4	1.7
	3cm	31	30.5	0.8	30.3	0.8
	5cm	31	50.6	1.4	49.9	2.4
Endo-Probe	1cm	31	11.3	2.5	11.0	2.2
	3cm	31	30.2	0.5	30.3	0.8
	5cm	21	49.9	2.6	50.1	0.7
	MCN	31	39.4	6.2	38.8	5.1

All probes exhibited excellent reliability at all depth conditions (Table 5). While the linear and curvilinear probe yielded ICC≥0.950 at all depth conditions, the reliability of the endoprobe matched this only for the 1cm and 3cm depth conditions. Beyond the 3cm target depth, the reliability of the endoprobe decreased slightly, with ICC = 0.935 at the MCN depths and ICC = 0.848 at the 5cm depth. The 95% confidence interval of the ICCs for the linear probe at the 5cm depth condition did not overlap those from shallower depths acquired using the same probe. Moreover, the 95% confidence interval of the ICCs for the 5cm depth condition for the endoprobe only overlapped those from the endoprobe at the MCN depth condition and the linear probe at 5cm. Both these findings may suggest significant increase in the variability of SWE measures with depth for the endoprobe and linear probe.

Table 5 Reliability test results for shear wave elastography (SWE) estimates of the elastic modulus (E) data in oil-in-gelatin homogeneous tissue mimicking phantoms. SWE data was collected using a linear, curvilinear, and endocavity probe at target depths of 1cm, 3cm, and 5cm. In the case of the endoprobe only, a maximum consistent depth (MCN) at which signal appeared to be present and consistent with shallower depths was also collected for comparison. SWE data was collection taken as an average of data collected over two repeated imaging sessions. Results include the intraclass correlation coefficient (ICC), the lower bound (LB) and upper bound (95%) on the 95% confidence interval (CI), and the significance of the ICC (p-Value).

Probe	Depth	Sample Size	ICC	95% CI		p-Value
				LB	UB	
Linear Probe	1cm	31	0.996	0.991	0.998	<0.001
	3cm	31	0.995	0.990	0.997	<0.001
	5cm	30	0.950	0.901	0.975	<0.001
Curved Probe	1cm	31	0.983	0.966	0.992	<0.001
	3cm	31	0.982	0.964	0.991	<0.001
	5cm	31	0.991	0.982	0.996	<0.001
Endo-Probe	1cm	31	0.980	0.957	0.990	<0.001
	3cm	31	0.972	0.944	0.986	<0.001
	5cm	21	0.848	0.697	0.924	<0.001
	MCN	31	0.935	0.869	0.967	<0.001

Preliminary assessment and visualization of SWE agreement with MTE testing outcomes was done using scatter plots for the linear (Figure 24A, C, E), curvilinear (Figure 24B, D, F), and endoprobe data (Figure 25). Data visualization showed positive linear trends in the linear and curvilinear data for all depth conditions, although variance in the data was high. It was also observed that the slope of the data for linear and curvilinear probes at all conditions tended to trend below a perfect correlation line. The endoprobe data for the 1cm and MCN depth conditions exhibited similar trends to the linear and curvilinear probe. In contrast, the scatterplots for the endoprobe SWE stiffness measured at the 3cm and 5cm conditions all showed trends of slopes aligned more closely to the perfect correlation line. Regardless, the 3cm, MCN, and 5cm conditions for the endoprobe all exhibited a qualitative increase in the variance in the data. Further, the 5cm condition for the endoprobe showed qualitatively the weakest relationship between SWE and MTE measures of the elastic modulus.

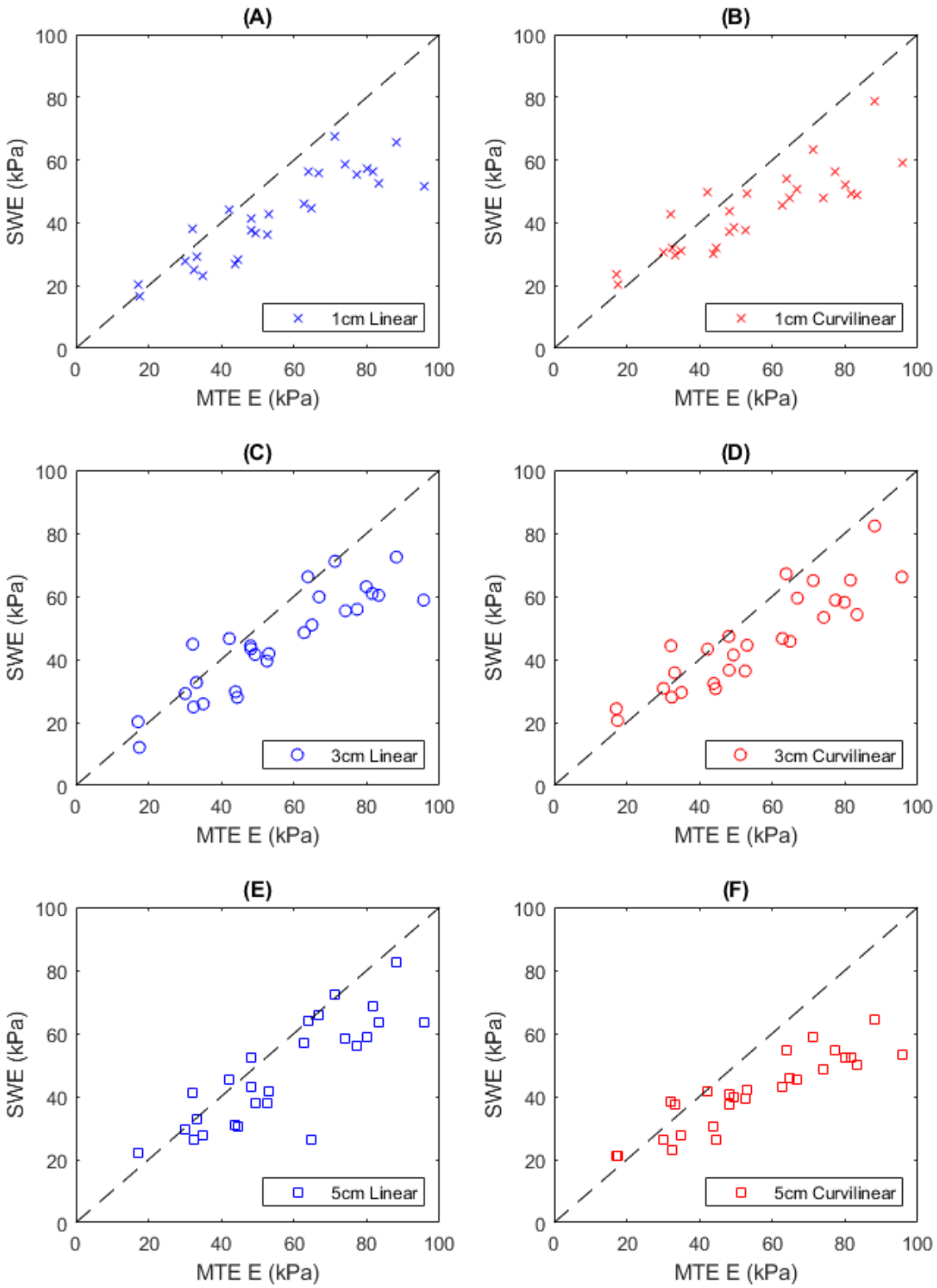

Figure 24 Agreement of the elastic modulus (E) in kilopascals (kPa), measured by shear wave elastography (SWE) and unconfined ramp compression mechanical testing (MTE) in a series of homogeneous oil-in-gelatin tissue mimicking phantoms. SWE measurements were taken as an average of two repeated imaging sessions. SWE data was acquired using a linear probe (A,C,E) (blue markers), a curvilinear probe (B,D,E) (red markers), and an endoprobe (see following figure). SWE measurements were taken at target depths of 1cm ('x'), 3cm ('o'), 5cm ('□'). The black dashed line indicates the line of equality in all plots.

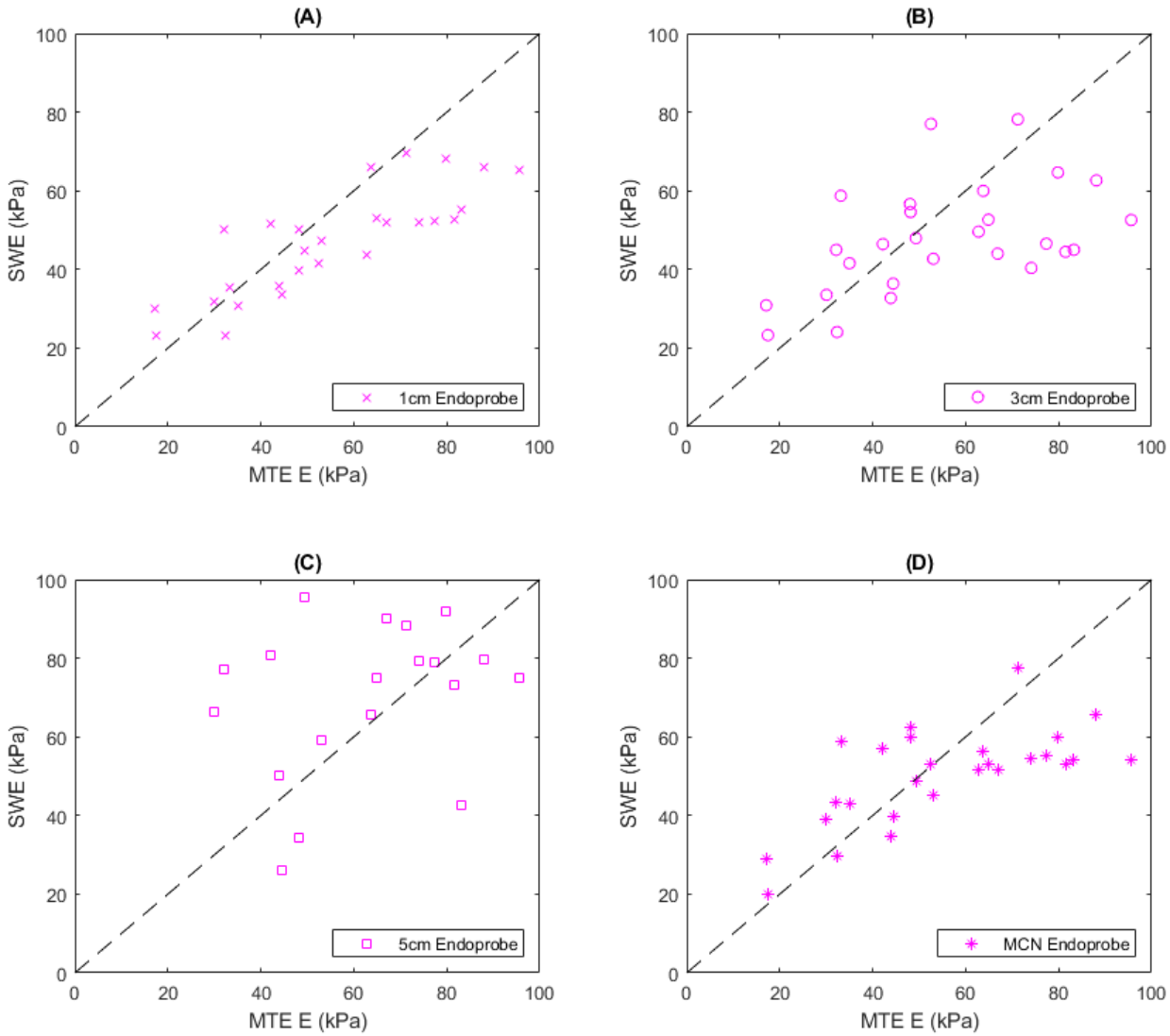

Figure 25 Agreement of the elastic modulus (E) in kilopascals (kPa), measured by shear wave elastography (SWE) and unconfined ramp compression mechanical testing (MTE) in a series of homogeneous oil-in-gelatin tissue mimicking phantoms. SWE measurements were taken as an average of two repeated imaging sessions. SWE data was acquired using a linear probe (see previous figure), a curvilinear probe (see previous figure), and an endoprobe (A,B,C,D). SWE measurements were taken at target depths of 1cm ('x'), 3cm ('o'), 5cm ('□') and a maximum consistent depth (MCN, '') at which signal appeared to be present and consistent with shallower depths.*

The first method of quantifying the relationship between MTE and SWE outcomes was the use of Pearson's r correlation for all probes and all depth conditions (Table 6). The linear and curvilinear probes yielded stiffness measures that were very strongly correlated with MTE outcomes at all depths (r>0.7), with the linear probe yielding consistent correlations across all depths (r = 0.89) and the curvilinear probe yielding the strongest correlation with MTE at the 5cm depth condition (r = 0.90). Correlations of endoprobe SWE stiffness and MTE stiffness were very strong at the 1cm depth condition (r = 0.83) but decreased to moderate correlations for the 3cm (r = 0.51) and MCN (r = 0.67) depth

conditions. There was no significant correlation between MTE outcomes and endoprobe SWE outcomes at the 5cm depth condition.

Table 6 Pearson's correlation coefficients (r) for shear wave elastography (SWE) measures of the elastic modulus (E) in oil-in-gelatin homogeneous tissue mimicking phantoms with respect to unconfined ramp compression mechanical testing (MTE). MTE testing strained samples at a rate of 0.055Hz and E was calculated in the toe region of the stress-strain curve. SWE data was collected using a linear, curvilinear, and endocavity probe at target depths of 1cm, 3cm, and 5cm. In the case of the endoprobe only, a maximum consistent depth (MCN) at which signal appeared to be present and consistent with shallower depths was also collected for comparison. SWE data was averaged across two repeated imaging sessions. Shapiro-Wilk testing was used to confirm the normality of the data.

Probe	Depth	Sample Size	Pearson's Correlation	
			r	p-Value
Linear Probe	1cm	27	0.89	<0.001
	3cm	27	0.89	<0.001
	5cm	26	0.89	<0.001
Curved Probe	1cm	27	0.85	<0.001
	3cm	27	0.89	<0.001
	5cm	27	0.90	<0.001
Endo-Probe	1cm	27	0.83	<0.001
	3cm	27	0.51	0.007
	5cm	21	0.18	0.442
	MCN	27	0.67	<0.001

The second method to evaluate the relationship between MTE and SWE outcomes was the use of Bland Altman analyses (Table 7, Table 8). Results showed a significant negative MD for all depth conditions for the linear (range = [-9.66kPa, -12.80kPa]) and curvilinear (range = [-8.92kPa, -13.83kPa]) probes. All conditions for the linear and curvilinear probe exhibited high, but consistent, variance on the MD, with the standard deviation (STD) of the MD ranging from 9.77 kPa to 12.61 kPa. In contrast, the endoprobe only yielded significant negative MDs for the 1cm depth condition (-8.23 kPa), with an STD of 12.89 kPa. While the 3cm and MCN conditions for the endoprobe did not exhibit a significant MD, the STD of the MD were higher than those observed in the linear and curvilinear probes (3cm = 18.95 kPa, MCN = 16.23 kPa). Finally, the 5cm depth condition for the endoprobe exhibited a significant positive MD of 12.17 kPa and the highest STD of the MD at 21.67 kPa. Kolmogorov-Smirnov tests for all cases confirmed that SWE data and MTE data were all derived from the same probability distribution.

Table 7 Bland Altman (BA) test results for shear wave elastography (SWE) estimates of the elastic modulus (E) data in oil-in-gelatin homogeneous tissue mimicking phantoms compared to unconfined ramp compression testing (MTE). SWE data was collected using a linear, curvilinear, and endocavity probe at target depths of 1cm, 3cm, and 5cm. In the case of the endoprobe only, a maximum consistent depth (MCN) at which signal appeared to be present and consistent with shallower depths was also collected for comparison. SWE data was averaged across two repeated imaging sessions. MTE samples were strained at a rate of 0.055Hz and E was calculated using a linear model in the toe region of the stress strain curve. BA results include the mean difference (MD), significance of the MD (p), standard deviation (STD) of the MD, standard error (SE) of the MD, and the lower bound (LB) and upper bound (UB) on the MD 95% limits of agreement (LOA). Results from a Kolmogorov-Smirnov test was included to test the likelihood that data was derived from the same population.

Probe	Depth	Sample Size	Mean Difference				95% LOA		KS Test
			MD (kPa)	p-Value	STD (kPa)	SE (kPa)	LB (kPa)	UB (kPa)	p-Value
Linear Probe	1cm	27	-12.80	<0.001	11.10	0.41	-34.56	8.95	0.94
	3cm	27	-9.66	<0.001	10.40	0.39	-30.04	10.72	1.00
	5cm	26	-8.05	0.001	9.77	0.38	-27.20	11.09	0.86
Curved Probe	1cm	27	-11.38	<0.001	12.61	0.47	-36.10	13.35	0.93
	3cm	27	-8.92	<0.001	10.70	0.40	-29.90	12.05	0.98
	5cm	27	-13.83	<0.001	12.15	0.45	-37.64	9.99	0.93
Endo-Probe	1cm	27	-8.23	0.003	12.89	0.48	-33.49	17.04	0.95
	3cm	27	-7.25	0.057	18.95	0.70	-44.39	29.89	0.78
	5cm	21	12.17	0.018	21.67	1.03	-30.31	54.65	0.88
	MCN	27	-5.11	0.114	16.23	0.60	-36.92	26.70	0.95

The third method used to evaluate the relationship between MTE and SWE outcomes was linear regression analyses (Table 8). In contrast to the Bland Altman analyses, linear regression only identified a single case with a statistically significant bias: the curvilinear probe at the 5cm depth condition (B_0 = -16.81 kPa, p=0.017). Results showed that the elastic modulus measured by SWE was a significant predictor for the MTE modulus for all probes and conditions, except for the endoprobe at the 5cm depth condition (p = 0.442). For all linear and curvilinear probe conditions, the coefficient of the SWE modulus in the linear regression ranged from 1.22 to 1.73, which aligned with qualitative observations from the scatterplots. The coefficient of endoprobe SWE stiffness measures at the 1cm and MCN depth conditions fell in this same range, while the endoprobe 3cm depth condition was the only case in which coefficient was less than 1 (B_1 = 0.95, p = 0.001). and the SWE modulus measured by the endoprobe at the 5cm depth condition was not a significant predictor for the MTE modulus (p = 0.442). Finally, the fit of the models was quite high for the linear probe at all depth conditions (Adj R^2 = 0.79 to 0.80) and the curvilinear probe at the 3cm (Adj R^2 = 0.79) and 5cm (Adj R^2 = 0.82) depth conditions. However, the fit

was lower for the curvilinear probe at the 1cm depth condition (Adj R^2 = 0.73) and for the endoprobe at the 1cm (Adj R^2 = 0.73). The fit of the models for the endoprobe at the 3cm (Adj R^2 = 0.32), the MCN (Adj R^2 = 0.54) conditions were even worse. Finally, the 5cm depth for the endoprobe yielded a model fit of effectively zero (Adj R^2 = -0.02).

Table 8 Linear regression results for shear wave elastography (SWE) estimates of the elastic modulus (E) data as a predictor for E measured by unconfined ramp compression testing (MTE). Measured were performed on oil-in-gelatin homogeneous tissue mimicking phantoms. SWE data was collected using a linear, curvilinear, and endocavity probe at target depths of 1cm, 3cm, and 5cm. In the case of the endoprobe only, a maximum consistent depth (MCN) at which signal appeared to be present and consistent with shallower depths was also collected for comparison. SWE data was averaged over two repeated imaging sessions. MTE samples were strained at a rate of 0.055Hz and E was calculated using a linear model in the toe region of the stress strain curve. Models were constructed for each target depth for each probe. The number of observations (n), coefficients for the intercept (B_0) and the SWE data (B_{SWE}), 95% confidence intervals (CIs), adjusted R^2 (Adj R^2), and standard error of the estimate (SEE) are given here for all models.

Probe	Depth	n	Intercept		SWE E		Model Fit	
			B_0 (95% CI)	p-Value	B_1 (95% CI)	p-Value	Adj R^2	SEE (kPa)
Linear Probe	1cm	27	-6.40 (-13.19, 6.40)	0.314	1.44 (1.14, 1.73)	<0.001	0.79	10.84
	3cm	27	-3.52 (-15.74, 8.71)	0.560	1.27 (1.02, 1.53)	<0.001	0.79	10.83
	5cm	26	-3.22 (-15.71, 9.25)	0.599	1.22 (0.97, 1.47)	<0.001	0.80	10.43
Curved Probe	1cm	27	-11.88 (-28.07, 4.32)	0.144	1.51 (1.15, 1.87)	<0.001	0.73	12.26
	3cm	27	-7.44 (-20.65, 5.77)	0.257	1.34 (1.06, 1.61)	<0.001	0.79	10.99
	5cm	27	-16.81 (-30.30, -3.31)	0.017	1.73 (1.41, 2.05)	<0.001	0.82	10.04
Endo-Probe	1cm	27	-12.15 (-28.57, 4.27)	0.140	1.42 (1.08, 1.77)	<0.001	0.73	12.35
	3cm	27	8.53 (-17.47, 34.53)	0.506	0.95 (0.42, 1.42)	0.001	0.32	19.54
	MCN	27	-7.55 (-30.44, 15.35)	0.504	1.25 (0.80, 1.70)	<0.001	0.54	16.13
	5cm	21	45.14 (-0.40, 90.67)	0.052	0.23 (-0.38, 0.83)	0.442	-0.02	18.94

3.4 Discussion

To the authors' knowledge, this study provides the largest sample size of any elastography validation phantom study previously published. While the statistical value of this larger sample size is well understood [219], [248]–[252], findings from this study show that validation of elastography requires a larger number of phantoms in order to provide accurate estimates of the variability in SWE outcomes across a range of stiffnesses. Findings from this study provide a detailed quantification of the performance of the Aixplorer (SuperSonic Imagine, Aix-en-Provence, France) SWE endoprobe and will be essential in guiding the clinical applicability of this tool moving forwards. Moreover, this study places the performance of the SWE endoprobe within the context of the much more thoroughly studied SWE linear

probe and the SWE curvilinear probe, a comparison that is highly relevant when considering the clinical requirements of gynecological SWE.

3.4.1 Oil-in-Gelatin Phantoms for SWE Validation

The oil-in-gelatin phantoms used in this study performed exceptionally well as an economical accessible method for validating SWE (Table 2). The 200 Bloom gelatin combined with several 220 Bloom gelatin phantoms yielded an acceptable range of stiffnesses (15 kPa < elastic modulus < 100 kPa) and showed good agreement to the stiffness range predicted from the literature (20kPa < storage modulus < 100kPa [82], [84], [253]). However, the 220 Bloom gelatin did not extend the ceiling on material stiffness as expected and increasing oil concentrations did not yield a linear decrease in material stiffness. This may have been due to controls around the manufacturing processes, testing procedures [174], [246], or the exact make/model of materials being used. While dynamic MTE is more faithful to the loading applied by SWE, the findings here, combined with a systematic comparison of quasistatic and dynamic MTE for SWE applications [95] suggest that MTE speed may not be as relevant to SWE validation as some other parameters (Section 5). While other studies have shown lower stiffness estimates from quasi-static compared to dynamic testing outcomes [174], [246] the use of quasistatic ramp compression MTE combined with oil-in-gelatin phantoms appeared to perform well in this validation of SWE.

3.4.2 Reliability of SWE

Standardization of SWE target depths (i.e. 1cm, 3cm, MCN, 5cm) was consistent across the two imaging sessions (Table 4), and the reliability of the SWE stiffness outcomes was excellent for all probes at all depth conditions (Table 5). However, this was to be expected with the use of homogeneous TMM phantoms in a highly controlled bench test setting. The key finding in this instance was the decrease in reliability that occurred with depth in the case of the endoprobe and linear probe. For SWE using the

endoprobe, the 1cm depth condition yielded high reliability (0.957 < ICC 95% CI < 0.990), comparable to the performance of the curvilinear probe overall and to the linear probe at shallow (i.e. 1cm, 3cm) depth conditions. However, with increased target depth endoprobe reliability decreased, particularly at the MCN (average depth = 39.1 mm; 0.869 < ICC 95% CI < 0.967) and 5cm (0.697 < ICC 95% CI < 0.924) depth conditions. Similarly, the reliability of the linear probe at 5cm (0.901 < ICC 95% CI < 0.975) was lower than at shallower depths (0.990 < ICC 95% CI < 0.998). Both the linear probe and endoprobe are not rated for measurements in depths beyond 3cm, thus these findings are in line with the manufacturer's recommendations (Table 2). While all ICC values were excellent, the TMM phantoms were homogeneous and the tissue depths were controlled; reliability may be lower when used in-vivo.

3.4.3 Validity of SWE

Correlation analyses (Table 6) showed strong relationships between MTE and SWE outcomes for both the linear and curvilinear probes at all depths (0.89 < r < 0.90), while curvilinear stiffness measures at 1cm were slightly lower (r = 0.85). The linear and curvilinear probes tended to underestimate material stiffness (-8.05 kPa < MD < -13.83 kPa, 1.22 < B_{SWE} < 1.73), yet variance in SWE accuracy was consistent with depth (9.77 kPa < MD STD < 12.61 kPa) and SWE stiffness always was a significant predictor of MTE stiffness (0.73 < AdjR^2 < 0.80). In contrast, endoprobe SWE and MTE showed the highest correlation at a depth of 1cm (r = 0.83) and decreased with depth, becoming non-significant at a depth of 5cm. At 1cm depths, the endoprobe validity was similar to the linear and curvilinear probe (MD = -8.23 kPa, MD STD = 12.89 kPa; B_{SWE} = 1.42, AdjR^2 = 0.73). However, with increasing depth, the variance in estimation accuracy increased (16.23 kPa < MD STD < 21.67 kPa) and the strength of the relationship with MTE decreased (-0.02 < AdjR^2 < 0.54).

Interestingly, the linear and curvilinear probe stiffness estimates consistently underestimated material stiffness, while this was only the case for the endoprobe at the 1cm target depth, where the

probe exhibited the best performance. Referring to the manufacturer recommendations (Table 2), the variability in stiffness estimates for each probe was consistently lower when target depths were within the recommended ranges. While neither the linear probe nor the endoprobe are recommended for use at target depths beyond 3cm (Table 2), this highly controlled data set suggests that the linear probe may indeed be feasible for use at depths beyond 3cm. In contrast, the endoprobe performance is in question at depths beyond 1cm.

3.4.4 Endoprobe SWE Performance

Combining the findings from this work, a series of conclusions can be drawn. While exact agreement of the endoprobe SWE at 1cm does not deviate from findings in other probes at a range of depths, the quality of the relationship between endoprobe SWE at 1cm and MTE is still poorer than that of the linear (1cm, 3cm, 5cm) and curvilinear probe (3cm, 5cm), as indicated by lower correlation coefficients and linear regressions that describe little of the variance in the data ($AdjR^2$). Interestingly, the linear probe at the 5cm depth condition and the curvilinear probe at the 1cm depth condition, which are both beyond the manufacturer's recommended depths (Table 2), performed equivalently or better than the endoprobe at the 1cm depth across all outcomes in these highly controlled conditions. However, depending on the range of stiffnesses expected in healthy and pathological tissue for a given clinical application, this may not prohibit clinical applicability. Validation of endoprobe SWE imaging at 1cm target depths in vivo against MTE is highly recommended prior to large scale trials for diagnostic and treatment planning purposes.

Considering endoprobe SWE of deeper targets, similar concerns around feasibility under in vivo conditions arise. Compared to the linear and curvilinear probes, correlations for both conditions were substantially lower, variance of the MD increased, and model fits were much lower. Interestingly, considering all of these outcomes, the endoprobe appeared to perform better at the MCN condition

compared to the 3cm condition, however performance at the MCN condition was still substantially poorer than the linear and curvilinear probes at all conditions. As well, variance of the target depth for the MCN condition was high (39.1 ± 8.0 cm) compared to that of the endoprobe 3cm condition (30.3 ± 0.9 cm). Finally, over the range of phantom stiffnesses tested, while the reliability of the endoprobe at the 5cm depth condition was indeed “excellent”, SWE measures of material stiffness were not valid,. As with the 1cm depth condition for the endoprobe, clinical utility of the endoprobe at the 3cm and MCN depth conditions may exist, depending on expectations around healthy and pathological tissues of interest. Regardless, further validation through in vivo studies with ex vivo MTE is necessary to support any recommendations around clinical viability of this SWE system.

3.4.5 SWE Manufacturer’s Guidelines

Consulting data from the SWE manufacturer and the literature, several observations can be made. The SWE modality used in this study (Aixplorer, SuperSonic Imagine, Aix-en-provence, France) is quoted to have an estimation accuracy equal to the larger of ±30% or 3kPa [108]. These estimation accuracy values are derived from testing on a single rectangular polymer phantom (CIRS049 Quality Assurance Elasticity Phantom, CIRS, Norfolk, USA) which includes only four spherical targets over a limited stiffness range (29kPa background; 8.4kPa, 17.7kPa, 47.7kPa, and 80.1kPa inclusions) [108]. Further, estimation accuracy as a percentage of the true outcome may not be the best representation of error on the system, as different MTE methods can yield different estimates of stiffness for the same material [89], [95]. Regardless, the Bland-Altman analysis presented combined with the scatterplots suggests that accuracy of endoprobe SWE when compared to quasi-static ramp compression MTE appears to depend on target depth and also may not be as accurate as these guidelines suggest.

The value of an adequately large sample size presented in this study cannot be overstated. In a phantom that mimicked intra-cavitary imaging of prostate masses, Cao et al. [81] used the same SWE

endoprobe to measure a heterogeneous TMM phantom with an inclusion of one stiffness at 30.6mm and an inclusion of a second stiffness at depths of 64.0 mm, 52.4 mm, 43.8 mm, and 36.6 mm. The stiffness of the two inclusions was compared to quasi-static MTE. SWE measures were 86.2±4.5 kPa and 271.5±25.7 kPa, respectively, while MTE outcomes were 104.3±5.6 kPa and 297.3±6.7 kPa, respectively [81]. Based on findings in the study, Cao et al. [81] concluded that there was "good" SWE reliability at the four shallower depths, and "good" agreement between SWE and MTE. Interestingly, Cao et al.'s [81] work paints a very different picture of SWE endoprobe validity compared to this study. The small sample size in Cao et al.'s [81] study limited quantitative statistical analysis of the findings, which may have misrepresented the validity of the technology. Since the publishing of Cao et al.'s [81] findings, several clinical studies investigating the feasibility of endoprobe SWE for gynecological applications have been published [121], [209], [257]. Yet findings from these studies may require retrospective consideration within the context of this work. Further, prior to clinical investigations, in vivo validation of endoprobe SWE is required in healthy and pathological tissues of interest to justify clinical applicability.

3.4.6 Limitations

As with any research, the findings here must be considered in the context of the limitations of this work. The material stiffness of the phantoms measured by MTE did not decrease monotonically with increasing oil concentrations. Rather, MTE outcomes showed a decreasing trend with some variability. Reasons for this may have been rooted in phantom manufacturing methods or in the MTE testing approach, which may have implications for other findings presented here. In terms of phantom manufacturing, exact tools for measurement were not available (i.e. pipettes) and so digital scales, beakers, and small volume syringes were used. Slight changes in proportions of certain ingredients (e.g. formalin) could significantly alter material stiffness. Additionally, the ramp compression MTE methods required a perfectly flat contact surface between the phantom sample and the compression platen,

which was sometimes difficult to achieve using the tools available. While multiple visual and loading checks were performed to ensure even surface contact of every sample, this may still have created a bias in the measured MTE outcomes for some samples.

The ramp compression models included in this work assume a linear elastic material. While the oil-in-gelatin phantoms here were indeed homogeneous and isotropic, other factors such as viscoelasticity, friction, and non-parallel surfaces during mechanical testing may have impacted outcomes. Quasi-static testing rates and small deformations, lubricated testing surfaces (safflower oil), and prescribed cutting jigs were used, respectively, in an attempt to eliminate these factors. However, viscoelasticity of the phantom materials may have been responsible for trends across the testing rates. Friction between the loading jig and the material during testing could have increased estimates of the elastic modulus. Further, non-parallel testing surfaces would have elongated to the toe region of the stress-strain curves and decreased the measured elastic moduli.

In comparing mechanical testing and elastography outcomes, another limitation to this work is the use of quasi-static mechanical testing as a comparator for shear wave elastography loading, which is dynamic in nature. Some groups have implemented dynamic indentation mechanical testing for SWE applications, as it is thought to better represent the dynamic loading of SWE in vivo [90], [106], [291]. While quasi-static tissue testing does not simulate the high loading frequencies observed in SWE [115], it can still provide accurate, efficient, and accessible means of characterizing tissue stiffness [71], [72], [172] and is often selected for estimating tissue stiffness [71], [72], [113], [172]. In a comparison of a dynamic and quasi-static mechanical testing methodologies, Omari et al. [89] observed that quasi-static testing results exhibited comparable trends to those observed with dynamic testing, though generally yielding larger amplitude outcomes. Further, Oudry et al. [95] observed consistent results between dynamic and quasi-static mechanical testing when compared to SWE testing outcomes. While the optimal solution for matching mechanical testing protocols to SWE would be quantitative metrics

describing the SWE excitation protocols and resulting shear waves, this former is proprietary information owned by SuperSonic Imagine™ and our team did not have the equipment required to quantify the latter.

The use of homogenous phantoms is another limitation of this study. The manufacture of homogenous phantoms was highly economical and accessible and allowed for the manufacture of a much larger sample size than may have been possible in the case of heterogenous phantoms or commercially available phantoms. However, while the properties of these phantoms have been found to be representative of those found in human tissue [82], [84], [253], human tissue is not homogeneous or isotropic and thus the real-world translatability of this model is limited. Yet, homogenous phantoms provide a highly controlled preliminary testing medium for SWE. Thus, poor performance in homogeneous phantoms is an important finding and can guide the development and application of the modality moving forwards. Future work may benefit from further investigation of endoprobe SWE performance in adequate sample sizes of heterogeneous TMM phantoms.

Another area of concern was the stiffness range in the TMM phantoms. Considering that the maximum range of the SWE system used in this study was 300 kPa, the range of TMM phantom stiffnesses in this study covered less than 1/3 of this range. With an aim towards gynecological applications of endoprobe SWE and knowing that pathological gynecological tissues may exceed the ceiling of the current sample (95.60 kPa) [121], [207], [209], any future studies of endoprobe SWE in phantoms would benefit from a larger range of stiffness. This may also be beneficial to understand whether there is any value to endoprobe SWE for discriminating low stiffness tissues from high stiffness tissues.

The findings of this study raise concerns around the failure of endoprobe SWE measurements in soft TMM phantoms (< 35 kPa) and deep targets (5cm). Initially, these failures were thought to be due

to the composition of the TMM phantoms; however, good performance of the linear and curvilinear probe SWE for this depth condition suggested that the limitation may be technological rather than methodological. Regardless, this decreased the sample size and range of stiffnesses available for statistical analysis at the 5cm condition for the endoprobe. This may have had an impact on the poor statistical outcomes for this particular case. Regardless, scatterplots showed that the 5cm condition did indeed show much higher variance and poorer linearity over the available stiffness range. Any phantom studies of endoprobe SWE moving forward should ensure that the phantom materials allow for endoprobe SWE measures at deep targets.

Finally, excitation sequences for endoprobe SWE (and any curved probe) are often automatically adjusted based on the azimuth of the region of interest with respect to the principal axis of the probe. This was not accounted for in this validation for the endoprobe or the curvilinear probe. Anecdotally, our team has observed differences in probe performance during preliminary testing of in vivo endoprobe SWE with the azimuth of the SWE region of interest. Thus, SWE validation for any curved probe, including the endoprobe, should be performed at a range of azimuth angles for each target depth to improve the characterization of SWE performance and provide a better understanding of limitations.

3.5 Conclusion

Findings from this study suggest that, although reliability of endoprobe SWE was excellent for all target depths, endoprobe SWE outcomes showed higher variance than those of the linear or curvilinear probe. Endoprobe SWE validity at 1cm depths was poorer than that of the linear and curvilinear probe for all depth conditions. However, depending on the clinical application, endoprobe SWE at shallow depths (e.g. 1cm) may be feasible. In addition, the validity of the SWE data acquired from the 3cm and MCN depth conditions was substantially lower than that of the 1cm depth condition. However, endoprobe SWE at 3cm and MCN depths may still have clinical applicability depending on the

mechanical properties of the healthy and pathological tissues of interest. Finally, endoprobe SWE was not valid at 5cm depths, though this finding may have been impacted by the sample size reduction at this condition due to data acquisition failure. Interestingly, while the endoprobe was not rated for depths beyond 3cm, the linear and curvilinear SWE probes performed exceptionally well beyond the manufacturer's given depth parameters, better than the endoprobe at its recommended depths. Future studies of endoprobe SWE should look towards in vivo validation, particularly focusing on adequate sample sizes for clear statistical characterization of probe performance.

4 Study 2: The Experimental Validity of Flat Tip Indentation for Estimating Soft Tissue Stiffness in a Tissue Mimicking Phantom Model

4.1 Introduction

Soft tissue material properties can provide insight into pathology [54], [106], [123], [124], [258], delineate the pathomechanics of various conditions [259]–[261], aid in the development of tissue prostheses [262]–[264], and more. Yet, the study of soft tissue mechanics is complex. Fresh tissue is difficult to obtain, requiring the contributions of many collaborators across multiple research and clinical departments. There are often departmental costs and methodology costs associated with the acquisition and testing of fresh soft tissue. Further, soft tissue is delicate; desiccation can quickly alter mechanical properties [84], while freezing and other storage methods may significantly impact material properties [231], [232], [265]–[268] [453], [455], [480]–[483]. Thus, when a researcher needs to characterize the material properties of fresh soft tissue via mechanical tissues testing, their methods and mathematical models for estimating material properties must be rigorously tested and finely tuned before ever handling a single fresh tissue sample.

In-house manufactured tissue mimicking material (TMM) phantoms are an economical method for validating mechanical tissue testing methods and models, allowing for the study of an adequate sample size with appropriately tuned mechanical properties. While many different TMMs have been developed and validated in the literature [81], [83], [233], [254], the manufacture of oil-in-gelatin dispersions [82], [84] is particularly accessible [87]. TMM phantoms made from oil-in-gelatin dispersions have been well documented in the literature [82]–[85], [87], [254]. The material properties of oil-in-gelatin TMMs lie well within the range of properties displayed by human soft tissues [82], [87]. Further, oil-in-gelatin TMMs are inexpensive, easy to manufacture, and slight modifications can allow for tuning of the mechanical properties making oil-in-gelatin TMM phantoms ideal for developing

adequately large samples with a range of relevant mechanical properties for the validation of mechanical tissue testing methods and mathematical models.

Soft tissue mechanical testing methodologies are extremely varied throughout the literature. Both tensile and compressive mechanical tissue testing can be used to estimate material properties, depending on the relevant in vivo loading regimes being studied [54], [223]. Compressive testing requires adequately sized samples with uniform geometries, which is not always possible with fresh tissue samples [88]. Similarly, tensile testing may cause tissue damage, and is vulnerable to error due to slipping at the tensile grips [88]. Further, limitations around the surgical sampling procedures for fresh tissue (e.g. minimally invasive approaches), geometrical irregularities (e.g. non-uniform tissue resection), sample geometry (e.g. surgical restrictions), and intact state (e.g. pathology restrictions) can easily prohibit the use of both tensile and compressive testing methodologies.

The flat-tip indentation test is a non-destructive mechanical testing method that addresses many of the limitations of both tensile and compressive testing [71], [90], [112]. The flat-tip indenter requires few components and is accessible with the use of a quasi-static, linear elastic material models. Measures of indentation stiffness (i.e. the slope of the force-displacement curve) are used with various indentation models [109]–[112], [114] and correction factors [88], [111] to estimate the true elastic modulus of a material, where the standard ramp compression test functions as the gold standard comparator for indentation testing [88], [111].

In a review of flat-tip indentation models for biological tissues, Delaine-Smith et al. [88] assessed the impact of geometric factors (i.e. sample thickness (T_s), indenter diameter (Φ_i), sample diameter (Φ_s)) on the performance of four mathematical models in a small sample of hydrogel polymers (n=7, 8kPa<$E_{2.5\text{-}7.5\%}$<45kPa). Their findings indicated that the Oliver and Pharr model [109], [110] performed best (i.e. <=10% error) in cases of "ideal" geometric relationships (T_s:Φ_i>=1:1 and Φ_s:Φ_i>=4:1), yet when samples deviated from these "ideal" relationships (T_s:Φ_i<1:1 and/or Φ_s:Φ_i<4:1), Zhang et al.'s [111]

improved Hayes [112] model showed the best agreement with ramp compression testing. While Delaine-Smith et al.'s [88] work was impressively rigorous, there were several limitations. Delaine-Smith et al. [88] focused on relatively large tissue strains (i.e. 2.5% to 7.5% and 15% to 20%), thus the performance of these models may not be adequate closer to the 0% region of the stress strain curve, which may be particularly relevant to small strain applications [115]. Sample sizes in this study were small (n<=7), yet appropriate statistical tests for validation require sample sizes between n=19 (correlation: α=0.05; β=0.20; r= 0.60) [248], [249] and n=26 (Bland Altman: 80% power; β=0.20; α=0.05; mean difference $\approx$ 4 $\pm$ 2kPa; maximum mean difference $\approx$ 10kPa) [77], [252]. Further, material models were only tested on moduli ranging from 5kPa to 45kPa (2.5% to 7.5% strain), whereas healthy and pathological tissue moduli may easily be beyond double the ceiling on this testing range [54], [71], [89], [209]. Delaine-Smith et al. [88] published correction factors to improve model performance, yet these values were only validated in two small samples (bovine cartilage n = 6; omental tumor n = 3).

Due to the complex nature of characterizing fresh soft tissue mechanical properties using mechanical tissue testing, investigators require a robust validation of indentation models, an evaluation of potential mediators impacting model validity, and guidelines around model performance. Delaine-Smith et al.'s [88] findings around the impact of specimen geometry on the validity of flat-tip indentation testing provides essential information around boundary conditions for the purposes of study design and validation. Yet, the validity of these models and model corrections needs to be more thoroughly characterized using larger sample sizes over a larger range of stiffnesses, especially for small strain applications and small sample geometries. The objectives of this study were to: (1) investigate the validity of the Oliver and Pharr indentation model [109], [110] and Zhang et al.'s [111] improved Hayes [112] indentation model against ramp compression testing for an adequately sized sample of oil-in-gelatin TMM phantoms over a 100 kPa range of 2.5% to 7.5% moduli; (2) investigate the impact of sample geometry (i.e. thickness), quasi-static testing speed, and strain range on model validity; (3)

evaluate the correction equations developed by Delaine-Smith et al. [88]; and (4) provide recommendations around implementing indentation models in experimental settings. Findings from this study will enhance the recommendations made by Delaine-Smith et al. [88] and support the use of flat tip indentation testing for soft tissue characterization for a range of research applications.

4.2 Methods

4.2.1 Indentation Models

Two indentation models were assessed in this work: the Snedden [110] model, which was popularized by Oliver and Pharr [109] (OP), and the Hayes model [112] with Zhang et al.'s [111] geometric correction factors (HZ). The OP [109] assumes quasi-static testing conditions to calculate the elastic modulus of a homogeneous semi-infinite linear elastic medium under a rigid flat end indenter tip with a small strain assumption (Figure 16). The analytic solution by Boussinesq [114] is used to derive the elastic modulus of the material. The "effective" elastic modulus (E) [88], which assumes the modulus of the indenter is substantially higher than that of the TMM sample, was used here. The effective modulus was expressed as a function of the indentation stiffness (S, the slope of the force-displacement curve over the strain range of interest) and the diameter of the indenter tip (Φ_i), with no conversion factor [72], [172] (Equation 10).

$$E = \frac{S}{\Phi \mathrm{i}} \tag{16}$$

The HZ [112] model assumes a lateral infinite isotropic elastic material with a finite thickness resting on a rigid half space [72] under a rigid flat tip indenter (Figure 16). This model assumes adhesion at the sample-support plate interface, negligible shear tractions at the indenter-sample interface, infinitesimal deformation (<0.1% strain), and a frictionless indenter surface [111], [112]. However, to account for larger deformations and non-linearity, Zhang et al.'s changes were implemented [112]. The effective elastic modulus (E) for indentation testing performed using a flat-end cylindrical indenter (Equation 12) was expressed as a function of the Poisson's ratio (ν), the indentation stiffness (S), the

indenter diameter (Φ_i), the thickness of the tissue sample (T_S), and a geometric constant (κ) developed by Zhang et al. [111] was used. Zhang et al.'s [111] constant has been found to improve calculation of the shear and elastic modulus for large strains (up to 20%) [88] and linear interpolation of the constants presented by Zhang et al. [111] can be used for estimation of the elastic modulus at these larger strains [88].

$$E = \frac{S}{\Phi\mathrm{i} * \kappa(v, \Phi\mathrm{i}/T_S)} \tag{17}$$

Delaine-Smith et al.'s correction equations, developed through a series of experimental indentation and compression tests on hydrogels, were also used here. These corrections took the form of linear equations to improve the agreement of both the HZ [111], [112] and OP [109] indentation models with ramp compression testing for strain ranges of 2.5% to 7.5% and 15% to 20%.

4.2.2 Preparation of Oil-in-Gelatin TMM Phantoms

Oil-in-gelatin phantoms were manufactured according to the methods described by Madsen et al. 2006 [253]. In brief, the phantoms were composed of a solvent (water), a matrix (gelatin), and a series of additives (propylene glycol, safflower oil, liquid surfactant, formalin), which function to tune the acoustic, mechanical, and physical properties of the phantoms. First the molten gelatin solution was mixed; water, propylene glycol (5.09% by volume, P4347, Sigma-Aldrich Canada Co., Oakville, Canada), and 200 Bloom gelatin (13.06% by volume Nitta Gelatin, Morrisville, USA) were combined in a beaker. A thermometer was placed in the beaker, the beaker was covered with plastic wrap, and then the beaker placed in a double boiler, and heated to 90°C to produce clarified molten gelatin [253]. The molten gelatin was then cooled in an ice bath to 55°C. At this point, the molten gelatin solution was then combined with safflower oil (Loblaws, Brampton, Canada) and stirred to produce oil droplets (<1mm diameter) [253]. The method of stirring to yield oil droplets in the gelatin matrix involve taking a

standard dinner spoon and bending the spoon at 90^{o} to the handle. The spoon was then placed in the mixture in the beaker and stirred about a horizontal axis. This method encourages the dispersion of the oil droplets, while minimizing air introduction into the mixture. Following this, liquid surfactant (1.1% by volume, Liquid Ivory Ultra, Proctor and Gamble, Toronto, Canada) was added to the mixture to preserve the emulsion and stirred vigorously until the mixture because opaque. Formalin (0.735% by volume, F8775, Sigma-Aldrich Canada Co., Oakville, Canada) was then added to the oil-in-gelatin solution and the mixture was stirred to complete the manufacture of the TMM solution [253].

The oil-in-gelatin TMM solution was cast into a cylindrical mould with a height and diameter each of 7.5cm and placed under positive gauge pressure [253]. The mold included a syringe embedded in the outer was that. When the mixture was in the mold and the syringe was engaged, the material was placed under a positive gauge pressure. After 24 hours, cross-linking of the gelatin had increased the melting temperature well above room temperature. Molds were then removed to yield a cylindrical homogeneous TMM phantom (Figure 22A). Phantoms were placed in safflower oil to prevent desiccation until testing [253]. A total of n=27 phantoms were manufactured, to yield adequate statistical power for the purposes of this study. The ratio of safflower oil in the phantoms was varied between 2.5% and 67.5% in 2.5% increments to yield a uniform spread across a physiologically relevant range of healthy and pathological tissue stiffnesses (20kPa < storage modulus < 100kPa) [82], [84], [253]. Additionally, six extra phantoms were manufactured according to the same procedures using a stiffer 220 Bloom gelatin (13.06% by volume, Sigma-Aldrich, St. Louis, USA) to extend the upper end of the range of stiffnesses over which SWE could be validated. In the end, with two manufacturing failures, the total sample of phantoms was n = 31.

It should be noted here that Madsen et al. [82], [253] observed slight variations in elastic contrasts and strain ratios measured in heterogeneous phantoms made using this TMM. Their team also observed a decrease in the amplitude of the storage modulus measured over a period of 16 months

[253]. Regardless, our study purely aimed to validate measures of the indentation modulus against ramp compression measures. Indentation and ramp compression measures for a given phantom were obtained on the same day, thus eliminating any concerns regarding long-term temporal stability of mechanical properties.

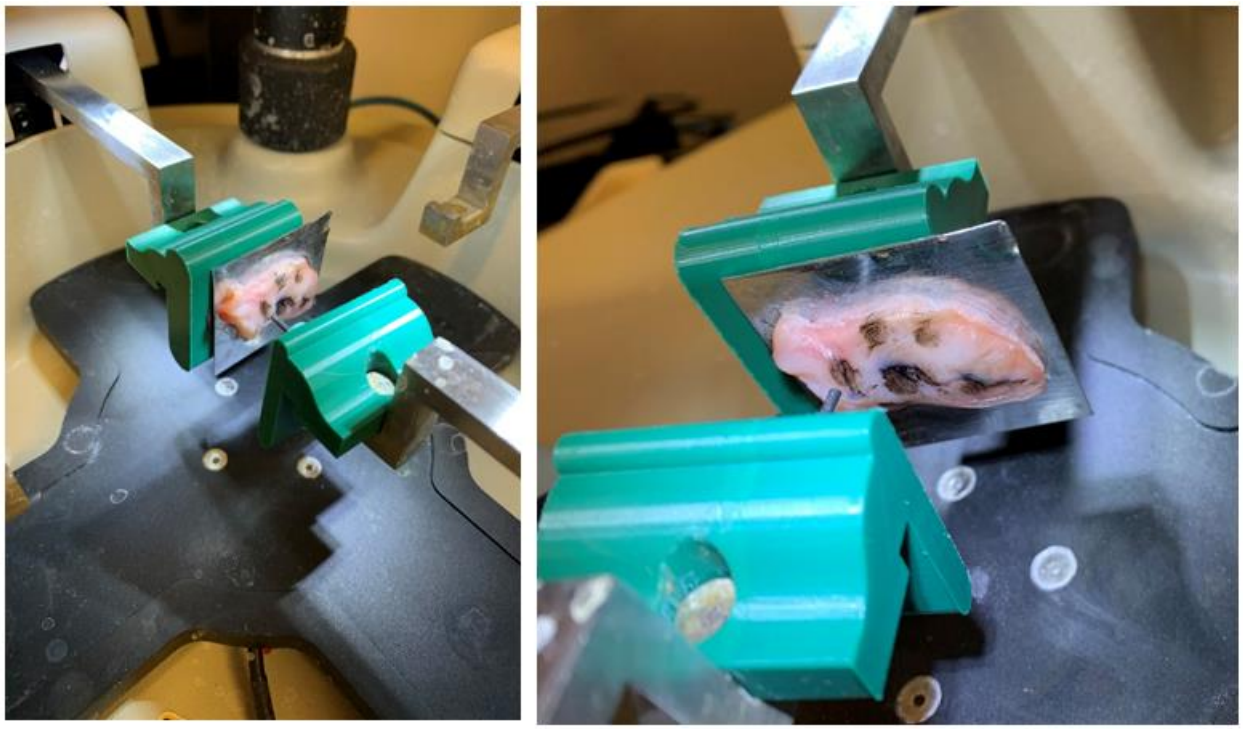

Figure 26 Example of indentation and ramp compression test setup on the Cellscale material testing system using samples of porcine cervix tissue.The 3D printed adapters (green) were used to support the sample & sample stage as well as the indenter tip or ramp compression platen, as appropriate.The plate supporting the tissue is 5cm square and the indenter tip is 1.6mm diameter.

4.2.3 Ramp Compression and Indentation Testing

To validate the OP [109], [110] and HZ [111], [112] indentation models, unconfined ramp quasi-static compression testing was performed in conjunction with indentation testing under a variety of testing parameters. Mechanical properties of the phantoms were measured using the BioTester materials testing system (CellScale, Waterloo, Canada), with a 23N (5.5 mN resolution, 3.5 mN noise floor) load cell and a positional accuracy of 1um. The load cells and displacement controls on the system were calibrated on an annual basis (CellScale, Waterloo, Canada) and monitored for deviations that may

impact testing. Three-dimensional printed adapters made from polyactide (PLA) with 90% infill were secured to the material testing system for ramp and indentation testing. Ramp compression testing was conducted using a 30mm square flat stainless steel compression platen, while indentation testing was conducted using a rigid, cylindrical, flat-ended indenter with a diameter of 1.6mm. Ramp compression and indentation testing were performed by straining the samples to 25% for 20 cycles at a rate of 0.01 Hz, 0.055 Hz, and 0.1 Hz. To ensure that the boundary conditions met the assumptions of the indentation models, sample thickness (T_s) and sample diameter (Φ_s) were adjusted according to the recommendations in the literature (T_s:Φ_i>1, Φ_s:Φ_i>2, Φ_s:T_s>3) [88], [110]–[114].

First, a large and small geometry TMM sample was cut from the phantom, to represent two potential cases of tissue sampling. Anecdotally, our team has had better success collaborating with pathology teams when asking for less than 5mm thick samples of tissue. Thus, the larger TMM sample geometry was treated as over 5 mm thick, with a square cross section of at least 17mm and the smaller TMM sample geometry was less than 5 mm thick with a square cross section of at least 12mm. TMM samples were fixed to a steel support stage and inserted into the mechanical testing system one at a time (Figure 26). The TMM sample cross section dimensions were taken as an average of three trials measured using a Vernier caliper. The TMM sample thickness was calculated as an average of three trials measured as the distance between the support stage and the top of the TMM sample when loaded to 15 mN, taken using the BioTester materials testing system (CellScale, Waterloo, Canada). The indenter or ramp compression platen was then withdrawn from the TMM sample surface to a distance of 500 um. Testing then commenced and the TMM sample was compressed using either the ramp compression platen (i.e. large geometry TMM sample) or the indenter (i.e. large and small geometry TMM samples) at a testing speed of 0.01Hz for 20 cycles. The TMM sample was rested for 5 minutes after testing and bathed in Safflower oil to eliminate any effects of material desiccation. Testing was then repeated for all speeds (i.e. 0.01 Hz, 0.055 Hz, 0.10 Hz) and for all testing conditions (i.e. large

geometry TMM sample ramp compression, large geometry TMM sample indentation, small geometry TMM sample indentation) for a total of 9 tests per phantom.

4.2.4 Data Processing

For each test, the first 10 cycles of loading were treated as preconditioning [127] and the final 10 cycles were used for data processing. The final 10 loading cycles were ensemble averaged and a low pass Butterworth filter (3 Hz cut-off, 2nd order, dual pass) was applied to minimize noise in the data signals. Any bias in the signal was identified as an average of the unloaded period prior to contact of the ramp compression platen or indenter and the signal was zeroed. Contact was detected automatically using a 15 mN force threshold and then verified by visual inspection. In cases where residual noise confounded the algorithm, manual identification of the surface contact was used.

Effective modulus calculations were performed using three strain ranges from the force-displacement curves: (i) in the toe region of the curve from surface contact (i.e. 0% strain) up to a linear threshold, (ii) from 2.5% to 7.5% strain, and (iii) from 15% to 20% strain (Figure 23). The stiffness (i.e. slope of the force-displacement curve) was extracted from the force-displacement curve over the appropriate region and then was used to calculate the effective indentation modulus. For case (i), the stiffness was calculated using methods previously published by Zhai et al. [172]. In brief, beginning from the surface contact point (i.e. 0% strain), a data window with a length of 5% of the tip diameter was identified. A linear regression was chosen to fit a linear model to the window, in order to limit the potential impact of residual noise on a tangent calculation. The error was calculated as the mean absolute difference between the linear model and the force-displacement data window. The data window was then extended one sample at a time and the procedure was repeated for each new data window. The procedure was halted when the error exceeded the 15 mN threshold and the stiffness was taken as the slope of the linear model in this data window. It was observed that the calculated ramp

compression modulus always showed significant correlations with the indentation modulus and the strain at the error threshold of the indentation data always exceeded that of the ramp compression data. Thus, rather than matching the ramp compression linear threshold with that of the indentation modulus, instead a unique linear threshold was determined for both the ramp compression data and the indentation data in each case, to improve the agreement of indentation outcomes with ramp compression outcomes. This strain range will be referred to as the Zhai [172] strain region throughout the remainder of this chapter.

For cases (ii) and (iii), the stiffness was taken simply as the slope of the tangent model fit over the 2.5% to 7.5% and 15% to 20% strain ranges of the force-displacement curve, respectively. The HZ [111] and OP [109] models were then used to calculate the effective modulus with and without Delaine-Smith et al.'s [88] correction equation. As in Amador et al. [72], Poisson's ratio was set to 0.475 to align closely with the incompressibility assumption, while sitting in a range that keeps $\kappa(\nu,a/h)$ fairly constant for the testing parameters. In the case of the ramp compression testing, the modulus was taken as the slope of the stress-strain curve at the strain ranges determined by (ii) and (iii) [228].

4.2.5 Statistical Analysis

Initially, the loading-unloading cycles and the ensemble average of the final ten loading cycles were visualized. The span of the toe region (strain, %) was reported. To evaluate the consistency of phantom properties, Pearson's correlations were used to assess the relationship between volume percent of oil in the phantoms and the span of the toe region. As well, a two-way analysis of variance was used to compare the span of the toe region across the different mechanical tests and testing rates, in order to assess the potential impact of hysteresis and friction on mechanical testing outcomes.

The large number of testing parameters included in the methodology yielded a high dimensionality problem that precluded multivariate analysis of the data set. With this in mind, the relationship

between unconfined ramp compression and indentation outcomes was evaluated on a case-by-case basis using a series of approaches often implemented in sensitivity analyses (MATLAB, Mathworks, Natick, USA). Initially relationships between indentation and ramp compression outcomes were qualitatively evaluated using scatter plots. Pearson's or Spearman's correlation analyses were then implemented to quantitatively characterize the relationship, as appropriate. Bland Altman analyses were used to quantify the exact agreement between indentation and ramp compression outcomes. In order to provide bounds on problem, two indentation models across all parameters were selected as representative best and worst relationships with ramp compression testing, as quantified by correlations and Bland Altman analyses, and plots for both outcomes were generated. Trends across the validation outcomes were observed for the various indentation testing parameters (size, speed, strain) and models (HZ, OP) to guide parameter selection moving forward. The level of significance was set to $\alpha = 0.05$ for all statistical tests.

4.3 Results

Individual plots showing the force-displacement curves were visualized for repeated loading-unloading cycles (Figure 27A) and for the ensemble average of the final ten loading cycles (Figure 27B). Minor hysteresis was clearly visualized in the initial portion of the loading-unloading cycles. The span of the toe range showed a significant positive correlation with the volume percent of oil in the phantoms for all mechanical tests (Figure 28,

Table 9). While there was no significant different in the span of the toe region and the testing rate, the span of the toe region was significantly larger for the indentation tests in small geometry samples ($p<0.001$) than that measured in the indentation test in large geometry samples and in ramp testing ($p<0.001$). Similarly, the span of toe region was also significantly larger for the indentation tests in large geometry samples compared to that measured in the ramp compression testing ($p<0.001$).

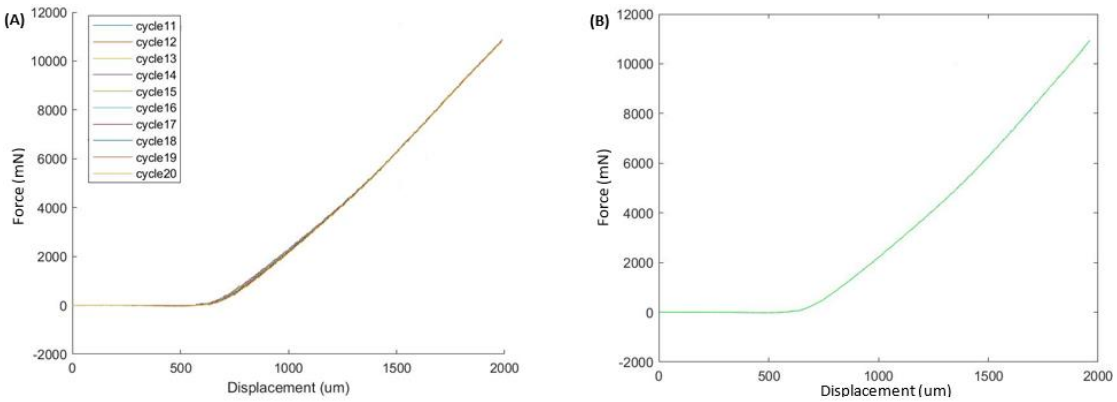

Figure 27 Individual force-displacement curves for repeated loading cycles of mechanical testing (A) and for the ensemble average across the final 10 loading cycles. Force was measured in millinewtons (mN) and displacement was measured in micrometers (um). Hysteresis is visible in the first half of the repeated loading curves (A).

Table 9 The mean and standard deviation (STD) strain span of the toe region of the load-displacement curve is reported for all tests conducted at all testing rates. The strain span of the toe region showed significant correlations with the oil % volume in the phantoms for all cases.

Mechanical Test	Testing Rate (Hz)	Strain Span of Toe Region (Mean ± STD %)	Correlation with Oil Volume %	
			r	p
Indent - Small	0.01	17.12 ± 5.64	0.85	<0.001
Indent – Small	0.055	15.12 ± 4.77	0.85	<0.001
Indent – Small	0.1	16.15 ± 4.93	0.86	<0.001
Indent - Large	0.01	11.89 ± 3.81	0.89	<0.001
Indent – Large	0.055	11.66 ± 3.96	0.89	<0.001
Indent – Large	0.1	11.68 ± 4.08	0.89	<0.001
Ramp	0.01	1.98 ± 0.54	0.37	0.082
Ramp	0.055	1.73 ± 0.60	0.57	0.005
Ramp	0.1	1.84 ± 0.76	0.62	0.001

Scatterplots visualizing the agreement between indentation testing and ramp compression outcomes for the 0.01Hz (Figure 29), 0.055Hz (Figure 30), and 0.1Hz (Figure 31) testing speeds are presented here. Each individual plot includes data from both small (blue) and large (red) geometry samples for a given model (OP or HZ) at a given strain (Zhai [172], 2.5%-7.5%, or 15%-20%) tested at a given speed (0.01Hz, 0.055Hz, 0.1 Hz). Either ramp or indentation testing failed for up to six cases depending on the testing parameters, due to hardware and/or software malfunctions. As such, the resulting sample size differed slightly between the various testing cases, with sample sizes ranging from n = 24 to n = 28.

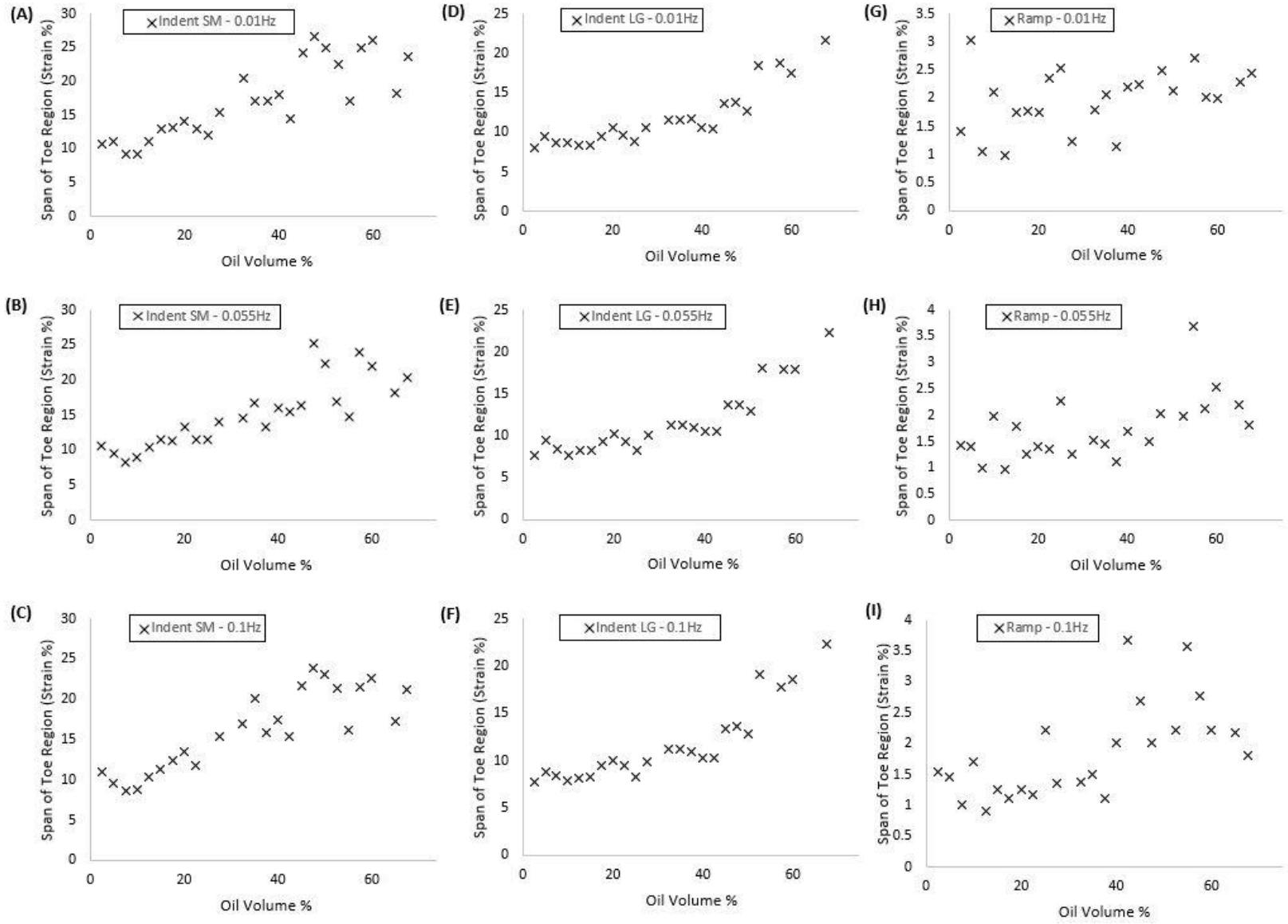

Figure 28 Scatterplots visualizing the span of the strain region, measured in % strain, as a function of the oil volume percentage in each phantom. Data is visualized for the indentation testing with the small geometry samples (Indent SM), the large geometry samples (Indent LG), and ramp tests at the 0.01Hz, 0.055Hz, and 0.1Hz testing rates

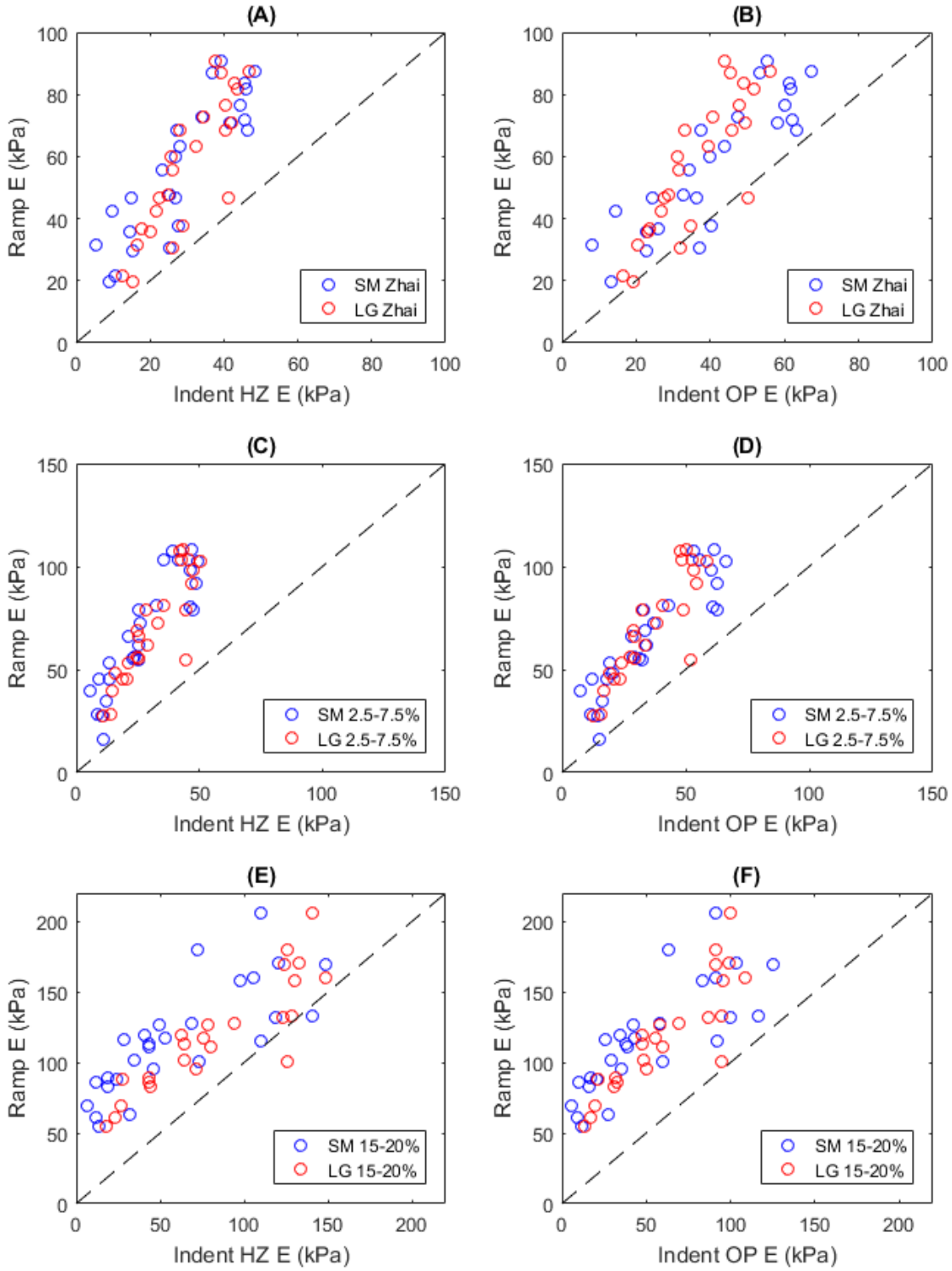

Figure 29 Agreement of elastic modulus (E) in kilopascals (kPa) from unconfined ramp compression testing (Ramp) and flat cylindrical tip indentation testing (Indent) in homogeneous oil-in-gelatin tissue mimicking phantoms. E was calculated using linear elastic models on the force-displacement or stress-strain curve in the toe region (A, B) using Zhai et al.'s [172] *methods, from 2.5% to 7.5% strain (C, D), and from 15% to 20% strain (E, F). Data are separated by small (SM) geometry (thickness < 5mm) or a large (LG) geometry (thickness > 5mm) and Hayes-Zhang (HZ E)* [111], [112] *(A, C, E) or Oliver Pharr (OP E) indentation model* [109] *(B, D, F). Testing rate was 0.01 Hz for all cases. For each plot a equality between parameters is indicated by the dashed black line.*

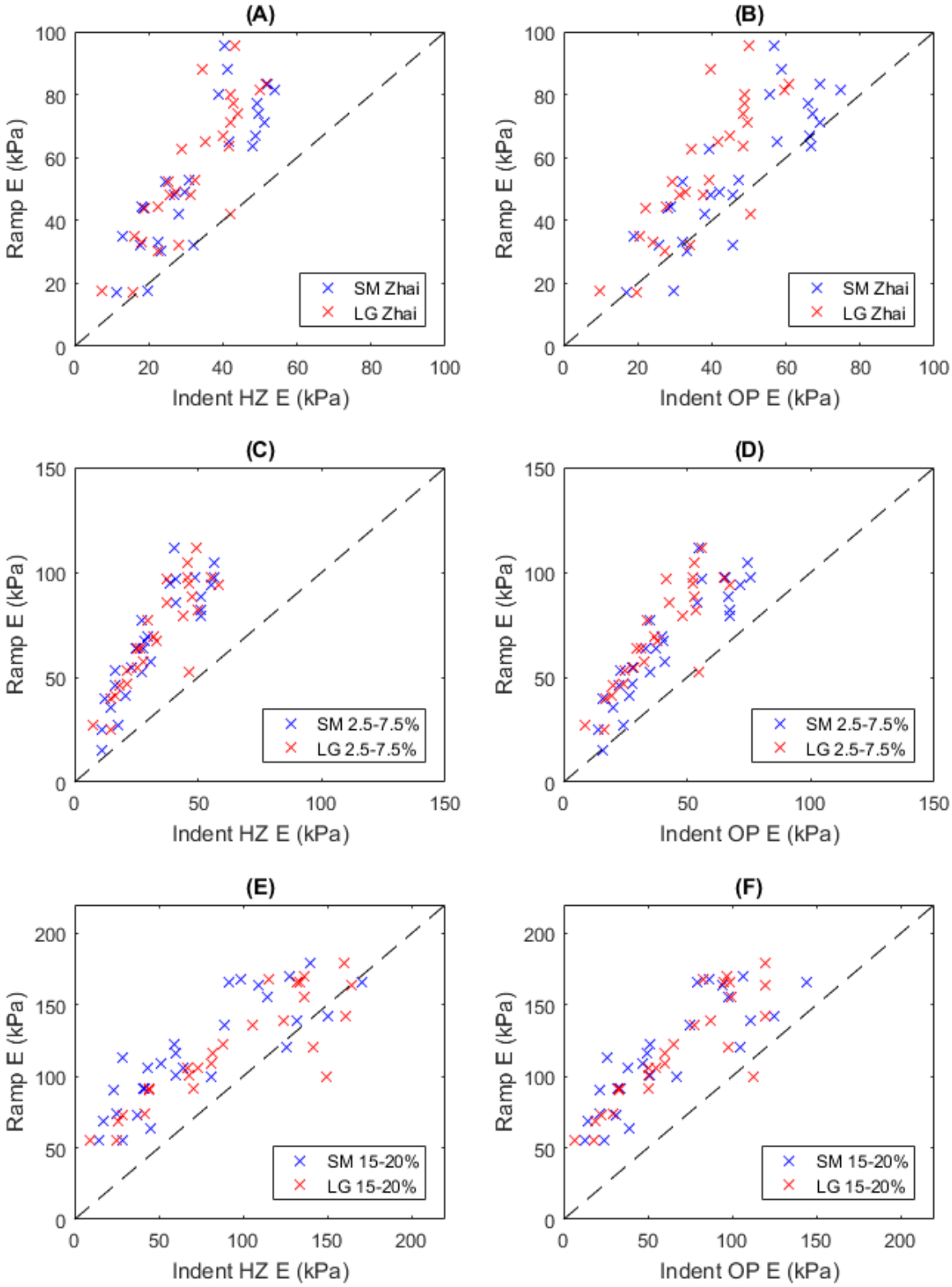

Figure 30 Agreement of elastic modulus (E) in kilopascals (kPa) from unconfined ramp compression testing (Ramp) and flat cylindrical tip indentation testing (Indent) in homogeneous oil-in-gelatin tissue mimicking phantoms. E was calculated using linear elastic models on the force-displacement or stress-strain curve in the toe region (A, B) using Zhai et al.'s [172] *methods, from 2.5% to 7.5% strain (C, D), and from 15% to 20% strain (E, F). Data is separated by small (SM) geometry (thickness < 5mm) or a large (LG) geometry (thickness > 5mm) and Hayes-Zhang (HZ E)* [111], [112] *(A, C, E) or Oliver Pharr (OP E) indentation model* [109] *(B, D, F). Testing rate was 0.055 Hz for all cases. For each plot, equality between parameters is indicated by the dashed black line.*

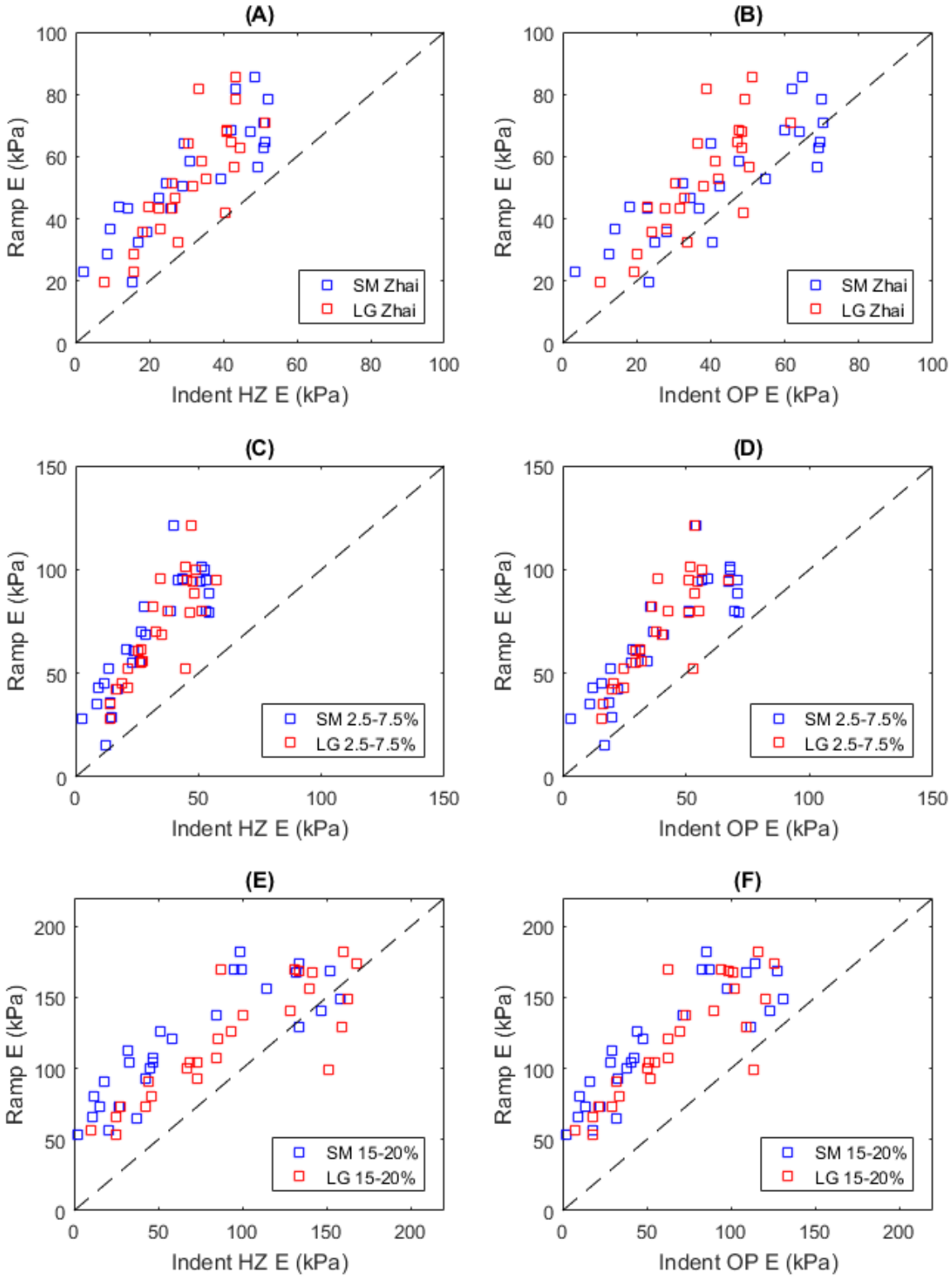

Figure 31 Agreement of elastic modulus (E) in kilopascals (kPa) from unconfined ramp compression testing (Ramp) and flat cylindrical tip indentation testing (Indent) in homogeneous oil-in-gelatin tissue mimicking phantoms. E was calculated using linear elastic models on the force-displacement or stress-strain curve in the toe region (A, B) using Zhai et al.'s [172] *methods, from 2.5% to 7.5% strain (C, D), and from 15% to 20% strain (E, F). Data are separated by small (SM) geometry (thickness < 5mm) or a large (LG) geometry (thickness > 5mm) and Hayes-Zhang (HZ E)* [111], [112] *(A, C, E) or Oliver Pharr (OP E) indentation model* [109] *(B, D, F). Testing rate was 0.1 Hz for all cases. For each plot, equality between parameters is indicated by the dashed black line.*

Qualitative analysis of the scatterplots suggested good agreement between ramp compression and indentation testing across all testing conditions and models. Qualitatively, there appeared to be little impact of indentation model, sample geometry, or testing speed on ramp compression and indentation agreement. The 2.5% to 7.5% moduli and the Zhai [172] moduli demonstrated similar trends, though the 2.5% to 7.5% moduli did appear to be qualitatively higher. In contrast, the 15%-20% moduli exhibited much higher values with larger variability in the data. Data visualization suggested a bias (significant mean difference) and slopes that trended above the perfect correlation line for all indentation testing parameters and models when compared to ramp compression.

Correlation coefficients (CC) investigating the relationship between indentation and ramp compression moduli at all testing parameters were very strong (CC > 0.7) and highly significant ($p<0.001$) (Figure 32). The highest correlations between ramp and indentation outcomes were observed in the small geometry samples for the 2.5% to 7.5% moduli at the 0.01Hz and 0.055Hz (CC= 0.91) testing speeds. Interestingly, large geometry samples exhibited the highest correlations also at the low testing speed (0.01Hz), for the 2.5% to 7.5% ($0.88 \leq CC \leq 0.89$) and the 15%-20% ($0.89 \leq CC \leq 0.90$) moduli. The lowest correlations across all testing parameters were observed for the Zhai [172] moduli at the 0.1 Hz testing speed ($0.77 \leq CC \leq 0.80$). Regardless, the relationship between indentation and ramp compression was consistently strong for all conditions.

When comparing indentation models, the HZ and OP model yielded almost identical CCs for each set of testing parameters. Sample geometry yielded slight deviations between the correlations of indentation and ramp outcomes only for the 15% to 20% moduli at the 0.01Hz speed (small: $0.85 \leq$ correlation ≤ 0.86; large: $0.89 \leq$ correlation ≤ 0.90). Otherwise, correlations did not appear to differ substantially between large and small geometry TMM samples. Considering the potential impact of testing speed, the correlation between indentation and ramp compression moduli decreased above 0.01Hz testing speed for the Zhai [172] moduli, and above 0.055Hz testing speed for the 2.5% to 7.5%

moduli. However, the 15% to 20% moduli correlations only decreased above 0.01Hz testing speed for large geometry samples. Considering the impact of strain range, small geometry samples generally exhibited the highest correlations between ramp and indentation outcomes for 2.5% to 7.5% moduli at the two lowest testing speeds, however this trend was not present for large geometry samples.

Table 10 Correlation coefficients for the elastic moduli (E) calculated from unconfined ramp compression testing (Ramp) and flat cylindrical tip indentation testing (Indent) in homogeneous oil-in-gelatin tissue mimicking phantoms. Testing was conducted on material samples with small (SM) geometry (thickness < 5mm) and a large (LG) geometry (thickness > 5mm) at three quasi-static testing rates (0.01 Hz, 0.055 Hz, 0.1 Hz). E was calculated using linear elastic models on the force-displacement or stress-strain curve. in the toe region using Zhai et al.'s [172] *methods (Zhai), from 2.5% to 7.5% strain, or from 15% to 20% strain. For indentation moduli, the Hayes-Zhang (HZ)* [111], [112] *or Oliver Pharr (OP) indentation model* [109] *were used. The number of observations (n) included in each test is given. Correlations were calculated using either a Pearson's or Spearman's correlation test as appropriate. All correlations were significant to the level of p<0.0001.*

Testing Rate	Strain	SM			LG		
		n	HZ	OP	n	HZ	OP
0.01 Hz	Zhai [172]	26	0.88	0.88	24	0.86	0.85
	2.5% - 7.5%	27	0.91	0.91	24	0.89	0.88
	15% - 20%	27	0.85	0.86	24	0.90	0.89
0.055 Hz	Zhai [172]	27	0.84	0.84	26	0.85	0.83
	2.5% - 7.5%	28	0.91	0.92	26	0.87	0.87
	15% - 20%	28	0.85	0.86	26	0.87	0.87
0.1 Hz	Zhai [172]	26	0.79	0.80	26	0.79	0.77
	2.5% - 7.5%	27	0.85	0.86	25	0.84	0.84
	15% - 20%	27	0.86	0.87	26	0.85	0.85

Bland-Altman analyses of the agreement between ramp compression and indentation outcomes calculated using the small (Table 11) and large (*Table 12*) TMM samples further confirmed qualitative observations from the scatterplots. Significant ($p<0.001$) positive mean differences (MDs) were observed for all testing conditions and models, ranging from 8.79 kPa to 64.96 kPa. Standard deviation (STD) of the MDs, an indicator of variance in agreement of indentation and ramp compression outcomes, ranged from 11.83 kPa to 57.79 kPa. The best agreement was generally observed for small geometry samples with the OP model used to calculate the Zhai [172] moduli (MDs $\leq$15 kPa, STD MD $\leq$13 kPa). The poorest agreement was generally observed for the OP model used to calculate the 15% to 20% moduli. This was observed in both large and small geometry samples (MDs $\geq$50 kPa, STD MD $\geq$19 kPa).

Comparing indentation model agreement with ramp compression outcomes, the HZ MDs were generally higher than the OP MDs at low strains (Zhai [172] and 2.5% to 7.5%) while the trend reversed for the 15% to 20% moduli. The STD of the MDs did not differ substantially across models. Sample geometry appeared to only be a factor for the 15% to 20% moduli, where larger geometry samples generally exhibited substantially lower MDs than small geometry samples. STD of the MD was generally consistent between sample geometries across all testing parameters. Differences in agreement between indentation and ramp outcomes with testing speed were only observed for large sample geometries and 15% to 20% moduli, with testing speeds above 0.01Hz resulting in a 7kPa to 15kPa reduction of the MD. Again, STDs of the MD were consistent across testing speeds for all parameters. Considering the agreement across the different strain ranges, there was generally improved agreement (lower MDs and STDs of the MD) of the Zhai [172] moduli compared to the 15% to 20% moduli. In comparison, MDs of the 2.5% to 7.5% moduli were generally higher than those of the Zhai [172] moduli, but STDs of the MD were fairly consistent between the two strains. Variance in the MDs was consistently high (>20kPa) for the 15%-20% moduli under all testing conditions and indentation models.

Table 11 Bland Altman test results for exact agreement of the elastic moduli (E) calculated from unconfined ramp compression testing (Ramp) and flat cylindrical tip indentation testing (Indent) in homogeneous oil-in-gelatin tissue mimicking phantoms for samples with small (SM) geometry (thickness < 5mm). Testing was conducted at three quasi-static testing rates (0.01 Hz, 0.055 Hz, 0.1 Hz). E was calculated using linear elastic models on the force-displacement or stress-strain curve. in the toe region using Zhai et al.'s [172] *methods (Zhai), from 2.5% to 7.5% strain, or from 15% to 20% strain. For indentation moduli, the Hayes-Zhang (HZ)* [111], [112] *or Oliver Pharr indentation model* [109] *were used. The number of observations (n), mean difference (MD), standard deviation of the mean difference (STD), standard error of the mean difference (SE), and the 95% confidence interval (CI) on the mean difference are included. All MDs were significant to the level of p<0.001.*

Rate (Hz)	Strain Range (%)	HZ					OP				
		n	MD (kPa)	STD (kPa)	SE	95% CI	n	MD (kPa)	STD (kPa)	SE	95% CI
0.01	Zhai [172]	26	28.02	12.12	0.47	(4.26,51.78)	26	15.35	10.54	0.41	(-4.31,37.01)
	2.5 – 7.5	27	39.82	15.38	0.57	(9.68,69.96)	27	30.97	12.72	0.47	(6.04,55.90)
	15 – 20	27	55.72	26.93	1.00	(2.93,108.50)	27	64.96	23.91	0.89	(18.09,111.83)
0.055	Zhai [172]	27	22.10	12.96	0.48	(0.67, 47.51)	27	8.79	11.83	0.44	(-14.39,31.97)
	2.5 – 7.5	28	34.85	14.67	0.52	(6.07,63.64)	28	24.37	12.22	0.44	(0.43,48.32)
	15 – 20	28	41.74	24.02	0.86	(-5.35,88.83)	28	52.84	20.20	0.72	(12.24,92.44)
0.1	Zhai [172]	26	23.14	12.67	0.49	(-1.70,47.97)	26	10.57	13.35	0.51	(-15.60,36.73)
	2.5 – 7.5	27	36.82	14.88	0.55	(7.66,65.99)	27	26.85	13.10	0.48	(1.20,52.51)
	15 – 20	27	48.95	25.68	0.95	(-1.38,99.28)	27	59.19	21.08	0.78	(17.88,100.51)

Table 12 Bland Altman test results for exact agreement of the elastic moduli (E) calculated from unconfined ramp compression testing (Ramp) and flat cylindrical tip indentation testing (Indent) in homogeneous oil-in-gelatin tissue mimicking phantoms for samples with large (LG) geometry (thickness > 5mm). Testing was conducted at three quasi-static testing rates (0.01 Hz, 0.055 Hz, 0.1 Hz). E was calculated using linear elastic models on the force-displacement or stress-strain curve. in the toe region using Zhai et al.'s [172] *methods (Zhai), from 2.5% to 7.5% strain, or from 15% to 20% strain. For indentation moduli, the Hayes-Zhang (HZ)* [111], [112] *or Oliver Pharr indentation model* [109] *were used. The number of observations (n), mean difference (MD), standard deviation of the mean difference (STD), standard error of the mean difference (SE), and the 95% confidence interval (CI) on the mean difference are included. All MDs were significant to the level of $p<0.001$.*

Rate (Hz)	Strain Range (%)	HZ					OP				
		n	MD (kPa)	STD (kPa)	SE	95% CI	n	MD	STD (kPa)	SE (kPa)	95% CI
0.01	Zhai [172]	24	26.53	14.20	0.59	(-1.30,54.36)	24	20.68	13.67	0.57	(-6.12,47.48)
	2.5 – 7.5	24	38.46	15.39	0.64	(8.30,68.62)	24	33.89	14.39	0.60	(5.68,62.10)
	15 – 20	24	35.54	19.85	0.83	(-3.37,74.45)	24	57.79	19.02	0.79	(20.52,95.07)
0.055	Zhai [172]	26	24.10	13.34	0.51	(-2.04,50.24)	26	18.27	13.14	0.51	(-7.48,44.01)
	2.5 – 7.5	26	36.20	13.96	0.54	(8.84,63.56)	26	31.45	13.21	0.51	(5.54,57.36)
	15 – 20	26	25.10	23.88	0.92	(-21.69,71.90)	26	50.12	18.73	0.72	(13.41,86.83)
0.1	Zhai [172]	26	22.63	13.60	0.52	(-4.03,49.29)	26	16.80	13.46	0.52	(-9.59,43.19)
	2.5 – 7.5	25	36.52	15.05	0.50	(7.03,66.02)	25	31.65	14.36	0.57	(3.50,59.79)
	15 – 20	26	25.53	26.03	1.00	(-25.49,76.56)	26	50.77	21.09	0.81	(0.34,92.11)

The efficacy of the Delaine-Smith [88] correction was investigated. Knowing that correlations are invariant to linear transformations, only the Bland-Altman analysis was re-examined for the Delaine-Smith et al.'s [88] correction to the HZ and OP model data. There were five cases for the HZ model and no cases for the OP model in which the Delaine-Smith [88] correction reduced MDs to levels of non-significance while maintaining low STDs of the MDs (<15 kPa). Two of these cases were for the small sample geometry (HZ Zhai [172] at 0.01 Hz, HZ 2.5%-7.5% at 0.055Hz) and three were for the large sample geometry (HZ Zhai [172] at 0.01 Hz, HZ 2.5%-7.5% at 0.055 Hz, HZ 2.5%-7.5% at 0.1Hz), while all cases were for moduli calculated over the Zhai [172] or 2.5%-7.5% strain ranges. For the HZ model applied to data from both small and large geometry samples, the correction resulted in substantial increases to the STD of the MD for all moduli calculated from 15%-20% strains. For the OP model applied to both sample geometry conditions, the correction had no substantial impact on STDs of the MD, while MDs were unaffected or increased.

Table 13 Bland Altman test results for exact agreement of the elastic moduli (E) calculated from unconfined ramp compression testing (Ramp) and Delaine-Smith et al.'s [88] *linear regression correction for flat cylindrical tip indentation testing (Indent) of homogeneous oil-in-gelatin tissue mimicking phantoms for samples with small (SM) geometry (thickness < 5mm). Testing was conducted at three quasi-static testing rates (0.01 Hz, 0.055 Hz, 0.1 Hz). E was calculated using linear elastic models on the force-displacement or stress-strain curve. in the toe region using Zhai et al.'s* [172] *methods (Zhai), from 2.5% to 7.5% strain, or from 15% to 20% strain. For indentation moduli, the Hayes-Zhang (HZ)* [111], [112] *or Oliver Pharr indentation model* [109] *were used. The number of observations (n), mean difference (MD), standard deviation of the mean difference (STD), standard error of the mean difference (SE), and the 95% confidence interval (CI) on the mean difference are included. MDs significant to the level of p<0.05 are marked with *.*

Rate (Hz)	Strain Range (%)	HZ					OP				
		n	MD (kPa)	STD (kPa)	SE	95% CI	n	MD (kPa)	STD (kPa)	SE	95% CI
0.01	Zhai [172]	27	-0.40	12.82	0.49	(-25.53,24.73)	27	22.58*	11.54	0.44	(-25.53,24.73)
	2.5 – 7.5	27	12.64*	12.58	0.47	(-12.02,37.29)	27	36.42*	14.62	0.54	(7.77,65.07)
	15 – 20	27	-31.08*	77.34	2.86	(-182.66,120.50)	27	63.01*	24.09	0.89	(15.79,110.23)
0.055	Zhai [172]	28	-10.81*	14.13	0.52	(-38.50,16.88)	28	16.22*	12.56	0.47	(-8.39,40.83)
	2.5 – 7.5	28	3.09	13.41	0.48	(-23.20,29.39)	28	31.04*	13.89	0.50	(3.81,58.27)
	15 – 20	28	-63.54*	79.18	2.83	(-218.74,91.66)	28	50.66*	20.42	0.73	(10.64,90.69)
0.1	Zhai [172]	27	-7.80*	19.09	0.73	(-45.22,29.61)	27	17.47*	12.62	0.49	(-7.26,42.20)
	2.5 – 7.5	27	6.67*	16.42	0.61	(-25.52,38.85)	27	33.10*	14.21	0.53	(5.25,60.96)
	15 – 20	27	-48.60*	88.23	3.26	(-221.54,124.33)	27	57.11*	21.37	0.79	(15.22,99.00)

Table 14 Bland Altman test results for exact agreement of the elastic moduli (E) calculated from unconfined ramp compression testing (Ramp) and Delaine-Smith et al.'s [88] *linear regression correction for flat cylindrical tip indentation testing (Indent) of homogeneous oil-in-gelatin tissue mimicking phantoms for samples with large (LG) geometry (thickness > 5mm). Testing was conducted at three quasi-static testing rates (0.01 Hz, 0.055 Hz, 0.1 Hz). E was calculated using linear elastic models on the force-displacement or stress-strain curve. in the toe region using Zhai et al.'s* [172] *methods (Zhai), from 2.5% to 7.5% strain, or from 15% to 20% strain. For indentation moduli, the Hayes-Zhang (HZ)* [111], [112] *or Oliver Pharr indentation model* [109] *were used. The number of observations (n), mean difference (MD), standard deviation of the mean difference (STD), standard error of the mean difference (SE), and the 95% confidence interval (CI) on the mean difference are included. MDs significant to the level of p<0.05 are marked with *.*

Rate (Hz)	Strain Range (%)	HZ					OP				
		n	MD (kPa)	STD (kPa)	SE	95% CI	n	MD (kPa)	STD (kPa)	SE	95% CI
0.01	Zhai [172]	24	-3.78	11.35	0.47	(-26.03,18.47)	24	26.18*	14.93	0.62	(-3.09,55.45)
	2.5 – 7.5	24	7.18*	11.86	0.49	(-16.06,30.42)	24	39.34*	16.09	0.67	(7.80,70.88)
	15 – 20	24	-82.91*	69.85	2.91	(-219.83,54.00)	24	55.65*	18.91	0.79	(18.59,92.71)
0.055	Zhai [172]	26	-7.73*	12.21	0.47	(-31.66,16.20)	26	24.06*	14.25	0.55	(-3.87,51.99)
	2.5 – 7.5	26	2.68	13.60	0.52	(-23.98,29.33)	26	37.38*	14.68	0.56	(8.61,66.14)
	15 – 20	26	-106.57*	85.26	3.28	(-273.69,60.55)	26	47.85*	18.83	0.72	(10.95,84.75)
0.1	Zhai [172]	26	-9.20*	13.90	0.53	(-36.40,18.08)	26	22.58*	14.24	0.55	(-5.33,50.49)
	2.5 – 7.5	25	2.02	14.15	0.57	(-25.72,29.75)	25	37.79*	15.64	0.63	(7.13,68.45)
	15 – 20	26	-107.17	88.02	3.39	(-279.68,65.34)	26	48.49*	21.18	0.81	(6.99,89.99)

Combining findings from the correlation and Bland-Altman analyses, a representative best case and a representative worst case were selected for graphical representation. The small sample with the OP model used to calculate the Zhai [172] modulus at 0.01 Hz was selected as a representation of the best case due to its high correlation (CC = 0.88) combined with the low variance in agreement with ramp

compression (MD STD = 10.54 kPa) and relatively low MD (MD = 15.35 kPa) (Figure 32A and B). Despite its high correlation (CC = 0.86), the small sample with the HZ model used to calculate the 15%-20% modulus yielded one of the highest MDs (MD = 48.95 kPa) and one of the highest variances on the MD (STD MD = 25.68 kPa) (Figure 32C and D). Correlation plots effectively visualized that the slope of the trendline for the best-case condition (Figure 32A) was almost 1 and that the bias and variability of the agreement between ramp compression and indentation outcomes were the main factors impacting model validity (Figure 32A and B). Interestingly, the agreement of ramp compression and the worst-case

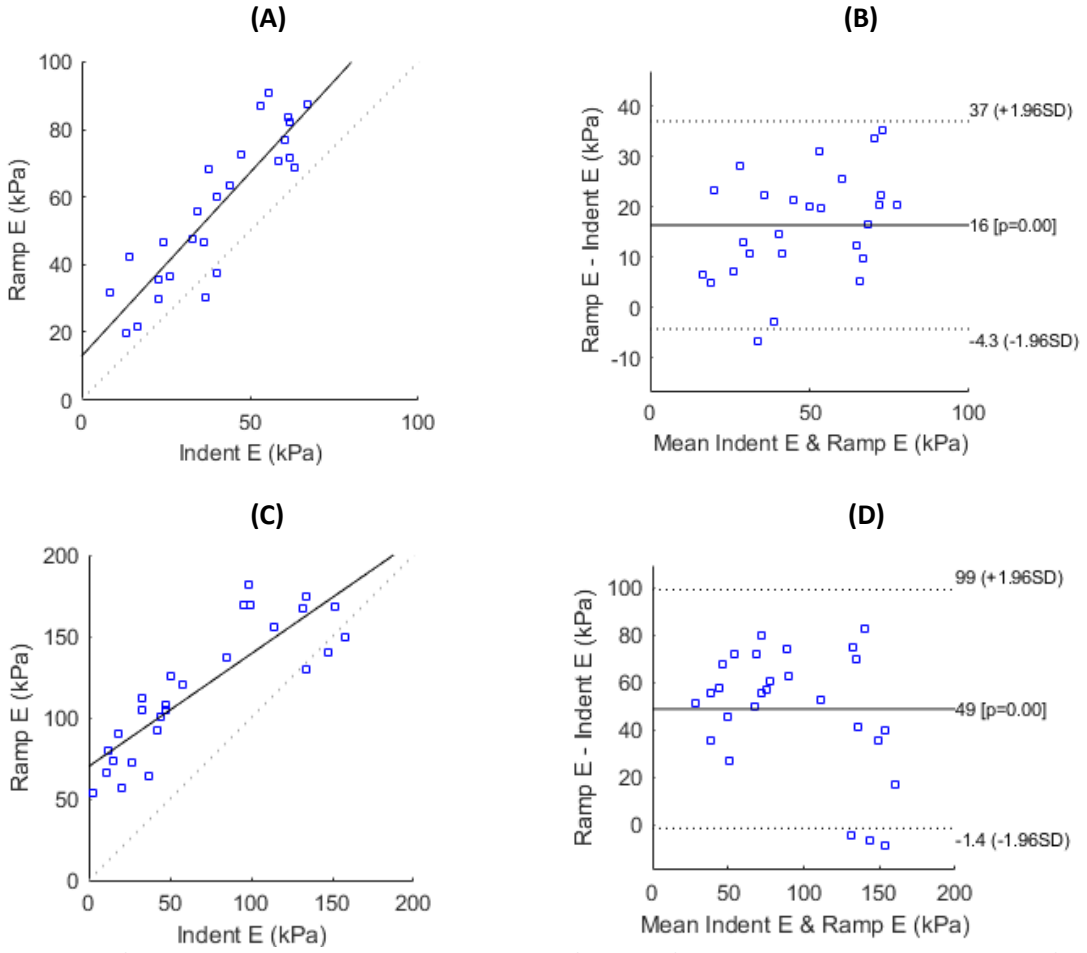

Figure 32 Agreement of elastic modulus (E) calculated in kilopascals (kPa) from unconfined ramp compression testing (Ramp) and flat cylindrical tip indentation testing (Indent) in small samples (thickness < 5mm) of homogeneous oil-in-gelatin tissue mimicking phantoms shown using correlation plots (A, C) and Bland Altman plots (B, D) for two cases. Agreement of indentation E with ramp E yielded the lowest variability (standard deviation (SD) of the mean difference) for the Oliver Pharr model [109] *model with testing conducted at 0.01 Hz with E calculated using Zhai et al's* [172] *methods (A, B). Agreement of indentation E with ramp E yielded the highest variability for the Hayes-Zhang model* [111], [112] *with testing conducted at 0.1 Hz with E calculated from 15% to 20% strain on the force-displacement curve (C, D). Correlation plots (A,C) show a perfect correlation (dashed line) and the true correlation of the indentation and ramp data (solid line). Bland Altman plots show the mean difference (solid line) and 95% confidence interval on the limits of agreement (dashed line).*

condition appeared to be similarly rooted in a substantial bias and high variance (Figure 32C and D), but also a significant deviation in the trendline from a slope of 1 (Figure 32C).

4.4 Discussion

Findings from this work provided a thorough characterization of the agreement between indentation and ramp compression testing for a variety of testing parameters and models, further enhancing the work done by Delaine-Smith et al. [88]. The results here continue to support the use of indentation testing as an accessible, economical method for characterizing soft tissue material properties. However, the large sample size facilitated a more robust quantification of the agreement between indentation and ramp compression estimates of the elastic modulus under a variety of testing parameters (speed, strain range, sample geometry) for two common indentation models (OP, HZ).

4.4.1 Indentation Model

When the data are separated to determine differences in the OP and HZ indentation moduli agreement with ramp compression moduli, a few observations were made. The scatterplots (Figure 29, Figure 30, Figure 31) and correlation outcomes (Table 10) do not reveal any substantial differences between OP and HZ agreement with ramp compression outcomes. Trends in the data (e.g. variance, trendlines, biases) appear strikingly similar, while correlations of HZ and OP indentation outcomes with ramp compression outcomes were also almost identical for all testing conditions (speed, strain, sample geometry). The Bland-Altman analyses (Table 11,

Table 12) suggest a possible interaction between the indentation model and the strain range. For the Zhai [172] and 2.5%-7.5% strain ranges outcomes, the HZ model yielded MDs that were 6kPa to 14kPa larger than for the OP model, depending on sample geometry. In contrast, for the 15%-20% moduli, the OP model yielded MDs that were 9kPa to 25kPa larger than for the HZ model. However, the STD of the

MDs between the indentation and ramp compression outcomes did not vary substantially (<5kPa) between the HZ and OP models.

The findings from this study suggest that the OP model may provide more accurate outcomes when working in low strain ranges (Zhai [172] or 2.5%-7.5%), while the HZ model may improve validity for indentation moduli calculated over larger strain ranges (15%-20%). Interestingly, Delaine-Smith et al. [88] also observed higher deviation between indentation and ramp compression testing for the HZ compared to the OP model, however this deviation was observed at both the 2.5%-7.5% and the 15%-20% strain ranges with a qualitatively much better fit between the ramp compression moduli and the OP moduli than the HZ moduli. Coefficients from Delaine-Smith et al. [88] correction equations for both models also indicate a much larger deviation between the HZ model and ramp compression moduli at the both the 2.5%-7.5% and 15%-20% strain ranges, compared to the OP model. However, the data presented by Delaine-Smith et al. [88] were limited to n = 7 samples, included a smaller range of material stiffnesses, and more robust analyses were not included. The Zhang et al. [111] correction for the HZ model was developed particularly for larger strain applications (up to 20%), thus findings here do indeed align with the intended application of the HZ model.

4.4.2 Sample Geometry

When sample geometry was maintained above thresholds indicated in the literature (T_s:Φ_i>1, Φ_s:Φ_i>2, Φ_s:T_s>3) [88], [110]–[114], several observations can again be made. Referring to the scatterplots (Figure 29, Figure 30, Figure 31) and the correlation outcomes (Table 10), TMM sample geometry did not appear to impact the agreement between indentation and ramp compression outcomes. Variance in the data did not differ substantially between small and large geometry samples and trends in the scatterplots were consistent across the two conditions, as were biases. Similarly, correlations did not differ between large and small sample geometries by more than 0.04, and higher correlations did not

appear to be associated with a particular geometry condition. Referring to the Bland-Alman results (Table 11, *Table 12*), an interaction between TMM sample geometry and strain range may exist. In the case of the Zhai [172] and 2.5%-7.5% moduli, MDs were almost identical when small and large geometry outcomes were compared; there was generally less than 6kPa separating the small and large sample MDs. In contrast, 15%-20% strain moduli MDs were up to 22kPa higher for small sample geometries compared to large sample geometries. The STDs of the MDs showed fairly good agreement between small and large geometry samples, with generally less than 6kPa difference in agreement.

General trends in the data suggested that sample geometry was not a major consideration at the lower strain ranges (Zhai [172] and 2.5%-7.5%). However, when indentation for larger strain applications is desired (i.e. 15%-20%), larger sample geometries (i.e. T_s>5mm) generally appeared to improve exact agreement. Interestingly, recommendations around sample geometry for indentation testing are often reported throughout the literature as a function of sample thickness (T_s), sample diameter (Φ_s), and indenter diameter (Φ_i). Reviewing several indentation studies, the following guidelines were recommended to yield outcomes that are invariant to sample geometry: $T_s:\Phi_i>1$, $\Phi_s:\Phi_i>2$, $\Phi_s:T_s>3$ [88], [110]–[114]. Moreover, Delaine-Smith et al. [88] (n = 7) observed that the OP model functioned superiorly for sample geometries with $T_s:\Phi_i>1$ and $\Phi_s:\Phi_i>4$, while the HZ model was superior for specimens with $T_s:\Phi_i<1$ and/or $\Phi_s:\Phi_i<4$. Our sample geometries ranged over $1.9<T_s:\Phi_i<5.0$, $6.3<\Phi_s:\Phi_i<13.7$, $1.9<\Phi_s:T_s<5.0$, which satisfy recommendations from both Delaine-Smith et al. [88] and the general literature [88], [110]–[114]. However, depending on the strain range, these findings suggested that even at these well accepted geometric conditions, sample geometry may still impact the validity of indentation testing. Further study of sample geometry impacts on indentation testing validity may be required.

4.4.3 Testing Speed

Analyzing the impact of testing speed on the agreement of indentation and ramp compression outcomes, scatterplots did not indicate any noticeable impact in variance in the data, trendlines, or biases. Interestingly, the correlation analysis suggested a possible interaction between testing speed, and strain range. Correlations between indentation and ramp compression outcomes at the highest testing rate (0.1Hz) were up to 0.09 lower than those at the lowest testing rate (0.01Hz), but only for the Zhai [172] strain range. For all other cases, deviations in correlation coefficients across speeds were generally <0.05. MDs calculated in the Bland Altman analysis again suggested a possible interaction between the speed and strain range. Moduli calculated from the lowest testing rate over the 15%-20% strain range exhibited MDs that were up to 15kPa higher than those calculated at the higher testing speeds. Again, STDs of the MD did not appear to change substantially with testing speed.

The agreement of indentation and ramp compression moduli also exhibited a possible interaction with the strain range. Generally, for indentation moduli calculated in the Zhai [172] strain range, a lower testing rate of 0.01Hz yielded the best agreement with ramp compression outcomes. In contrast, indentation moduli calculated over the 2.5%-7.5% and 15%-20% strain ranges yielded similar results at all testing speeds. These findings did not agree with those of Delaine-Smith et al. [88], who found that load-displacement profiles deviated only beyond 5% strain across 0.1%/s, 1%/s, and 10%/s testing speeds. As a reference, the testing frequencies used in the study corresponded approximately to strain rates of 0.03%/s, 0.19%/s, and 0.34%/s for small samples and 0.06%/s, 0.32%/s, and 0.58%/s for large samples, respectively. While speed standardization according to frequency, rather than strain rate, is an approach more conducive to dynamic testing, this does not appear to have confounded the results in this case, due to the relatively consistent findings for sample geometry and testing speeds. Further, the lower minimum testing speed used in this study may have illuminated that the definition of a quasi-static indentation testing speed should not be assumed. Appropriate quasi-static testing speeds for the

model and material of interest should be confirmed prior to commencing large scale data acquisition in fresh tissues.

4.4.4 Strain Range

Visual inspection of the scatterplots suggests increased biases and larger variability in the data for the 15%-20% strain range, compared to the two lower strain ranges. The trends of the data exhibited a higher slope for the Zhai [172] and 2.5%-7.5% strain ranges compared to the 15%-20% strain range. A possible interaction between speed and strain is indicated by different correlations across strain ranges with different testing speeds. At the 0.01Hz testing rate, indentation outcomes correlated fairly well (<0.05 difference in CCs) across the three strain ranges. However, CCs between the Zhai [172] ramp compression moduli decreased to <0.80 at the 0.1Hz testing rate, while 2.5%-7.5% and 15%-20% moduli remained more consistent. Thus, there was a larger range in CCs between indentation and ramp compression outcome across the three strain ranges at the 0.1Hz testing rate. However, all correlations remained excellent, suggesting that this may not be an important trend. Bland Altman analyses suggested a possible interaction between sample geometry, model, and strain range. Small samples for all models and large samples for the OP model showed that MD increased from the Zhai [172] moduli to the 2.5%-7.5% and then again to the 15%-20% moduli. The 15%-20% MDs were generally 20kPa to 45kPa higher than the Zhai [172] moduli. This trend was not consistently observed for the HZ model applied to data from the large samples. Finally, across all models and testing conditions, STD of the MD was notably higher for outcomes from the 15%-20% strain range, compared to both the Zhai [172] and the 2.5%-7.5% cases.

Findings from this study suggested that indentation moduli calculated at larger strains (i.e. 15%-20%) may exhibit lower with ramp compression moduli in terms of the MD and/or the STD of the MD, compared to outcomes from the lower strain ranges. While Delaine-Smith et al. [88] did not explicitly

discuss the quality of agreement between indentation and ramp compression outcomes across the different strain rates, the coefficients of their proposed corrections for the HZ and OP models at 2.5%-7.5% and 15%-20% strain do indeed suggest higher observed deviations between 15%-20% moduli compared to the lower strain moduli for both the HZ and OP model. Considering the potential sources of error and the potential for error propagation with increasing strain, this finding may be mechanically valid. For example, two common sources of error in mechanical testing studies are (i) the determination of surface contact, (ii) ensuring level and even surface contact. Should either of these sources of error be present in testing, there would be a shift in the stress-strain curve that may not be as prominent in the toe region, but with increasing strain would be far more pronounced. This error could impact both indentation and ramp compression approaches, decreasing the quality of agreement. Thus, with increased accuracy in determining surface contact and in ensuring even surface contact, lower agreement at high strains may be alleviated.

4.4.5 Evaluation of Delaine-Smith et al.'s [88] Indentation Model Corrections

Findings around the efficacy of Delaine-Smith et al.'s [88] corrections for the HZ and OP models were not ideal. Corrections only improved agreement between indentation and ramp compression outcomes for five of 36 cases. When corrections were effective, it was only in the case of HZ models applied to low strains (i.e. Zhai [172] or 2.5%-7.5%). Beyond this, sample geometry and testing rate did not appear to be determining factors around model success and in many cases, applying the correction actually decreased agreement between indentation and ramp compression outcomes. It was theorized that poor performance of the model corrections may be due in part to the large number of conditions investigated here that Delaine-Smith et al. [88] did not incorporate into their model development. Thus, Delaine-Smith et al.'s [88] corrections do not appear to be robust and changes to a variety of testing parameters may invalidate the correction. Additionally, the OP correction did not appear to improve

indentation and ramp compression agreement at all in this case. With this in mind, application of Delaine-Smith et al.'s [88] correction equations is not recommended without thorough validation over the range of material properties expected for the tissues of interest.

4.4.6 Error Bounds and Selecting the Appropriate Testing Conditions

Using a combination of scatterplot, correlation, and Bland-Altman analysis findings, representative best and worst cases were selected. The small sample with the OP calculation of the Zhai [172] modulus at the 0.01 Hz testing rate and the small sample with HZ calculation of the 15% to 20% modulus at the 0.1Hz testing rate were treated as the best case and worst case, respectively (Figure 32). Correlations between indentation and ramp compression outcomes for both the best (CC = 0.88) and worst case (CC = 0.86) were high, which was consistent with the entire data set. However, the MD (best = 15.35 kPa, worst = 48.95 kPa) and STD of the MD (best = 10.54 kPa, worst = 25.68) were quite different. Thus, there was an extremely large range on the possible error in indentation outcomes that appeared to depend on a variety of factors including the indentation model, strain range, sample geometry, and testing speed, with the strain range possibly exhibiting important interactions with all of these variables. With this in mind, parameter selection for indentation testing to characterize tissue properties is highly dependent on the relevant in vivo strains applied to the tissues of interest. Depending on the relevant strains, recommendations around the appropriate indentation model (OP = low strain, HZ = high strain), sample geometry (high strain = large, low strain = small or large), testing speed (Zhai [172] strain = low speed, 2.5%-7.5% or 15%-20% = any rate up to 0.1 Hz) will vary. Further, while there is an extensive data set provided between this study and that of Delaine-Smith et al. [88], it is highly recommended that selected testing parameters and models be validated on a case-by-case basis with a sample of TMMs.

4.4.7 Mechanical Testing Outcomes

Load displacement curves from indentation testing and ramp compression testing visualized the presence of minor hysteresis, confirming the viscoelastic nature of the oil-in-gelatin phantoms tested in this study. The span of the toe region, measured as strain in %, was used to assess non-linearity of the phantoms, along with the presents of friction. The toe region of phantoms was significantly largest for the indentation testing in small samples ($15.12\% < \varepsilon_{toe} < 17.12\%$, $p<0.001$). The second largest toe region was observed for the indentation testing in the large geometry samples ($11.66\% < \varepsilon_{toe} < 11.89\%$, $p<0.001$). The smallest toe region was observed for the ramp compression testing ($1.73\% < \varepsilon_{toe} < 1.84\%$). Finally, there were significant positive correlations between the span of the toe region and the volume % of oil in each phantom, which were consistently observed across all tests and testing rates. These findings suggest the notable presence of non-linearity, viscoelasticity, and the possibility of friction.

4.4.8 Limitations

The findings from this study need to be considered within the context of the limitations of this work. The indentation and ramp compression models included in this work assume a linear elastic material. While the oil-in-gelatin phantoms here were indeed homogeneous and isotropic, other factors such as the presence of viscoelasticity, friction, and non-parallel surfaces during mechanical testing may have impacted outcomes. Quasi-static testing rates and small deformations, lubricated testing surfaces (safflower oil), and prescribed cutting jigs were used, respectively, in an attempt to eliminate these factors. However, viscoelasticity of the phantom materials may have been responsible for trends across the testing rates. Friction between the loading jig and the material during testing could have increased estimates of the elastic modulus. However, in this cases friction was not included as a study outcome. Further, non-parallel testing surfaces would have elongated to the toe region of the stress-strain curves and decreased the measured elastic moduli.

In comparing mechanical testing and elastography outcomes, another limitation to this work is the use of quasi-static mechanical testing as a comparator for shear wave elastography loading, which is dynamic in nature. Some groups have implemented dynamic indentation mechanical testing for SWE applications, as it is thought to better represent the dynamic loading of SWE in vivo [90], [106], [291]. While quasi-static tissue testing does not simulate the high loading frequencies observed in SWE [115], it can still provide accurate, efficient, and accessible means of characterizing tissue stiffness [71], [72], [172] and is often selected for estimating tissue stiffness [71], [72], [113], [172]. In a comparison of a dynamic and quasi-static mechanical testing methodologies, Omari et al. [89] observed that quasi-static testing results exhibited comparable trends to those observed with dynamic testing, though generally yielding larger amplitude outcomes. Further, Oudry et al. [95] observed consistent results between dynamic and quasi-static mechanical testing when compared to SWE testing outcomes.

It should be noted that the Zhai [172] strain range over which the modulus was calculated was set from 0% to the error threshold for a linear model. Thus, the peak strain over which the modulus was calculated was determined on a case-by-case basis. In the case of the ramp compression tests, it was initially intended that the peak strain would be matched to the corresponding indentation tests, however the indentation peak strain always exceeded the error threshold for a linear model on the ramp compression tests. Further, preliminary analyses showed better agreement with strain ranges individualized to each loading curve. Thus, strain ranges for the Zhai [172] strain range did not agree exactly between the indentation and ramp compression modulus calculations.

Similarly, the use of a testing frequency, rather than a set strain rate, combined with slightly variable sample geometries yielded strain rates that were slightly variable at each testing frequency. This may have been a source of some of the relatively variance in the agreement between the indentation and ramp testing outcomes. However, the strain rates for each testing frequency were always on the same order of magnitude and did not deviate substantially within a given frequency

condition and sample geometry condition due to general consistency of the sample geometries. Regardless, future quasi-static validation of indentation testing parameters is recommended to parameterize testing speed as a strain rate rather than a frequency.

In Zhang et al.'s [111] development of the updated coefficients for the Hayes model [112], finite element modelling showed that friction between the indenter tip and test surface increases with the ratio of the indenter diameter (Φ_i) to the indentation depth (h). While this effect can be ignored at smaller $^{\Phi i}/_{h}$, friction should be considered for larger ratios ($^{\Phi i}/_{h} > 2$) as it can theoretically cause substantial error in estimates of the elastic modulus. In reality, error may be up to 33% for $^{\Phi i}/_{h} = 2$. With the knowledge that the indenter diameter for this study was 1.6mm, sample thickness for small samples was less than 5mm, and indention was performed up to 25% strain, friction between the indenter and material surface may have been a substantial source of error and may have decreased the agreement of indentation and ramp compression outcomes. This potential source of error may be adjusted by testing over a smaller strain range and adjusting the indenter diameter, while maintaining the necessary boundary conditions for the model being applied [88], [110]–[114].

Deviations between findings here and those of Delaine-Smith et al. [88] may have also been impacted by preloading of the samples. Delaine-Smith et al. [88] preloaded all samples to 0.5mN, whereas in this study samples were not preloaded, and were completely unloaded prior to testing and in between loading cycles. Further, samples in this study were preconditioned over 10 loading cycles and then moduli were calculated from an ensemble average of 10 loading cycles after preconditioning. In contrast, Delaine-Smith et al. [88] did not discuss preconditioning or the number of loading trials used to generate each estimate of the modulus. We suspect that preconditioning was likely a negligible source of error due to the small amplitude used by Delaine-Smith et al. [88]. However, the use of ensemble averaging across multiple loading cycles in this study may have yielded more robust estimates of the

elastic modulus. Regardless, these different approaches may have been another source of some of the disagreement between findings from this study and those of Delaine-Smith et al. [88].

4.5 Conclusion

Findings from this study indicated strong relationships between indentation and ramp compression outcomes for both HZ and OP models. However, the exact agreement of indentation models with ramp compression moduli was dependent on the strain range over which the modulus was calculated, where the OP model showed better agreement at low strain ranges and the HZ model showed better agreement at high strain ranges. Considering the range of testing parameters, sample geometry did not appear to be a mediator except, perhaps, at high strain ranges, in which case outcomes from testing on larger samples (>5mm) exhibited better agreement. Similarly, testing rate was only a potential mediator for outcomes calculated at specific strain ranges, where indentation outcomes calculated at the Zhai [172] strain range showed the best agreement with ramp compression outcomes for the lowest testing rate (0.01Hz). Beyond this, testing rate did not appear to impact the agreement of indentation and ramp compression outcomes. Finally, high strain ranges yielded the poorest agreement between indentation and ramp compression outcomes, while the low strain ranges performed relatively well. The Delaine-Smith et al. [88] corrections for the OP and HZ models did not improve agreement with ramp compression outcomes consistently over the parameters considered in this study. Guidelines around parameter selection for indentation test of soft tissue are dependent on the relevant in vivo strains applied to the tissues of interest and validation of testing parameters and models using a sample of TMMs is recommended prior to ex vivo indentation testing of soft tissues.

5 Study 3: Flat Tip Indentation Testing as a Validation Tool for Ultrasound Elastography in a Tissue Mimicking Homogeneous Phantom Model

5.1 Introduction

Ultrasound elastography (UE) is a medical imaging modality capable of estimating tissue stiffness. Similar to manual palpation used by physicians, a pressure or load is applied to the tissue and different responses (soft vs. stiff) can indicate areas of potential pathology. Shear wave elastography (SWE), a UE method employed by many commercial elastography systems (e.g. SuperSonic Imagine, Aix-en-Provence, France [115]), uses acoustic radiation force from ultrasound or external vibrators to generate shear waves in soft tissue [115]. The mechanical relationship between shear wave speed and the elastic modulus of soft tissue allows for SWE estimation of tissue "stiffness" (i.e. the elastic modulus; kPa), under a series of assumptions. Since its development, SWE has been suggested as a method for screening and monitoring a variety of pathologies [29], [32], [277]–[282], [269]–[276]. SWE has been shown to improve sensitivity and specificity of medical imaging diagnosis for some breast and liver pathologies [270], [272], [273], [276], [277], [279], [280]. More recently, SWE displaced liver biopsy as the standard of care for staging liver fibrosis in cases of chronic hepatitis B and C [60], [270], [272], [277], [283]–[287]. Research shows that tissue stiffness correlates significantly with tissue histology for many pathologies [38], [56], [270]–[273], [277], [288]–[290]. Yet, the adoption of SWE is dependent on the accessibility of validation techniques for each relevant clinical application.

In order to assess the validity and clinical utility of SWE for characterizing soft tissue properties, mechanical testing is generally regarded as the gold standard in material characterization [54], [71], [72], [89], [106], [113], [172], [186]. Mechanical testing of solid materials involves controlled deformation of a material, while measuring force and displacement [127]. The force-displacement curve

can then be used in combination with various assumptions and mathematical models to estimate the elastic modulus (E). While materials science differentiates E from the concept of tissue stiffness, for the sake of clinical terminology and accessibility, the terms will be used interchangeably here.

Mechanical testing for SWE validation may involve loading the tissues in compression or tension. While tensile testing is most appropriate for tissues loaded under tension in vivo (i.e. muscles, tendons, blood vessels) [94], [170], [225], [231]–[233], it requires gripping or clamping of the sample. Thus, tensile testing outcomes may be vulnerable to error due to sample slipping at the grips or may result in damage of the soft tissue by the grips [88]. Compression mechanical testing is often used as the gold standard for SWE applications in tissues that are not subject to primarily tensile loads in vivo [54], [89], [90], [106], [113], [224]–[227]. Specifically, unconfined ramp compression testing of soft tissues is generally regarded as the ideal method for validating SWE. Previous work by our team investigating the validity of linear, curvilinear, and endoprobe SWE using unconfined ramp mechanical testing in homogeneous tissue mimicking phantoms showed acceptable agreement of linear probe and curvilinear probe SWE up to 5cm target depths, and endoprobe SWE below 3cm target depths (Section 3). Yet mechanical testing of fresh healthy and pathological tissues, which is required for validating SWE as a clinical tool, is not ideally suited to unconfined ramp compression mechanical testing.

Limitations around the surgical sampling procedures for fresh tissue (e.g. minimally invasive approaches), geometrical irregularities (e.g. non-uniform tissue resection), sample geometries (e.g. surgical restrictions), and intact state (e.g. pathology restrictions) can easily prohibit the use of unconfined ramp compression mechanical testing for SWE validation [88]. Further, SWE is meant to provide local estimates of tissue stiffness [71], [106], while unconfined ramp compression testing estimates bulk or global stiffness properties of tissue. Flat tip indentation testing addresses many of the limitations of unconfined ramp compression testing for SWE applications. Indentation testing is more robust in cases of non-uniform geometries and small samples; it allows for local characterization of

heterogeneous tissues and stiffness mapping, and it has already seen some use in the literature as a tool for SWE validation [71], [106], [172]. Previous work has demonstrated the agreement between indentation and unconfined ramp testing under a variety of testing parameters using multiple material models (Section 4). Yet to date, there has been no investigation of optimal indentation testing parameters for validation of SWE.

Some groups have implemented dynamic indentation mechanical testing for SWE applications, as it is thought to better represent the dynamic loading of SWE in vivo [90], [106], [291]. In these cases, the complex elastic modulus can be derived from cyclic (sinusoidal), small amplitude, high frequency deformations of the tissue [127], [229]. While quasi-static tissue testing does not simulate the high loading frequencies observed in SWE [115], it can still provide accurate, efficient, and economical means of characterizing tissue stiffness [71], [72], [172] and is often selected for estimating tissue stiffness [71], [72], [113], [172]. In a comparison of a dynamic and quasi-static mechanical testing methodologies, Omari et al. [89] observed that quasi-static testing results exhibited comparable trends to those observed with dynamic testing, though generally yielding larger amplitude outcomes. Further, Oudry et al. [95] observed consistent results between dynamic and quasi-static mechanical testing when compared to SWE testing outcomes.

While quasi-static indentation mechanical testing provides a rapid, economical, non-destructive tool for validating SWE, testing parameters studied in the literature are highly variable. The definition of "quasi-static" testing rates has not been well characterized. When considering a series of "quasi-static" indentation mechanical testing studies, testing rates ranged from approximately 0.01 Hz to 0.1 Hz [71], [72], [113], [172]. Yet, Kiss et al. [54] treated 0.1 Hz as a dynamic testing method. In a series of gel and tissue samples (thickness (T_s)≈3.5mm), Delaine-Smith et al. [88] observed that the accuracy of indentation mechanical testing was impacted by geometric relationships between T_s, indenter diameter (Φ_i), and sample diameter (Φ_s), where T_s:Φ_i>=1:1 and Φ_s:Φ_i>=4:1 yielded the most accurate estimates of

tissue stiffness. However, sample thicknesses in the SWE literature quite variable [109]–[114] and other thresholds around sample and indenter geometry have also been recommended (T_s:Φ_i>1, Φ_s:Φ_i>2, Φ_s:T_s>3) [88], [110]–[114]. Further, the small (n=7) sample validation by Delaine-Smith et al. [88] may be statistically inadequate. Further, Delaine-Smith et al. [88] investigated primarily larger deformations (2.5% ≤ strain ≤ 7.5%, 15% ≤ strain ≤ 20%), while the mechanical validation of SWE may be better suited to the toe region of the stress-strain curve (0% ≤ strain ≤ threshold) to ensure loading regimes similar to those of SWE [72], [172]. Finally, many indentation testing models exist [109]–[114] and the implication of this for SWE validation has yet to be investigated.

The use of quasi-static indentation mechanical testing as a tool to validate the accuracy and clinical utility of SWE for a wide array of pathologies requires a clear characterization of indentation testing parameters and their potential impact on agreement with SWE measures. The purpose of this study was to provide a systematic investigation of the impact of indentation testing parameters and material models on the agreement between indentation testing and SWE. More specifically, we aimed to investigate the impact of (1) two indentation models, (2) two sample geometries, (3) three quasi-static testing speeds, (4) and three strain ranges on the agreement of indentation stiffness with SWE measures of stiffness in a series of homogeneous oil-in-gelatin tissue mimicking (TMM) phantoms. Findings from this study will provide guidance around indentation testing parameters as a validation tool for SWE measures of stiffness.

5.2 Methods

5.2.1 Indentation Models

Two indentation models were assessed in this work: the Snedden [110] model, which was popularized by Oliver and Pharr [109] (OP), and the Hayes model [112] with Zhang et al.'s [111] geometric correction factors (HZ). The OP [109] model assumes quasi-static testing conditions to

calculate the elastic modulus of a homogeneous semi-infinite linear elastic medium under a rigid flat end indenter tip with a small strain assumption (Figure 16). The analytic solution by Boussinesq [114] is used to derive the elastic modulus of the material. The "effective" elastic modulus (E) [88], which assumes the modulus of the indenter is substantially higher than that of the TMM sample, was used here. The effective modulus was expressed as a function of the indentation stiffness (S, the slope of the force-displacement curve over the range of strains of interest) and the diameter of the indenter tip (Φ_i), with no conversion factor [72], [172] (Equation 10).

$$E = \frac{S}{\Phi \mathrm{i}} \tag{18}$$

The Hayes model [112] assumes a lateral infinite isotropic elastic material with a finite thickness resting on a rigid half space [72] under a rigid flat tip indenter (Figure 16). This model assumes adhesion at the sample-support plate interface, negligible shear tractions at the indenter-sample interface, infinitesimal deformation (<0.1% strain), and a frictionless indenter surface [111], [112]. However, to account for larger deformations and non-linearity, Zhang et al.'s changes were implemented [112]. The HZ effective elastic modulus (E) for indentation testing performed using a flat-end cylindrical indenter (Equation 12) was expressed as a function of Poisson's ratio (v), the indentation stiffness (S), the indenter diameter (Φ_i), the thickness of the tissue sample (T_S), and a geometric constant (κ) developed by Zhang et al. [111]. Zhang et al.'s [111] constant has been found to improve calculation of the shear and elastic modulus calculations for large strains (up to 20%) [88] and linear interpolation of the constants presented by Zhang et al. [111] can be used for estimation of the elastic modulus at these larger strains [88].

$$E = \frac{S}{\Phi \mathrm{i} * \kappa(v, \Phi \mathrm{i}/T_S)} \tag{19}$$

5.2.2 Preparation of Oil-in-Gelatin Phantoms

Oil-in-gelatin phantoms were manufactured according to the methods described by Madsen et al. 2006 [253]. In brief, the phantoms were composed of a solvent (water), a matrix (gelatin), and a series of additives (propylene glycol, safflower oil, liquid surfactant, formalin), which function to tune the acoustic, mechanical, and physical properties of the phantoms. First the molten gelatin solution was mixed; water, propylene glycol (5.09% by volume, P4347, Sigma-Aldrich Canada Co., Oakville, Canada), and 200 Bloom gelatin (13.06% by volume Nitta Gelatin, Morrisville, USA) were combined in a beaker. A thermometer was placed in the beaker, the beaker was covered with plastic wrap, and then the beaker placed in a double boiler, and heated to 90^{o}C to produce clarified molten gelatin [253]. The molten gelatin was then cooled in an ice bath to 55^{o}C. At this point, the molten gelatin solution was then combined with safflower oil (Loblaws, Brampton, Canada) and stirred to produce oil droplets (<1mm diameter) [253]. The method of stirring to yield oil droplets in the gelatin matrix involve taking a standard dinner spoon and bending the spoon at 90^{o} to the handle. The spoon was then placed in the mixture in the beaker and stirred about a horizontal axis. This method encourages the dispersion of the oil droplets, while minimizing air introduction into the mixture. Following this, liquid surfactant (1.1% by volume, Liquid Ivory Ultra, Proctor and Gamble, Toronto, Canada) was added to the mixture to preserve the emulsion and stirred vigorously until the mixture because opaque. Formalin (0.735% by volume, F8775, Sigma-Aldrich Canada Co., Oakville, Canada) was then added to the oil-in-gelatin solution and the mixture was stirred to complete the manufacture of the TMM solution [253].

The oil-in-gelatin TMM solution was cast into a cylindrical mould with a height and diameter each of 7.5cm and placed under positive gauge pressure [253]. The mold included a syringe embedded in the outer was that. When the mixture was in the mold and the syringe was engaged, the material was placed under a positive gauge pressure. After 24 hours, cross-linking of the gelatin had increased the melting temperature well above room temperature. Molds were then removed to yield a cylindrical

homogeneous TMM phantom (Figure 22A). Phantoms were placed in safflower oil to prevent desiccation until testing [253]. A total of n=27 phantoms were manufactured, to yield adequate statistical power for the purposes of this study. The ratio of safflower oil in the phantoms was varied between 2.5% and 67.5% in 2.5% increments to yield a uniform spread across a physiologically relevant range of healthy and pathological tissue stiffnesses (20kPa < storage modulus < 100kPa) [82], [84], [253]. Additionally, six extra phantoms were manufactured according to the same procedures using a stiffer 220 Bloom gelatin (13.06% by volume, Sigma-Aldrich, St. Louis, USA) to extend the upper end of the range of stiffnesses over which SWE could be validated. In the end, with two manufacturing failures, the total sample of phantoms was n = 31.

It should be noted here that Madsen et al. [82], [253] observed slight variations in elastic contrasts and strain ratios measured in heterogeneous phantoms made using this TMM. Their team also observed decrease in the amplitude of the storage modulus measured over a period of 16 months [253]. Regardless, our study purely aimed to validate measures of SWE stiffness against MTE measures. SWE and MTE measures for a given phantom were obtained on the same day, thus eliminating any concerns regarding long-term temporal stability of mechanical properties.

5.2.3 Ultrasound Elastography Imaging

Previous work validating SWE against unconfined ramp compression testing in TMM phantoms demonstrated acceptable agreement of linear probe and curvilinear probe SWE up to 5cm target depths, and endoprobe SWE below 3cm target depths (Section 3). Similar levels agreement between mechanical testing and SWE were observed for all probes and target depths listed above. Further, there has been ample literature supporting the validity of the Aixplorer (SuperSonic Imagine, Aix-en-Provence, France) linear probe for SWE acquisition, particularly at superficial depths [73]–[75], [77], [170]. This combination of evidence resulted in the selection of the linear SWE probe (SL15-4, Aixplorer, SuperSonic

Imagine, Aix-en-provence, France) as a representative case for evaluating concurrent validity across the indentation testing parameters and models of interest in this study [108] (Table 2). This probe uses proprietary excitation sequences that are partially detailed in the literature [115].

Table 15 Aixplorer (SuperSonic Imagine, Aix-en-Provence, France) shear wave elastography (SWE) ultrasound imaging superficial linear probe used for testing and its specifications [108].

Model	Type	Imaging Frequency Range (MHz)	Nominal Centre Frequency (MHz)	SWE Penetration Range (mm)	SWE Spatial Resolution (mm)
SL15-4	Linear Probe	4.0 to 15.0	8.5	2.5 to 30	2.0

The SWE imaging procedure was executed with the phantom suspended in a safflower oil bath, in order to minimize confounding factors [175]. SWE measurements were taken in a mid-longitudinal plane of the phantom. The probe was inserted into the saline bath and centered to visualize a B-mode image of the target region. The SWE region of interest (ROI) was set to its minimum size and placed along the central axis of the probe. The maximum stiffness of the imaging system was set to 180kPa and the penetration mode, which appeared to act as a spatial filter, was enabled for consistency of visualization. The probe was fixed in place and three UE cineloops of at least 10 frames each were acquired at the desired depth. Again, considering previous findings (Section 3) along with literature supporting the use of this probe, particularly at superficial depths [73]–[75], [77], [170], a 1cm target depth was selected as a representative case for evaluating concurrent validity across the indentation testing parameters and models of interest in this study. Two identical imaging sessions were acquired on the same testing day to support a separate reliability analysis (Section 3).

5.2.4 Quasi-Static Indentation Testing

Mechanical properties of phantoms were measured using the BioTester materials testing system (CellScale, Waterloo, Canada), with a 23N (5.5 mN resolution, 3.5 mN noise floor) load cell and a

positional accuracy of 1um. The load cells and displacement controls on the system were calibrated on an annual basis (CellScale, Waterloo, Canada) and monitored for deviations that may impact testing. Three-dimensional printed adapters made from polyactide (PLA) with 90% infill were secured to the material testing system for indentation testing. Indentation testing was conducted using a rigid, cylindrical, flat-ended steel indenter with a diameter of 1.6mm. Testing was performed by straining the samples to 25% for 20 cycles at a rate of 0.01 Hz, 0.055 Hz, and 0.1 Hz. To ensure a that the boundary conditions met the assumptions of the indentation models, sample thickness (T_s) and sample diameter (Φ_s) were adjusted according to the recommendations in the literature (T_s:Φ_i>1, Φ_s:Φ_i>2, Φ_s:T_s>3) [88], [110]–[114]. Previous findings (Section 4) had suggested that regardless of adherence to sample geometry recommendations in the literature, sample geometry may still be a relevant factor in validity of indentation models. Thus, while maintaining these recommended geometric relationships, sample thickness was changed to investigate whether a larger or smaller sample geometry could alter agreement of indentation testing outcomes with SWE.

First, a large and small geometry sample was cut from the TMM phantom, to represent two cases of tissue sampling. Anecdotally, our team has had better success collaborating with pathology teams when asking for less than 5mm thick samples of tissue. Thus, the larger geometry sample was treated as over 5 mm thick with a square cross section of at least 17mm and the small geometry sample was less than 5 mm thick with a square cross section of at least 12mm. Samples were fixed to a steel support stage and inserted into the mechanical testing system one at a time. The sample cross section dimensions were taken as an average of three trials measured using a Vernier caliper. The sample thickness was calculated as an average of three trials, each measured as the distance between the support stage and the top of the sample when loaded to 15 mN, and was taken using the BioTester materials testing system (CellScale, Waterloo, Canada). The indenter was then withdrawn from the sample surface to a distance of 500 um. Testing then commenced and the sample was compressed by

the indenter at a testing speed of 0.01Hz for 20 cycles. The sample was rested for 5 minutes after testing and bathed in safflower oil to eliminate any effects of material desiccation. Testing was then repeated for all speeds (i.e. 0.01 Hz, 0.055 Hz, 0.10 Hz) and for all testing conditions (i.e. large geometry sample and small geometry sample) for a total of 6 tests per phantom.

5.2.5 Data Processing

SWE stiffness measures (kPa) were calculated as a median of 10 frames and the average of 3 trials for a circular ROI of 5 mm diameter, centered at the target depth of interest in the frame. Due to previously reported excellent reliability (intraclass correlation (95% confidence interval) = 0.996 (0.991, 0.998), Section 3), SWE data were averaged across the two imaging sessions for all phantoms. For each mechanical testing signal, the final 10 cycles of loading were ensemble averaged and a low pass Butterworth filter (3 Hz cut-off, 2^{nd} order, dual pass) was applied to minimize noise in the data signals. Any bias in the signal was identified as an average of the unloaded period prior to contact of the indenter tip and the signal was zeroed. Contact was detected automatically using a 15 mN force threshold and then verified by visual inspection. In cases where residual noise confounded the algorithm, manual identification of the surface contact was used.

The effective modulus calculations were performed using three strain ranges from the force-displacement curves: (i) in the toe region of the curve from surface contact up to a linear threshold, (ii) from 2.5% to 7.5% strain, and (iii) from 15% to 20% strain. The stiffness (i.e. slope of the force-displacement curve) was extracted from the force-displacement curve over the appropriate region and then was used to calculate the effective indentation modulus. For case (i), the stiffness was calculated using methods previously published by Zhai et al. [172] (Figure 23). In brief, beginning from the surface contact point (i.e. 0% strain), a data window with a length of 5% of the tip diameter was identified. A linear regression was chosen to fit a linear model to the window, in order to limit the impact of residual

noise on a tangent calculation. The error was calculated as the mean absolute difference between the linear model and the force-displacement data in the data window. The data window was then extended by one sample at a time and the procedure was repeated for each new data window. The procedure was halted when the error exceeded the 15 mN threshold and the stiffness was taken as the slope of the linear model in this data window. Moving forward this strain range is referred to as the Zhai [172] strain region.

For cases (ii) and (iii), the stiffness was taken simply as the slope of tangent model fit over the 2.5% to 7.5% and 15% to 20% strain regions of the force-displacement curve, respectively. The Hayes' model with Zhang et al.'s correction [111] and the Oliver and Pharr [109] model were then used to calculate the effective modulus with and without Delaine-Smith et al.'s [88] correction equation. As in Amador et al. [72], Poisson's ratio was set to 0.475 to align closely with the incompressibility assumption, while sitting in a range that keeps $\kappa(v,a/h)$ fairly constant for the testing parameters.

5.2.6 Statistical Analysis

The large number of indentation parameters included in the methodology yielded a high dimensionality problem that precluded multivariate analysis of the data set without the incorporation of dimensionality reduction. With this in mind, the relationship between SWE and indentation outcomes was evaluated on a case-by-case basis using a series of approaches often implemented in sensitivity analyses. Initially relationships between indentation outcomes and SWE were qualitatively evaluated using scatter plots. Pearson's or Spearman's correlations were then implemented to quantitatively characterize the relationship, as appropriate. Bland Altman analyses were used to quantify exact agreement between indentation and SWE outcomes. Trends across the validation outcomes for the various indentation testing parameters (geometry, speed, strain) and models (HZ, OP) were observed to

guide indentation parameter selection for SWE applications moving forward. The level of significance was set to $\alpha = 0.05$ for all statistical tests.

5.3 Results

Scatterplots visualizing the agreement between indentation testing and SWE outcomes are presented here. Indentation parameters including 0.01Hz (Figure 33), 0.055Hz (Figure 34), and 0.1Hz (Figure 35) testing speeds are shown. Each individual plot includes data from both small (blue) and large (red) geometry samples for a given model (OP or HZ) at a given strain (Zhai [172], 2.5%-7.5%, or 15%-20%) tested at the given speed (0.01Hz, 0.055Hz, 0.1Hz). SWE outcomes are from a linear probe with SWE measurements taken at a 1cm target depth. Qualitative analysis of the scatterplots suggested strong relationships between indentation and SWE outcomes for all testing parameters and models.

Data visualization suggested a bias (significant mean difference) for all HZ indentation outcomes, while several OP models did not exhibit a noticeable bias. The HZ model appeared to yield low variability in agreement between indentation and SWE across all testing parameters, while the OP model outcomes appeared to demonstrate higher variability in the agreement between of SWE and indentation outcomes, specifically at the Zhai [172] and 2.5%-7.5% strains. Small and large geometry sample data showed very similar trends in slopes and biases. Similarly, increased testing rate did not appear to impact the agreement between SWE and indentation outcomes. For Zhai [172] and 2.5%-7.5% strains, there was good agreement between SWE and indentation testing across all testing conditions and models. Indentation moduli calculated from 15%-20% strain show higher deviation in agreement with SWE, with trendlines consistently falling below a perfect (1.0) correlation line.

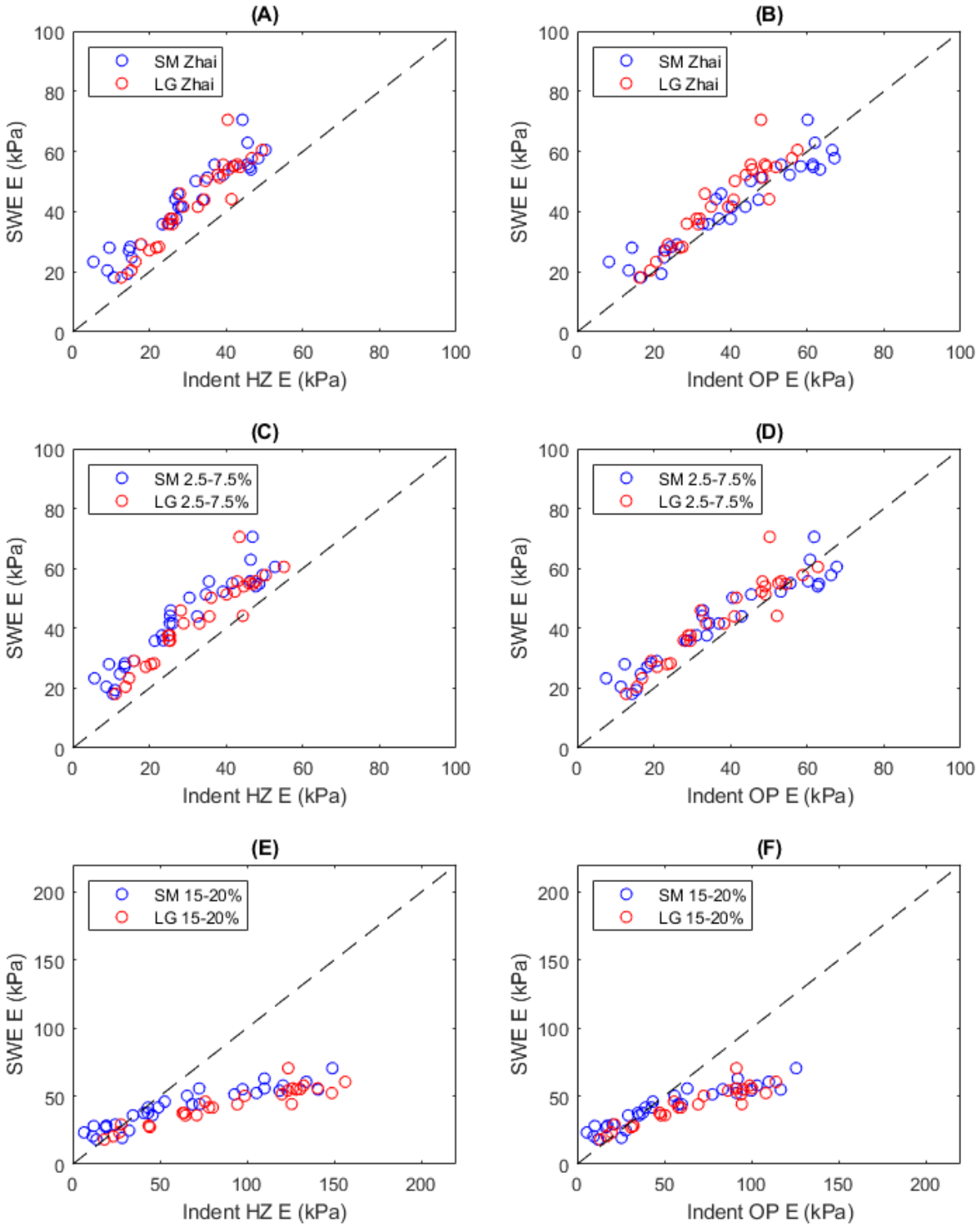

Figure 33 Agreement of elastic modulus (E) in kilopascals (kPa) from shear wave elastography (SWE) imaging and flat cylindrical tip indentation testing (Indent) in homogeneous oil-in-gelatin tissue mimicking phantoms. E was calculated using linear elastic models on the force-displacement or stress-strain curve in the toe region (A, B) using Zhai et al.'s [172] *methods, from 2.5% to 7.5% strain (C, D), and from 15% to 20% strain (E, F). Data are separated by small (SM) geometry (thickness < 5mm) or a large (LG) geometry (thickness > 5mm) and Hayes-Zhang (HZ E)* [111], [112] *(A, C, E) or Oliver Pharr (OP E) indentation model* [109] *(B, D, F). Testing rate was 0.01 Hz for all cases. Equality of outcomes is shown on each plot by a black dashed line.*

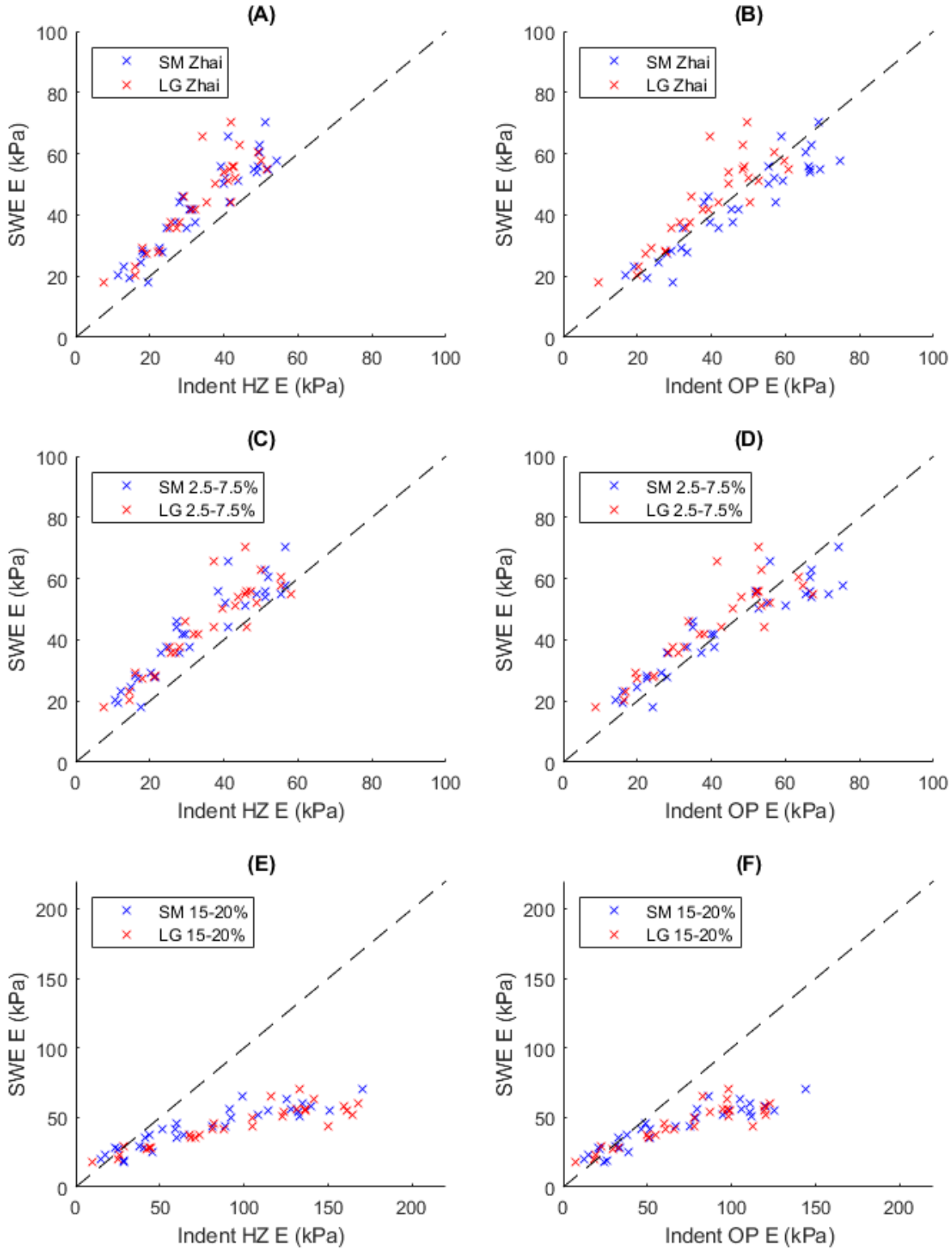

Figure 34 Agreement of elastic modulus (E) in kilopascals (kPa) from shear wave elastography (SWE) imaging and flat cylindrical tip indentation testing (Indent) in homogeneous oil-in-gelatin tissue mimicking phantoms. E was calculated using linear elastic models on the force-displacement or stress-strain curve in the toe region (A, B) using Zhai et al.'s [172] *methods, from 2.5% to 7.5% strain (C, D), and from 15% to 20% strain (E, F). Data were separated by small (SM) geometry (thickness < 5mm) or a large (LG) geometry (thickness > 5mm) and Hayes-Zhang (HZ E)* [111], [112] *(A, C, E) or Oliver Pharr (OP E) indentation model* [109] *(B, D, F). Testing rate was 0.055 Hz for all cases. Equality of outcomes is shown on each plot by a black dashed line.*

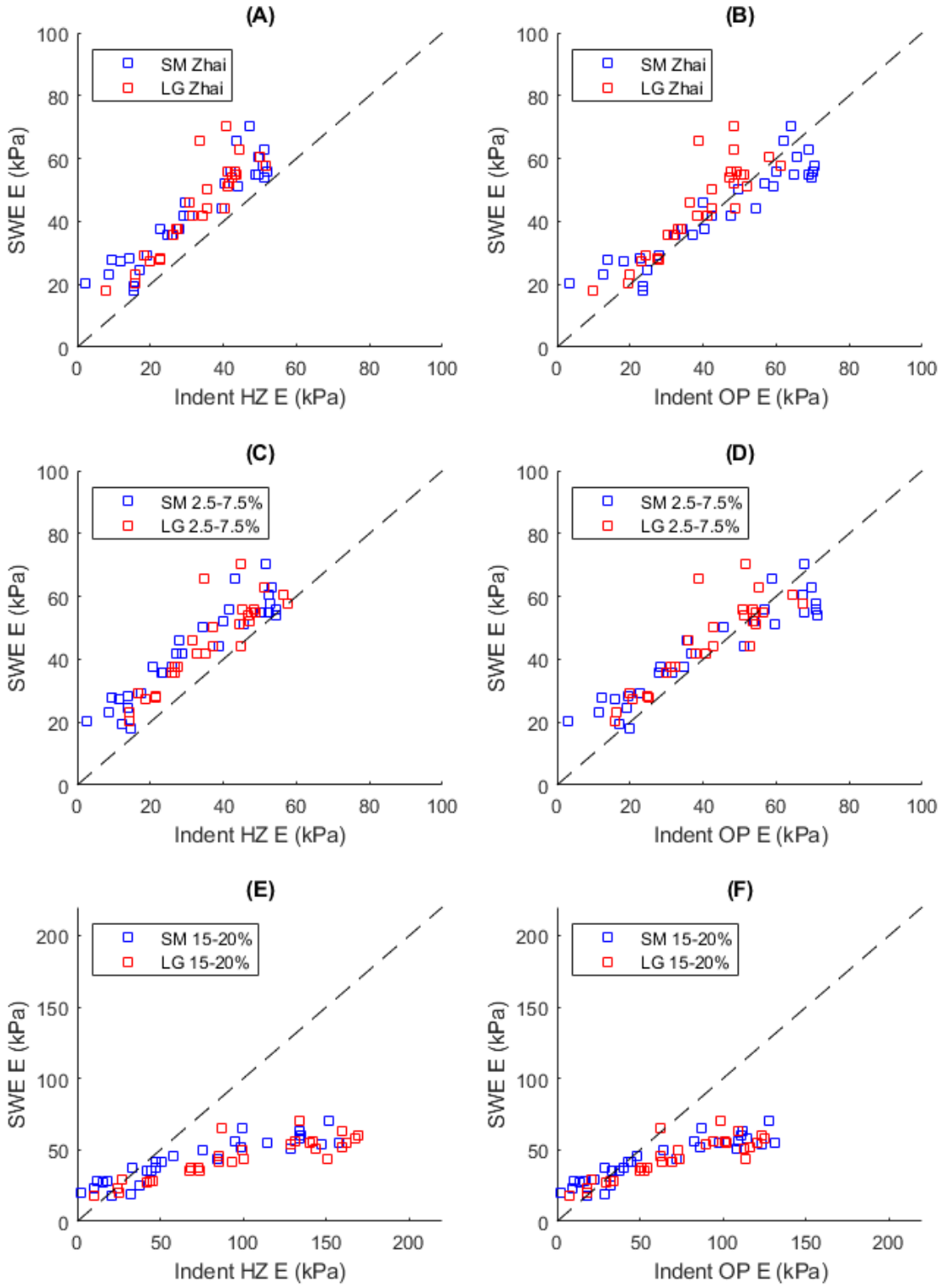

Figure 35 Agreement of elastic modulus (E) in kilopascals (kPa) from shear wave elastography (SWE) imaging and flat cylindrical tip indentation testing (Indent) in homogeneous oil-in-gelatin tissue mimicking phantoms. E was calculated using linear elastic models on the force-displacement or stress-strain curve in the toe region (A, B) using Zhai et al.'s [172] *methods, from 2.5% to 7.5% strain (C, D), and from 15% to 20% strain (E, F). Data were separated by small (SM) geometry (thickness < 5mm) or a large (LG) geometry (thickness > 5mm) and Hayes-Zhang (HZ E)* [111], [112] *(A, C, E) or Oliver Pharr (OP E) indentation model* [109] *(B, D, F). Testing rate was 0.1 Hz for all cases. Equality of outcomes is shown on each plot by a black dashed line.*

Table 16 Correlation coefficients for the elastic moduli (E) in kilopascals (kPa) from shear wave elastography (SWE) imaging and flat cylindrical tip indentation testing (Indent) in homogeneous oil-in-gelatin tissue mimicking phantoms. Testing was conducted on material samples with small (SM) geometry (thickness < 5mm) and a large (LG) geometry (thickness > 5mm) at three quasi-static testing rates (0.01 Hz, 0.055 Hz, 0.1 Hz). E was calculated using linear elastic models on the force-displacement or stress-strain curve. in the toe region using Zhai et al.'s [172] *methods (Zhai), from 2.5% to 7.5% strain, or from 15% to 20% strain. For indentation moduli, the Hayes-Zhang (HZ)* [111], [112] *or Oliver Pharr (OP) indentation model* [109] *were used. The number of observations (n) included in each test is given. Correlations were calculated using either a Pearson's or Spearman's correlation test as appropriate. All correlations were significant to the level of p<0.0001.*

Testing Rate	Strain	SM			LG		
		n	HZ	OP	n	HZ	OP
0.01 Hz	Zhai [172]	30	0.95	0.95	27	0.94	0.93
	2.5% - 7.5%	30	0.95	0.95	27	0.94	0.93
	15% - 20%	30	0.94	0.95	27	0.93	0.93
0.055 Hz	Zhai [172]	31	0.93	0.93	29	0.90	0.88
	2.5% - 7.5%	31	0.92	0.92	29	0.90	0.89
	15% - 20%	31	0.92	0.92	29	0.90	0.89
0.1 Hz	Zhai [172]	30	0.92	0.93	29	0.90	0.88
	2.5% - 7.5%	30	0.92	0.92	28	0.88	0.87
	15% - 20%	30	0.92	0.91	29	0.87	0.86

Correlation coefficients (CCs) between indentation and SWE outcomes were consistently very high (CC > 0.85, $p<0.001$) (Table 16). HZ and OP correlations with SWE were almost identical. Indentation testing conducted on larger geometry samples yielded slightly lower correlations for the OP indentation modulus at high testing speeds (0.055Hz and 0.1Hz CCs $\leq$0.90) compared to small geometry outcomes. However, the differences in the CCs between indentation and SWE across geometry conditions was never more than 0.05. Comparing across testing speeds, the lowest testing rate of 0.01Hz yielded the highest correlations between indentation and SWE outcomes (correlation > 0.92), however this trend in decreasing correlations with increasing testing rate was most observable in the OP data. Correlations between indentation and SWE outcomes were consistent across strain ranges and never differed by more than 0.02. The highest correlations with SWE were observed for indentation testing at 0.01Hz in small samples with the moduli calculated over the Zhai [172] and 2.5%-7.5% strains using the HZ model.

Findings from Bland-Altman analyses of indentation and SWE agreement for small (Table 17)

and large (Table 18) samples aligned with observations from qualitative analysis of scatterplot data and quantitative correlation analyses. The OP model consistently yielded mean differences (MDs) that were 5 kPa to 25 kPa lower than the HZ model. The OP model was also the only model to generate non-significant MDs. However, the standard deviations (STDs) of the MD tended to be equivalent or higher for the OP moduli compared to the HZ moduli at Zhai [172] and 2.5%-7.5% strains, yet high strains (15%-20%) yielded larger STDs of the MD for the HZ model. MDs for larger sample geometry outcomes calculated at large strains (15%-20%) were noticeably larger than the same outcomes for small geometry samples. However, at Zhai [172] and 2.5%-7.5% strains and the OP modulus, MDs between indentation and SWE outcomes were generally larger in large geometry samples compared to small geometry samples. This trend was not observed for HZ moduli calculated at Zhai [172] and 2.5%-7.5% strains. Larger geometry outcome STDs of the MD for the HZ model were slightly higher than in small geometry samples, while the trend was the opposite for the OP model. Regardless, the MDs of the STD never deviated between sample geometries by more than 3 kPa. Increased testing speed did not appear to substantially impact Bland-Altman outcomes. Across all testing parameters and models, 15%-20% indentation moduli exhibited large, significant negative mean differences (MDs) ranging from -18.96 kPa to -53.59 kPa and high standard deviation (STD) of the MDs ranging from 19.37 kPa to 37.94 kPa. These outcomes were substantially larger than the MDs (non-sigificant $< MD_{Zhai}[172] < 13.18$ kPa , non-sigificant $< MD_{2.5\%-7.5\%} < 13.85$ kPa) and the STDs of the MDs (4.46 kPa $< MD_{Zhai}[172] < 8.37$ kPa , $4.51 < MD_{2.5\%-7.5\%} < 9.42$ kPa) for both the Zhai [172] and 2.5%-7.5% strains.

Table 17 Bland Altman test results for exact agreement of the elastic moduli (E) in kilopascals (kPa) from shear wave elastography (SWE) imaging and flat cylindrical tip indentation testing (Indent) in homogeneous oil-in-gelatin tissue mimicking phantoms for samples with small (SM) geometry (thickness < 5mm). Testing was conducted at three quasi-static testing rates (0.01 Hz, 0.055 Hz, 0.1 Hz). E was calculated using linear elastic models on the force-displacement or stress-strain curve. in the toe region using Zhai et al.'s [172] *methods (Zhai), from 2.5% to 7.5% strain, or from 15% to 20% strain. For indentation moduli, the Hayes-Zhang (HZ)* [111], [112] *or Oliver Pharr indentation model* [109] *were used. The number of observations (n), mean difference (MD), standard deviation of the mean difference (STD), standard error of the mean difference (SE), and the 95% confidence interval (CI) of the mean difference are included. MDs that were significant to the level of p<0.05 are indicated by *.*

Rate (Hz)	Strain Range (%)	HZ					OP				
		n	MD (kPa)	STD (kPa)	SE	95% CI	n	MD (kPa)	STD (kPa)	SE	95% CI
0.01	Zhai [172]	30	13.18*	4.46	0.15	(4.43,21.92)	30	1.40	6.13	0.20	(-10.62,13.43)
	2.5 – 7.5	30	13.85*	4.51	0.15	(5.02,22.68)	30	4.70*	6.79	0.23	(-8.61,18.01)
	15 – 20	30	-22.35*	30.33	1.01	(-81.80,37.09)	30	-12.41*	23.32	0.78	(-58.11,33.31)
0.055	Zhai [172]	31	9.36*	5.43	0.18	(-1.29,20.01)	31	-4.00*	6.44	0.21	(-16.62,8.62)
	2.5 – 7.5	31	9.72*	5.59	0.18	(-1.24,20.67)	31	-1.10	7.89	0.25	(-16.56,14.36)
	15 – 20	31	-35.48*	32.32	1.04	(-98.82,27.86)	31	-23.54*	25.00	0.81	(-72.54,25.47)
0.1	Zhai [172]	30	11.19*	5.51	0.18	(0.40,21.99)	30	-1.49	8.37	0.28	(-17.89,14.91)
	2.5 – 7.5	30	11.31*	5.90	0.20	(-0.25,22.86)	30	1.00	9.42	0.31	(-17.47,19.47)
	15 – 20	30	-30.06*	36.84	1.23	(-102.27,42.16)	30	-18.96*	28.78	0.96	(-75.36,37.45)

Table 18 Bland Altman test results for exact agreement of the elastic moduli (E) in kilopascals (kPa) from shear wave elastography (SWE) imaging and flat cylindrical tip indentation testing (Indent) in homogeneous oil-in-gelatin tissue mimicking phantoms for samples with large (LG) geometry (thickness > 5mm). Testing was conducted at three quasi-static testing rates (0.01 Hz, 0.055 Hz, 0.1 Hz). E was calculated using linear elastic models on the force-displacement or stress-strain curve. in the toe region using Zhai et al.'s [172] *methods (Zhai), from 2.5% to 7.5% strain, or from 15% to 20% strain. For indentation moduli, the Hayes-Zhang (HZ)* [111], [112] *or Oliver Pharr indentation model* [109] *were used. The number of observations (n), mean difference (MD), standard deviation of the mean difference (STD), standard error of the mean difference (SE), and the 95% confidence interval (CI) on the mean difference are included. MDs that were significant to the level of p<0.05 are indicated by *.*

Rate (Hz)	Strain Range (%)	HZ					OP				
		n	MD (kPa)	STD (kPa)	SE (kPa)	95% CI	n	MD (kPa)	STD (kPa)	SE	95% CI
0.01	Zhai [172]	27	11.38*	5.25	0.19	(1.09,21.67)	27	5.26*	5.05	0.19	(1.09,21.67)
	2.5 – 7.5	27	10.14*	4.78	0.18	(0.78,19.50)	27	5.26*	5.21	0.19	(-4.95,15.48)
	15 – 20	27	-45.06*	30.54	1.13	(-104.92,14.80)	27	-21.79*	19.37	0.72	(-59.74,16.17)
0.055	Zhai [172]	29	11.33*	6.38	0.22	(-1.17,23.83)	29	5.17*	6.86	0.24	(-8.27,18.61)
	2.5 – 7.5	29	9.39*	6.35	0.22	(-3.06,21.84)	29	4.30*	7.45	0.26	(-10.31,18.90)
	15 – 20	29	-52.37*	35.74	1.23	(-122.41,17.67)	29	-26.57*	23.44	0.81	(-72.52,19.38)
0.1	Zhai [172]	29	11.41*	6.36	0.22	(-1.05,23.87)	29	5.30*	6.62	0.23	(-7.67,18.28)
	2.5 – 7.5	28	9.36*	6.39	0.23	(-3.16,21.89)	28	4.17*	7.25	0.26	(-10.04,18.39)
	15 – 20	29	-53.59*	37.94	1.31	(-127.95,20.77)	29	-27.41*	25.24	0.87	(-76.89,22.06)

5.4 Discussion

Validation of SWE estimates of tissue stiffness is an essential step to support to the clinical adoption of SWE for diagnostic and treatment planning purposes. Quasi-static flat tip indentation testing is ideal for SWE validation [71], [72], [172], yet testing parameters vary widely across the literature [71], [72], [88], [90], [91], [93], [106], [111]. Results from this and previous (Section 3, Section 4) studies support the use of indentation testing as a criterion standard for validating SWE estimates of tissue stiffness. Moreover, results from this work provide substantial insight into the impact of indentation testing parameters on agreement with SWE estimates of material stiffness, including indentation model, sample geometry, quasi-static testing rate, and strain range.

5.4.1 Indentation Model

Indentation and SWE outcome agreement may be impacted by the selected indentation model, where several important cases may optimize agreement. Analysis of the scatterplots (Figure 33, Figure 34, Figure 35) suggested some key differences in bias and variance in the agreement of outcomes and, in particular, a possible interaction between the indentation model and strain range. The HZ model appeared to yield less variable estimates of stiffness compared to the OP model at low strains (Zhai [172] and 2.5%-7.5% strains), while this trend was not apparent at high strains (15%-20%). Similarly, scatterplots suggested a significant bias for the HZ model across all testing parameters, while the OP model exhibited less bias in small geometry samples at low strains (Zhai [172] and 2.5%-7.5% strains). Correlation analyses (Table 16) did not show any substantial differences in model performance across all testing parameters. Bland-Altman results (Table 17, Table 18) showed lower MDs for OP model agreement with SWE. While the HZ model yielded the lowest STDs of the MD overall, OP and HZ STDs of the MD were generally similar for low strains (Zhai [172] and 2.5%-7.5% strains). At high strains (15%-20%), OP STDs of the MD were well below those of the HZ model.

In summary, the HZ and MD models yielded the best agreement between indentation and SWE outcomes for low strain estimates of the moduli (Zhai [172] and 2.5%-7.5% strains). While the OP model exhibited lower MDs between indentation and SWE, the HZ model better reduces STDs of the MD slightly at low strains (Zhai [172] and 2.5%-7.5% strains). At high strains (15%-20%), the OP model yielded substantially lower MDs and STDs of the MD compared to the HZ model. With this in mind, model selection is dependent on the strain range being used for modulus calculation and whether the particular application requires a lower MD or a lower STD of the MD. With the high correlations and lower STDs of the MD between HZ and SWE at low testing speeds (0.01Hz), a bias correction of the HZ model may in fact provide the best agreement between indentation and SWE outcomes.

5.4.2 Sample Geometry

Considering the sample geometry when dimensions were maintained above thresholds indicated in the literature (T_s:Φ_i>1, Φ_s:Φ_i>2, Φ_s:T_s>3) [88], [110]–[114], several observations were made. Scatterplots (Figure 33, Figure 34, Figure 35) did not reveal any substantial differences in agreement between indentation and SWE for small and large sample geometries. The correlation analyses (Table 16) suggested a possible interaction between sample geometry and testing speed, with small geometry samples tested at the lowest rate (0.01Hz, $0.94 \leq$ correlation ≤ 0.95) yielding higher correlations than large geometry samples tested at the highest rate (0.1Hz, $0.85 \leq$ correlation ≤ 0.90). The Bland-Altman (Table 17, Table 18) analysis also suggested a possible interaction between sample geometry and strain, with moduli measured at high strains (15%-20%) yielding higher MDs for large samples compared to small samples. A possible interaction between sample geometry and model was also observed in the case of low strains (Zhai [172] and 2.5%-7.5%), where large geometry samples exhibited higher MDs when the OP model was used to calculate the indentation modulus. Sample geometry did not appear to substantially impact STDs of the MDs across any conditions.

Overall, these findings suggest that at low testing rates (0.01 Hz) and low strains (Zhai [172] and 2.5%-7.5%), sample geometry was only somewhat a mediating factor for the OP model, with larger sample geometries yielded larger MDs. However, at high strains (15%-20%), indentation testing in large samples yielded poorer agreement with SWE compared to small samples. Thus, sample geometry is only a factor of concern if higher indentation testing rates, the OP model, and/or high strain ranges (15%-20%) are used for modulus calculation. In these cases, smaller sample geometries (<5mm) may optimize agreement between SWE and indentation outcomes. This finding may suggest a possible relationship between the boundary conditions and strain amplitudes. In fact Zhang et al. [111] noted that friction between the indenter tip and test surface increased with the ratio of the indenter diameter (Φ_i) to the indentation depth (h), where error may be up to 33% for $\Phi i/_h = 2$ and increases substantially beyond this threshold. Thus, the choice of the indenter tip diameter in this study may have reduced accuracy and thus agreement between large geometry sample outcomes and SWE.

5.4.3 Testing Speed

Considering outcomes grouped by testing speed, scatterplots (Figure 33, Figure 34, Figure 35) did not suggest any qualitative relationship between speed of indentation testing and agreement with SWE. Correlations (Table 16) showed a possible interaction between speed, sample geometry, and model, where there was a slight decrease in the correlation between SWE and OP indentation modulus for speeds above 0.01Hz in large sample geometries, compared to outcomes at 0.01Hz. Interestingly, the Bland-Altman analyses suggested a possible interaction between testing speed and strain range, with a slight increase in MDs and STDs of the MD at speeds above 0.01Hz for moduli calculated at high strains (15%-20%), again compared to outcomes at 0.01Hz. Summarizing these findings, it appeared that the best agreement between indentation and SWE outcomes was observed for indentation testing conducted at low speed (0.01 Hz) with moduli calculated at low strains (Zhai [172] and 2.5%-7.5%). This

outcome was not surprising in this sample of viscoelastic TMM phantoms, as the lowest speed likely best approximated the quasi-static assumption of the indentation models being applied. In the case that higher quasi-static testing rates were required, if the MD is not a major source of concern, the HZ model with or without a bias correction may provide better agreement between indentation and SWE outcomes.

5.4.4 Strain Range

Comparing the agreement between indentation and SWE estimates of tissue stiffness over three different strain ranges, the results definitively demonstrated that indentation moduli calculated at high strains (15%-20%) yielded poorer agreement between SWE and indentation outcomes than those calculated at low strains (Zhai [172] and 2.5%-7.5%). While this trend was evident in the scatterplots (Figure 33, Figure 34, Figure 35), the correlation analyses were not impacted (Table 16) However, the Bland-Altman analyses (Table 17, Table 18) revealed higher MDs and STDs of the MD at high strains (15%-20%) compared to low strains (Zhai [172] and 2.5%-7.5%) across all conditions. In fact, this aligns well with the mechanics of SWE loading in vivo. The type of SWE excitation used in this study (SuperSonic Imagine, Aix-en-Provence, France) [115], employs moving dipolar sources, generated by acoustic radiation force (ARF), to remotely excite shear waves in the tissue. Constructive interference between these shear waves yields quasi-plane shear waves of objectively small amplitudes (~100 um in phantoms, ~40 um in vivo [115]). With this knowledge, it is understood that SWE loading regimes likely operate in the toe region of the stress-strain curve, which would explain the better agreement between SWE and indentation moduli calculated at low strains (Zhai [172] and 2.5%-7.5%).

5.4.5 General Recommendations

The most important recommendation from this study is the use of low strain ranges (Zhai [172] and 2.5%-7.5%) for calculating indentation moduli as a criterion standard for SWE estimates of tissue

stiffness. With this in mind, selection of the indentation model (i.e. OP or HZ) is dependent on the nature of the agreement required. At low strains (Zhai [172] and 2.5%-7.5%), the HZ model may minimize STD of the MD while the OP model has a lower MD. Thus, if variability in the agreement is not a major concern, the OP model may be the optimal choice. However, considering the slightly lower STDs of the MD in the HZ model and the very high correlations, a bias correction of the HZ model may perform comparably. In terms of sample geometry, the choice of small or large geometry samples will likely be dependent on clinical factors around fresh tissue sampling. However, at low strains (Zhai [172] and 2.5%-7.5%), if the HZ model is used, sample geometry does not appear to be a mediating factor, while in the case of the OP model, small sample geometries (<5mm) may optimize the agreement between SWE and indentation. Finally, in terms of testing rate, the best agreement between indentation and SWE stiffness measures was observed at the lowest testing rate (0.01Hz), however in the case of higher testing rates the HZ model may be the optimal choice.

5.4.6 Limitations

As with any work, findings from this study need to be considered within the context of the limitations of this work. The indentation models included in this work assume a linear elastic material. While the oil-in-gelatin phantoms here were indeed homogeneous and isotropic, other factors such as viscoelasticity, friction, and non-parallel surfaces during mechanical testing may have impacted outcomes. Quasi-static testing rates and small deformations, lubricated testing surfaces (safflower oil), and prescribed cutting jigs were used, respectively, in an attempt to eliminate these factors. However, viscoelasticity of the phantom materials may have been responsible for trends across the testing rates. Friction between the loading jig and the material during testing could have increased estimates of the elastic modulus. Further, non-parallel testing surfaces would have elongated to the toe region of the stress-strain curves and decreased the measured elastic moduli.

In comparing mechanical testing and elastography outcomes, another limitation to this work is the use of quasi-static mechanical testing as a comparator for shear wave elastography loading, which is dynamic in nature. Some groups have implemented dynamic indentation mechanical testing for SWE applications, as it is thought to better represent the dynamic loading of SWE in vivo [90], [106], [291]. While quasi-static tissue testing does not simulate the high loading frequencies observed in SWE [115], it can still provide accurate, efficient, and accessible means of characterizing tissue stiffness [71], [72], [172] and is often selected for estimating tissue stiffness [71], [72], [113], [172]. In a comparison of a dynamic and quasi-static mechanical testing methodologies, Omari et al. [89] observed that quasi-static testing results exhibited comparable trends to those observed with dynamic testing, though generally yielding larger amplitude outcomes. If the implications of Omari et al.'s [89] findings are considered here, quasi-static mechanical testing outcomes may be overestimating material stiffness. When comparing mechanical testing outcomes to SWE estimates of material stiffness, there were significant biases and overestimation of the elastic modulus for many of the low strain outcomes, however at high strains mechanical testing underestimated SWE stiffness consistently. Moreover, Oudry et al. [95] observed consistent results between dynamic and quasi-static mechanical testing when compared to SWE testing outcomes. Further research is required to understand the impact of quasi-static mechanical testing parameters on over- or under-estimation of the SWE modulus.

It should be noted that the Zhai [172] strain range over which the modulus was calculated was set from 0% to the error threshold for a linear model. Thus, the peak strain over which the modulus was calculated was determined on a case-by-case basis. Thus, strain ranges for the Zhai [172] strain range were somewhat variable and may have reduced agreement between SWE and indentation outcomes. Setting a fixed limit for this strain range (e.g. 0% to 10%) may function to improve agreement, depending on the linearity of the stress-strain curves in this region.

Similarly, the use of a testing frequency, rather than a set strain rate, combined with slightly variable sample geometries yielded strain rates that were slightly variable under each testing frequency. Testing frequencies were used to govern loading rates in this study, despite the quasi-static nature of the mechanical testing, as they could be directly compared to SWE loading rates quoted in the literature. Regardless, this may have been a source of the variance in agreement between the indentation and SWE outcomes. Strain rates for each testing frequency were always of the same order of magnitude and did not deviate substantially across each frequency condition and sample size, due to general consistency of the sample geometries. Regardless, future quasi-static validation of indentation testing parameters is recommended to parameterize testing speed as a strain rate rather than a frequency.

For Zhang et al.'s [111] updated coefficients for the Hayes model [112], finite element modelling showed that friction between the indenter tip and test surface increases with the ratio of the indenter diameter (Φ_i) to the indentation depth (h). While this effect can be ignored at smaller $^{\Phi i}/_{h}$, friction should be considered for larger ratios ($^{\Phi i}/_{h} > 2$) as it can theoretically cause substantial error in the estimates of the elastic modulus. In fact, error may be up to 33% for $^{\Phi i}/_{h} = 2$. With the knowledge that the indenter diameter for this study was 1.6mm, sample thickness for small samples was less than 5mm, and indention was performed up to 25% strain, friction between the indenter and material surface may have been a substantial source of error and decreased the agreement of indentation and SWE outcomes.

5.5 Conclusion

Findings from this study indicated very strong relationships between indentation and SWE estimates of tissue stiffness regardless of testing conditions. However, there were several parameters that optimized agreement between indentation and SWE outcomes. In particular, indentation moduli should be calculated at low strains (Zhai [172] and 2.5%-7.5%), which are thought to mimic SWE loading regimes [115]. The choice of indentation model is dependent on the particular metrics of interest; however, the OP indentation model may objectively yield better agreement with SWE outcomes, compared to the HZ model. Small sample geometries (<5mm) and slow testing rates (0.01 Hz) will optimize agreement between indentation and SWE measures of material stiffness. Conditions for deviations from any of these recommended parameters were elaborated on here, with further recommendations as necessary. Finally, specific recommendations around parameter selection for the indentation testing of soft tissue are dependent on the relevant in vivo strains applied to the tissues of interest. Validation of testing parameters and models using a small sample of TMMs is recommended prior to proceeding with ex vivo indentation testing of soft tissues.

6 Study 4: The Reliability and Potential Confounders on In Vivo Shear Wave Elastography Measurements of Uterine Tissue Stiffness

6.1 Introduction

Uterine fibroids (UFs), endometriosis, and adenomyosis are gynecological disorders that can all cause significant symptoms (i.e. excessive bleeding, gynecological pain, and infertility) [1]–[7], with prevalences estimated between 10% and 30% in premenopausal women, depending on the disorder [1], [2], [14], [5], [7]–[13]. UFs are benign tumors of the myometrium [8], endometriosis is the extra-uterine growth of endometriotic cysts and/or lesions [6], and adenomyosis is the growth of endometrial glands deep in the myometrium causing myometrial hypertrophy and/or hyperplasia [15]. All of these disorders are associated with clinical struggles around diagnosis and/or treatment planning [4], [6], [23]–[25], [7], [16]–[22]. Further, these three disorders can co-occur, further confounding clinical decision making [6], [7], [26].

In cases of UFs, diagnosis on ultrasound imaging (USI) can often be performed with high diagnostic accuracy [9], [21], [292], [293]. Yet medical management, used in many cases to avoid the inherent risks of surgery [16]–[18], is complicated by negative side effects [4], [16], [17], [19]–[22], variable non-response rates [17], [19]–[23], and recurrence after therapy cessation [17], [20], [21], [24]. These factors may be associated with various tumor properties that cannot be visualized on USI [294]–[298]. Similarly, while ovarian and deep endometriosis diagnosis is possible on USI [6], [7], [25], improved diagnostic accuracy, thorough lesion mapping, and differentiation of lesion characteristics, is a necessity to support surgical management [6]. Adenomyosis diagnosis on USI is also possible for trained clinicians [6], [299], [300]. However, focal adenomyosis and UFs can be visually similar on USI [6]. Yet, UFs push and deform the myometrium, while adenomyosis penetrates between myometrial cells [6].

Clinically UF and adenomyosis treatment are markedly distinct [6], thus requiring clear pre-operative differentiation.

Ultrasound elastography, a medical imaging modality able to visualize tissue stiffness, has improved diagnosis and staging of many diverse pathologies [58], [61], [67], [69], [101]–[103], [283], [301], and may provide invaluable insight into diagnosis and treatment planning for gynecological pathologies [50]–[52], [54], [167], [174], [209], [247], [302]. Shear wave elastography (SWE) (e.g. SuperSonic Imagine, Aix-en-Provence, France [115]) uses acoustic radiation force (ARF) or external vibrators to remotely excite shear waves in the tissue. The speed of these waves, which can be estimated through USI processing techniques, can be used to estimate tissue stiffness in soft tissues providing unique insight into various pathologies. SWE is able to visualize tissue stiffness ranging from exceptionally soft (e.g. fatty tissues) to exceptionally hard (e.g. ablated lesions). The clinical utility of tissue stiffness, measured by SWE, lies in the observed relationships between the microstructure (i.e. histology) of healthy and pathological human tissue and the macroscopic stiffness of those same tissues [27]–[36].

Using SWE in a small sample of women (n=30) with deep endometriosis, measures of endometriosis lesion stiffness (n = 34 lesions, median [range] = 123.0 kPa [40.9, 295.1] kPa) showed a positive correlation with lesion fibrosis, as identified by Masson trichrome staining ($r = 0.89$, $p < 0.001$) [257]. Lesion stiffness also correlated negatively with vascular density ($r = -0.91$, $p<0.001$) [257]. However, endometriosis lesion thickness was not recorded and studies have found that guided mode propagation can bias findings in tissue with thickness $\leq$15mm, which may limit the applicability of these findings [190]. Another study comparing SWE stiffness of uteruses with adenomyosis lesions (n=39, median [range] = 72.7 kPa [22.3, 274.2] kPa), those with non-adenomyosis lesions (n=14, median [range] = 28.3 kPa [12.7, 59.5] kPa), and healthy uteruses (n=56, median [range] = 24.4 kPa [17.9, 32.4] kPa) found adenomyotic lesions were significantly the stiffest tissue ($p<0.05$) [209], with no significant

difference between the latter two groups [209]. Neither study included thorough characterization of participant demographics or anthropometrics.

Considering studies of women with no known pathology, Soliman et al. [222] found that endometrium tissue (n=32, mean ± STD = 12.6 ± 1.8 kPa) was significantly softer than the myometrium (n=32, mean ± STD = 23.9 ± 1.8 kPa, $p<0.001$). A second study by Zhang et al. [121] observed that cervix tissue (n=14, mean ± STD = 84.3 ± 12.0 kPa) was stiffer than myometrium tissue (n = 14, mean ± STD = 69.1 ± 10.8 kPa). However, myometrium stiffness was significantly different between the two studies ($p<0.0001$). One explanation for this could be that the first study employed supersonic shear imaging (SSI) and the second study used acoustic radiation force imaging (ARFI). ARFI and SSI are two unique SWE modalities. Research into the variability of stiffness outcomes acquired using linear probes across different SWE systems has suggested that measurements may vary by as much as 18% in a highly controlled phantom experiment, depending on target depth. Yet, the variability in endoprobe SWE across systems is unknown and variability across systems during in vivo SWE is likely higher.

The reliability of SWE has yet to be systematically evaluated in healthy or pathological uterine tissues, however Peralta et al. [167] found the reliability of SWE to measure cervix stiffness, using Cronbach's alpha (Cα) as an outcome, to range from 0.897 to 0.941 within-rater and 0.861 to 0.936 between-raters.

While SWE shows exciting potential for gynecological applications, a wide array of technical limitations plagues the current literature. As previously noted, studies may use different SWE imaging systems. In the literature, variability across elastography systems has been related to target depth [78], [80] and, although cervix stiffness during pregnancy does not appear to relate to target depth [120], the myometrium is a deeper tissue and there is currently no reporting around gynecological target depth in the elastography literature. Moreover, depending on the position and flexion of the uterus (Figure 36),

depth and residual stresses in the anterior and posterior uterine segments may vary drastically, making uterus position/flexion and target depth in the uterus all potentially relevant factors that could impact SWE measures of tissues stiffness. Finally, measurements in thin tissues are another source of potential error, where elastography validity appears to decrease due to the phenomenon of guided mode propagation [190]. While methods have been developed to address this confounding factor [175], [191], the SWE measured stiffness appears to decrease in tissues with thickness <15mm [175], which may preclude the use of UE in thin gynecological tissues, such as the endometrium.

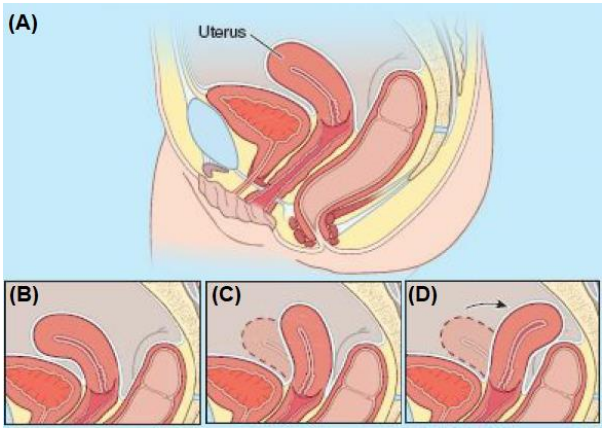

Figure 36 Mid-sagittal plane diagram showing the position of a uterus showing (A) normal anteversion and anteflexion, (B) excessive anteflexion, (C) retroversion, and (D) retroversion with retroflexion. Reproduced from [181] *© 2006, with permission from Wolters Kluwer Health, Inc. Measurements in thin tissues, such as the endometrium, are another source of potential error, where elastography validity appears to decrease due to the phenomenon of guided mode propagation [190].*

There is also a distinct lack of thorough reporting around elastography studies of uterine disorders in the literature. Often, pre- and post-menopausal study participants may be grouped together, despite well documented changes occurring in gynecological tissue during menopause [94], [303], [304]. Age [303], [305], obesity [306], [307], and pregnancy [308], [309] all impact the uterus mechanically and hormonally, yet these relevant factors are often omitted from study reporting. Finally, hormonal changes throughout the menstrual cycle result in physiological changes to endometrium, the endometrium-myometrium junctional zone, and the myometrium [181], [314]–[316]. Yet it is not yet clear whether these changes alter SWE measures of uterine tissue stiffness [121].

In the same way that elastography has improved the diagnosis and staging in pathologies of the breast, liver, and other tissues [58], [61], [67], [69], [101]–[103], [283], [301], we expect that gynecological SWE [50]–[52], [54], [167], [174], [209], [247], [302], may provide necessary insight for treatment planning in cases of UFs, adenomyosis, and endometriosis, particularly in relation to the use of medical therapies. However, before we can evaluate gynecologic SWE as a diagnostic tool for treatment planning, we must systematically assess the reliability of SWE in gynecological tissues, provide a clear characterization of "healthy" uterine tissue stiffness, and investigate of the impact natural hormone variations across the menstrual cycle on uterine tissue stiffness measured by UE. The purpose of this study was to: (i) establish the within-day and between-day reliability of SSI measures of uterine tissue stiffness in women with no known uterine disorders; (ii) investigate the effect of phase in the menstrual cycle on SSI measures of tissue in women with no known uterine disorders; (iii) investigate the impact of target site in the uterus and depth of target site on tissue stiffness; (iv) provide a qualitative evaluation of any potential confounders on measures of uterine tissue stiffness in women with no known uterine disorders. This work is an essential step in establishing gynecological UE as a feasible tool for clinical use and, to the author's knowledge, no study has explicitly investigated any of these important features using gynecological SWE.

6.2 Methods

6.2.1 Participants

Data were acquired as a part of a larger ongoing observational study, which was approved by the institutional research ethics boards (20170872-01H, H-08-18-790). Participants with no known history of uterine pathologies were recruited from the local community using posters and word of mouth. Inclusion criteria were: aged 18 or older, intact uterus, no previous gynecological surgery, not currently pregnant, >6 months post-partum (if recently pregnant), premenopausal, regular period or a period suppressed through the use of hormonal birth control. Participants were subclassified as either

currently using a hormonal birth control (HBC) or not currently using any hormonal birth control methods (CON).

6.2.2 Standardization of SWE Imaging Visits

Upon recruitment, participants with regular menstrual cycles were asked to provide details on their cycle (i.e. average duration of cycle, average duration of bleeding, most recent day one of cycle). Participants in the CON group were scheduled for three imaging visits. The first visit (V1) was scheduled in the proliferative phase of the menstrual cycle, approximately day 7 of the menstrual cycle, when estrogen and progesterone are expected to be lower. The second visit (V2) was scheduled in the secretory phase of the menstrual cycle, approximately 7 days after a positive over-the-counter ovulation test, when progesterone levels were expected to be high, and estrogen was expected to be between low and medium levels. The third visit (V3) was scheduled within 48 hours of V2, in the secretory phase of the menstrual cycle. For participants in the CON group, V1 included two repeated SWE imaging sessions, while V2 and V3 each included only a single SWE imaging session. Participants in the HBC group were scheduled for only two visits, due to the variability in types and mechanisms of action of hormonal birth control being used. For participants in the HBC group, V1 included two repeated SWE imaging sessions, and V2, scheduled within 48 hours of V1, included only a single SWE imaging session. For participants in the HBC group, the scheduling of V1 and V2 was not standardized, however menstrual cycle data were recorded.

6.2.3 Data Acquisition

Upon their first visit to the institution, participants provided written informed consent. Demographic and anthropometric information was acquired, including age, race/ethnicity, weight, height, gravidity, parity, and details of contraceptive use. Participants then completed the Menstrual

Bleeding Questionnaire (MBQ) [317], a standardized validated questionnaire to evaluate the impact of their menstrual bleeding on quality of life. A MBQ score of 0 is the lowest possible score, indicating a less pronounced impact of menstrual bleeding on quality of life, while 75 is the maximum score. Participants were then instructed to void their bladder prior to USI and SWE imaging.

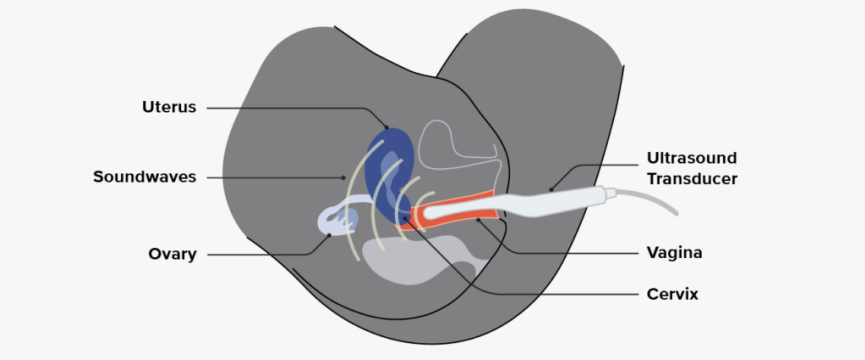

Figure 37 Graphical representation of the endoprobe position in the vagina with respect to an anteverted uterus. The probe imaging surface is placed further anteriorly to visualize the fundus.

USI and SWE were conducted using the SuperSonic Ultrafast™ Aixplorer® (SuperSonic Imagine, Aix-en-Provence, France). Imaging was conducted with participants lying in the lithotomy position, with hips flexed, abducted, and legs resting in stirrups. A transvaginal endoprobe (Table 2) was inserted into the vagina to visualize the uterus (Figure 37). Imaging was performed only endovaginally using the endoprobe, as this is the only probe with wide spread clinical utility for imaging in uterine pathologies that can also visualize a healthy unaffected uterus. Indeed the other two probes would not be appropriate for this application as the linear and curvilinear probes do not have an adequate view angle to see the whole uterus nor the penetration depth for the uterus sites to be clearly visualized. Three measurements of uterine volume (cm^3) and endometrial thickness (mm) were recorded using B-mode ultrasound. Uterus position (neutral, retroverted, anteverted), uterus flexion (neutral, retroflexed, anteflexed), and bladder fullness (empty, minimal residual, moderate residual) post-voiding were also recorded.

Table 19 Aixplorer (SuperSonic Imagine, Aix-en-provence, France) shear wave elastography (SWE) ultrasound imaging probe used for testing and its specifications [108].

Model	Type	Imaging Frequency Range (MHz)	Nominal Centre Frequency (MHz)	SWE Penetration Range (mm)	SWE Spatial Resolution (mm)
SE12-3	Endoprobe	3.0 to 12.0	7.5	2.5 to 30	2.0

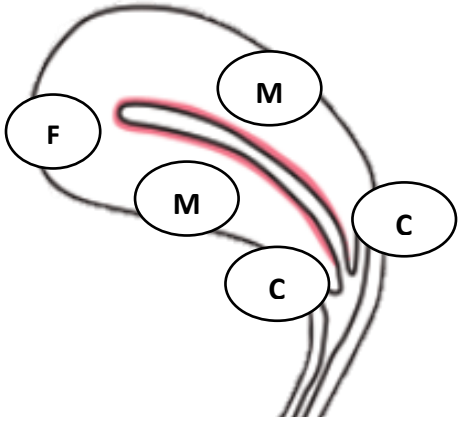

Figure 38 Target sites for shear wave elastography (SWE) measurements of tissue stiffness in an anteverted uterus. Target sites included the anterior cervix (CA), posterior cervix (CP), anterior myometrium (MA), posterior myometrium (MP), and the fundus (FU).

In the mid-sagittal plane of the uterus, SWE measures of uterine tissue stiffness were acquired at the anterior cervix (CA), posterior cervix (CP), anterior myometrium (MA), posterior myometrium (MP), and in the fundus (FU) (Figure 38). At each target site, three cineloops of at least 10 frames of SWE data were acquired. For each SWE trial for a given target site, a single measure of depth (mm) and tissue stiffness (kPa) was taken from a 5mm circular region of interest (RO) as a median of 10 frames. No tissue stiffness measurements were acquired in the endometrium, due to the well-documented limitations around SWE measurements in thin tissues [189]–[191] and variable endometrium thickness over the course of the menstrual cycle. Additionally, no measures were acquired at the MP site for participants with intra-uterine devices (IUDs) due to the potential of shadowing and reflection to confound measures of tissue stiffness.

At V1, after the first imaging session, the endoprobe was removed from the vagina, the SWE system was rebooted, and a subsequent SWE imaging session was completed following the same protocol to allow for estimation of within-day reliability. After V1, participants in the CON group were given a box of over-the-counter ovulation tests. V2 and V3 for CON were booked after a positive ovulation test, while participants in the HBC group returned within 48 hours for V2. For both HBC and

CON participants, follow-up visits included only a single repetition of the USI and SWE imaging protocol (single session) that was conducted in V1.

6.2.4 Statistical Analysis and Outcomes

For each target site and imaging session, depth and stiffness measures were averaged across three trials. ROI placement was checked to ensure consistency between imaging sessions and visits. Intra-class correlation coefficients (ICCs; two-way mixed effects, absolute agreement, multiple measurements [256]) were used to assess within-day and between-day (within the secretory phase) reliability of UE stiffness measures [164], [318]. According to the definitions given by Cicchetti et al. [105], ICC$\leq$0.40 was poor, 0.40<ICC$\leq$0.60 was fair, 0.60<ICC$\leq$0.75 was good, 0.75<ICC was excellent. Due to issues around consistent acquisition of complete data sets, pair-wise comparisons (Student's T-test or Wilcoxon Rank Sum test, as appropriate) were used to test for significant differences of SWE measures of tissue stiffness between the proliferative and secretory phase of the menstrual cycle and Cohen's d was used, where appropriate, to indicate effect size. One-way analysis of variance (ANOVAs) with a Tukey post-hoc test was used to identify significant differences in target stiffness and target depths. Correlation analyses (Pearson's or Spearman's, as appropriate) were used to identify any relationship between tissue stiffness and target depth at each target site. Finally, case examples of potential confounding factors were identified to direct future research.

SWE data from V1 for both the CON and HBC participants was used to evaluate within-day reliability of SWE measures of uterine tissue stiffness at different target sites in the uterus. SWE data from SWE data from V1 and V2 (<48 hours apart) in the HBC group and from V2 and V3 (<48 hours apart) in the control group were used to evaluate between-day reliability of SWE measures of uterine tissue stiffness at different target sites in the uterus. SWE data from participants in the CON group collected in the proliferative phase of the menstrual cycle (V1) and data from participants in the CON

group collected in the secretory phase of the menstrual cycle (averaged across V2 and V3) was used to evaluate whether there was a significant difference between SWE measures of uterine tissue stiffness at different target sites in the uterus that were taken at different phases in the menstrual cycle. Depth and stiffness of the target sites across all visits and SWE imaging sessions for all participants in the HBC and CON groups were used to characterize uterine tissue stiffness and evaluate whether there was a significant relationship between depth or target site significantly impacted SWE measures of tissue stiffness. The level of significance was set to $\alpha = 0.05$ for all statistical tests.

6.3 Results

6.3.1 Study Sample Characterization

A total of 32 participants were included in the study, with 21 belonging to the CON group and 11 belonging to the HBC group. Demographics and anthropometric data are presented each for the CON group, the HBC group, and the combined study group (ALL) in Table 20

Table 20. Uterus volume, endometrial thickness, uterus position (neutral, retroverted, anteverted), uterus flexion (neutral, retroflexed, anteflexed), and bladder fullness (empty, minimal residual, moderate residual) are given are given in

Table 21. Note that the position of one participant's uterus (CON group) changed from retroverted to anteverted between V1 and V2, which tends to be quite uncommon [319]. Measures of target depth and stiffness are given each for the CON group, the HBC group, and the combined study group in Table 22.

Table 20 Demographic and anthropometric characteristics of participants in the control (CON), hormonal birth control (HBC) and combined (ALL) study groups. Visit and ovulation day are given as day in the menstrual cycle. Menstrual Bleeding Questionnaire (MBQ) scores are given on an integer scale of 0 to 75, where 0 indicates a low impact of menstrual bleeding on quality of life. Values are indicated as mean ± standard deviation or median [range] and "-" indicates that parameter is not applicable or was not measured. Study visits are denoted as visit 1 (V1), visit 2 (V2), or visit 3 (V3).

	CON (n = 21)	HBC (n = 11)	ALL (n = 32)
Age (years)	31.5 ± 7.2	27.7 ± 4.2	30.2 ± 6.5
BMI (kg/m^2)	22.8 ± 3.23	22.4 ± 2.9	22.7 ± 3.1
Gravidity	0 [0,4]	0 [0,0]	0 [0,4]
Parity	0 [0,4]	0 [0,0]	0 [0,4]
Cycle Length (days)	29 [27,40]	28 [21,35]	28 [21,40]
Bleeding Length (days)	5 [2,8]	5 [4,8]	5 [2,8]

MBQ Score	13 [4,36]	8 [0,22]	11 [0,36]
V1 Day in Cycle	8 [3,14]	11 [5,26]	9 [3,26]
Ovulation Day in Cycle	13 [8,18]	-	-
V2 Day in Cycle	19 [14,25]	13 [6,27]	19 [6,27]
V3 Day in Cycle	20 [16,26]	-	20 [16,26]
Ethnicity	Asian (n = 4) Latin (n = 2) White (n = 15)	Asian (n = 2) Latin (n = 2) White (n = 7)	Asian (n = 6) Latin (n = 4) White (n = 22)
Hormonal Birth Control Use	-	Mirena IUD (n = 5) Kylena IUD (n = 2) Evra Patch (n = 1) Alysena Pill (n = 3)	Mirena IUD (n = 5) Kylena IUD (n = 2) Evra Patch (n = 1) Alysena Pill (n = 3)

Table 21 Uterus characterization for the control (CON) and hormonal birth control (HBC) study groups, assessed at visit 1 (V1), visit 2 (V2), and visit 3 (V3). Visit day in cycle and (CON only) day with respect to ovulation test (Days After Ovulation) are given as the median [range]. Uterus position is classified as anteverted (A), retroverted (R), or neutral (0). Uterus flexion is classified as anteflexed (A), retroflexed (R), or neutral (0). Bladder fullness following voiding is classified as completely empty (0), minimal residual (1), or moderate residual (2).

Group	Visit	Day in Cycle	Days After Ovulation	Endometrium Thickness (mm)	Uterine Volume (cm^3)	Uterus Position	Uterus Flexion	Bladder Fullness
CON	V1	8 [3,14]	-6 [-9,-1]	4.2 ± 0.3	54.5 ± 19.0	0 (n= 0) R (n = 4) A (n = 18)	0 (n= 15) R (n = 3) A (n = 4)	0 (n = 14) 1 (n = 4) 2 (n = 4)
	V2	19 [14,25]	7 [4,11]	10.9 ± 0.3	61.6 ± 19.5	0 (n= 0) R (n = 3) A (n = 19)	0 (n= 15) R (n = 3) A (n = 4)	0 (n = 14) 1 (n = 4) 2 (n = 4)
	V3	20 [16,26]	8 [5,12]	10.0 ± 0.3	60.5 ± 16.4	0 (n= 0) R (n = 3) A (n = 19)	0 (n= 15) R (n = 3) A (n = 4)	0 (n = 14) 1 (n = 4) 2 (n = 4)
HBC	V1	11 [5,26]	-	2.9 ± 1.6	42.5 ± 9.5	0 (n= 0) R (n = 2) A (n = 8)	0 (n= 7) R (n = 2) A (n = 1)	0 (n = 5) 1 (n = 3) 2 (n = 2)
	V2	13 [6,27]	-	3.7 ± 2.5	41.9 ± 9.9	0 (n= 0) R (n = 2) A (n = 8)	0 (n= 6) R (n = 3) A (n = 1)	0 (n = 4) 1 (n = 4) 2 (n = 2)

Table 22 Shear wave elastography (SWE) measures of uterine tissue stiffness in kilopascals (kPa). Participants were (HBC) or were not (CON) using hormonal birth control (HBC). Uterus sites included the anterior cervix (CA), the posterior cervix (CP), the anterior myometrium (MA), the posterior myometrium (MP), and the fundus (FU). Site depth was recorded for all measures. Outcomes are given as mean ± standard deviation.

Site	Visit	CON		HBC	
		Depth (mm)	SWE (kPa)	Depth (mm)	SWE (kPa)
CA	V1S1	11.8 ± 6.6	42.7 ± 28.4	8.6 ± 3.3	44.7 ± 21.9
	V1S2	13.3 ± 6.0	42.0 ± 24.6	10.4 ± 3.2	38.7 ± 16.2
	V2S1	8.4 ± 4.5	44.0 ± 17.3	10.7 ± 4.9	47.1 ± 23.0
	V3S1	11.3 ± 6.1	49.4 ± 17.5	-	-
CP	V1S1	18.6 ± 8.0	73.3 ± 17.9	15.4 ± 9.0	59.4 ± 24.4
	V1S2	22.8 ±7.9	79.5 ± 29.6	14.7 ± 6.3	51.8 ± 19.3
	V2S1	21.0 ±6.7	77.7 ± 22.9	14.2 ± 7.2	62.0 ± 30.0

	V3S1	21.4 ± 8.9	79.9 ± 32.8	-	-
MA	V1S1	15.9 ± 6.6	49.7 ± 13.6	13.9 ± 4.8	28.2 ± 11.4
	V1S2	18.0 ± 5.7	50.2 ± 20.5	17.4 ± 4.9	29.4 ± 9.7
	V2S1	15.6 ± 6.4	41.3 ± 14.5	16.5 ± 5.5	45.4 ± 16.0
	V3S1	15.5 ± 6.3	42.9 ± 14.7	-	-
MP	V1S1	24.4 ± 6.1	57.5 ± 22.0	21.0 ± 8.4	46.6 ± 25.3
	V1S2	25.2 ± 6.0	60.2 ± 18.5	20.9 ± 8.6	38.9 ± 22.3
	V2S1	27.3 ± 7.8	64.7 ± 22.7	21.2 ± 8.6	39.3 ± 14.3
	V3S1	26.8 ± 8.2	56.7 ± 22.0	-	-
FU	V1S1	13.9 ± 4.3	51.3 ± 21.1	15.4 ± 7.5	55.9 ± 22.9
	V1S2	16.9 ± 6.9	57.6 ± 19.5	15.9 ± 4.9	53.6 ± 24.3
	V2S1	16.1 ± 4.5	54.2 ± 21.1	16.6 ± 5.7	46.9 ± 15.3
	V3S1	16.8 ± 5.5	52.5 ± 17.6	-	-

6.3.2 Observations on Study Sample

One participant (CON) had a copper IUD. In line with the methods used for the HBC group, measurements of tissue stiffness were not acquired at the MP uterine site (anteverted uterus), posterior to the IUD. Measures of tissue stiffness at all other uterine sites for this participant deviated by less than one standard deviation from group averages and thus were retained (Figure 39A). Another participant (CON) had undergone a c-section (anteverted uterus) leaving a region of scar tissue that was substantially stiffer than the adjacent myometrial tissue (Figure 39B). For this case, SWE measures of the MA were taken far from the c-section scar where myometrial tissue stiffness had stabilized. A third participant (HBC) reported a historic diagnosis of endometriosis with no surgical or pathology-based confirmation and no recent (>10 years) symptoms of endometriosis (Figure 39C). Tissue stiffness at all uterine sites deviated less than one standard deviation from the group mean. Considering the lack of recent history, lack of surgical/biopsy diagnosis, and the knowledge that stiff extra-uterine lesions are the primary concern for SWE of endometriosis, rather than impacts on intrauterine tissue stiffness [40], [257], data from this participant were retained.

6.3.3 SWE Reliability and Phase Outcomes

Considering both the CON and HBC groups, within-day and between-day reliability findings are given in Table 23 and *Table 24*, respectively. Pairewise comparisons show no significant difference across target site tissue stiffness between imaging sessions within-day, however target depths of the CP, MA, and FU sites differed across imaging sessions. Within-day reliability of SWE measures of uterine tissue stiffness was excellent for all target sites. Comparing depth and stiffness between days, only the CA site exhibited significant differences between days. Between-day reliability was poor for in the MA site, good in the FU and MP sites, and was excellent both cervix sites. Considering the CON group, there were no differences in stiffness between the proliferative and secretory phases of the menstrual cycle (

Table 25). Effect sizes were small at all sites except for the MA which yielded a medium effect size. These findings suggested no impact of phase in the menstrual cycle on measures uterine tissue stiffness.

6.3.4 Depth and Stiffness of Uterine Target Sites

In order to provide a thorough characterization of uterine tissue stiffness, measures of target stiffness and depth were averaged across all visits and imaging sessions for all groups (Table 26). Comparing between sites, results showed significant differences ($p<0.001$). Post-hoc pairwise comparisons showed that posterior sites were stiffer (either significantly or approaching significance) than anterior sites for both the cervix (CA vs CP, $p<0.001$) and the myometrium (MA vs MP, $p=0.064$). Additionally, the posterior cervix was significantly stiffer than all myometrium sites (MA $p<0.001$, MP $p=0.025$, FU $p=0.015$). In terms of target site depth, on average the anterior cervix was significantly shallower than all other sites (CP $p<0.001$, MA $p=0.007$, MP $p<0.001$, FU $p=0.009$), while the posterior myometrium was significantly deeper than all sites (CA $p<0.001$, CP $p=0.012$, MA $p=0.013$, FU $p=0.012$). The MA, FU, and CP sites were not significantly different in terms of target site depth ($p>0.100$). Finally, target site depth exhibited weak, but significant correlations with CP and MA stiffness and moderate significant correlations with CA, MP, and FU stiffness (Figure 40).

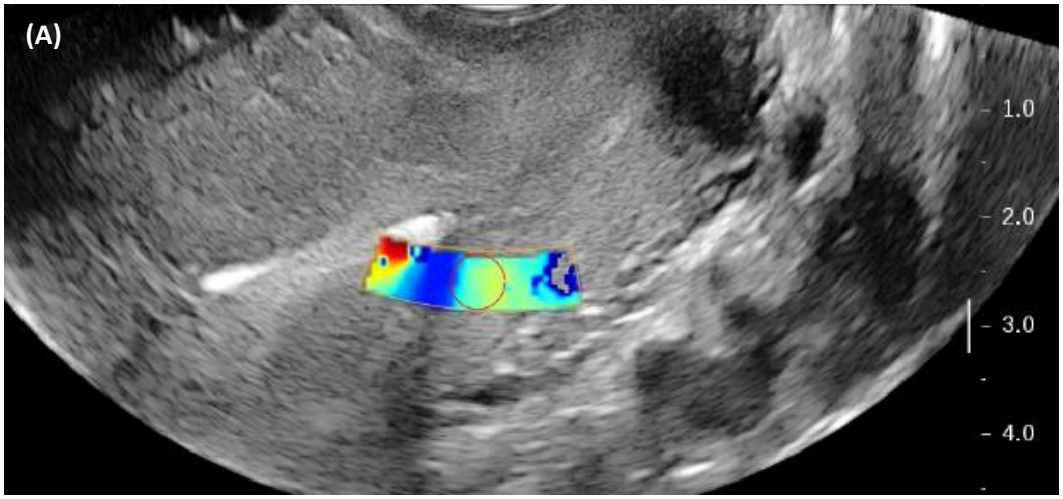

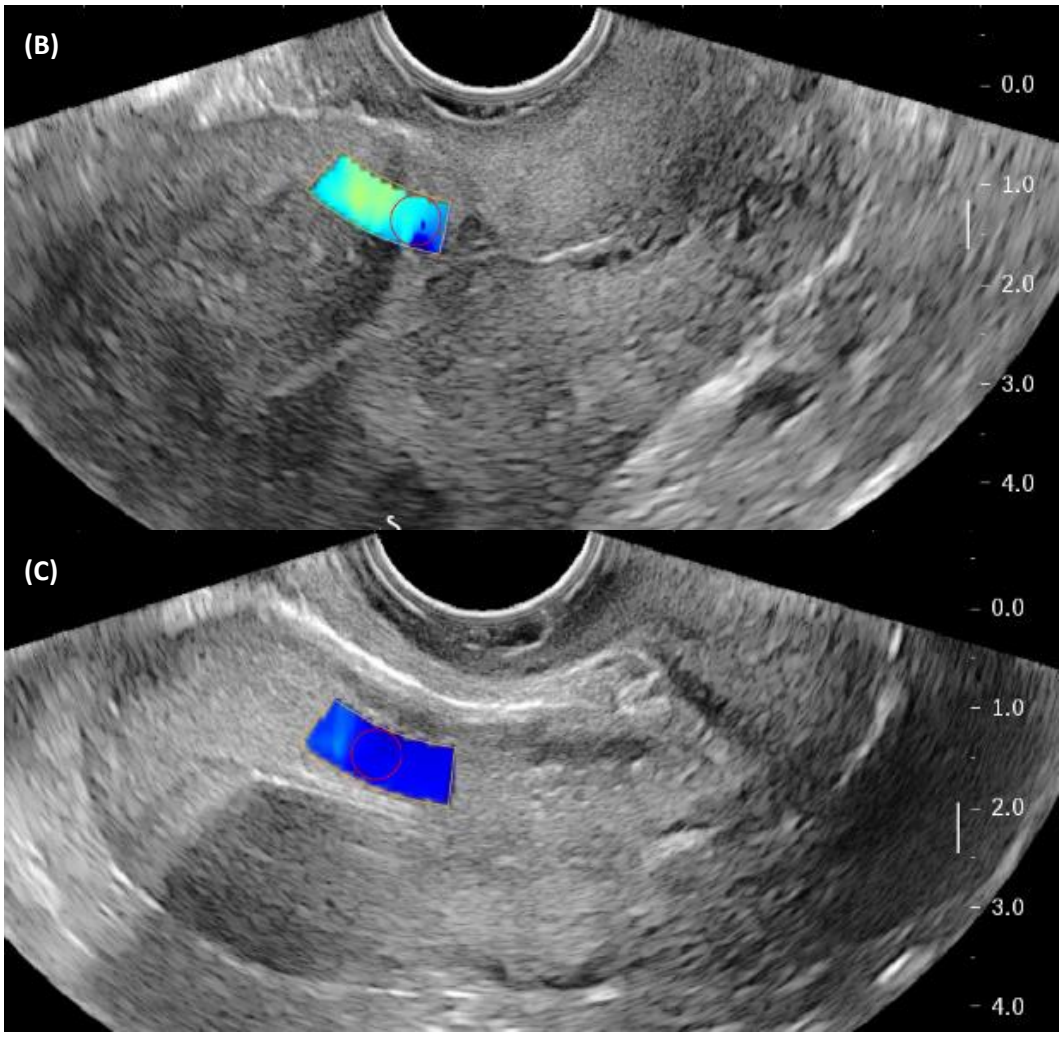

Figure 39 Visualization of SWE data from three participants. The first participant (A) had a copper intrauterine device (IUD). Measures of the posterior myometrium were excluded for this participant due to stiffness artifacts near the IUD that may have confounded measures of tissue stiffness. The second (B) participant had a c-section scar in the anterior myometrium (MA) which led to measures of increased tissue stiffness in this region. For this participant, MA measures of tissue stiffness were taken far from the scar to avoid any confounding of tissue stiffness measures by the scar tissue. The third participant (C) had a historic diagnosis of endometriosis, but no recent history of symptoms (>10 years), and no surgical/biopsy diagnosis. With the knowledge that stiff extra-uterine lesions are the primary concern for SWE of endometriosis, rather than impacts on intrauterine tissue stiffness [40], [257], *tissue stiffness data from this participant was retained in the study.*

Table 23 Within-day reliability of measures of uterine tissue stiffness measured in kilopascals (kPa) using shear wave elastography (SWE) in participants with no known uterine pathology who are (HBC) and are not (CON) using hormonal birth control. Target sites included the anterior cervix (CA), the posterior cervix (CP), the anterior myometrium (MA), the posterior myometrium (MP), and the fundus (FU). Target site depth was recorded for all measures. SWE and depth outcomes (mean ± standard deviation) were taken during visit 1, session 1 (V1S1) and repeated the same day during visit 1 session 2 (V1S2). Within-day reliability is given using intraclass correlation coefficients (ICCs) with the 95% lower bound (LB) and upper bound (UB). Significant differences ($p<0.05$) in depth of target site within-day are indicated by "". There were no significant differences between stiffness measured by SWE between V1S1 and V1S2 for any sites.*

Site	n	Visit	CON + HBC		Within-Day Reliability	
			Depth (mm)	SWE (kPa)	ICC (LB,UB)	p
CA	30	V1S1	10.7 ± 5.9	43.4 ± 26.3	0.90 (0.80,0.96)	<0.001
		V1S2	12.3 ± 5.4	40.9 ± 21.9		
CP	22	V1S1	15.7 ± 8.1*	65.0 ± 22.7	0.82 (0.58,0.92)	<0.001
		V1S2	19.0 ± 8.2*	70.4 ± 30.1		
MA	26	V1S1	15.3 ± 6.1*	43.4 ± 16.1	0.81 (0.58,0.92)	<0.001

		V1S2	17.8 ± 5.4*	43.8 ± 20.2		
MP	19	V1S1	23.1 ± 7.1	52.6 ± 21.8	0.79 (0.45,0.92)	0.001
		V1S2	23.8 ± 7.0	53.5 ± 21.7		
FU	18	V1S1	13.6 ± 4.1*	54.1 ± 21.0	0.78 (0.40,0.92)	0.002
		V1S2	16.5 ± 6.0*	55.8 ± 20.2		

Table 24 Shear wave elastography (SWE) measures of uterine tissue stiffness in kilopascals (kPa) between-days in participants with no known uterine pathology, using (HBC) and not (CON) using hormonal birth control. Target sites are the anterior (CA) and posterior cervix (CP), the anterior (MA) and posterior myometrium (MA), and the fundus (FU). SWE and depth outcomes (mean ± standard deviation) were averaged across visit 2 and visit 3 (CON) or across visit 1 (average of two sessions) and visit 2 (HBC). Reliability (intraclass correlation coefficients, ICCs) and 95% confidence interval (lower bound, LB; upper bound, UB) are shown. Significant differences ($p<0.05$) are indicated by "".*

Site	n	Day	CON + HBC		Between-Day Reliability	
			Depth (mm)	SWE (kPa)	ICC (LB,UB)	p
CA	31	Day 1	8.8 ± 3.9*	42.7 ± 17.6*	0.86 (0.69,0.93)	<0.001
		Day 2	11.1 ± 5.6*	47.8 ± 19.4*		
CP	27	Day 1	18.8 ± 7.6	71.6 ± 25.4	0.87 (0.72,0.94)	<0.001
		Day 2	19.0 ± 9.1	74.5 ± 33.2		
MA	30	Day 1	15.5 ± 5.8	37.9 ± 14.0	0.25 (-0.49,0.64)	0.207
		Day 2	15.9 ± 6.0	43.6 ± 14.9		
MP	19	Day 1	24.8 ± 8.8	55.8 ± 22.8	0.74 (0.35,0.90)	0.002
		Day 2	24.4 ± 8.7	48.9 ± 21.1		
FU	18	Day 1	16.6 ± 6.0	56.0 ± 19.9	0.65 (0.10,0.87)	0.017
		Day 2	16.9 ± 5.7	50.3 ± 16.1		

Table 25 Measures of uterine tissue stiffness measured in kilopascals (kPa) using shear wave elastography (SWE) in participants with no known uterine pathology who are not (CON) using hormonal birth control. Target sites included the anterior (CA) and posterior cervix (CP), the anterior (MA) and posterior myometrium (MA), and the fundus (FU). SWE and depth outcomes (mean ± standard deviation) were taken in the proliferative phase of the menstrual cycle during visit 1 (averaged across two imaging sessions) and repeated during the secretory phase of the menstrual cycle at visit 2 and visit 3 (averaged across two visits). Effect size for pairwise comparisons between SWE tissue stiffness is given as Cohen's d.

Site	n	Phase	CON				
			Depth (mm)	p	SWE (kPa)	p	Cohen's d
CA	19	Proliferative	12.0 ± 5.8	0.32	39.6 ± 22.8	0.09	0.18
		Secretory	9.9 ± 5.0		47.7 ± 15.6		
CP	18	Proliferative	21.5 ± 7.5	0.66	75.6 ± 21.5	0.69	0.13
		Secretory	20.7 ± 7.2		77.5 ± 25.1		
MA	18	Proliferative	16.9 ± 5.3	0.17	50.0 ± 15.6	0.14	0.59
		Secretory	15.6 ± 6.0		41.4 ± 9.9		
MP	15	Proliferative	24.4 ± 6.4	0.30	58.6 ± 19.2	0.80	0.14
		Secretory	26.8 ± 7.9		59.2 ± 19.1		
FU	10	Proliferative	15.6 ± 5.2	0.81	56.1 ± 17.9	0.33	0.11
		Secretory	16.0 ± 4.7		49.5 ± 22.3		

Table 26 Characterization of uterine tissue stiffness measured in kilopascals (kPa) using shear wave elastography (SWE) in participants with no known uterine pathology who are (HBC) and are not (CON) using hormonal birth control. Target sites included the anterior cervix (CA), the posterior cervix (CP), the anterior myometrium (MA), the posterior myometrium (MP), and the fundus (FU). Depth of the target site was recorded for all measures. SWE and depth outcomes (mean ± standard deviation) were averaged from four (CON) or three (HBC) imaging sessions spaced across three (CON) or two (HBC) days of the menstrual cycle. Correlation coefficients (CC) between depth and SWE measures are given.

Site	n	CON + HBC		CC	P
		Depth (mm)	SWE (kPa)		
CA	32	10.9 ± 4.4	44.4 ± 18.9	0.57	<0.001
CP	32	19.5 ± 7.4	71.0 ± 24.9	0.31	<0.001
MA	30	16.0 ± 5.0	42.5 ± 11.9	0.40	0.001
MP	26	24.6 ± 7.0	56.0 ± 18.9	0.56	0.003
FU	29	16.0 ± 5.1	53.2 ± 16.7	0.72	0.015

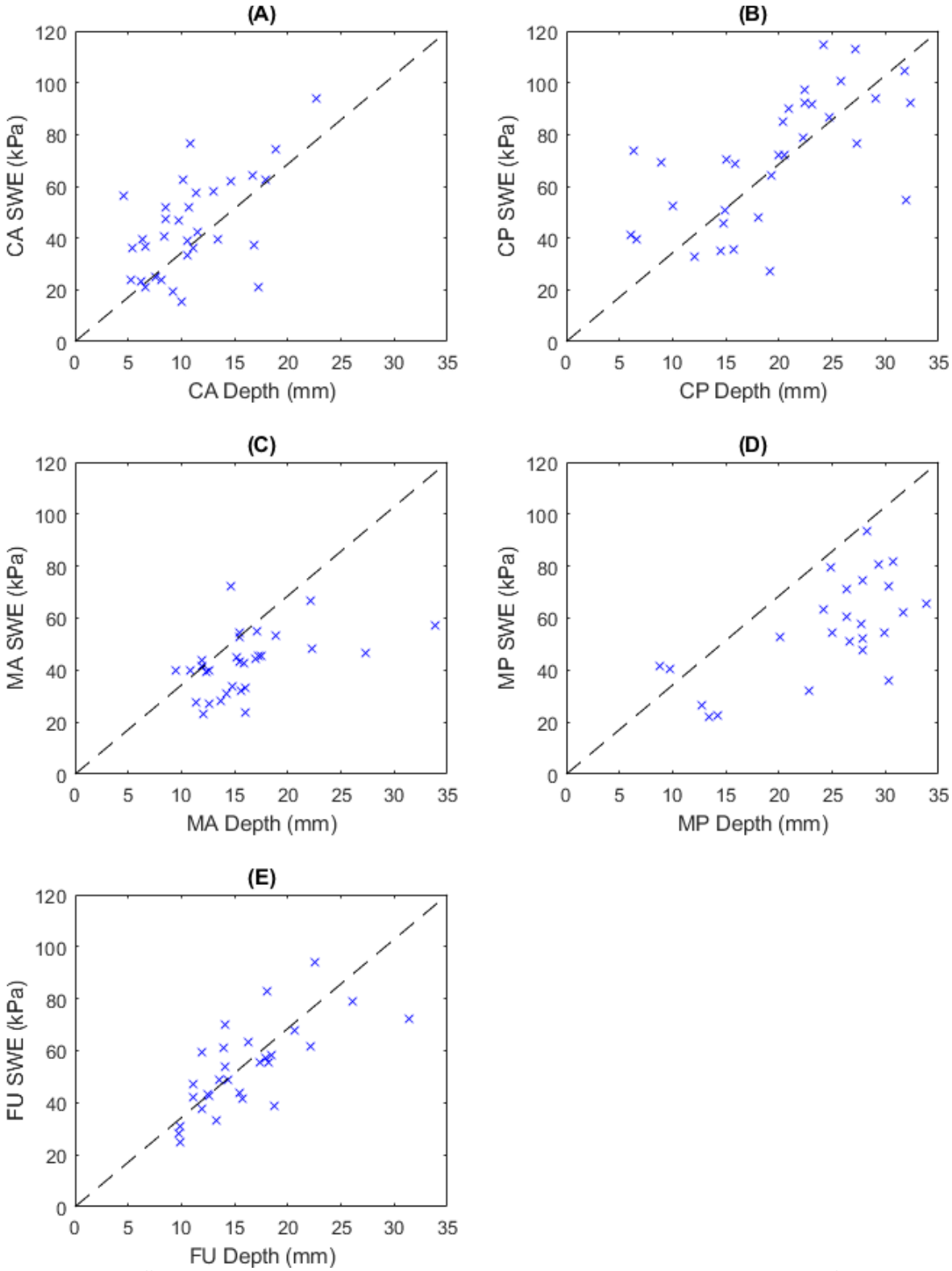

Figure 40 Tissue stiffness measured in kilopascals (kPa) using shear wave elastography (SWE) compared to the depth of the target tissue. Stiffness was measured at five target sites in the uterus, including the anterior cervix (CA) (A), the posterior cervix (CP) (B), the anterior myometrium (MA) (C), the posterior myometrium (MP) (D), and the fundus (FU) (E) and depth of target sites (mm). Measures were taken in participants with no known uterine pathology who are (HBC) and are not (CON) using hormonal birth control. A correlation of 1 is shown by the black dashed line.

6.4 Discussion

To date, our team has observed inadequate characterization of study sample demographics, anthropometrics, and uterus morphology for gynecological SWE reporting. To our knowledge, this is the first study of uterine elastography to provide a complete characterization of the study sample, including factors that may be relevant to gynecological tissue stiffness outcomes measured by SWE.

6.4.1 Reliability of SWE in the Uterus

In line with previous findings on the reliability of SWE for a variety of populations and target tissues [99]–[101], [165], our data demonstrated excellent within-day reliability of measures of uterine tissue stiffness (0.78<ICC<0.90). This was particularly interesting as several sites (CP, MA, FU) exhibited significant differences in target depths between the two imaging sessions. In fact, phantom studies of SWE have suggested that depth of the target can decrease accuracy of SWE measurements of tissue stiffness in linear probes [80], [200] (Section 3). Post-hoc analysis included calculation of the 97.5% confidence intervals and effect sizes for target depth within-day. There was significant overlap in the 97.5% confidence internals within-day (i.e. between sessions) for the CP (session 1 = (0.7 mm, 33.8 mm), session 2 = (3.8 mm, 36.1 mm), Cohen's d = 0.32), MA (session 1 = (3.4 mm, 27.0 mm), session 2 = (7.2 mm, 28.3 mm), Cohen's d = 0.45), and FU (session 1 = (3.0 mm, 26.1 mm), session 2 = (4.8 mm, 28.1 mm), Cohen's d = 0.35) sites and effect sizes for all sites were small to medium. Further, we used multiple pairwise comparisons because the power of multivariate analyses would have been negatively impacted by the incomplete data sets. This may have been a factor in the significant differences in depth across sessions. Regardless of whether depth was a significant factor in this analysis, the SWE endoprobe indeed yielded excellent within-day reliability across all uterine target sites investigated in this study.

In terms of between-day reliability, SWE data from all target sites in the uterus yielded good to excellent between-day reliability ($0.65<ICC<0.87$, $p<0.02$) except for the MA site (ICC=0.25, p=0.21) which has poor reliability. Pairwise comparisons of site depth and stiffness between-days revealed significant differences at only the CA site in terms of depth and stiffness. This finding for CA stiffness was of concern. Post-hoc analyses showed that the 97.5% confidence interval for CA stiffness (day 1 = (8.2 kPa, 77.2 kPa), day 2 = (9.8 kPa, 85.8 kPa)) and depth (day 1 = (1.1 mm, 16.4 mm), day 2 = (0.2 mm, 22.0 mm)) overlapped significantly, although the means between-days did differ. The between-day difference in CA depth (p=0.003) and CA stiffness (p=0.03) were both significant. Further, while the difference in depth between days exhibited a moderate effect size (Cohen's d = 0.49), the difference in stiffness yielded a much smaller effect size (Cohen's d = 0.28). Based on the significant moderate correlation between depth and stiffness at the CA site (rho = 0.57, $p<0.001$), it is theorized that the deeper positioning of the CA site on day 2 could have yielded significantly higher measures of CA tissue stiffness. Regardless of this finding, the between-day reliability of stiffness measures taken at the CA site was indeed excellent. However, the implications of this finding will be considered further here.

Regarding the poor between-day reliability of measures of MA tissue stiffness (ICC=0.25, p=0.21), a retrospective review of the between-day MA data yielded 10 participants in which measures of MA tissue stiffness differed between-days by over 20kPa. Deviations in these cases were qualitatively attributed to changes in ROI placement (n = 10) with respect to the imaging probe, which was not observed in the other participants with complete MA data sets (n=19). Interestingly, one of the 10 cases exhibiting significant deviations in MA site stiffness was that of a nulliparous uterus that changed from a retroverted anteflexed position on day 1 to an anteverted position on day 2.

Issues around consistency of target depth, imaging plane, and ROI placement were considered throughout data acquisition and processing for this study. In order to address this, data processing involved referencing target site data across multiple imaging sessions to ensure that the ROI placement

was consistent (position, depth). However, even with exceptional effort to standardize ROI placement, the reliability of MA stiffness measures was still poor. When these 10 cases were “cleaned” from the complete MA data set, mean MA tissue stiffness did not change from the complete data set for day 1 (day 1 complete = 37.9 ± 14.0 kPa, day 1 cleaned = 35.9 ± 11.1 kPa, $p = 0.60$) or day 2 (day 2 complete = 43.6 ± 14.9, day 2 cleaned = 39.7 ± 10.7, $p = 0.37$). Further, ICC analysis of the “cleaned” MA data set revealed substantially improved between-day reliability (ICC = 0.72, 95% CI = (0.32,0.89), $p = 0.003$, $n = 20$). Thus, it appears that the SWE system may have the potential to yield good to excellent reliability at all target sites in the uterus, however methods to ensure consistency of ROI placement (plane of imaging, depth, position) must be developed and validated. High between-day reliability is essential to clinical utility, if SWE imaging is to be useful for monitoring gynecological pathologies and response to treatment.

6.4.2 SWE Outcomes Across the Menstrual Cycle

As the first study to systematically investigate the impact of phase in the menstrual cycle on SWE measures of uterine tissue stiffness, findings from this study will provide an essential foundation for the design of gynecological SWE protocols moving forward. Measures of uterine tissue stiffness exhibited no significant difference between phases of the menstrual cycle at any of the target sites. Further, effect sizes at all sites were small to moderate, suggesting substantial overlap in the distributions of each site between phases. This is an important first step to understanding limitations around gynecological SWE. However, these findings should not be generalized to pathological gynecological tissues. As an example, although conflicting findings have been presented in the literature [320], multiple studies have shown that UFs exhibit higher levels of estrogen receptor [321], [322] than unaffected uterine tissue, and may exhibit an enhanced response to estrogen [321], [323], [324]. As such, while no impact of the phase of

the menstrual cycle was seen in a sample of healthy females with no uterine pathology, it is essential that this result is confirmed n cases of UFs and other relevant uterine pathologies.

6.4.3 Target Site and SWE Stiffness

In terms of characterizing tissue stiffness and depths at target sites in the uterus, posterior sites were either trending towards significance or significantly stiffer than their anterior counterparts for both the cervix (CA = 44.4 ± 18.9 kPa, CP = 71.0 ± 24.9 kPa, $p < 0.001$) and myometrium (MA = 42.5 ± 11.9 kPa, MP = 56.0 ± 18.9 kPa, $p = 0.064$). The CP site was also significantly stiffer than all regions of the myometrium (MA = 42.5 ± 11.9 kPa, $p < 0.001$; MP = 56.0 ± 18.9 kPa, $p = 0.025$; FU = 53.2 ± 16.7, $p = 0.015$) while the CA site was not.

Placing these findings in the context of the literature, SWE findings of a stiffer CP compared to the CA aligned with previous findings in hysterectomy specimens [325], as well as qualitative estimates of tissue stiffness made using strain elastography [120]. Comparing measures of cervix stiffness presented here to those measured by Zhang et al. [121] used the same SWE system as the current study, yet the mean (anterior and posterior) cervix stiffness (83.0 ± 11.9 kPa, n = 32) in their sample was significantly higher than both CP (CP = 71.0 ± 24.9 kPa, n = 32, $p = 0.014$) and CA (CA = 44.4 ± 18.9 kPa, n = 32, $p < 0.001$) stiffness in the current study. Moreover, Zhang et al.'s [121] measures of mean (anterior, posterior, and fundus) unaffected myometrium stiffness (69.1 ± 10.8 kPa, n = 26) were significantly higher than measures of MA (MA = 42.5 ± 11.9 kPa, n = 30, $p < 0.001$), MP (MP = 56.0 ± 18.9 kPa, n = 26, $p = 0.001$), and FU (FU = 53.2 ± 16.7, n = 29, $p < 0.001$) stiffness observed in the current study's sample. However, it appears that Zhang et al. [121] included participants in their control group who had pelvic pain and/or abnormal uterine bleeding, but no pathology on MRI. As well, there was a second study group of participants with adenomyosis and/or UFs confirmed on MRI. Yet, it is not clear which participants' data were used to formulate these average measures of cervix and myometrium

stiffness (i.e. those with or without an MRI diagnosed uterine pathology). Thus, increased stiffness measured by Zhang et al. [121] could be an artifact of uterine pathologies, an artifact of the gynecological symptoms, or even an artifact of the probe compression required to obtain clear data in large, complex uteruses [121]. The only demographic data provided by Zhang et al. [121] described the age of the study sample (mean = 36.8 years, range = [22,52] years) and the premenopausal status of all participants.

In another investigation of gynecological SWE using the same system, Acar et al. [209] took SWE measurements of myometrium stiffness in participants with no gynecological symptoms and sonographically unremarkable uteruses. Acar et al.'s [209] acquired measures of mean myometrium tissue stiffness (28.3 kPa, [5%,95%] = [12.7 kPa, 59.5 kPa], n = 56) in their healthy control group. Assuming a normal distribution of Acar et al.'s [209] data (standard deviation = 14.2 kPa), myometrium stiffness measured by Acar et al. [209] was significantly lower than measures of MA (MA = 42.5 ± 11.9 kPa, n = 30, $p < 0.001$), MP (MP = 56.0 ± 18.9 kPa, n = 26, $p < 0.001$), and FU (FU = 53.2 ± 16.7, n = 29, $p < 0.001$) stiffness in the current study sample. Similar to Zhang et al. [121], the only descriptive factor of Acar et al.'s [209] study sample was the age of the participants (median = 30 years, [5%,95%] = [21,45] years). The study group appeared to be a mixture of menopausal and premenopausal participants, although a clear description was not provided. While no details were given around myometrium target site (anterior vs. posterior vs. fundus), figures from the published work suggest measures may have been taken primarily in the anterior myometrium.

In fact, our findings of significantly higher CP stiffness with respect to the CA site is consistent with the findings of Hernandez-Andrade et al. [120], who measured cervical stiffness in a sample of pregnant participants (n = 154). Hernandez-Andrade et al. [120] observed a significant difference between the posterior (median = 9.7 kPa, [25%,75%] = [6.8 kPa, 15.9 kPa]) and anterior (median = 5.9 kPa, [25%,75%] = [5.1 kPa, 10.8 kPa]) cervix wall stiffness at the external os, however there was no

significant difference at the internal os (posterior median = 20.3 kPa, [25%,75%] = [12 kPa, 38.9 kPa]; anterior median = 15.9 kPa, [25%,75%] = [9.7 kPa, 41.1 kPa]). Hernandez-Andrade et al. [120] also measured target depth at the external os (anterior median = 8.1 mm, [25%,75%] = [6.4 mm, 9.7 mm]; posterior median = 19.5 mm, [25%,75%] = [17.0 mm, 22.1 mm]) and internal os (anterior median = 10.4 mm, [25%,75%] = [8.7 mm, 12.3 mm]; posterior median = 21.9 mm, [25%,75%] = [20.4 mm, 24.4 mm]) for both anterior and posterior cervix sites. The study sample had a median age of 24 years ([25%,75%] = [21 years, 27 years]), only 21% (n = 32) of participants were nulliparous, gestational age ranged from 14 to 29 weeks, and participants were primarily African American (92%, n = 142). In contrast, the study sample here was significantly older (age = 30.2 ± 6.5, $p<0.001$), primarily nulliparous (81%, n = 26), nonpregnant, and primarily white (69%, n = 22). While it is difficult to compare cervix stiffness between these substantially different groups, qualitatively our study group exhibited higher anterior and posterior cervix stiffness. While our study methods did not differentiate internal and external os for our CP and CA sites, the imaging researcher (CC) aimed to acquire data mid-way between the internal and external os. Regardless, further investigation of the relationship between age, pregnancy, and parity and cervix tissue stiffness is required to better understand the value of these findings.

6.4.4 Target Site Depth and SWE Stiffness

In terms of target site depth, which has yet to be reported in gynecological SWE applications, the CA (CA = 10.9 ± 4.4 mm) site was significantly ($p<0.02$) shallower than all other sites, while the MP (MP = 24.6 ± 7.0 mm) site was significantly deeper than all other sites (CP = 19.5 ± 7.4 mm, MA = 16.0 ± 5.0 mm, FU = 16.0 ± 5.1 mm). Considering that our sample was made up of primarily anteverted uteruses (n = 27), these depth findings align well with the morphology of a healthy anteverted uterus (Figure 38). Further, target depth exhibited significant weak (CP = 0.31, MA = 0.40) or moderate (CA = 0.57, MP = 0.56, FU = 0.72) correlated with target stiffness at all sites in the uterus.

Hernandez-Andrade et al. [120] did not observe any relationship between target depth and target stiffness in their sample. In contrast, findings from this work and from our previous work (Section 3) suggest that target depth may be a relevant finding moving forwards. While correlations between target depth and SWE stiffness were weak for the CP and MA sites, they were moderate for the MP, FU, and CA sites. Previous findings from a validation of endoprobe SWE in tissue mimicking phantoms showed a significant decrease in the validity of endoprobe SWE at target depths of 3cm and 5cm, compared to 1cm depths (Section 3). Moreover, endoprobe SWE at deeper target depths (3cm and 5cm) similarly exhibited poor validity compared to linear probe and curvilinear probe SWE at those same depths in homogeneous tissue mimicking phantoms (Section 3). In fact, previous studies of a variety of SWE probes show changes in the validity of measurements with target depth [73]–[75], [81]. In this study, target sites were measured at a large range of depths across participants (97.5 % confidence interval CA = [2.2 mm, 19.6 mm], CP = [4.9 mm, 34.0 mm], MA = [6.2 mm, 25.8 mm], MP = [10.8 mm, 38.3 mm], FU = [6.1 mm, 25.8 mm]). In contrast, the depth of target sites in Hernandez-Andrade et al.'s [120] study exhibited a much smaller range at each site of interest (internal os: anterior = [8.7 mm, 12.3 mm], posterior = [20.4 mm, 24.4 mm]; external os: anterior = [6.4 mm, 9.7 mm], posterior = [17.0 mm, 22.1 mm]). Thus, Hernandez-Andrade et al.'s [120] sample may not have included a large enough range of depths to delineate a significant relationship between stiffness and target depth. Regardless, this work was not intended as a causative investigation of target depth and stiffness in the uterus. Until a systematic study of the in vivo relationship between uterine tissue target depth and stiffness is published, it is recommended that all studies of in vivo elastography include measures of target depth and check for significant relationships.

As with any novel measurement, the importance of thorough and standardized reporting cannot be overstated. While it is clear that measures of uterine tissue stiffness in this study are lower than those presented by Zhang et al. [121] and higher than those presented by Acar et al. [209], the lack of sample

and uterus characterization in these studies limits our ability to perform any critical comparison. While phase of the menstrual cycle does not appear to influence measures of uterine stiffness made using SWE in healthy participants, thorough characterization of factors that may contribute to tissue stiffness, such as demographic/anthropometric factors (e.g. age, BMI, parity, menopausal status), factors that may related to gynecological pathologies (e.g. use of hormonal birth control, MBQ), and uterus features (e.g. volume, endometrial thickness, position) should be recorded.

6.4.5 Potential Confounders on Gynecological SWE

Some qualitative observations from the dataset may be important to future investigations. Retroverted and anteverted uteruses (Figure 41A and Figure 41B) exhibited different patterns of stiffness across target sites; anterior sites in anteverted uteruses (Figure 41B) appeared to be softer than those in retroverted uteruses (Figure 41A). Moreover, in one case a nulliparous uterus changed orientation from retroverted (Figure 41C) to anteverted (Figure 41D) between visits, yielding significant changes to SWE measures at various sites. While this phenomenon could be an artifact of increased target depth decreasing the accuracy of measures, the differences may relate to the concept often of residual stresses in tissue. For example, blood vessels are known to hold residual circumferential stress [326], thought to be an integral part of the mechanosensory feedback system [327]. Depending on the anatomical position of a uterus (Figure 36), aspects of the anterior and the posterior wall of the uterus could each be in compression or tension, holding residual stresses due to the natural curvature of the organ. This phenomenon has yet to be identified and systematically investigated in the literature.

As has already been quantitatively evaluated, target depth may relate to SWE stiffness measures of the uterus. Moreover, we surmise that target depth also appears to impact the quality and uniformity of data (Figure 41E and Figure 41F). Deeper target sites tended to be more vulnerable to SWE data acquisition failure, as exhibited by the substantially larger number of complete data sets for the CA site

(shallow, n = 32) compared to the deeper MP site (n = 19). Further, although all participants were asked to void the bladder prior to imaging, some demonstrated a residual volume of liquid in the bladder (Figure 41H). Although it is well documented that positioning of the uterus is known can change with bladder filling [319], residual volume was not expected to be a significant factor in this case. Residual volume sometimes appeared to push the uterus deeper (Figure 41G) or generate pressure on the uterus that may have increased SWE measures of tissue stiffness.

Participants with IUDs exhibited shadowing and high stiffness artifacts in the MP site posterior to the IUD. In this study, we chose to omit MP data in participants with IUDs to avoid confounding the characterization of "healthy" uterine tissue. However, many people with uteruses rely on IUDs as a method of birth control or for managing gynecological pathologies. Thus, it may be relevant to gain a thorough understanding of the impact of IUDs on uterine tissue stiffness. Another interesting case included high stiffness measures at the c-section scar in the anterior uterus of one participant. While tissue beyond the bounds of the scar (visualized through B-mode ultrasound) yielded measurements in line with the rest of the study sample, scarring from previous surgeries should be considered when strategizing around study recruitment and applicability of gynecological SWE.

6.4.6 Limitations

As with any study, the findings presented here must be considered within the limitations of the work. Incomplete data sets across the multiple visits and imaging sessions were a major limitation of this work. In many cases, this resulted in the use of multiple pairwise comparisons, which are known to be vulnerable to spurious findings of significance. Another concern was the use of an SWE endoprobe that was indeed not rated for uses beyond depths of 3 cm (Table 2) and had been found to have decreased validity at depths of 3cm and beyond (Section 3). Further, it is unclear at this point whether the correlation between depth and tissue stiffness is an artifact of probe performance in deep tissues or in

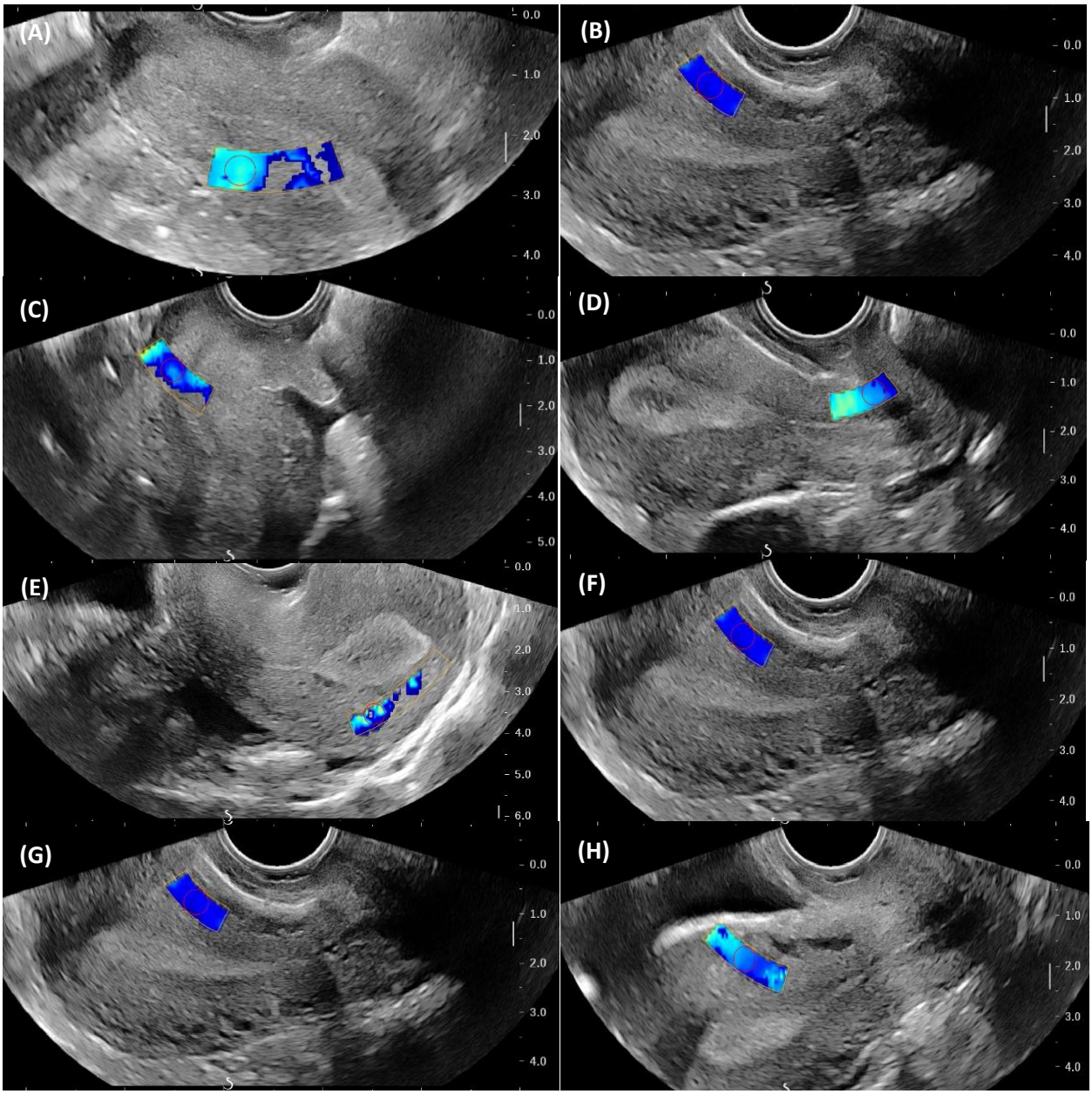

Figure 41 Qualitative visualization of potential confounders: potential for residual stresses in the anterior myometrium of a retroverted uterus (A) compared to an anteverted uterus (B); the case of a uterus that changed from a retroverted position (C) to an anteverted position (D) between two visits less than 48 hours apart; issues around infill and target depth (E), compared to a shallow uniform site (F); and a bladder with residual volume (H) potentially confounding measures of anterior myometrium stiffness compared to the same uterus with a completely voided bladder (G).

fact a true finding. A systematic validation of this probe in fresh human tissue could provide a bases for SWE imaging of deep tissues in the uterus, however, without this evidence, there are major concerns around the validity of stiffness measures in deep uterine tissues. This is particularly relevant for gynecological pathologies, which can increase the volume of the uterus and depth of the relevant target

sites. Homogeneity of the study sample was another area of concern. The primarily white, nulliparous, young (<35 years old) study sample is not representative of patients visiting gynecology clinics for the treatment of uterine disorders. Gynecological SWE data from more heterogeneous study samples will improve the characterization of “healthy” uterine tissue.

6.5 Conclusion

Within- and between-day reliability of SWE measures ranged from good to excellent, except for those taken in the anterior myometrium. This was attributed to issues around standardization ROI placement at the target site over multiple visits. Development of future methodologies must address this issue as well in order for SWE to be a feasible tool for use in clinical settings. The phase in the menstrual cycle does not appear to impact SWE measures of uterine tissue stiffness. While findings did not suggest a causative relationship between target depth and SWE tissue stiffness, strong correlations between these outcomes combined with evidence from SWE phantom studies suggest that the relationship between target depth and SWE stiffness must be more thoroughly investigated prior to implementation in the study and evaluation of uterine pathologies. Finally, the findings suggest that uterine tissue stiffness does not appear to be homogeneous. Stiffness varied significantly between the anterior and posterior regions of the uterus and between the cervix and myometrium tissue. This is an important factor to consider moving forward, as the interaction between uterine site-dependent stiffnesses and pathology has not yet been identified. Further validation of gynecological SWE and more thorough study of potential confounding factors is recommended.

7 Discussion

7.1 Summary

Although UE has been in development since the late 1980s [138], [151], [328], studies of UE are ubiquitous in the medical imaging literature [33], [36], [269]–[282] and it has recently seen clinical uptake for use in liver pathologies [64], [269], [276], [278], [283]–[287]. Yet investigations into gynecological applications of SWE lag far behind much more common applications such as breast and liver screening [270], [272], [273], [276], [277], [279], [280]. A review of the elastography validation literature suggested that this was in part due to a lack of validation studies for endovaginal SWE probes, lack of standardization around reporting, and no consideration of potential confounders. In an effort to enhance the base of evidence in this currently sparse field, the purpose of this thesis was to assess the feasibility of endoprobe SWE for in vivo assessment of uterine tissue stiffness. This systematic assessment of gynecological SWE feasibility will provide direction and support technological improvements required for desired performance of endoprobe SWE and has the potential to catalyze the currently sparse field of gynecological elastography.

Phantom studies often function as the first step in demonstrating the applicability of elastography for a given clinical application [81], [138], [144], [169], yet only a single SWE endoprobe phantom study could be found in the literature [87], which exhibited many limitations. To fill this gap, the first study in this thesis documented the reliability and validity of endoprobe, linear probe, and curvilinear probe SWE at three target depths in a large sample of TMM phantoms using MTE as a criterion standard. While the reliability of endoprobe SWE measures of tissue stiffness was acceptable at all target depths, endoprobe agreement with MTE outcomes showed higher variance and weaker relationships than those same outcomes measured using a curvilinear and linear probe at all depths. Endoprobe performance was acceptable at 1cm, but degraded substantially at the 3cm target depth and at the maximum consistent depth condition (3.91 cm ± 0.57 cm), with SWE endoprobe estimates of TMM stiffness at 5cm exhibiting

no significant relationship with MTE outcomes. Further, endoprobe performance at 1cm depths was worse than both the linear and curvilinear probes at all target depths. In fact, the curvilinear and linear probe SWE exhibited excellent reliability and validity even at target depths which were outside of the manufacturer's recommended parameters for clinical use.

The second step in demonstrating the feasibility of elastography for clinical applications is the validation of SWE stiffness outcomes using fresh tissues [71], [138], [246]. While quasi-static flat tip indentation testing is an ideal criterion standard [71], [90], [112], variable testing and modeling parameters in the literature [109]–[112], [114] and limited validation of soft tissue indentation [88] were identified as barriers to performing such a validation. Thus, the second study in this thesis documented the validity of quasi-static flat tip indentation testing under a variety of parameters against the criterion standard of ramp compression testing. Exact agreement between indentation and ramp compression were optimized in the low strain region of the loading curve (<10%) when using the Oliver Pharr [109] and at low testing rates (0.01Hz), regardless of sample geometry. High strain ranges (15% to 20%) yielded the lowest agreement between indentation and ramp compression testing, but agreement was slightly improved with larger sample geometries (T_s > 5mm) compared to smaller geometries (T_s < 5mm). The performance of indentation model corrections in the literature was inconsistent. Yet, findings did indeed show strong relationships between indentation and ramp outcomes for all conditions, suggesting that testing parameters for characterization of soft tissue moduli can be matched to the relevant in vivo loading regimes as needed.

While the second study in this thesis evaluated the validity of indentation testing, optimal mechanical testing parameters for validating SWE have not yet been systematically studied in the literature [95]. Thus, the third study in this thesis provided a systematic investigation of the agreement between SWE and indentation modulus under a variety of indentation parameters. Similar to the previous study, very strong relationships between indentation and SWE measures of the elastic modulus

were observed across all testing conditions and mathematical models. Regardless, lower strains (Zhai [172] and 2.5%-7.5%), which are thought to mimic SWE loading regimes [115], yielded the best agreement between SWE and indentation outcomes. Further, small sample geometries (<5mm) tested at the lowest testing rates (0.01Hz) also yielded optimal agreement between SWE and indentation testing. The Hayes-Zhang [111], [112] model yielded the lowest variance in agreement for these conditions, but a bias correction is recommended prior to implementation. As well, it was recommended that a small sample of TMM phantoms always be used to validate testing methods and data processing prior to fresh tissue testing.

Finally, the last study in this thesis investigated the in vivo reliability of uterine SWE and the impact of phase in the menstrual cycle, target site in the uterus, and target depth on SWE outcomes. Within- and between day reliability ranged from good to excellent, except for target sites in the anterior myometrium where more robust methods of standardizing the target site may be required. The findings suggest that phase in the menstrual cycle does not impact SWE outcomes. However, posterior regions of the uterus tended to be stiffer than anterior regions, and the posterior cervix was significantly stiffer than all myometrium sites, where the anterior cervix was not. While the causative impacts of target depth on SWE measurements of uterine tissue stiffness cannot be determined based on the study design, significant weak to moderate correlations between target stiffness and depth suggest the need for future investigation. Potential confounders that were identified included uterus orientation, signal quality at deep targets, residual bladder volume, C-section scars, and IUDs.

7.2 Implications

7.2.1 The Utility of Endoprobe SWE for Gynecological Applications

The in vivo study of SWE performance (Section 6) suggests the potential for utility of gynecological SWE, pending the development of robust methods for standardizing target and site further investigation around potential confounding factors, including target depth. However, when

viewed within the context of the first study in this thesis (Section 3), there are several considerations around the utility of endoprobe SWE which must be considered. Findings around validity of endoprobe SWE in phantoms revealed that, even at 1cm target depths, endoprobe SWE agreement with MTE was consistently poorer than that of linear and curvilinear probe SWE across all target depths. Endoprobe SWE validity degraded at the 3cm depth in phantoms, and at the 5cm target depth there was no significant relationship between endprobe SWE measures of stiffness and MTE outcomes, suggesting that endoprobe SWE may only be useful for tissues very close to the probe.

The depth of the anterior and posterior cervix sites ranged from 2.3mm to 34.0mm, while anterior myometrium and fundus sites were between 6.0mm and 26.0mm deep, and posterior myometrium sites were between 10.9mm and 38.3 mm deep. Considering these outcomes within the context of Study 1 (Section 6), in homogeneous phantoms the mean difference between SWE stiffness and MTE ranged from -5.11 kPa to -8.23 kPa up to the maximum consistent depth condition (3.91 cm ± 0.57 cm), the standard deviation on this difference ranged from 12.89kPa to 18.95kPa. Knowing that target sites in the uterus exhibited a relatively wide range of stiffness at these depths (CA = 44.4 ± 18.9 kPa, CP = 71.0 ± 24.9 kPa, MA = 42.5 ± 11.9 kPa, MP = 56.0 ± 18.9 kPa, FU = 53.2 ± 16.7), this high variability in agreement between SWE and MTE becomes a concern.

Considering the findings of two other pilot studies of SWE in uterine pathologies that used the same elastography system studied here (Aixplorer, SuperSonic Imagine, Aix-en-Provence, France) provides further context for these outcomes. Acar et al. [209] observed the SWE stiffness of adenomyosis lesions (median [5%,95%] = 72.7 [22.3, 274.2] kPa, n = 14), non-adenomyosis lesions (28.3 [12.7, 59.5] kPa, n = 14), and asymptomatic myometrium tissue (24.4 [17.9, 32.4] kPa, n = 56). Similarly, Zhang et al. [121] compared asymptomatic cervix (mean ± STD = 83.0 ± 11.9 kPa, n = 34) and myometrium (69.1 ± 10.8 kPa, n = 34) stiffness measured by SWE to the stiffness of adenomyosis lesions (72.0 ± 18.8 kPa, n = 6) and uterine fibroid lesions (94.08 ± 18.8 kPa, n = 12). As noted previously,

compared to measures of unaffected myometrium stiffness in this work, Acar et al.'s [209] SWE measures of unaffected myometrium stiffness were significantly lower ($p<0.001$) and Zhang et al.'s [121] measures were significantly higher ($p\leq0.001$).

Initial concerns about the variability in SWE measures of unaffected myometrium across these three studies could be attributed to biological variability, however the high variance in the validity of endoprobe SWE could also be the source of these findings. Further, when considering Zhang et al. [121] and Acar et al.'s [209] measures of lesion stiffness, the impact of these pathologies on uterus volume and target depth must also be considered. The presence of adenomyosis and uterine fibroids may both substantially increase the volume of the uterus [300], which increases the depth of the targets. Knowing that the depth of target measurements in uteruses with no known pathology ranged up to 38.3 mm, concerns around validity become even more pronounced when considering SWE for adenomyosis and uterine fibroids. Zhang et al. [121] noted that "…larger and more globular uteri posed subjective technical challenges…particularly in the more deeply positioned posterior myometrium." Findings from this thesis (Section 6) indicate similar problems in healthy uteruses, but more importantly the ceiling on the rated depth for the SWE used in this thesis (Aixplorer, SuperSonic Imagine, Aix-en-Provence, France) is 3cm and SWE measures of phantom stiffness at 5cm were not valid. While the phantom sample in this thesis was reduced for the 5cm depth condition, at this point the combination of uterine enlargement that is expected with adenomyosis and/or uterine fibroids and the poor performance of SWE at 5cm depths may limit the clinical utility of gynecological SWE for these applications.

7.2.2 Quasi-static Flat-tip Indentation for SWE Validation

Considering the findings around mechanical testing, quasi-static flat-tip indentation was shown to be valid under a range of testing parameters, with a clear quantification of mean differences and variability in agreement with ramp compression, the criterion standard. Further, indentation testing

outcomes showed strong agreement with SWE outcomes under a variety of testing parameter. Optimal testing parameters were recommended to potentially enhance the strength of these relationships in fresh tissue testing. In a SWE validation study focused on applications in breast tumors, Lee et al. [71] observed significant moderate correlations between peak stiffness (kPa) measured by SWE (SL15-4 probe) and indentation ($r=0.530$, $p=0.003$), however no significant relationship was found in terms of mean ($r=0.163$, $p=0.390$) and minimum ($r=0.191$, $p=0.312$) stiffness. SWE mean, peak, and minimum values were measured spatially over the region of interest and the number of trials and/or frames was not indicated. Tissue samples were 5mm thick, the indenter diameter was 1.0mm or 2.4mm, testing rate was 0.001Hz, and the Oliver Pharr [109] model was applied at a strain equivalent to the tissue compression applied by the SWE probe in vivo ($\varepsilon = 10.9\% \pm 1.9\%$). The assumed value of Poisson's ratio was not given.

Correlations between phantom indentation and SWE outcomes obtained using a linear probe in this thesis (mean over the region of interest, median 10 frames, mean of 3 trials) were consistently very strong and highly significant. Compared to the methods applied in this thesis, Lee et al. [71] applied a loading rate below the slowest rate applied here, which most certainly would have satisfied the quasi-static assumption of the Oliver Pharr [109] model. Moreover, Lee et al. [71] matched the strains for modulus calculation to the in vivo loads applied during SWE imaging (range = [6.9%, 13.0%]). While the literature shows that this level of strain should not impact SWE outcomes in breast imaging [168], the findings in this thesis suggest that increasing the strain of modulus estimation did indeed decrease the quality of agreement between indentation and SWE. Further, Lee et al. [71] appeared to calculate an instantaneous modulus, whereas moduli in this thesis were always calculated over a strain range. Knowing the noise in the indentation signals observed in this study, which was similarly reported by Zhai et al. [172], an instantaneous estimate of strain may be less robust that the strain range method used here. Thus, standardization of in vivo SWE tissue compression that is in the low end of the stress-strain

curve (<10%), combined with the use of a strain range for calculating the elastic modulus may yield a more robust methodology resulting in improved agreement between SWE and indentation outcomes. However, the lower strength of the relationship between peak SWE stiffness and indentation reported by Lee et al. [71] may be due to the heterogeneity in the tissues or poor agreement between the in vivo tissue and the assumptions required for SWE. A more thorough quantitative analysis (i.e. Bland Altman analysis) and thorough presentation of Lee et al.'s [71] data set the would provide better insight into the quantitative nature of the agreement and possibly aid in directing the development of standardized testing methods moving forward.

7.3 Future Work

While findings from this thesis suggest caution in the application of this particular SWE system (Aixplorer, SuperSonic Imagine, Aix-en-Provence, France) for in-vivo uterine tissue research, the expected stiffness profiles for adenomyotic and fibroid uteruses are still not currently well documented. There may also be cases of more superficially localized adenomyosis, uterine fibroids or other uterine pathologies in which gynecological SWE could support treatment planning. Moreover, as SWE technology advances to meet the needs of diagnosis and treatment planning for uterine pathologies, data on the mechanical properties of pathological uterine tissue will be essential for establishing the in vivo validity of gynecological SWE, which will, in turn, support clinical uptake. Thus, the characterization of pathological uterine tissue ex vivo is an essential next step in establishing the feasibility of gynecological SWE. Further, this thesis provides the validation of indentation testing under a variety of parameters and the concurrent validation of SWE and indentation to support this work moving forward.

Different SWE measurement systems implement unique excitation sequences and incorporate additional features that may be more amenable to gynecological SWE. Thus, concerns around the validity of gynecological SWE observed in this thesis (Aixplorer, SuperSonic Imagine, Aix-en-Provence, France) may not translate to other systems. Future work should also aim to investigate the validity of

other SWE systems that apply unique excitation sequences to estimate the stiffness of gynecological tissues using homogeneous and heterogeneous phantoms. Looking forward, it is recommended that these future investigations include a wider range of target stiffnesses to better represent potential cases of highly stiff gynecological tissues [121], [209], which may require alternative phantom materials, such as those used by Cao et al. [81]. Further, future studies should aim to include adequately large sample sizes for characterizing SWE validity using TMM phantoms, while maintaining the thorough and quantitative nature of the statistical analysis provided here. Due to the decrease in SWE endoprobe validity metrics at each subsequent target depth and its relatively poor performance compared to the linear and curvilinear SWE probes, it is recommended that including target depths at 1cm intervals, rather than 2cm intervals, will provide a more thorough characterization of probe performance. Finally, knowing that the parameters for excitation sequences for endoprobe SWE (and any curved probe) are often automatically adjusted based on the azimuth of the region of interest with respect to the principal axis of the probe, SWE validation should be performed at a range of azimuth angles for each target depth.

7.4 Conclusion

This thesis aimed to establish the feasibility of endoprobe SWE for use as a diagnostic and treatment planning tool for uterine pathologies. In the process of doing so, suitable parameters for mechanical validation were investigated. Quasi-static flat tip indentation testing under a variety of parameters was demonstrated to be a suitable criterion standard for evaluating SWE performance. The findings from this thesis thatendoprobe SWE is currently most suitable for gynecological tissue target depths at or below 3cm depths, such as the cervix or superficial endometriosis lesions. Future work should aim to establish technological feasibility for deeper gynecological tissues (e.g. myometrium, fundus, uterine fibroids). At these superficial depths, the performance of endoprobe SWE was similar to

that of linear and curvilinear probes for the same imaging system. These findings suggest that gynecological elastography may have clinical value in superficial tissues, however further development is required to support its use in bulky uteruses and for deep targets that occur with uterine pathology.

Linear probe elastography has been in development since the late 1980s [138], [151], [328], yet it only became a recommended tool for staging liver fibrosis in Canada in 2018 [283], almost 30 years after the first publications on the modality [328]. Knowing that the development and research of gynecological elastography often lags behind more common applications, the performance data for gynecological elastography in superficial tissues is an impressive achievement at this stage of technological development. This thesis provides key contributions to the evidence that was provided for liver elastography prior to clinical adoption: a robust quantification of performance of a state-of-the-art SWE system and recommended tools for future validation efforts. Looking forward, as the technological capacity of endoprobe SWE advances to match the ambitious goals of the clinical researchers who aim to use it to improve the quality of care for gynecological pathologies, this work shows the limitations of the current technology, and of validation methods, and provides a roadmap to support clinical adoption in the future.

8 References

[1] A. Zimmermann, D. Bernuit, C. Gerlinger, M. Schaefers, and K. Geppert, “Prevalence, symptoms and management of uterine fibroids: an international internet-based survey of 21,746 women,” *BMC Womens Heal.*, vol. 12, p. 6, 2012.

[2] E. Downes *et al.*, “The burden of uterine fibroids in five European countries,” *Eur J Obs. Gynecol Reprod Biol*, vol. 152, no. 1, pp. 96–102, 2010.

[3] E. A. Pritts, W. H. Parker, and D. L. Olive, “Fibroids and infertility: an updated systematic review of the evidence,” *Fertil Steril*, vol. 91, no. 4, pp. 1215–1223, 2009.

[4] G. A. Vilos, C. Allaire, P. Y. Laberge, and N. Leyland, “The management of uterine leiomyomas,” *J Obs. Gynaecol Can*, vol. 37, no. 2, pp. 157–178, 2015.

[5] B. Eskenazi and M. L. Warner, “EPIDEMIOLOGY OF ENDOMETRIOSIS,” *Obstet. Gynecol. Clin. North Am.*, vol. 24, no. 2, pp. 235–258, Jun. 1997.

[6] T. Van den Bosch and D. Van Schoubroeck, “Ultrasound diagnosis of endometriosis and adenomyosis: State of the art,” *Best Pract. Res. Clin. Obstet. Gynaecol.*, vol. 51, pp. 16–24, Aug. 2018.

[7] C. Exacoustos, L. Manganaro, and E. Zupi, “Imaging for the evaluation of endometriosis and adenomyosis,” *Best Pract. Res. Clin. Obstet. Gynaecol.*, vol. 28, no. 5, pp. 655–681, Jul. 2014.

[8] S. F. Cramer and A. Patel, “The frequency of uterine leiomyomas,” *Am J Clin Pathol*, vol. 94, no. 4, pp. 435–438, 1990.

[9] D. D. Baird, D. B. Dunson, M. C. Hill, D. Cousins, and J. M. Schectman, “High cumulative incidence of uterine leiomyoma in black and white women: ultrasound evidence,” *Am J Obs. Gynecol*, vol. 188, no. 1, pp. 100–107, 2003.

[10] L. M. Marshall *et al.*, “Variation in the incidence of uterine leiomyoma among premenopausal women by age and race,” *Obs. Gynecol*, vol. 90, no. 6, pp. 967–973, 1997.

[11] V. C. Buttram Jr. and R. C. Reiter, “Uterine leiomyomata: etiology, symptomatology, and management,” *Fertil Steril*, vol. 36, no. 4, pp. 433–445, 1981.

[12] P. Y. Laberge, G. A. Vilos, A. G. Vilos, and P. M. Janiszewski, “Burden of symptomatic uterine fibroids in Canadian women: a cohort study,” *Curr Med Res Opin*, vol. 32, no. 1, pp. 165–175, 2016.

[13] P. Vercellini, P. Viganò, E. Somigliana, R. Daguati, A. Abbiati, and L. Fedele, “Adenomyosis: epidemiological factors,” *Best Pract. Res. Clin. Obstet. Gynaecol.*, vol. 20, no. 4, pp. 465–477, Aug. 2006.

[14] J. Naftalin, W. Hoo, K. Pateman, D. Mavrelos, T. Holland, and D. Jurkovic, “How common is adenomyosis? A prospective study of prevalence using transvaginal ultrasound in a gynaecology clinic,” *Hum. Reprod.*, vol. 27, no. 12, pp. 3432–3439, Dec. 2012.

[15] A. Ferenczy, “Pathophysiology of adenomyosis,” *Hum. Reprod. Update*, vol. 4, no. 4, pp. 312–322, 1998.

[16] J. Donnez and M. M. Dolmans, “Uterine fibroid management: from the present to the future,” *Hum Reprod Updat.*, vol. 22, no. 6, pp. 665–686, 2016.

[17] S. S. Singh and L. Belland, “Contemporary management of uterine fibroids: focus on emerging medical treatments,” *Curr Med Res Opin*, vol. 31, no. 1, pp. 1–12, 2015.

[18] E. A. Stewart, “Uterine fibroids,” *Lancet*, vol. 357, no. 9252, pp. 293–298, 2001.

[19] N. Chabbert-Buffet, A. Pintiaux-Kairis, and P. Bouchard, “Effects of the progesterone receptor modulator VA2914 in a continuous low dose on the hypothalamic-pituitary-ovarian axis and endometrium in normal women: a prospective, randomized, placebo-controlled trial.,” *J. Clin. Endocrinol. Metab.*, vol. 92, no. 9, pp. 3582–3589, Sep. 2007.

[20] K. S. Gurusamy, J. Vaughan, I. S. Fraser, L. M. Best, and T. Richards, “Medical Therapies for

Uterine Fibroids - A Systematic Review and Network Meta-Analysis of Randomised Controlled Trials," *PLoS One*, vol. 11, no. 2, p. e0149631, 2016.
[21] A. T. Khan, M. Shehmar, and J. K. Gupta, "Uterine fibroids: current perspectives," *Int J Womens Heal.*, vol. 6, pp. 95–114, Jan. 2014.
[22] J. Donnez *et al.*, "Ulipristal acetate versus placebo for fibroid treatment before surgery," *N Engl J Med*, vol. 366, no. 5, pp. 409–420, 2012.
[23] M. J. Lee *et al.*, "Uterine fibroid shrinkage after short-term use of selective progesterone receptor modulator or gonadotropin-releasing hormone agonist," *Obs. Gynecol Sci*, vol. 60, no. 1, pp. 69–73, 2017.
[24] N. Chabbert-Buffet, N. Esber, and P. Bouchard, "Fibroid growth and medical options for treatment," *Fertil Steril*, vol. 102, no. 3, pp. 630–639, 2014.
[25] S. Guerriero *et al.*, "Transvaginal ultrasound vs magnetic resonance imaging for diagnosing deep infiltrating endometriosis: systematic review and meta-analysis," *Ultrasound Obstet. Gynecol.*, vol. 51, no. 5, pp. 586–595, May 2018.
[26] A. Z. Cockerham, "Adenomyosis: A Challenge in Clinical Gynecology," *J. Midwifery Womens. Health*, vol. 57, no. 3, pp. 212–220, May 2012.
[27] R. J. DeWall, T. Varghese, and C. L. Brace, "Quantifying local stiffness variations in radiofrequency ablations with dynamic indentation," *IEEE Trans. Biomed. Eng.*, vol. 59, no. 3, pp. 728–735, 2012.
[28] E. C. Bass, N. A. Duncan, J. S. Hariharan, J. Dusick, H. U. Bueff, and J. C. Lotz, "Frozen storage affects the compressive creep behavior of the porcine intervertebral disc," *Spine (Phila Pa 1976)*, vol. 22, no. 24, pp. 2867–2876, 1997.
[29] J. Bercoff *et al.*, "In vivo breast tumor detection using transient elastography," *Ultrasound Med Biol*, vol. 29, no. 10, pp. 1387–1396, 2003.
[30] P. Clavert, J. F. Kempf, F. Bonnomet, P. Boutemy, L. Marcelin, and J. L. Kahn, "Effects of freezing/thawing on the biomechanical properties of human tendons," *Surg Radiol Anat*, vol. 23, no. 4, pp. 259–262, 2001.
[31] M. Muller *et al.*, "Assessment of the Cervix in Pregnant Women Using Shear Wave Elastography: A Feasibility Study," *Ultrasound Med Biol*, vol. 41, no. 11, pp. 2789–2797, 2015.
[32] R. J. Andrade *et al.*, "Non-invasive assessment of sciatic nerve stiffness during human ankle motion using ultrasound shear wave elastography," *J Biomech*, vol. 49, no. 3, pp. 326–331, 2016.
[33] T. A. Krouskop, T. M. Wheeler, F. Kallel, B. S. Garra, and T. Hall, "Elastic moduli of breast and prostate tissues under compression," *Ultrason Imaging*, vol. 20, no. 4, pp. 260–274, 1998.
[34] L. Peralta *et al.*, "In Vivo Evaluation of Cervical Stiffness Evolution during Induced Ripening Using Shear Wave Elastography, Histology and 2 Photon Excitation Microscopy: Insight from an Animal Model," *PLoS One*, vol. 10, no. 8, p. e0133377, 2015.
[35] E. Mazza, A. Nava, D. Hahnloser, W. Jochum, and M. Bajka, "The mechanical response of human liver and its relation to histology: an in vivo study," *Med Image Anal*, vol. 11, no. 6, pp. 663–672, 2007.
[36] Y. C. Fung, *Biomechanics: Mechanical Properties of Living Tissues*, 2nd ed. New York, NY, USA: Springer-Verlag.
[37] B. Stoelinga, W. J. Hehenkamp, H. A. Brolmann, and J. A. Huirne, "Real-time elastography for assessment of uterine disorders," *Ultrasound Obs. Gynecol*, vol. 43, no. 2, pp. 218–226, 2014.
[38] S. Acar, E. Millar, M. Mitkova, and V. Mitkov, "Value of ultrasound shear wave elastography in the diagnosis of adenomyosis," *Ultrasound*, vol. 24, no. 4, pp. 205–213, 2016.
[39] M. L. Frank *et al.*, "Importance of Transvaginal Elastography in the Diagnosis of Uterine Fibroids and Adenomyosis," *Ultraschall Med*, vol. 37, no. 4, pp. 373–378, 2016.
[40] G. Szabó, I. Madár, A. Bokor, and J. Rigó, "Transvaginal Strain Elastosonography May Help in the Differential Diagnosis of Endometriosis?," *Diagnostics*, vol. 11, no. 1, p. 100, Jan. 2021.

[41] D. Larsson, “Accuracy Assessment of Shear Wave Elastography fro Arterial Applications by Mechanical Testing,” KTH Royal Institute of Technology, Stockholm, Sweden, 2014.
[42] L. Zhai, M. L. Palmeri, R. R. Bouchard, R. W. Nightingale, and K. R. Nightingale, “An integrated indenter-ARFI imaging system for tissue stiffness quantification,” *Ultrason Imaging*, vol. 30, no. 2, pp. 95–111, 2008.
[43] T. Varghese, “Ultrasound Elastography,” in *Advances in Medical Physics: 2010*, vol. 3, A. B. Wolbarst, A. Karellas, E. A. Krupinski, and W. R. Hendee, Eds. Madison, WI, USA: Medical Physics Publishing, pp. 37–54.
[44] A. Zorgani, “Passive Elastography: Tomography and Mechanical Characterization of Biological Tissue,” Universite de Lyon, Lyon, France, 2016.
[45] L. Gao, K. J. Parker, R. M. Lerner, and S. F. Levinson, “Imaging of the elastic properties of tissue--a review,” *Ultrasound Med Biol*, vol. 22, no. 8, pp. 959–977, 1996.
[46] M. Fatemi and J. F. Greenleaf, “Imaging the Viscoelastic Properties of Tissue,” in *Topics in Applied Physics: Imaging of Complex Media with Acoustic and Seismic Waves*, vol. 84, M. Fink, W. A. Kuperman, J. P. Montagner, and A. Tourin, Eds. Berlin, Heidelberg, Germany: Springer, pp. 257–276.
[47] J. Bamber *et al.*, “EFSUMB guidelines and recommendations on the clinical use of ultrasound elastography. Part 1: Basic principles and technology,” *Ultraschall Med*, vol. 34, no. 2, pp. 169–184, 2013.
[48] P. Czuczwar, S. Wozniak, P. Szkodziak, M. J. Kudla, K. Pyra, and T. Paszkowski, “Elastography Improves the Diagnostic Accuracy of Sonography in Differentiating Endometrial Polyps and Submucosal Fibroids,” *J Ultrasound Med*, vol. 35, no. 11, pp. 2389–2395, 2016.
[49] P. Krzysztof, Z. Katarzyna, S. F. Malgorzata, W. Dariusz, and K. Juliusz, “The role of elastography in the differential diagnosis of endometrial pathologies, preliminary,” *Ginekol. Pol.*, vol. 82, no. 7, pp. 494–497, 2011.
[50] M. Frank *et al.*, “Importance of Transvaginal Elastography in the Diagnosis of Uterine Fibroids and Adenomyosis,” *Ultraschall der Medizin - Eur. J. Ultrasound*, vol. 37, no. 04, pp. 373–378, Aug. 2015.
[51] B. Stoelinga, W. J. Hehenkamp, H. A. Brolmann, and J. A. Huirne, “Real-time elastography for assessment of uterine disorders,” *Ultrasound Obs. Gynecol*, vol. 43, no. 2, pp. 218–226, 2014.
[52] O. Ami *et al.*, “Real-time transvaginal elastosonography of uterine fibroids,” *Ultrasound Obs. Gynecol*, vol. 34, no. 4, pp. 486–488, 2009.
[53] M. R. Metin *et al.*, “Differentiation between endometrial carcinoma and atypical endometrial hyperplasia with transvaginal sonographic elastography,” *Diagn. Interv. Imaging*, vol. 97, no. 4, pp. 425–431, 2016.
[54] M. Z. Kiss *et al.*, “Frequency-dependent complex modulus of the uterus: preliminary results,” *Phys. Med. Biol.*, vol. 51, no. 15, pp. 3683–3695, 2006.
[55] E. A. Omari, T. Varghese, M. A. Kliewer, J. Harter, and E. M. Hartenbach, “Dynamic and quasi-static mechanical testing for characterization of the viscoelastic properties of human uterine tissue,” *J Biomech*, vol. 48, no. 10, pp. 1730–1736, 2015.
[56] M. A. Hobson *et al.*, “In vitro uterine strain imaging: preliminary results,” *J Ultrasound Med*, vol. 26, no. 7, pp. 899–908, 2007.
[57] L. N. Su, S. L. Guo, B. X. Li, and P. Yang, “Diagnostic value of magnetic resonance elastography for detecting and staging of hepatic fibrosis: a meta-analysis,” *Clin Radiol*, vol. 69, no. 12, pp. e545-52, 2014.
[58] L. Castera, X. Forns, and A. Alberti, “Non-invasive evaluation of liver fibrosis using transient elastography,” *J Hepatol*, vol. 48, no. 5, pp. 835–847, 2008.
[59] S. Ichikawa *et al.*, “Comparison of the diagnostic accuracies of magnetic resonance elastography

and transient elastography for hepatic fibrosis," *Magn. Reson. Imaging*, vol. 33, no. 1, pp. 26–30, 2015.
[60] M. Friedrich-Rust *et al.*, "Performance of transient elastography for the staging of liver fibrosis: a meta-analysis," *Gastroenterology*, vol. 134, no. 4, pp. 960–974, 2008.
[61] A. Guibal *et al.*, "Shear wave elastography: An accurate technique to stage liver fibrosis in chronic liver diseases," *Diagn Interv Imaging*, vol. 97, no. 1, pp. 91–99, 2016.
[62] I. Sporea *et al.*, "Acoustic radiation force impulse and supersonic shear imaging versus transient elastography for liver fibrosis assessment," *Ultrasound Med. Biol.*, vol. 39, no. 11, pp. 1933–1941, 2013.
[63] B. S. Garra *et al.*, "Elastography of breast lesions: initial clinical results," *Radiology*, vol. 202, no. 1, pp. 79–86, 1997.
[64] J. Bercoff *et al.*, "In vivo breast tumor detection using transient elastography," *Ultrasound Med Biol*, vol. 29, no. 10, pp. 1387–1396, 2003.
[65] A. Thomas *et al.*, "Real-time elastography - An advanced method of ultrasound: First results in 108 patients with breast lesions," *Ultrasound Obstet. Gynecol.*, vol. 28, no. 3, pp. 335–340, 2006.
[66] N. Cho, K. M. Woo, S. P. Jeong, H. C. Joo, M. Jang, and H. S. Min, "Nonpalpable breast masses: Evaluation by US elastography," *Korean J. Radiol.*, vol. 9, no. 2, pp. 111–118, 2008.
[67] W. A. Berg *et al.*, "Shear-wave elastography improves the specificity of breast US: the BE1 multinational study of 939 masses," *Radiology*, vol. 262, no. 2, pp. 435–449, 2012.
[68] J. M. Chang *et al.*, "Clinical application of shear wave elastography (SWE) in the diagnosis of benign and malignant breast diseases," *Breast Cancer Res. Treat.*, vol. 129, no. 1, pp. 89–97, 2011.
[69] A. Evans *et al.*, "Differentiating benign from malignant solid breast masses: value of shear wave elastography according to lesion stiffness combined with greyscale ultrasound according to BI-RADS classification," *Br J Cancer*, vol. 107, no. 2, pp. 224–229, 2012.
[70] A. Athanasiou *et al.*, "Breast Lesions: Quantitative Elastography with Supersonic Shear Imaging—Preliminary Results," *Radiology*, vol. 256, no. 1, pp. 297–303, Jul. 2010.
[71] S. H. Lee *et al.*, "Shear-wave elastographic features of breast cancers: comparison with mechanical elasticity and histopathologic characteristics," *Invest Radiol*, vol. 49, no. 3, pp. 147–155, 2014.
[72] C. Amador, M. W. Urban, S. Chen, Q. Chen, K. N. An, and J. F. Greenleaf, "Shear elastic modulus estimation from indentation and SDUV on gelatin phantoms," *IEEE Trans Biomed Eng*, vol. 58, no. 6, pp. 1706–1714, 2011.
[73] H. J. Shin, M.-J. Kim, H. Y. Kim, Y. H. Roh, and M.-J. Lee, "Comparison of shear wave velocities on ultrasound elastography between different machines, transducers, and acquisition depths: a phantom study.," *Eur. Radiol.*, vol. 26, no. 10, pp. 3361–3367, Oct. 2016.
[74] J. R. Dillman *et al.*, "Superficial ultrasound shear wave speed measurements in soft and hard elasticity phantoms: repeatability and reproducibility using two ultrasound systems," *Pediatr. Radiol.*, vol. 45, no. 3, pp. 376–385, Mar. 2015.
[75] S. Franchi-Abella, C. Elie, and J.-M. Correas, "Performances and Limitations of Several Ultrasound-Based Elastography Techniques: A Phantom Study," *Ultrasound Med. Biol.*, vol. 43, no. 10, pp. 2402–2415, Oct. 2017.
[76] C. H. Suh *et al.*, "Determination of normal hepatic elasticity by using real-time shear-wave elastography," *Radiology*, vol. 271, no. 3, pp. 895–900, 2014.
[77] C. H. Suh, H. M. Yoon, S. C. Jung, and Y. J. Choi, "Accuracy and precision of ultrasound shear wave elasticity measurements according to target elasticity and acquisition depth: A phantom study," *PLoS One*, vol. 14, no. 7, p. e0219621, Jul. 2019.
[78] J. Hwang, H. M. Yoon, A. Y. Jung, J. S. Lee, and Y. A. Cho, "Comparison of 2-Dimensional Shear

Wave Elastographic Measurements Using ElastQ Imaging and SuperSonic Shear Imaging: Phantom Study and Clinical Pilot Study," *J Ultrasound Med*, 2019.
[79] C. Pellot-Barakat, L. Chami, J. M. Correas, M. Lefort, and O. Lucidarme, "Does motion affect liver stiffness estimates in shear wave elastography? Phantom and clinical study," *Eur. J. Radiol.*, vol. 85, no. 9, pp. 1645–1650, Sep. 2016.
[80] M. Palmeri *et al.*, "RSNA QIBA ultrasound shear wave speed Phase II phantom study in viscoelastic media," in *2015 IEEE International Ultrasonics Symposium (IUS)*, 2015, pp. 1–4.
[81] R. Cao, Z. Huang, T. Varghese, and G. Nabi, "Tissue mimicking materials for the detection of prostate cancer using shear wave elastography: a validation study.," *Med. Phys.*, vol. 40, no. 2, p. 22903, Feb. 2013.
[82] E. L. Madsen, M. A. Hobson, H. Shi, T. Varghese, and G. R. Frank, "Stability of heterogeneous elastography phantoms made from oil dispersions in aqueous gels," *Ultrasound Med Biol*, vol. 32, no. 2, pp. 261–270, 2006.
[83] E. L. Madsen, M. A. Hobson, H. Shi, T. Varghese, and G. R. Frank, "Tissue-mimicking agar/gelatin materials for use in heterogeneous elastography phantoms," *Phys Med Biol*, vol. 50, no. 23, pp. 5597–5618, 2005.
[84] E. L. Madsen, G. R. Frank, T. A. Krouskop, T. Varghese, F. Kallel, and J. Ophir, "Tissue-Mimicking Oil-in-Gelatin Dispersions for Use in Heterogeneous Elastography Phantoms," *Ultrason. Imaging*, vol. 25, no. 1, pp. 17–38, Jan. 2003.
[85] M. A. Hobson *et al.*, "Anthropomorphic Phantoms for Assessment of Strain Imaging Methods Involving Saline-Infused Sonohysterography," *Ultrasound Med. Biol.*, vol. 34, no. 10, pp. 1622–1637, Oct. 2008.
[86] T. J. Hall, M. Bilgen, M. F. Insana, and T. A. Krouskop, "Phantom Materials for Elastography," *IEEE Trans. Ultrason. Ferroelectr. Freq. Control*, vol. 44, no. 6, p. 11, 1997.
[87] Y. Cao, G.-Y. Li, X. Zhang, and Y.-L. Lui, "Tissue-mimicking materials for elastography phantoms: A review," *Extrem. Mech. Lett.*, vol. 17, p. 9, 2017.
[88] R. M. Delaine-Smith, S. Burney, F. R. Balkwill, and M. M. Knight, "Experimental validation of a flat punch indentation methodology calibrated against unconfined compression tests for determination of soft tissue biomechanics," *J. Mech. Behav. Biomed. Mater.*, vol. 60, pp. 401–415, Jul. 2016.
[89] E. A. A. Omari, T. Varghese, M. A. A. Kliewer, J. Harter, and E. M. M. Hartenbach, "Dynamic and quasi-static mechanical testing for characterization of the viscoelastic properties of human uterine tissue," *J Biomech*, vol. 48, no. 10, pp. 1730–1736, 2015.
[90] T. P. Prevost, G. Jin, M. A. de Moya, H. B. Alam, S. Suresh, and S. Socrate, "Dynamic mechanical response of brain tissue in indentation in vivo, in situ and in vitro," *Acta Biomater*, vol. 7, no. 12, pp. 4090–4101, 2011.
[91] A. Samani and D. Plewes, "A method to measure the hyperelastic parameters of ex vivo breast tissue samples.," *Phys. Med. Biol.*, vol. 49, no. 18, pp. 4395–4405, Sep. 2004.
[92] O. R. Boughton *et al.*, "Measuring bone stiffness using spherical indentation," *PLoS One*, vol. 13, no. 7, p. 18, 2018.
[93] C. T. McKee, J. A. Last, P. Russell, and C. J. Murphy, "Indentation Versus Tensile Measurements of Young's Modulus for Soft Biological Tissues," *Tissue Eng. Part B Rev.*, vol. 17, no. 3, pp. 155–164, Jun. 2011.
[94] W. Yao *et al.*, "Measuring the compressive viscoelastic mechanical properties of human cervical tissue using indentation," *J Mech Behav Biomed Mater*, vol. 34, pp. 18–26, 2014.
[95] J. Oudry, T. Lynch, J. Vappou, L. Sandrin, and V. Miette, "Comparison of four different techniques to evaluate the elastic properties of phantom in elastography: is there a gold standard?," *Phys. Med. Biol.*, vol. 59, no. 19, pp. 5775–5793, Oct. 2014.

[96] P. Czuczwar, S. Wozniak, P. Szkodziak, M. J. Kudla, K. Pyra, and T. Paszkowski, “Elastography Improves the Diagnostic Accuracy of Sonography in Differentiating Endometrial Polyps and Submucosal Fibroids,” *J Ultrasound Med*, vol. 35, no. 11, pp. 2389–2395, 2016.
[97] D. E. Jondal *et al.*, “Uterine fibroids: correlations between MRI appearance and stiffness via magnetic resonance elastography,” *Abdom Radiol (NY)*, vol. 43, no. 6, pp. 1456–1463, 2018.
[98] E. Nieuwold, N. Green, N. Hills, and L. McLean, “Reliability and Concurrent Validity of Inter-Rectus Distance and Linea Alba Stiffness in Women with and without Diastasis Recti Abdominis,” *Physiotherapy Congress, Montreal18*. Canadian Physiotherapy Association, Montreal, Canada, p. 100.
[99] L. Lacourpaille, F. Hug, K. Bouillard, J. Y. Hogrel, and A. Nordez, “Supersonic shear imaging provides a reliable measurement of resting muscle shear elastic modulus,” *Physiol Meas*, vol. 33, no. 3, pp. N19-28, 2012.
[100] H. Woo, J. Y. Lee, J. H. Yoon, W. Kim, B. Cho, and B. I. Choi, “Comparison of the Reliability of Acoustic Radiation Force Impulse Imaging and Supersonic Shear Imaging in Measurement of Liver Stiffness,” *Radiology*, vol. 277, no. 3, pp. 881–886, 2015.
[101] J. M. Hudson, L. Milot, C. Parry, R. Williams, and P. N. Burns, “Inter- and intra-operator reliability and repeatability of shear wave elastography in the liver: a study in healthy volunteers,” *Ultrasound Med Biol*, vol. 39, no. 6, pp. 950–955, 2013.
[102] D. O. Cosgrove *et al.*, “Shear wave elastography for breast masses is highly reproducible,” *Eur Radiol*, vol. 22, no. 5, pp. 1023–1032, 2012.
[103] H. S. Mun, S. H. Choi, S. H. Kook, Y. Choi, W. K. Jeong, and Y. Kim, “Validation of intra- and interobserver reproducibility of shearwave elastography: Phantom study,” *Ultrasonics*, vol. 53, no. 5, pp. 1039–1043, 2013.
[104] T. K. Koo, J. Y. Guo, J. H. Cohen, and K. J. Parker, “Relationship between shear elastic modulus and passive muscle force: an ex-vivo study,” *J Biomech*, vol. 46, no. 12, pp. 2053–2059, 2013.
[105] D. V Cicchetti, “Guidelines, criteria, and rules of thumb for evaluating normed and standardized assessment instruments in psychology,” *Psychol. Assess.*, vol. 6, no. 4, pp. 284–290, 1994.
[106] R. J. DeWall, T. Varghese, and C. L. Brace, “Quantifying local stiffness variations in radiofrequency ablations with dynamic indentation,” *IEEE Trans. Biomed. Eng.*, vol. 59, no. 3, pp. 728–735, 2012.
[107] A. M. Alfuraih, P. O’Connor, E. Hensor, A. L. Tan, P. Emery, and R. J. Wakefield, “The effect of unit, depth, and probe load on the reliability of muscle shear wave elastography: Variables affecting reliability of SWE.,” *J. Clin. Ultrasound*, vol. 46, no. 2, pp. 108–115, Feb. 2018.
[108] “Aixplorer MultiWave User’s Guide,” vol. SSIP01154. SuperSonic Imagine S.A., Aix-en-provence, France, pp. 330–332, 2017.
[109] W. C. Oliver and G. M. Pharr, “An improved technique for determining hardness and elastic modulus using load and displacement sensing indentation experiments,” *J. Mater. Res.*, vol. 7, no. 6, pp. 1564–1583, Jun. 1992.
[110] I. N. Sneddon, “The relation between load and penetration in the axisymmetric boussinesq problem for a punch of arbitrary profile,” *Int. J. Eng. Sci.*, vol. 3, no. 1, pp. 47–57, May 1965.
[111] M. Zhang, Y. P. Zheng, and A. F. T. Mak, “Estimating the effective Young’s modulus of soft tissues from indentation tests—nonlinear finite element analysis of effects of friction and large deformation,” *Med. Eng. Phys.*, vol. 19, no. 6, pp. 512–517, Sep. 1997.
[112] W. C. Hayes, L. M. Keer, G. Herrmann, and L. F. Mockros, “A mathematical analysis for indentation tests of articular cartilage,” *J Biomech*, vol. 5, no. 5, pp. 541–551, 1972.
[113] T. A. Krouskop, T. M. Wheeler, F. Kallel, B. S. Garra, and T. Hall, “Elastic moduli of breast and prostate tissues under compression,” *Ultrason Imaging*, vol. 20, no. 4, pp. 260–274, 1998.
[114] S. Timoshenko and J. N. Goodier, *Theory of elasticity*. New York, NY, USA: McGraw-Hill, 1971.
[115] J. Bercoff, M. Tanter, and M. Fink, “Supersonic shear imaging: a new technique for soft tissue

elasticity mapping," *IEEE Trans Ultrason Ferroelectr Freq Control*, vol. 51, no. 4, pp. 396–409, 2004.
[116] K. Englund, B. Lindblom, K. Carlstrom, I. Gustavsson, P. Sjoblom, and A. Blanck, "Gene expression and tissue concentrations of IGF-I in human myometrium and fibroids under different hormonal conditions," *Mol Hum Reprod*, vol. 6, no. 10, pp. 915–920, 2000.
[117] M. R. Soules and K. S. McCarty Jr., "Leiomyomas: steroid receptor content. Variation within normal menstrual cycles," *Am J Obs. Gynecol*, vol. 143, no. 1, pp. 6–11, 1982.
[118] D. Dixon *et al.*, "Cell proliferation and apoptosis in human uterine leiomyomas and myometria," *Virchows Arch*, vol. 441, no. 1, pp. 53–62, 2002.
[119] K. Kawaguchi, S. Fujii, I. Konishi, Y. Nanbu, H. Nonogaki, and T. Mori, "Mitotic activity in uterine leiomyomas during the menstrual cycle," *Am J Obs. Gynecol*, vol. 160, no. 3, pp. 637–641, 1989.
[120] E. Hernandez-Andrade *et al.*, "Effect of depth on shear-wave elastography estimated in the internal and external cervical os during pregnancy," *J Perinat Med*, vol. 42, no. 5, pp. 549–557, 2014.
[121] M. Zhang *et al.*, "Transvaginal Ultrasound Shear Wave Elastography for the Evaluation of Benign Uterine Pathologies: A Prospective Pilot Study," *J. Ultrasound Med.*, vol. 38, no. 1, pp. 149–155, Jan. 2019.
[122] W. F. Bynum, *Companion Encyclopedia of the History of Medicine*. Routledge, 2013.
[123] G. H. Cantuaria, R. Angioli, L. Frost, R. Duncan, and M. A. Penalver, "Comparison of bimanual examination with ultrasound examination before hysterectomy for uterine leiomyoma," *Obs. Gynecol*, vol. 92, no. 1, pp. 109–112, 1998.
[124] E. Strobel, P. Sladkevicius, L. Rovas, F. De Smet, E. D. Karlsson, and L. Valentin, "Bishop score and ultrasound assessment of the cervix for prediction of time to onset of labor and time to delivery in prolonged pregnancy," *Ultrasound Obstet. Gynecol.*, vol. 28, no. 3, pp. 298–305, Sep. 2006.
[125] S. K. Laughon, J. Zhang, J. Troendle, L. Sun, and U. M. Reddy, "Using a Simplified Bishop Score to Predict Vaginal Delivery," *Obstet. Gynecol.*, vol. 117, no. 4, pp. 805–811, Apr. 2011.
[126] K. Hancke, V. Heilmann, P. Straka, R. Kreienberg, and C. Kurzeder, "Pretreatment Staging of Cervical Cancer: Is Imaging Better Than Palpation?," *Ann. Surg. Oncol.*, vol. 15, no. 10, pp. 2856–2861, Oct. 2008.
[127] Y. C. Fung, *Biomechanics: Mechanical Properties of Living Tissues*, 2nd ed. New York, NY, USA: Springer-Verlag, 1993.
[128] H. M. Curtiss, J. T. Finnoff, E. Peck, J. Hollman, J. Muir, and J. Smith, "Accuracy of Ultrasound-Guided and Palpation-Guided Knee Injections By an Experienced and Less-Experienced Injector Using a Superolateral Approach: A Cadaveric Study," *PM&R*, vol. 3, no. 6, pp. 507–515, Jun. 2011.
[129] C. Myburgh, H. H. Lauridsen, A. H. Larsen, and J. Hartvigsen, "Standardized manual palpation of myofascial trigger points in relation to neck/shoulder pain; the influence of clinical experience on inter-examiner reproducibility," *Man. Ther.*, vol. 16, no. 2, pp. 136–140, Apr. 2011.
[130] H.-L. Anders *et al.*, "Standardized simulated palpation training – Development of a Palpation Trainer and assessment of palpatory skills in experienced and inexperienced clinicians," *Man. Ther.*, vol. 15, no. 3, pp. 254–260, Jun. 2010.
[131] E. . Billis, N. . Foster, and C. . Wright, "Reproducibility and repeatability: errors of three groups of physiotherapists in locating spinal levels by palpation," *Man. Ther.*, vol. 8, no. 4, pp. 223–232, Nov. 2003.
[132] S. Brearley, C. P. Shearman, and M. H. Simms, "Peripheral pulse palpation: an unreliable physical sign," *Ann. R. Coll. Surg. Engl.*, vol. 74, no. 3, pp. 169–171, May 1992.
[133] W. G. Kernohan, G. E. Nugent, P. E. Haugh, B. P. Trainor, and R. A. Mollan, "Sensitivity of manual palpation in testing the neonatal hip.," *Clin. Orthop. Relat. Res.*, no. 294, pp. 211–215, Sep. 1993.
[134] H. A. Arango, M. S. Hoffman, W. S. Roberts, S. L. DeCesare, J. V Fiorica, and J. Drake, "Accuracy of

lymph node palpation to determine need for lymphadenectomy in gynecologic malignancies.," *Obstet. Gynecol.*, vol. 95, no. 4, pp. 553–556, Apr. 2000.
[135] P. P. Arrabal and D. A. Nagey, "Is manual palpation of uterine contractions accurate?," *Am. J. Obstet. Gynecol.*, vol. 174, no. 1, pp. 217–219, Jan. 1996.
[136] T. Shiina *et al.*, "WFUMB guidelines and recommendations for clinical use of ultrasound elastography: Part 1: basic principles and terminology," *Ultrasound Med Biol*, vol. 41, no. 5, pp. 1126–1147, 2015.
[137] J. E. Brandenburg *et al.*, "Ultrasound elastography: the new frontier in direct measurement of muscle stiffness," *Arch Phys Med Rehabil*, vol. 95, no. 11, pp. 2207–2219, 2014.
[138] J. Ophir, I. Céspedes, H. Ponnekanti, Y. Yazdi, and X. Li, "Elastography: A Quantitative Method for Imaging the Elasticity of Biological Tissues," *Ultrason. Imaging*, vol. 13, no. 2, pp. 111–134, 1991.
[139] R. Muthupillai, D. J. Lomas, P. J. Rossman, J. F. Greenleaf, A. Manduca, and R. L. Ehman, "Magnetic resonance elastography by direct visualization of propagating acoustic strain waves.," *Science*, vol. 269, no. 5232, pp. 1854–1857, Sep. 1995.
[140] J. Schmitt, "OCT elastography: imaging microscopic deformation and strain of tissue.," *Opt. Express*, vol. 3, no. 6, pp. 199–211, Sep. 1998.
[141] A. J. Fredman, J. L. Frolik, and B. S. Garra, "Lung strain profiles using computed tomography elastography.," *Conf. Proc. ... Annu. Int. Conf. IEEE Eng. Med. Biol. Soc. IEEE Eng. Med. Biol. Soc. Annu. Conf.*, vol. 2, pp. 1545–1548, 2004.
[142] I. B. Gultekin *et al.*, "Elastosonographic evaluation of patients with a sonographic finding of thickened endometrium," *Eur J Obs. Gynecol Reprod Biol*, vol. 198, pp. 105–109, 2016.
[143] M. L. Frank *et al.*, "Importance of Transvaginal Elastography in the Diagnosis of Uterine Fibroids and Adenomyosis," *Ultraschall Med*, vol. 37, no. 4, pp. 373–378, 2016.
[144] A. P. Sarvazyan, O. V Rudenko, S. D. Swanson, J. B. Fowlkes, and S. Y. Emelianov, "Shear wave elasticity imaging: a new ultrasonic technology of medical diagnostics.," *Ultrasound Med. Biol.*, vol. 24, no. 9, pp. 1419–1435, Nov. 1998.
[145] A. Sarvazyan, "Mechanical imaging: A new technology for medical diagnostics," *Int. J. Med. Inform.*, vol. 49, no. 2, pp. 195–216, Apr. 1998.
[146] R. P. Vito and S. A. Dixon, "Blood Vessel Constitutive Models—1995–2002," *Annu. Rev. Biomed. Eng.*, vol. 5, no. 1, pp. 413–439, Aug. 2003.
[147] M. O'Donnell, A. R. Skovoroda, B. M. Shapo, and S. Y. Emelianov, "Internal displacement and strain imaging using ultrasonic speckle tracking," *IEEE Trans. Ultrason. Ferroelectr. Freq. Control*, vol. 41, no. 3, pp. 314–325, 1994.
[148] T. J. Hall, Y. Zhu, and C. S. Spalding, "In vivo real-time freehand palpation imaging.," *Ultrasound Med. Biol.*, vol. 29, no. 3, pp. 427–435, Mar. 2003.
[149] A. Pesavento, A. Lorenz, S. Siebers, and H. Ermert, "New real-time strain imaging concepts using diagnostic ultrasound.," *Phys. Med. Biol.*, vol. 45, no. 6, pp. 1423–1435, Jun. 2000.
[150] E. Turgay, S. Salcudean, and R. Rohling, "Identifying the mechanical properties of tissue by ultrasound strain imaging.," *Ultrasound Med. Biol.*, vol. 32, no. 2, pp. 221–235, Feb. 2006.
[151] K. J. Parker, S. R. Huang, R. A. Musulin, and R. M. Lerner, "Tissue response to mechanical vibrations for 'sonoelasticity imaging,'" *Ultrasound Med. Biol.*, vol. 16, pp. 241–246, 1990.
[152] M. Fatemi and J. F. Greenleaf, "Probing the dynamics of tissue at low frequencies with the radiation force of ultrasound," *Phys. Med. Biol.*, vol. 45, pp. 1449–1464, 2000.
[153] T. Sugimoto, S. Ueha, and K. Itoh, "Tissue Hardness Measurement Using Ultrasonic Radiation Force –Theoretical Derivation of Tissue Hardness from the Relaxation Curve–," *Jpn. J. Appl. Phys.*, vol. 31, no. S1, p. 166, 1992.
[154] K. Nightingale, S. McAleavey, and G. Trahey, "Shear-wave generation using acoustic radiation force: in vivo and ex vivo results.," *Ultrasound Med. Biol.*, vol. 29, no. 12, pp. 1715–1723, Dec.

2003.
[155] L. Sandrin *et al.*, “Transient elastography: a new noninvasive method for assessment of hepatic fibrosis.,” *Ultrasound Med. Biol.*, vol. 29, no. 12, pp. 1705–1713, Dec. 2003.
[156] T. Varghese and H. Shi, “Elastographic imaging of thermal lesions in liver in-vivo using diaphragmatic stimuli.,” *Ultrason. Imaging*, vol. 26, no. 1, pp. 18–28, Jan. 2004.
[157] E. E. Konofagou, J. D’hooge, and J. Ophir, “Myocardial elastography--a feasibility study in vivo.,” *Ultrasound Med. Biol.*, vol. 28, no. 4, pp. 475–482, Apr. 2002.
[158] T. Varghese, J. A. Zagzebski, P. Rahko, and C. S. Breburda, “Ultrasonic imaging of myocardial strain using cardiac elastography.,” *Ultrason. Imaging*, vol. 25, no. 1, pp. 1–16, Jan. 2003.
[159] C. L. de Korte, J. A. Schaar, F. Mastik, P. W. Serruys, and A. F. van der Steen, “Intravascular elastography: from bench to bedside.,” *J. Interv. Cardiol.*, vol. 16, no. 3, pp. 253–259, Jun. 2003.
[160] J. Bercoff, M. Muller, M. Tanter, and M. Fink, “Study of viscous and elastic properties of soft tissue using supersonic shear imaging,” *IEEE Symposium on Ultrasonics*, vol. 1. IEEE, Honolulu, HI, USA, pp. 925–928, 2003.
[161] D. Cosgrove *et al.*, “EFSUMB guidelines and recommendations on the clinical use of ultrasound elastography. Part 2: Clinical applications,” *Ultraschall Med*, vol. 34, no. 3, pp. 238–253, 2013.
[162] M. Fatemi and J. F. Greenleaf, “Imaging the Viscoelastic Properties of Tissue,” in *Topics in Applied Physics: Imaging of Complex Media with Acoustic and Seismic Waves*, vol. 84, M. Fink, W. A. Kuperman, J. P. Montagner, and A. Tourin, Eds. Berlin, Heidelberg, Germany: Springer, 2002, pp. 257–276.
[163] R. Aljuraifani, R. E. Stafford, F. Hug, and P. W. Hodges, “Female striated urogenital sphincter contraction measured by shear wave elastography during pelvic floor muscle activation: Proof of concept and validation,” *Neurourol. Urodyn.*, no. October 2016, pp. 1–7, 2017.
[164] T. K. Koo and M. Y. Li, “A Guideline of Selecting and Reporting Intraclass Correlation Coefficients for Reliability Research,” *J Chiropr Med*, vol. 15, no. 2, pp. 155–163, 2016.
[165] G. Ferraioli *et al.*, “Reproducibility of real-time shear wave elastography in the evaluation of liver elasticity,” *Eur J Radiol*, vol. 81, no. 11, pp. 3102–3106, 2012.
[166] Z. J. Zhang and S. N. Fu, “Shear Elastic Modulus on Patellar Tendon Captured from Supersonic Shear Imaging: Correlation with Tangent Traction Modulus Computed from Material Testing System and Test-Retest Reliability.,” *PLoS One*, vol. 8, no. 6, p. e68216, 2013.
[167] L. Peralta *et al.*, “In Vivo Evaluation of Cervical Stiffness Evolution during Induced Ripening Using Shear Wave Elastography, Histology and 2 Photon Excitation Microscopy: Insight from an Animal Model,” *PLoS One*, vol. 10, no. 8, p. e0133377, 2015.
[168] R. G. Barr and Z. Zhang, “Effects of precompression on elasticity imaging of the breast: development of a clinically useful semiquantitative method of precompression assessment,” *J Ultrasound Med*, vol. 31, no. 6, pp. 895–902, 2012.
[169] N. Miyamoto, K. Hirata, H. Kanehisa, and Y. Yoshitake, “Validity of measurement of shear modulus by ultrasound shear wave elastography in human pennate muscle.,” *PLoS One*, vol. 10, no. 4, p. e0124311, 2015.
[170] E. Widman, E. Maksuti, D. Larsson, M. W. Urban, A. Bjallmark, and M. Larsson, “Shear wave elastography plaque characterization with mechanical testing validation: a phantom study.,” *Phys. Med. Biol.*, vol. 60, no. 8, pp. 3151–3174, Apr. 2015.
[171] J. A. Martin *et al.*, “In Vivo Measures of Shear Wave Speed as a Predictor of Tendon Elasticity and Strength,” *Ultrasound Med. Biol.*, vol. 41, no. 10, pp. 2722–2730, Oct. 2015.
[172] L. Zhai, M. L. Palmeri, R. R. Bouchard, R. W. Nightingale, and K. R. Nightingale, “An integrated indenter-ARFI imaging system for tissue stiffness quantification,” *Ultrason Imaging*, vol. 30, no. 2, pp. 95–111, 2008.
[173] S. Ogawa *et al.*, “Relationship between liver tissue stiffness and histopathological findings

analyzed by shear wave elastography and compression testing in rats with non-alcoholic steatohepatitis," *J. Med. Ultrason.*, vol. 43, no. 3, pp. 355–360, Jul. 2016.
[174] E. A. Omari, T. Varghese, M. A. Kliewer, J. Harter, and E. M. Hartenbach, "Dynamic and quasi-static mechanical testing for characterization of the viscoelastic properties of human uterine tissue," *J Biomech*, vol. 48, no. 10, pp. 1730–1736, 2015.
[175] J. Mo *et al.*, "Bias of shear wave elasticity measurements in thin layer samples and a simple correction strategy," *Springerplus*, vol. 5, no. 1, p. 1341, Dec. 2016.
[176] J.-L. Gennisson, N. Grenier, C. Combe, and M. Tanter, "Supersonic Shear Wave Elastography of In Vivo Pig Kidney: Influence of Blood Pressure, Urinary Pressure and Tissue Anisotropy," *Ultrasound Med. Biol.*, vol. 38, no. 9, pp. 1559–1567, Sep. 2012.
[177] K. Skerl, S. Vinnicombe, K. Thomson, D. McLean, E. Giannotti, and A. Evans, "Anisotropy of Solid Breast Lesions in 2D Shear Wave Elastography is an Indicator of Malignancy," *Acad. Radiol.*, vol. 23, no. 1, pp. 53–61, Jan. 2016.
[178] Y. Chen, Y. Gao, C. Chang, F. Wang, W. Zeng, and J. Chen, "Ultrasound shear wave elastography of breast lesions: correlation of anisotropy with clinical and histopathological findings," *Cancer Imaging*, vol. 18, no. 1, p. 11, Dec. 2018.
[179] S. Chatelin, J.-L. Gennisson, M. Bernal, M. Tanter, and M. Pernot, "Modelling the impulse diffraction field of shear waves in transverse isotropic viscoelastic medium," *Phys. Med. Biol.*, vol. 60, no. 9, pp. 3639–3654, May 2015.
[180] C. Papadacci, M. Tanter, M. Pernot, and M. Fink, "Ultrasound backscatter tensor imaging (BTI): analysis of the spatial coherence of ultrasonic speckle in anisotropic soft tissues," *IEEE Trans. Ultrason. Ferroelectr. Freq. Control*, vol. 61, no. 6, pp. 986–996, Jun. 2014.
[181] K. L. Moore and A. F. Dalley, "Pelvis and Perineum," in *Clinically Oriented Anatomy*, 5th editio., Baltimore, MD: Lippincott Williams & Wilkins, 2006, pp. 410–429.
[182] R. M. S. Sigrist, J. Liau, A. E. Kaffas, M. C. Chammas, and J. K. Willmann, "Ultrasound Elastography: Review of Techniques and Clinical Applications," *Theranostics*, vol. 7, no. 5, pp. 1303–1329, 2017.
[183] F. Hug, "Advancing Musculoskeletal Rehabilitation Using Elastography," *Aspetar Sport. Med. J.*, vol. 5, no. 1, p. 5, 2016.
[184] A. C. Lam, S. W. Pang, A. T. Ahuja, and K. S. Bhatia, "The influence of precompression on elasticity of thyroid nodules estimated by ultrasound shear wave elastography," *Eur Radiol*, vol. 26, no. 8, pp. 2845–2852, 2016.
[185] K. Mantsopoulos, N. Klintworth, H. Iro, and A. Bozzato, "Applicability of shear wave elastography of the major salivary glands: values in healthy patients and effects of gender, smoking and pre-compression," *Ultrasound Med Biol*, vol. 41, no. 9, pp. 2310–2318, 2015.
[186] R. J. Dewall, T. Varghese, M. A. Kliewer, J. M. Harter, and E. M. Hartenbach, "Compression-Dependent Viscoelastic Behavior of Human Cervix Tissue," *Ultrasound Imaging*, vol. 32, no. 4, pp. 214–228, 2010.
[187] T. Varghese, J. Ophir, and T. A. Krouskop, "Nonlinear stress-strain relationships in tissue and their effect on the contrast-to-noise ratio in elastograms," *Ultrasound Med Biol*, vol. 26, no. 5, pp. 839–851, 2000.
[188] T. J. Hall *et al.*, "Elastic nonlinearity imaging," in *2009 Annual International Conference of the IEEE Engineering in Medicine and Biology Society*, 2009, pp. 1967–1970.
[189] E. J.-H. Chang, Y. Guo, and W.-N. Lee, "Shear wave elastography for the characterization of arterial wall stiffness: A thin-plate phantom and ex vivo aorta study," in *2017 IEEE 14th International Symposium on Biomedical Imaging (ISBI 2017)*, 2017, pp. 275–278.
[190] G.-Y. Li and Y. Cao, "Mechanics of ultrasound elastography," *Proc. R. Soc. A Math. Phys. Eng. Sci.*, vol. 473, no. 2199, p. 20160841, Mar. 2017.
[191] M. Couade *et al.*, "Quantitative assessment of arterial wall biomechanical properties using shear

wave imaging," *Ultrasound Med Biol*, vol. 36, no. 10, pp. 1662–1676, 2010.
[192] M. Bernal, I. Nenadic, M. W. Urban, and J. F. Greenleaf, "Material property estimation for tubes and arteries using ultrasound radiation force and analysis of propagating modes," *J. Acoust. Soc. Am.*, vol. 129, no. 3, pp. 1344–1354, Mar. 2011.
[193] H. Kanai, "Propagation of spontaneously actuated pulsive vibration in human heart wall and in vivo viscoelasticity estimation," *IEEE Trans. Ultrason. Ferroelectr. Freq. Control*, vol. 52, no. 11, pp. 1931–1942, Nov. 2005.
[194] I. Nenadic *et al.*, "Noninvasive Evaluation of Bladder Wall Mechanical Properties as a Function of Filling Volume: Potential Application in Bladder Compliance Assessment," *PLoS One*, vol. 11, no. 6, p. e0157818, Jun. 2016.
[195] J. Brum, M. Bernal, J. L. Gennisson, and M. Tanter, "In vivo evaluation of the elastic anisotropy of the human Achilles tendon using shear wave dispersion analysis," *Phys. Med. Biol.*, vol. 59, no. 3, pp. 505–523, Feb. 2014.
[196] M. W. Urban, I. Z. Nenadic, B. Qiang, M. Bernal, S. Chen, and J. F. Greenleaf, "Characterization of material properties of soft solid thin layers with acoustic radiation force and wave propagation," *J. Acoust. Soc. Am.*, vol. 138, no. 4, pp. 2499–2507, Oct. 2015.
[197] G.-Y. Li, Q. He, L. Jia, P. He, J. Luo, and Y. Cao, "An Inverse Method to Determine Arterial Stiffness with Guided Axial Waves," *Ultrasound Med. Biol.*, vol. 43, no. 2, pp. 505–516, Feb. 2017.
[198] A. Pau and F. Lanza di Scalea, "Nonlinear guided wave propagation in prestressed plates," *J. Acoust. Soc. Am.*, vol. 137, no. 3, pp. 1529–1540, Mar. 2015.
[199] N. T. Nam, J. Merodio, R. W. Ogden, and P. C. Vinh, "The effect of initial stress on the propagation of surface waves in a layered half-space," *Int. J. Solids Struct.*, vol. 88–89, pp. 88–100, Jun. 2016.
[200] T. J. Hall *et al.*, "RSNA/QIBA: Shear wave speed as a biomarker for liver fibrosis staging," in *2013 IEEE International Ultrasonics Symposium (IUS)*, 2013, pp. 397–400.
[201] A. B. Rosskopf, E. Bachmann, J. G. Snedeker, C. W. A. Pfirrmann, and F. M. Buck, "Comparison of shear wave velocity measurements assessed with two different ultrasound systems in an ex-vivo tendon strain phantom," *Skeletal Radiol.*, vol. 45, no. 11, pp. 1541–1551, Nov. 2016.
[202] E. A. Stewart *et al.*, "Magnetic resonance elastography of uterine leiomyomas: a feasibility study," *Fertil. Steril.*, vol. 95, no. 1, pp. 281–284, Jan. 2011.
[203] D. E. Jondal *et al.*, "Uterine fibroids: correlations between MRI appearance and stiffness via magnetic resonance elastography," *Abdom Radiol (NY)*, vol. 43, no. 6, pp. 1456–1463, 2018.
[204] S. Ichikawa *et al.*, "Comparison of the diagnostic accuracies of magnetic resonance elastography and transient elastography for hepatic fibrosis," *Magn Reson Imaging*, vol. 33, no. 1, pp. 26–30, 2015.
[205] S. Ichikawa *et al.*, "MR-guided Focused Ultrasound for Uterine Fibroids: A Preliminary Study of Relationship between the Treatment Outcomes and Factors of MR Images Including Elastography," *Magn. Reson. Med. Sci.*, vol. 18, no. 1, pp. 82–87, 2019.
[206] G. Hesley, K. Gorny, and D. Woodrum, "MR elastography following focused ultrasound treatment of uterine fibroids," *J. Ther. Ultrasound*, vol. 2, no. Suppl 1, pp. A13–A13, Dec. 2014.
[207] S. Furukawa, S. Soeda, T. Watanabe, H. Nishiyama, and K. Fujimori, "The measurement of stiffness of uterine smooth muscle tumor by elastography," *Springerplus*, vol. 3, no. 1, pp. 1–5, 2014.
[208] D. E. Jondal *et al.*, "Uterine fibroids: correlations between MRI appearance and stiffness via magnetic resonance elastography," *Abdom. Radiol.*, 2017.
[209] S. Acar, E. Millar, M. Mitkova, and V. Mitkov, "Value of ultrasound shear wave elastography in the diagnosis of adenomyosis," *Ultrasound*, vol. 24, no. 4, pp. 205–213, 2016.
[210] M. Abdel Latif, M. Shady, H. Nabil, and Y. Mesbah, "Trans-vaginal sono-elastography in the differentiation of endometrial hyperplasia and endometrial carcinoma," *Egypt. J. Radiol. Nucl.*

Med., vol. 47, no. 3, pp. 1123–1131, Sep. 2016.
[211] X. Liu, D. Ding, Y. Ren, and S.-W. Guo, "Transvaginal Elastosonography as an Imaging Technique for Diagnosing Adenomyosis," *Reprod. Sci.*, vol. 25, no. 4, pp. 498–514, Apr. 2018.
[212] M. A. Hobson *et al.*, "In vitro uterine strain imaging: preliminary results," *J Ultrasound Med*, vol. 26, no. 7, pp. 899–908, Jul. 2007.
[213] M. S. Rein *et al.*, "Cytogenetic abnormalities in uterine myomas are associated with myoma size," *Mol Hum Reprod*, vol. 4, no. 1, pp. 83–86, 1998.
[214] C. Marigliano *et al.*, "First experience of real-time elastography with transvaginal approach in assessing response to MRgFUS treatment of uterine fibroids," *Radiol. Med.*, vol. 121, no. 12, pp. 926–934, Dec. 2016.
[215] C. Marigliano *et al.*, "First experience of real-time elastography with transvaginal approach in assessing response to MRgFUS treatment of uterine fibroids," *Radiol. Med.*, vol. 121, no. 12, pp. 926–934, Dec. 2016.
[216] Y. Wang, Z.-B. Wang, and Y.-H. Xu, "Efficacy, Efficiency, and Safety of Magnetic Resonance-Guided High-Intensity Focused Ultrasound for Ablation of Uterine Fibroids: Comparison with Ultrasound-Guided Method," *Korean J. Radiol.*, vol. 19, no. 4, p. 724, 2018.
[217] E. Nitta, K. Kanenishi, N. Itabashi, H. Tanaka, and T. Hata, "Real-time tissue elastography of uterine sarcoma.," *Archives of gynecology and obstetrics*, vol. 289, no. 2. Germany, pp. 463–465, Feb-2014.
[218] S. Woźniak, "The potential role of elastography in differentiating between endometrial polyps and submucosal fibroids: a preliminary study," *Menopausal Rev.*, vol. 2, pp. 130–133, 2015.
[219] M. A. Babyak, "What You See May Not Be What You Get: A Brief, Nontechnical Introduction to Overfitting in Regression-Type Models," *Psychosom. Med.*, vol. 66, no. 3, pp. 411–421, May 2004.
[220] W.-P. Zhao, J. Zhang, Z.-Y. Han, J.-P. Yao, X. Zhou, and P. Liang, "A clinical investigation treating different types of fibroids identified by MRI-T2WI imaging with ultrasound guided high intensity focused ultrasound," *Sci. Rep.*, vol. 7, no. 1, p. 10812, Dec. 2017.
[221] S. Furukawa, S. Soeda, T. Watanabe, H. Nishiyama, and K. Fujimori, "The measurement of stiffness of uterine smooth muscle tumor by elastography," *Springerplus*, vol. 3, no. 1, p. 294, 2014.
[222] A. A. Soliman, S. Wojcinski, and F. Degenhardt, "Ultrasonographic examination of the endometrium and myometrium using acoustic radiation force impulse (ARFI) imaging technology: An initial experience with a new method.," *Clin. Hemorheol. Microcirc.*, vol. 59, no. 3, pp. 235–243, 2015.
[223] M. R. Labrosse, R. Jafar, J. Ngu, and M. Boodhwani, "Planar biaxial testing of heart valve cusp replacement biomaterials: Experiments, theory and material constants," *Acta Biomater.*, vol. 45, pp. 303–320, Nov. 2016.
[224] S. Chatelin *et al.*, "In vivo liver tissue mechanical properties by transient elastography: Comparison with dynamic mechanical analysis," *Biorheology*, vol. 48, no. 2, pp. 75–88, 2011.
[225] C. Jacquemoud, K. Bruyere-Garnier, and M. Coret, "Methodology to determine failure characteristics of planar soft tissues using a dynamic tensile test," *J. Biomech.*, vol. 40, no. 2, pp. 468–475, Jan. 2007.
[226] S. Srinivasan, T. Krouskop, and J. Ophir, "Comparing elastographic strain images with modulus images obtained using nanoindentation: preliminary results using phantoms and tissue samples," *Ultrasound Med. Biol.*, vol. 30, no. 3, pp. 329–343, Mar. 2004.
[227] S. Srinivasan, T. Krouskop, and J. Ophir, "A quantitative comparison of modulus images obtained using nanoindentation with strain elastograms," *Ultrasound Med. Biol.*, vol. 30, no. 7, pp. 899–918, Jul. 2004.
[228] Y. C. Fung, *A First Couse in Continuum Mechanics*, 3rd ed. Englewood Cliffs, NJ, USA: Prentice

Hall, 1994.
[229] R. M. Christensen, *Theory of Viscoelasticity An Introduction*, 2nd ed. New York, NY, USA: Academic Press, Inc., 1982.
[230] T. W. Lambe and R. B. Whitman, *Soil Mechanics*. New York, NY, USA: Wiley & Sons, 1969.
[231] C. W. Smith, I. S. Young, and J. N. Kearney, "Mechanical properties of tendons: changes with sterilization and preservation," *J Biomech Eng*, vol. 118, no. 1, pp. 56–61, 1996.
[232] P. Clavert, J. F. Kempf, F. Bonnomet, P. Boutemy, L. Marcelin, and J. L. Kahn, "Effects of freezing/thawing on the biomechanical properties of human tendons," *Surg Radiol Anat*, vol. 23, no. 4, pp. 259–262, 2001.
[233] J. Fromageau, J. L. Gennisson, C. Schmitt, R. L. Maurice, R. Mongrain, and G. Cloutier, "Estimation of polyvinyl alcohol cryogel mechanical properties with four ultrasound elastography methods and comparison with gold standard testings," *IEEE Trans Ultrason Ferroelectr Freq Control*, vol. 54, no. 3, pp. 498–509, 2007.
[234] E. G. Herbert, W. C. Oliver, and G. M. Pharr, "Nanoindentation and the dynamic characterization of viscoelastic solids," *J. Phys. D. Appl. Phys.*, vol. 41, no. 7, p. 074021, Apr. 2008.
[235] S. J. Potts *et al.*, "Evaluating tumor heterogeneity in immunohistochemistry-stained breast cancer tissue," *Lab. Investig.*, vol. 92, no. 9, pp. 1342–1357, Sep. 2012.
[236] S. Kennedy *et al.*, "Optical breast cancer margin assessment: an observational study of the effects of tissue heterogeneity on optical contrast," *Breast Cancer Res.*, vol. 12, no. 6, p. R91, Dec. 2010.
[237] B. M. Schofield and C. Wood, "Length-tension relation in rabbit and human myometrium," *J. Physiol.*, vol. 175, no. 1, pp. 125–133, Dec. 1964.
[238] J. T. Conrad and W. Kuhn, "The active length-tension relationship in human uterine muscle," *Am. J. Obstet. Gynecol.*, vol. 97, no. 2, pp. 154–160, Jan. 1967.
[239] A. Csapo and M. Goodall, "Excitability, length tension relation and kinetics of uterine muscle contraction in relation to hormonal status," *J. Physiol.*, vol. 126, no. 2, pp. 384–395, Nov. 1954.
[240] C. Wood, "THE EXPANSILE BEHAVIOUR OF THE HUMAN UTERUS," *BJOG An Int. J. Obstet. Gynaecol.*, vol. 71, no. 4, pp. 615–620, Aug. 1964.
[241] J. T. Conrad, W. K. Kuhn, and W. L. Johnson, "Stress relaxation in human uterine muscle," *Am. J. Obstet. Gynecol.*, vol. 95, no. 2, pp. 254–265, May 1966.
[242] J. T. Conrad, W. L. Johnson, W. K. Kuhn, and C. A. Hunter, "Passive stretch relationships in human uterine muscle," *Am. J. Obstet. Gynecol.*, vol. 96, no. 8, pp. 1055–1059, Dec. 1966.
[243] G. W. Pearsall and V. L. Roberts, "Passive mechanical properties of uterine muscle (myometrium) tested in vitro," *J. Biomech.*, vol. 11, no. 4, pp. 167–176, Jan. 1978.
[244] S. J. Manoogian, C. McNally, J. D. Stitzel, and S. M. Duma, "Dynamic Biaxial Tissue Properties of Pregnant Porcine Uterine Tissue," 2008.
[245] K. M. Myers, A. P. Paskaleva, M. House, and S. Socrate, "Mechanical and biochemical properties of human cervical tissue," *Acta Biomater.*, vol. 4, no. 1, pp. 104–116, Jan. 2008.
[246] E. A. Omari, "Ultrasound Strain and Attenuation Imaging for Detection of Uterine Masses," University of Wisconsin-Madison, 2014.
[247] M. A. Hobson *et al.*, "In vitro uterine strain imaging: preliminary results," *J Ultrasound Med*, vol. 26, no. 7, pp. 899–908, Jul. 2007.
[248] N. T. Hulley SB, Cummings SR, Browner WS, Grady D, *Designing Clinical Research: an Epidemiologic Approach*, 4th ed. Philadelphia, PA: Lippincott Williams & Wilkins;, 2013.
[249] L.-J. Liaw, M.-J. Hsu, C.-F. Liao, M.-F. Liu, and A.-T. Hsu, "The Relationships Between Inter-recti Distance Measured by Ultrasound Imaging and Abdominal Muscle Function in Postpartum Women: A 6-Month Follow-up Study," *J. Orthop. Sport. Phys. Ther.*, vol. 41, no. 6, pp. 435–443, Jun. 2011.
[250] P. Peduzzi, J. Concato, A. R. Feinstein, and T. R. Holford, "Importance of events per independent

variable in proportional hazards regression analysis II. Accuracy and precision of regression estimates," *J. Clin. Epidemiol.*, vol. 48, no. 12, pp. 1503–1510, Dec. 1995.
[251] P. Peduzzi, J. Concato, E. Kemper, T. R. Holford, and A. R. Feinstein, "A simulation study of the number of events per variable in logistic regression analysis," *J. Clin. Epidemiol.*, vol. 49, no. 12, pp. 1373–1379, Dec. 1996.
[252] M.-J. Lu, W.-H. Zhong, Y.-X. Liu, H.-Z. Miao, Y.-C. Li, and M.-H. Ji, "Sample Size for Assessing Agreement between Two Methods of Measurement by Bland−Altman Method," *Int. J. Biostat.*, vol. 12, no. 2, Nov. 2016.
[253] E. L. Madsen *et al.*, "Anthropomorphic breast phantoms for testing elastography systems," *Ultrasound Med. Biol.*, vol. 32, no. 6, pp. 857–874, Jun. 2006.
[254] T. Z. Pavan, E. L. Madsen, G. R. Frank, O. C. A. Adilton, and T. J. Hall, "Nonlinear elastic behavior of phantom materials for elastography," *Phys Med Biol*, vol. 55, no. 9, pp. 2679–2692, 2010.
[255] S. L. Vieira, T. Z. Pavan, J. E. Junior, and A. A. O. Carneiro, "Paraffin-Gel Tissue-Mimicking Material for Ultrasound-Guided Needle Biopsy Phantom," *Ultrasound Med. Biol.*, vol. 39, no. 12, pp. 2477–2484, Dec. 2013.
[256] T. K. Koo and M. Y. Li, "A Guideline of Selecting and Reporting Intraclass Correlation Coefficients for Reliability Research," *J. Chiropr. Med.*, vol. 15, no. 2, pp. 155–163, Jun. 2016.
[257] D. Ding, Y. Chen, X. Liu, Z. Jiang, X. Cai, and S.-W. Guo, "Diagnosing Deep Endometriosis Using Transvaginal Elastosonography," *Reprod. Sci.*, vol. 27, no. 7, pp. 1411–1422, Jul. 2020.
[258] K. Hancke, V. Heilmann, P. Straka, R. Kreienberg, and C. Kurzeder, "Pretreatment Staging of Cervical Cancer: Is Imaging Better Than Palpation?," *Ann. Surg. Oncol.*, vol. 15, no. 10, pp. 2856–2861, Oct. 2008.
[259] K. C. G. Ng, M. Lamontagne, M. R. Labrosse, and P. E. Beaulé, "Hip Joint Stresses Due to Cam-Type Femoroacetabular Impingement: A Systematic Review of Finite Element Simulations," *PLoS One*, vol. 11, no. 1, p. e0147813, Jan. 2016.
[260] M. R. Labrosse, C. J. Beller, M. Boodhwani, C. Hudson, and B. Sohmer, "Subject-specific finite-element modeling of normal aortic valve biomechanics from 3D+t TEE images," *Med. Image Anal.*, vol. 20, no. 1, pp. 162–172, Feb. 2015.
[261] H. Maleki, S. Shahriari, L. G. Durand, M. R. Labrosse, and L. Kadem, "A metric for the stiffness of calcified aortic valves using a combined computational and experimental approach," *Med. Biol. Eng. Comput.*, vol. 52, no. 1, pp. 1–8, Jan. 2014.
[262] M. R. Labrosse, C. J. Beller, F. Robicsek, and M. J. Thubrikar, "Geometric modeling of functional trileaflet aortic valves: Development and clinical applications," *J. Biomech.*, vol. 39, no. 14, pp. 2665–2672, Jan. 2006.
[263] S. Ghouse *et al.*, "The design and in vivo testing of a locally stiffness-matched porous scaffold," *Appl. Mater. Today*, vol. 15, pp. 377–388, Jun. 2019.
[264] M. V. Anurov, S. M. Titkova, and A. P. Oettinger, "Biomechanical compatibility of surgical mesh and fascia being reinforced: dependence of experimental hernia defect repair results on anisotropic surgical mesh positioning," *Hernia*, vol. 16, no. 2, pp. 199–210, Apr. 2012.
[265] J. P. Callaghan and S. M. McGill, "Frozen storage increases the ultimate compressive load of porcine vertebrae," *J Orthop Res*, vol. 13, no. 5, pp. 809–812, 1995.
[266] E. C. Bass, N. A. Duncan, J. S. Hariharan, J. Dusick, H. U. Bueff, and J. C. Lotz, "Frozen storage affects the compressive creep behavior of the porcine intervertebral disc," *Spine (Phila Pa 1976)*, vol. 22, no. 24, pp. 2867–2876, 1997.
[267] T. L. Willett, R. Whiteside, P. M. Wild, U. P. Wyss, and T. Anastassiades, "Artefacts in the mechanical characterization of porcine articular cartilage due to freezing," *Proc Inst Mech Eng H*, vol. 219, no. 1, pp. 23–29, 2005.
[268] W. D. Turner, P. Vasseur, J. E. Gorek, J. J. Rodrigo, and J. R. Wedell, "An in vitro study of the

structural properties of deep-frozen versus freeze-dried, ethylene oxide-sterilized canine anterior cruciate ligament bone-ligament-bone preparations," *Clin Orthop Relat Res*, no. 230, pp. 251–256, 1988.
[269] A. Athanasiou *et al.*, "Breast lesions: quantitative elastography with supersonic shear imaging--preliminary results," *Radiology*, vol. 256, no. 1, pp. 297–303, 2010.
[270] J. Bamber *et al.*, "EFSUMB guidelines and recommendations on the clinical use of ultrasound elastography. Part 1: Basic principles and technology," *Ultraschall Med*, vol. 34, no. 2, pp. 169–184, 2013.
[271] D. O. Cosgrove *et al.*, "Shear wave elastography for breast masses is highly reproducible," *Eur Radiol*, vol. 22, no. 5, pp. 1023–1032, 2012.
[272] D. Cosgrove *et al.*, "EFSUMB guidelines and recommendations on the clinical use of ultrasound elastography. Part 2: Clinical applications," *Ultraschall Med*, vol. 34, no. 3, pp. 238–253, 2013.
[273] W. A. Berg *et al.*, "Shear-wave elastography improves the specificity of breast US: the BE1 multinational study of 939 masses," *Radiology*, vol. 262, no. 2, pp. 435–449, 2012.
[274] A. Evans *et al.*, "Differentiating benign from malignant solid breast masses: value of shear wave elastography according to lesion stiffness combined with greyscale ultrasound according to BI-RADS classification," *Br J Cancer*, vol. 107, no. 2, pp. 224–229, 2012.
[275] B. S. Garra *et al.*, "Elastography of breast lesions: initial clinical results," *Radiology*, vol. 202, no. 1, pp. 79–86, 1997.
[276] J. E. Brandenburg *et al.*, "Ultrasound elastography: the new frontier in direct measurement of muscle stiffness," *Arch Phys Med Rehabil*, vol. 95, no. 11, pp. 2207–2219, 2014.
[277] T. Shiina *et al.*, "WFUMB guidelines and recommendations for clinical use of ultrasound elastography: Part 1: basic principles and terminology," *Ultrasound Med Biol*, vol. 41, no. 5, pp. 1126–1147, 2015.
[278] L. Lacourpaille, F. Hug, K. Bouillard, J. Y. Hogrel, and A. Nordez, "Supersonic shear imaging provides a reliable measurement of resting muscle shear elastic modulus," *Physiol Meas*, vol. 33, no. 3, pp. N19-28, 2012.
[279] F. Hug, "Advancing Musculoskeletal Rehabilitation Using Elastography," *Aspetar Sport. Med. J.*, vol. 5, no. 1, p. 5.
[280] R. M. S. Sigrist, J. Liau, A. E. Kaffas, M. C. Chammas, and J. K. Willmann, "Ultrasound Elastography: Review of Techniques and Clinical Applications," *Theranostics*, vol. 7, no. 5, pp. 1303–1329, 2017.
[281] E. E. Drakonaki, G. M. Allen, and D. J. Wilson, "Ultrasound elastography for musculoskeletal applications," *Br J Radiol*, vol. 85, no. 1019, pp. 1435–1445, 2012.
[282] J. Ryu and W. K. Jeong, "Current status of musculoskeletal application of shear wave elastography," *Ultrasonography*, vol. 36, no. 3, pp. 185–197, 2017.
[283] H. Shah *et al.*, "The management of chronic hepatitis C: 2018 guideline update from the Canadian Association for the Study of the Liver," *Can. Med. Assoc. J.*, vol. 190, no. 22, pp. E677–E687, 2018.
[284] S. Ichikawa *et al.*, "Comparison of the diagnostic accuracies of magnetic resonance elastography and transient elastography for hepatic fibrosis," *Magn Reson Imaging*, vol. 33, no. 1, pp. 26–30, 2015.
[285] L. N. Su, S. L. Guo, B. X. Li, and P. Yang, "Diagnostic value of magnetic resonance elastography for detecting and staging of hepatic fibrosis: a meta-analysis," *Clin Radiol*, vol. 69, no. 12, pp. e545-52, 2014.
[286] L. Castera, X. Forns, and A. Alberti, "Non-invasive evaluation of liver fibrosis using transient elastography," *J Hepatol*, vol. 48, no. 5, pp. 835–847, 2008.
[287] A. Guibal *et al.*, "Shear wave elastography: An accurate technique to stage liver fibrosis in chronic liver diseases," *Diagn Interv Imaging*, vol. 97, no. 1, pp. 91–99, 2016.
[288] K. Preis, K. Zielinska, M. Swiatkowska-Freund, D. Wydra, and J. Kobierski, "The role of

elastography in the differential diagnosis of endometrial pathologies--preliminary report," *Ginekol Pol*, vol. 82, no. 7, pp. 494–497, 2011.
[289] A. Itoh *et al.*, "Breast disease: clinical application of US elastography for diagnosis," *Radiology*, vol. 239, no. 2, pp. 341–350, 2006.
[290] E. Mazza, A. Nava, M. Bauer, R. Winter, M. Bajka, and G. A. Holzapfel, "Mechanical properties of the human uterine cervix: an in vivo study," *Med Image Anal*, vol. 10, no. 2, pp. 125–136, 2006.
[291] A. C. Swann and B. B. Seedhom, "Improved techniques for measuring the indentation and thickness of articular cartilage," *Proc Inst Mech Eng H*, vol. 203, no. 3, pp. 143–150, 1989.
[292] C. Saccardi, S. Gizzo, M. Noventa, E. Ancona, A. Borghero, and P. S. Litta, "Limits and complications of laparoscopic myomectomy: which are the best predictors? A large cohort single-center experience," *Arch. Gynecol. Obstet.*, vol. 290, no. 5, pp. 951–956, Nov. 2014.
[293] S. K. Laughlin, J. C. Schroeder, and D. D. Baird, "New directions in the epidemiology of uterine fibroids," *Semin Reprod Med*, vol. 28, no. 3, pp. 204–217, 2010.
[294] X. Wu, V. A. Serna, J. Thomas, W. Qiang, M. L. Blumenfeld, and T. Kurita, "Subtype-Specific Tumor-Associated Fibroblasts Contribute to the Pathogenesis of Uterine Leiomyoma," *Cancer Res*, vol. 77, no. 24, pp. 6891–6901, 2017.
[295] M. Mehine *et al.*, "Integrated data analysis reveals uterine leiomyoma subtypes with distinct driver pathways and biomarkers," *Proc Natl Acad Sci U S A*, vol. 113, no. 5, pp. 1315–1320, 2016.
[296] M. Mehine, N. Makinen, H. R. Heinonen, L. A. Aaltonen, and P. Vahteristo, "Genomics of uterine leiomyomas: insights from high-throughput sequencing," *Fertil Steril*, vol. 102, no. 3, pp. 621–629, 2014.
[297] M. Mehine *et al.*, "Characterization of uterine leiomyomas by whole-genome sequencing," *N Engl J Med*, vol. 369, no. 1, pp. 43–53, 2013.
[298] N. Makinen, H. R. Heinonen, S. Moore, I. P. Tomlinson, Z. M. van der Spuy, and L. A. Aaltonen, "MED12 exon 2 mutations are common in uterine leiomyomas from South African patients," *Oncotarget*, vol. 2, no. 12, pp. 966–969, 2011.
[299] C. Exacoustos *et al.*, "Adenomyosis: three-dimensional sonographic findings of the junctional zone and correlation with histology," *Ultrasound Obstet. Gynecol.*, vol. 37, no. 4, pp. 471–479, Apr. 2011.
[300] M. Dueholm, "Transvaginal ultrasound for diagnosis of adenomyosis: a review," *Best Pract. Res. Clin. Obstet. Gynaecol.*, vol. 20, no. 4, pp. 569–582, Aug. 2006.
[301] M. Friedrich-Rust *et al.*, "Performance of transient elastography for the staging of liver fibrosis: a meta-analysis," *Gastroenterology*, vol. 134, no. 4, pp. 960–974, 2008.
[302] M. Muller *et al.*, "Assessment of the Cervix in Pregnant Women Using Shear Wave Elastography: A Feasibility Study," *Ultrasound Med Biol*, vol. 41, no. 11, pp. 2789–2797, 2015.
[303] M. Elmes *et al.*, "Maternal age effects on myometrial expression of contractile proteins, uterine gene expression, and contractile activity during labor in the rat," *Physiol Rep*, vol. 3, no. 4, 2015.
[304] B. S. Oxlund *et al.*, "Collagen concentration and biomechanical properties of samples from the lower uterine cervix in relation to age and parity in non-pregnant women," *Reprod. Biol. Endocrinol.*, vol. 8, no. 1, p. 82, Dec. 2010.
[305] S. Arrowsmith, H. Robinson, K. Noble, and S. Wray, "What do we know about what happens to myometrial function as women age?," *J Muscle Res Cell Motil*, vol. 33, no. 3–4, pp. 209–217, 2012.
[306] S. Okolo, "Incidence, aetiology and epidemiology of uterine fibroids," *Best Pr. Res Clin Obs. Gynaecol*, vol. 22, no. 4, pp. 571–588, 2008.
[307] S. A. Shikora, J. M. Niloff, B. R. Bistrian, R. A. Forse, and G. L. Blackburn, "Relationship between obesity and uterine leiomyomata," *Nutrition*, vol. 7, no. 4, pp. 251–255, 1991.
[308] A. O. Hammoud, R. Asaad, J. Berman, M. C. Treadwell, S. Blackwell, and M. P. Diamond, "Volume

change of uterine myomas during pregnancy: do myomas really grow?," *J Minim Invasive Gynecol*, vol. 13, no. 5, pp. 386–390, 2006.
[309] A. Aharoni, A. Reiter, D. Golan, Y. Paltiely, and M. Sharf, "Patterns of growth of uterine leiomyomas during pregnancy. A prospective longitudinal study," *Br J Obs. Gynaecol*, vol. 95, no. 5, pp. 510–513, 1988.
[310] T. A. Mahmood and A. Templeton, "Prevalence and genesis of endometriosis," *Hum. Reprod.*, vol. 6, no. 4, pp. 544–549, Apr. 1991.
[311] T. Bergholt, L. Eriksen, N. Berendt, M. Jacobsen, and J. B. Hertz, "Prevalence and risk factors of adenomyosis at hysterectomy," *Hum. Reprod.*, vol. 16, no. 11, pp. 2418–2421, Nov. 2001.
[312] N. A. Shadbolt, M. A. Parker, and L. A. Orthia, "Communicating endometriosis with young women to decrease diagnosis time," *Heal. Promot. J. Aust.*, vol. 24, no. 2, pp. 151–154, Aug. 2013.
[313] D. Bush, E. Brick, M. C. East, and N. Johnson, "Endometriosis education in schools: A New Zealand model examining the impact of an education program in schools on early recognition of symptoms suggesting endometriosis," *Aust. New Zeal. J. Obstet. Gynaecol.*, vol. 57, no. 4, pp. 452–457, Aug. 2017.
[314] A. Kido *et al.*, "Physiological changes of the human uterine myometrium during menstrual cycle: Preliminary evaluation using BOLD MR imaging," *J. Magn. Reson. Imaging*, vol. 26, no. 3, pp. 695–700, Sep. 2007.
[315] D. U. Silverthorn, B. R. Johnson, W. C. Ober, C. E. Ober, and A. C. Silverthorn, *Human Physiology: An Integrated Approach*, 7th ed. Glenview, IL, USA: Person Education, 2016.
[316] Y. L. He *et al.*, "Cyclic changes of the junctional zone on 3 T MRI images in young and middle-aged females during the menstrual cycle," *Clin. Radiol.*, vol. 71, no. 4, pp. 341–348, Apr. 2016.
[317] K. A. Matteson, D. M. Scott, C. A. Raker, and M. A. Clark, "The menstrual bleeding questionnaire: development and validation of a comprehensive patient-reported outcome instrument for heavy menstrual bleeding," *Bjog*, vol. 122, no. 5, pp. 681–689, 2015.
[318] P. E. Shrout and J. L. Fleiss, "Intraclass correlations: uses in assessing rater reliability," *Psychol Bull*, vol. 86, no. 2, pp. 420–428, 1979.
[319] D. Raissi, Q. Yu, and Q. Han, "Uterine anteversion after uterine fibroid embolization," *Radiol. Case Reports*, vol. 13, no. 6, pp. 1150–1153, Dec. 2018.
[320] A. O. Grings, V. Lora, G. D. Ferreira, I. S. Brum, H. von E. Corleta, and E. Capp, "Protein expression of estrogen receptors alpha and beta and aromatase in myometrium and uterine leiomyoma.," *Gynecol. Obstet. Invest.*, vol. 73, no. 2, pp. 113–117, 2012.
[321] D. D. Brandon *et al.*, "Estrogen receptor gene expression in human uterine leiomyomata.," *J. Clin. Endocrinol. Metab.*, vol. 80, no. 6, pp. 1876–1881, Jun. 1995.
[322] K. A. Kovacs, A. Oszter, P. M. Gocze, J. L. Kornyei, and I. Szabo, "Comparative analysis of cyclin D1 and oestrogen receptor (alpha and beta) levels in human leiomyoma and adjacent myometrium.," *Mol. Hum. Reprod.*, vol. 7, no. 11, pp. 1085–1091, Nov. 2001.
[323] J. Andersen, V. M. DyReyes, R. L. Barbieri, D. M. Coachman, and R. J. Miksicek, "Leiomyoma primary cultures have elevated transcriptional response to estrogen compared with autologous myometrial cultures," *J Soc Gynecol Investig*, vol. 2, no. 3, pp. 542–551, 1995.
[324] K. Pollow, J. Geilfuss, E. Boquoi, and B. Pollow, "Estrogen and progesterone binding proteins in normal human myometrium and leiomyoma tissue," *J Clin Chem Clin Biochem*, vol. 16, no. 9, pp. 503–511, 1978.
[325] L. C. Carlson, H. Feltovich, M. L. Palmeri, J. J. Dahl, A. Munoz del Rio, and T. J. Hall, "Estimation of shear wave speed in the human uterine cervix," *Ultrasound Obstet. Gynecol.*, vol. 43, no. 4, pp. 452–458, Apr. 2014.
[326] M. R. Labrosse, E. R. Gerson, J. P. Veinot, and C. J. Beller, "Mechanical characterization of human aortas from pressurization testing and a paradigm shift for circumferential residual stress," *J.*

Mech. Behav. Biomed. Mater., vol. 17, pp. 44–55, Jan. 2013.
[327] Y. C. Fung, E. Fukada, and J. J. Wang, "What principles governs the stress distribution in living organisms?," in *Biomechanics in Chilna, Japan, and USA*, 1983, pp. 1–13.
[328] R. M. Lerner, K. J. Parker, J. Holen, R. Gramiak, and R. C. Waag, "Sono-Elasticity: Medical Elasticity Images Derived from Ultrasound Signals in Mechanically Vibrated Targets," in *Acoustical Imaging*, 1988, pp. 317–327.
[329] R. J. Kurman, L. Hedrick Ellenson, and B. M. Ronnett, Eds., *Blaustein's Pathology of the Female Genital Tract*, 7th ed. Cham: Springer International Publishing, 2019.
[330] W. Jollie and R. M. Wynn, *Biology of the Uterus*, 2nd editio. Springer US, 1989.
[331] Yale Medical School, "Femal Reproductive System Lab," in *Histology*, p. Uterus.
[332] S. J. Holdsworth-Carson, M. Zaitseva, B. J. Vollenhoven, and P. A. Rogers, "Clonality of smooth muscle and fibroblast cell populations isolated from human fibroid and myometrial tissues," *Mol Hum Reprod*, vol. 20, no. 3, pp. 250–259, 2014.
[333] T. H. protein Atlas, "Endometrium," *SciLifeLab*. [Online]. Available: https://www.proteinatlas.org/learn/dictionary/normal/endometrium/anatomy. [Accessed: 12-Jun-2020].
[334] M. Uhlen *et al.*, "Towards a knowledge-based Human Protein Atlas," *Nat. Biotechnol.*, vol. 28, no. 12, pp. 1248–1250, Dec. 2010.
[335] J. Brosens, R. Campo, S. Gordts, and I. Brosens, "Submucous and outer myometrium leiomyomas are two distinct clinical entities.," *Fertility and sterility*, vol. 79, no. 6. United States, pp. 1452–1454, Jun-2003.
[336] R. E. Campbell, G. Gaidamaka, S.-K. Han, and A. E. Herbison, "Dendro-dendritic bundling and shared synapses between gonadotropin-releasing hormone neurons," *Proc. Natl. Acad. Sci. U. S. A.*, vol. 106, no. 26, pp. 10835–10840, Jun. 2009.
[337] K. J. Ryan, "Biochemistry of aromatase: significance to female reproductive physiology.," *Cancer Res.*, vol. 42, no. 8 Suppl, pp. 3342s-3344s, Aug. 1982.
[338] M. A. Clark, R. Finkel, J. A. Rey, and K. Whalen, *Pharmacology*, 5th ed. Baltimore, MD, USA: Lippincott Williams & Wilkins, 2011.
[339] J. G. Pierce and T. F. Parsons, "Glycoprotein Hormones: Structure and Function," *Annu. Rev. Biochem.*, vol. 50, no. 1, pp. 465–495, Jun. 1981.
[340] B. D. Sarkodie, B. O. Botwe, and E. K. Ofori, "Uterine fibroid characteristics and sonographic pattern among Ghanaian females undergoing pelvic ultrasound scan: a study at 3-major centres," *BMC Womens Heal.*, vol. 16, p. 10, 2016.
[341] S. E. Bulun, "Uterine fibroids," *N Engl J Med*, vol. 369, no. 14, pp. 1344–1355, 2013.
[342] E. A. Stewart, "Clinical practice. Uterine fibroids," *N Engl J Med*, vol. 372, no. 17, pp. 1646–1655, 2015.
[343] A. M. Soliman, H. Yang, E. X. Du, S. S. Kelkar, and C. Winkel, "The direct and indirect costs of uterine fibroid tumors: a systematic review of the literature between 2000 and 2013," *Am J Obs. Gynecol*, vol. 213, no. 2, pp. 141–160, 2015.
[344] A. M. Soliman, S. B. Anand, K. S. Coyne, J. Castelli-Haley, M. Snabes, and C. D. Owens, "Examining the Relationship Between Symptomatic Burden and Self-reported Productivity Losses Among Patients With Uterine Fibroids in the United States," *J Occup Env. Med*, vol. 59, no. 10, pp. 974–981, 2017.
[345] E. A. Stewart, W. K. Nicholson, L. Bradley, and B. J. Borah, "The burden of uterine fibroids for African-American women: results of a national survey," *J. Womens. Health (Larchmt).*, vol. 22, no. 10, pp. 807–816, 2013.
[346] (AFHSC) Armed Forces Health Surveillance Center, "Uterine fibroids, active component females, U.S. Armed Forces, 2001-2010," *MSMR*, vol. 18, no. 12, pp. 10–13, 2011.

[347] C. J. Zaloudek, M. R. Hendrickson, and R. A. Soslow, “Mesenchymal Tumors of the Uterus,” in *Blaustein’s Pathology of the Female Genital Tract*, 6th ed., R. J. Kurman, L. H. Ellenson, and B. M. Ronnett, Eds. Boston, MA: Springer US, 2011, pp. 453–527.
[348] H. Hricak *et al.*, “Uterine leiomyomas: correlation of MR, histopathologic findings, and symptoms,” *Radiology*, vol. 158, no. 2, pp. 385–391, 1986.
[349] H. Okizuka, K. Sugimura, M. Takemori, C. Obayashi, M. Kitao, and T. Ishida, “MR detection of degenerating uterine leiomyomas,” *J Comput Assist Tomogr*, vol. 17, no. 5, pp. 760–766, 1993.
[350] A. Tinelli and A. Malvasi, *Uterine Myoma, Myomectomy and Minimally Invasive Treatments*. Cham, Switzerland: Springer International Publishing, 2015.
[351] A. T. Khan, M. Shehmar, and J. K. Gupta, “Uterine fibroids: current perspectives,” *Int J Womens Heal.*, vol. 6, pp. 95–114, 2014.
[352] F. A. Aleem and M. Predanic, “The hemodynamic effect of GnRH agonist therapy on uterine leiomyoma vascularity: a prospective study using transvaginal color Doppler sonography.,” *Gynecol. Endocrinol.*, vol. 9, no. 3, pp. 253–258, Sep. 1995.
[353] S. Sudderuddin, E. Helbren, M. Telesca, R. Williamson, and A. Rockall, “MRI appearances of benign uterine disease,” *Clin Radiol*, vol. 69, no. 11, pp. 1095–1104, 2014.
[354] H. Ueda *et al.*, “Unusual appearances of uterine leiomyomas: MR imaging findings and their histopathologic backgrounds,” *Radiographics*, vol. 19 Spec No, pp. S131-45, 1999.
[355] E. Uthman, “Leiomyoma of the Uterus,” *Web Pathology*, 2020. [Online]. Available: https://www.webpathology.com/image.asp?case=570&n=1.
[356] R. Malik and G. Agarwaal, “A large cystic degenerating broad ligament leiomyoma masquerading as ovarian malignancy,” *J. Case Reports*, vol. 5, no. 2, pp. 486–489, 2015.
[357] S. Pal, S. Mondal, P. Mondal, G. Raychaudhuri, R. Pradhan, and S. Banerjee, “Severely calcified leiomyoma of broad ligament in a postmenopausal woman: Report of a rare case,” *J. Midlife. Health*, vol. 7, pp. 147–149, 2016.
[358] A. S. El-Agwany, “Myxoid degeneration in a huge uterine leiomyoma: An unusual benign pathology mimiking malignancy,” *Arch. Perinat. Med.*, vol. 20, no. 2, pp. 116–118, 2014.
[359] Y. Mikami, “Histopathology of Uterine Leiomyoma,” 2018, pp. 1–21.
[360] S. Wilde and S. Scott-Barrett, “Radiological appearances of uterine fibroids,” *Indian J. Radiol. Imaging*, vol. 19, no. 3, pp. 222–231, 2009.
[361] E. Murase, E. S. Siegelman, E. K. Outwater, L. A. Perez-Jaffe, and R. W. Tureck, “Uterine leiomyomas: histopathologic features, MR imaging findings, differential diagnosis, and treatment,” *Radiographics*, vol. 19, no. 5, pp. 1179–1197, 1999.
[362] D. P. Mayer and V. Shipilov, “Ultrasonography and magnetic resonance imaging of uterine fibroids,” *Obs. Gynecol Clin North Am*, vol. 22, no. 4, pp. 667–725, 1995.
[363] C. Aydin, S. Eriş, Y. Yalçin, and H. Sen Selim, “A giant cystic leiomyoma mimicking an ovarian malignancy,” *Int. J. Surg. Case Rep.*, vol. 4, no. 11, pp. 1010–1012, 2013.
[364] Y. O. Tanaka, M. Nishida, H. Tsunoda, Y. Okamoto, and H. Yoshikawa, “Smooth muscle tumors of uncertain malignant potential and leiomyosarcomas of the uterus: MR findings.,” *J. Magn. Reson. Imaging*, vol. 20, no. 6, pp. 998–1007, Dec. 2004.
[365] T. Aung *et al.*, “Uterine lipoleiomyoma: a histopathological review of 17 cases.,” *Pathol. Int.*, vol. 54, no. 10, pp. 751–758, Oct. 2004.
[366] X. Wang, D. Kumar, and J. D. Seidman, “Uterine lipoleiomyomas: a clinicopathologic study of 50 cases.,” *Int. J. Gynecol. Pathol.*, vol. 25, no. 3, pp. 239–242, Jul. 2006.
[367] J. Scurry and M. Hack, “Leiomyosarcoma arising in a lipoleiomyoma.,” *Gynecol. Oncol.*, vol. 39, no. 3, pp. 381–383, Dec. 1990.
[368] M. G. Munro, H. O. Critchley, M. S. Broder, and I. S. Fraser, “FIGO classification system (PALM-COEIN) for causes of abnormal uterine bleeding in nongravid women of reproductive age,” *Int J*

Gynaecol Obs., vol. 113, no. 1, pp. 3–13, 2011.
[369] G. E. Courtoy, J. Donnez, E. Marbaix, and M. M. Dolmans, "In vivo mechanisms of uterine myoma volume reduction with ulipristal acetate treatment," *Fertil Steril*, vol. 104, no. 2, pp. 426–34.e1, 2015.
[370] M. S. Islam, A. Ciavattini, F. Petraglia, M. Castellucci, and P. Ciarmela, "Extracellular matrix in uterine leiomyoma pathogenesis: a potential target for future therapeutics," *Hum. Reprod. Update*, vol. 24, no. 1, pp. 59–85, Jan. 2018.
[371] V. Medikare, L. R. Kandukuri, V. Ananthapur, M. Deenadayal, and P. Nallari, "The genetic bases of uterine fibroids; a review," *J Reprod Infertil*, vol. 12, no. 3, pp. 181–191, 2011.
[372] N. Chabbert-Buffet, N. Esber, and P. Bouchard, "Fibroid growth and medical options for treatment," *Fertil Steril*, vol. 102, no. 3, pp. 630–639, 2014.
[373] M. Ono *et al.*, "Role of stem cells in human uterine leiomyoma growth," *PLoS One*, vol. 7, no. 5, p. e36935, 2012.
[374] A. B. Moore *et al.*, "Human uterine leiomyoma-derived fibroblasts stimulate uterine leiomyoma cell proliferation and collagen type I production, and activate RTKs and TGF beta receptor signaling in coculture," *Cell Commun Signal*, vol. 8, p. 10, 2010.
[375] M. Zaitseva, B. J. Vollenhoven, and P. A. Rogers, "Retinoic acid pathway genes show significantly altered expression in uterine fibroids when compared with normal myometrium," *Mol Hum Reprod*, vol. 13, no. 8, pp. 577–585, 2007.
[376] A. A. Sandberg, "Updates on the cytogenetics and molecular genetics of bone and soft tissue tumors: leiomyoma," *Cancer Genet Cytogenet*, vol. 158, no. 1, pp. 1–26, 2005.
[377] E. A. N. V.-O. 16 Stewart 2019, "Differentiating uterine leiomyomas (fibroids) from uterine sarcomas," *UptoDate*. p. https://www.uptodate.com/contents/differentiating-, 2018.
[378] S. K. Laughlin-Tommaso and E. A. Stewart, "Moving Toward Individualized Medicine for Uterine Leiomyomas," *Obs. Gynecol*, vol. 132, no. 4, pp. 961–971, 2018.
[379] A. J. Tiltman, "The effect of progestins on the mitotic activity of uterine fibromyomas," *Int J Gynecol Pathol*, vol. 4, no. 2, pp. 89–96, 1985.
[380] D. D. Baird and D. B. Dunson, "Why is parity protective for uterine fibroids?," *Epidemiology*, vol. 14, no. 2, pp. 247–250, 2003.
[381] S. D. Peddada *et al.*, "Growth of uterine leiomyomata among premenopausal black and white women," *Proc Natl Acad Sci U S A*, vol. 105, no. 50, pp. 19887–19892, 2008.
[382] K. L. Gross and C. C. Morton, "Genetics and the development of fibroids," *Clin Obs. Gynecol*, vol. 44, no. 2, pp. 335–349, 2001.
[383] S. O. Okolo, C. C. Gentry, C. W. Perrett, and A. B. Maclean, "Familial prevalence of uterine fibroids is associated with distinct clinical and molecular features," *Hum Reprod*, vol. 20, no. 8, pp. 2321–2324, 2005.
[384] S. F. Cramer, J. Horiszny, A. Patel, and S. Sigrist, "The relation of fibrous degeneration to menopausal status in small uterine leiomyomas with evidence for postmenopausal origin of seedling myomas.," *Mod. Pathol. an Off. J. United States Can. Acad. Pathol. Inc*, vol. 9, no. 7, pp. 774–780, Jul. 1996.
[385] S. F. Cramer, C. Marchetti, J. Freedman, and A. Padela, "Relationship of myoma cell size and menopausal status in small uterine leiomyomas.," *Arch. Pathol. Lab. Med.*, vol. 124, no. 10, pp. 1448–1453, Oct. 2000.
[386] F. Loechel, J. W. Fox, G. Murphy, R. Albrechtsen, and U. M. Wewer, "ADAM 12-S cleaves IGFBP-3 and IGFBP-5 and is inhibited by TIMP-3," *Biochem Biophys Res Commun*, vol. 278, no. 3, pp. 511–515, 2000.
[387] A. Parker, C. Rees, J. Clarke, W. H. Busby Jr., and D. R. Clemmons, "Binding of insulin-like growth factor (IGF)-binding protein-5 to smooth-muscle cell extracellular matrix is a major determinant

of the cellular response to IGF-I," *Mol Biol Cell*, vol. 9, no. 9, pp. 2383–2392, 1998.
[388] G. Gullu, S. Karabulut, and M. Akkiprik, "Functional roles and clinical values of insulin-like growth factor-binding protein-5 in different types of cancers," *Chin J Cancer*, vol. 31, no. 6, pp. 266–280, 2012.
[389] S. Di Tommaso, A. Tinelli, A. Malvasi, and S. Massari, "Missense mutations in exon 2 of the MED12 gene are involved in IGF-2 overexpression in uterine leiomyoma," *Mol Hum Reprod*, vol. 20, no. 10, pp. 1009–1015, 2014.
[390] G. M. A. Ajabnoor *et al.*, "Expanded Somatic Mutation Spectrum of MED12 Gene in Uterine Leiomyomas of Saudi Arabian Women," *Front Genet*, vol. 9, p. 552, 2018.
[391] S. K. Halder, A. Laknaur, J. Miller, L. C. Layman, M. Diamond, and A. Al-Hendy, "Novel MED12 gene somatic mutations in women from the Southern United States with symptomatic uterine fibroids," *Mol. Genet. Genomics*, vol. 290, no. 2, pp. 505–511, 2015.
[392] E. M. Je, M. R. Kim, K. O. Min, N. J. Yoo, and S. H. Lee, "Mutational analysis of MED12 exon 2 in uterine leiomyoma and other common tumors," *Int J Cancer*, vol. 131, no. 6, pp. E1044-7, 2012.
[393] D. N. Markowski, S. Bartnitzke, T. Loning, N. Drieschner, B. M. Helmke, and J. Bullerdiek, "MED12 mutations in uterine fibroids--their relationship to cytogenetic subgroups," *Int J Cancer*, vol. 131, no. 7, pp. 1528–1536, 2012.
[394] M. M. McGuire, A. Yatsenko, L. Hoffner, M. Jones, U. Surti, and A. Rajkovic, "Whole exome sequencing in a random sample of North American women with leiomyomas identifies MED12 mutations in majority of uterine leiomyomas," *PLoS One*, vol. 7, no. 3, p. e33251, 2012.
[395] M. Fedele *et al.*, "Overexpression of the HMGA2 gene in transgenic mice leads to the onset of pituitary adenomas," *Oncogene*, vol. 21, no. 20, p. 12, 2002.
[396] J. C. Hodge *et al.*, "Expression profiling of uterine leiomyomata cytogenetic subgroups reveals distinct signatures in matched myometrium: transcriptional profilingof the t(12;14) and evidence in support of predisposing genetic heterogeneity," *Hum Mol Genet*, vol. 21, no. 10, pp. 2312–2329, 2012.
[397] J. Zhou *et al.*, "Deletion of the paired alpha 5(IV) and alpha 6(IV) collagen genes in inherited smooth muscle tumors," *Science (80-.).*, vol. 261, no. 5125, p. 1167, 1993.
[398] M. Sugimoto, T. Oohashi, and Y. Ninomiya, "The genes COL4A5 and COL4A6, coding for basement membrane collagen chains alpha 5(IV) and alpha 6(IV), are located head-to-head in close proximity on human chromosome Xq22 and COL4A6 is transcribed from two alternative promoters," *Proc. Natl. Acad. Sci.*, vol. 91, no. 24, p. 11679, 1994.
[399] X. Wang *et al.*, "Missense mutations in COL4A5 or COL4A6 genes may cause cerebrovascular fibromuscular dysplasia: Case report and literature review," *Medicine (Baltimore).*, vol. 97, no. 30, pp. e11538–e11538, 2018.
[400] J. Khoshnoodi, V. Pedchenko, and B. G. Hudson, "Mammalian collagen IV," *Microsc Res Tech*, vol. 71, no. 5, pp. 357–370, 2008.
[401] B. H. Qu, M. Karas, A. Koval, and D. LeRoith, "Insulin receptor substrate-4 enhances insulin-like growth factor-I-induced cell proliferation," *J Biol Chem*, vol. 274, no. 44, pp. 31179–31184, 1999.
[402] R. Lehtonen *et al.*, "Biallelic Inactivation of Fumarate Hydratase (FH) Occurs in Nonsyndromic Uterine Leiomyomas but Is Rare in Other Tumors," *Am. J. Pathol.*, vol. 164, no. 1, p. 6, 2004.
[403] D. Malhotra *et al.*, "Global mapping of binding sites for Nrf2 identifies novel targets in cell survival response through ChIP-Seq profiling and network analysis," *Nucleic Acids Res*, vol. 38, no. 17, pp. 5718–5734, 2010.
[404] N. Krishnamurthy and R. Kurzrock, "Targeting the Wnt/beta-catenin pathway in cancer: Update on effectors and inhibitors," *Cancer Treat Rev*, vol. 62, pp. 50–60, 2018.
[405] S. Hinuma *et al.*, "A prolactin-releasing peptide in the brain," *Nature*, vol. 393, no. 6682, pp. 272–276, 1998.

[406] B. V Varghese *et al.*, “Loss of the repressor REST in uterine fibroids promotes aberrant G protein-coupled receptor 10 expression and activates mammalian target of rapamycin pathway,” *Proc Natl Acad Sci U S A*, vol. 110, no. 6, pp. 2187–2192, 2013.
[407] L. A. Wise, J. R. Palmer, E. A. Stewart, and L. Rosenberg, “Polycystic ovary syndrome and risk of uterine leiomyomata,” *Fertil. Steril.*, vol. 87, no. 5, pp. 1108–1115, May 2007.
[408] L. A. Wise *et al.*, “Reproductive factors, hormonal contraception, and risk of uterine leiomyomata in African-American women: a prospective study.,” *Am. J. Epidemiol.*, vol. 159, no. 2, pp. 113–123, Jan. 2004.
[409] D. R. Velez Edwards, D. D. Baird, and K. E. Hartmann, “Association of age at menarche with increasing number of fibroids in a cohort of women who underwent standardized ultrasound assessment,” *Am J Epidemiol*, vol. 178, no. 3, pp. 426–433, 2013.
[410] E. Faerstein, M. Szklo, and N. Rosenshein, “Risk factors for uterine leiomyoma: a practice-based case-control study. I. African-American heritage, reproductive history, body size, and smoking,” *Am J Epidemiol*, vol. 153, no. 1, pp. 1–10, 2001.
[411] L. A. Wise *et al.*, “Influence of body size and body fat distribution on risk of uterine leiomyomata in U.S. black women.,” *Epidemiology*, vol. 16, no. 3, pp. 346–354, May 2005.
[412] W. D. Schlaff, E. A. Zerhouni, J. A. Huth, J. Chen, M. D. Damewood, and J. A. Rock, “A placebo-controlled trial of a depot gonadotropin-releasing hormone analogue (leuprolide) in the treatment of uterine leiomyomata,” *Obs. Gynecol*, vol. 74, no. 6, pp. 856–862, 1989.
[413] V. Bardsley, P. Cooper, and D. S. Peat, “Massive lymphocytic infiltration of uterine leiomyomas associated with GnRH agonist treatment,” *Histopathology*, vol. 33, no. 1, pp. 80–82, 1998.
[414] S. R. Howe, J. I. Everitt, M. M. Gottardis, and C. Walker, “Estrogen/antiestrogen responsiveness in an in vivo/in vitro model for myometrial tumorigenesis.,” *Ann. N. Y. Acad. Sci.*, vol. 761, pp. 373–375, Jun. 1995.
[415] S. R. Howe, M. M. Gottardis, J. I. Everitt, T. L. Goldsworthy, D. C. Wolf, and C. Walker, “Rodent model of reproductive tract leiomyomata. Establishment and characterization of tumor-derived cell lines.,” *Am. J. Pathol.*, vol. 146, no. 6, pp. 1568–1579, Jun. 1995.
[416] K. D. Burroughs, R. Fuchs-Young, B. Davis, and C. L. Walker, “Altered hormonal responsiveness of proliferation and apoptosis during myometrial maturation and the development of uterine leiomyomas in the rat.,” *Biol. Reprod.*, vol. 63, no. 5, pp. 1322–1330, Nov. 2000.
[417] T. Fotsis *et al.*, “Genistein, a dietary-derived inhibitor of in vitro angiogenesis.,” *Proc. Natl. Acad. Sci. U. S. A.*, vol. 90, no. 7, pp. 2690–2694, Apr. 1993.
[418] Y. Sadovsky, P. J. Kushner, J. M. Roberts, and R. K. Riemer, “Restoration of estrogen-dependent progesterone receptor expression in a uterine myocyte cell line.,” *Endocrinology*, vol. 132, no. 4, pp. 1609–1613, Apr. 1993.
[419] A. D. Adams, S. Hild-Petito, K. Donnelly, and A. T. Fazleabas, “Regulation of estrogen (E) and progestin (p) receptors (R) in leiomyomas during the cycle and leuprolide acetate treatment,” in *Proceedings of the forty-ninth annual meeting of the American Fertility Society*, 1993.
[420] D. D. Brandon *et al.*, “Progesterone receptor messenger ribonucleic acid and protein are overexpressed in human uterine leiomyomas.,” *Am. J. Obstet. Gynecol.*, vol. 169, no. 1, pp. 78–85, Jul. 1993.
[421] J. Fujimoto, R. Hirose, S. Ichigo, H. Sakaguchi, Y. Li, and T. Tamaya, “Expression of progesterone receptor form A and B mRNAs in uterine leiomyoma.,” *Tumour Biol.*, vol. 19, no. 2, pp. 126–131, 1998.
[422] W. T. Mixson and D. O. Hammond, “Response of fibromyomas to a progestin,” *Am. J. Obstet. Gynecol.*, vol. 82, pp. 754–60, 1961.
[423] B. R. Carr *et al.*, “An evaluation of the effect of gonadotropin-releasing hormone analogs and medroxyprogesterone acetate on uterine leiomyomata volume by magnetic resonance imaging:

a prospective, randomized, double blind, placebo-controlled, crossover trial.," *J. Clin. Endocrinol. Metab.*, vol. 76, no. 5, pp. 1217–1223, May 1993.
[424] A. J. Friedman *et al.*, "A prospective, randomized trial of gonadotropin-releasing hormone agonist plus estrogen-progestin or progestin 'add-back' regimens for women with leiomyomata uteri.," *J. Clin. Endocrinol. Metab.*, vol. 76, no. 6, pp. 1439–1445, Jun. 1993.
[425] T. Maruo *et al.*, "Effects of progesterone on uterine leiomyoma growth and apoptosis.," *Steroids*, vol. 65, no. 10–11, pp. 585–592, 2000.
[426] K. Kawaguchi *et al.*, "Immunohistochemical analysis of oestrogen receptors, progesterone receptors and Ki-67 in leiomyoma and myometrium during the menstrual cycle and pregnancy.," *Virchows Arch. A. Pathol. Anat. Histopathol.*, vol. 419, no. 4, pp. 309–315, 1991.
[427] A. Segaloff and J. C. Weed, "The progesterone therapy of human uterine leiomyomas.," *J. Clin. Endocrinol. Metab.*, vol. 9, no. 12, pp. 1273–91, illust, Dec. 1949.
[428] Z. Ying and Z. Weiyuan, "Dual actions of progesterone on uterine leiomyoma correlate with the ratio of progesterone receptor A:B.," *Gynecol. Endocrinol.*, vol. 25, no. 8, pp. 520–523, Aug. 2009.
[429] M. S. Islam *et al.*, "Complex networks of multiple factors in the pathogenesis of uterine leiomyoma.," *Fertil. Steril.*, vol. 100, no. 1, pp. 178–193, Jul. 2013.
[430] M. S. Rein, R. L. Barbieri, and A. J. Friedman, "Progesterone: a critical role in the pathogenesis of uterine myomas.," *Am. J. Obstet. Gynecol.*, vol. 172, no. 1 Pt 1, pp. 14–18, Jan. 1995.
[431] S. M. Hyder and G. M. Stancel, "Regulation of angiogenic growth factors in the female reproductive tract by estrogens and progestins.," *Mol. Endocrinol.*, vol. 13, no. 6, pp. 806–811, Jun. 1999.
[432] K. D. Burroughs, S. R. Howe, Y. Okubo, R. Fuchs-Young, D. LeRoith, and C. L. Walker, "Dysregulation of IGF-I signaling in uterine leiomyoma.," *J. Endocrinol.*, vol. 172, no. 1, pp. 83–93, Jan. 2002.
[433] R. F. Nicosia and S. Villaschi, "Autoregulation of angiogenesis by cells of the vessel wall.," *Int. Rev. Cytol.*, vol. 185, pp. 1–43, 1999.
[434] L. C. Giudice *et al.*, "Insulin-like growth factor (IGF), IGF binding protein (IGFBP), and IGF receptor gene expression and IGFBP synthesis in human uterine leiomyomata.," *Hum. Reprod.*, vol. 8, no. 11, pp. 1796–1806, Nov. 1993.
[435] C. C. Gentry, S. O. Okolo, L. F. Fong, J. C. Crow, A. B. Maclean, and C. W. Perrett, "Quantification of vascular endothelial growth factor-A in leiomyomas and adjacent myometrium.," *Clin. Sci. (Lond).*, vol. 101, no. 6, pp. 691–695, Dec. 2001.
[436] J. Donnez, P. Smoes, S. Gillerot, F. Casanas-Roux, and M. Nisolle, "Vascular endothelial growth factor (VEGF) in endometriosis," *Hum. Reprod.*, vol. 13, no. 6, pp. 1686–1690, Jun. 1998.
[437] P. Peitsidis and R. Agrawal, "Role of vascular endothelial growth factor in women with PCO and PCOS: a systematic review," *Reprod. Biomed. Online*, vol. 20, no. 4, pp. 444–452, Apr. 2010.
[438] E. D. Levens, R. Wesley, A. Premkumar, W. Blocker, and L. K. Nieman, "Magnetic resonance imaging and transvaginal ultrasound for determining fibroid burden: implications for research and clinical care," *Am J Obs. Gynecol*, vol. 200, no. 5, pp. 537.e1–7, 2009.
[439] M. Dueholm, E. Lundorf, E. S. Hansen, S. Ledertoug, and F. Olesen, "Accuracy of magnetic resonance imaging and transvaginal ultrasonography in the diagnosis, mapping, and measurement of uterine myomas," *Am J Obs. Gynecol*, vol. 186, no. 3, pp. 409–415, 2002.
[440] B. H. Gross, T. M. Silver, and M. H. Jaffe, "Sonographic features of uterine leiomyomas: analysis of 41 proven cases," *J. Ultrasound Med.*, vol. 2, no. 9, p. 6, 1983.
[441] C. R. Garcia and R. W. Tureck, "Submucosal leiomyomas and infertility," *Fertil Steril*, vol. 42, no. 1, pp. 16–19, 1984.
[442] S. L. Corson, "Hysteroscopic diagnosis and operative therapy of submucous myoma," *Obs. Gynecol Clin North Am*, vol. 22, no. 4, pp. 739–755, 1995.

[443] S. D. Quinn, J. Vedelago, E. Kashef, W. Gedroyc, and L. Regan, “Measurement of uterine fibroid volume: a comparative accuracy and validation of methods study,” *Eur J Obs. Gynecol Reprod Biol*, vol. 171, no. 1, pp. 161–165, 2013.
[444] G. D. Adamson, “Treatment of uterine fibroids: current findings with gonadotropin-releasing hormone agonists,” *Am J Obs. Gynecol*, vol. 166, no. 2, pp. 746–751, 1992.
[445] M. Engman, S. Granberg, A. R. Williams, C. X. Meng, P. G. Lalitkumar, and K. Gemzell-Danielsson, “Mifepristone for treatment of uterine leiomyoma. A prospective randomized placebo controlled trial,” *Hum Reprod*, vol. 24, no. 8, pp. 1870–1879, 2009.
[446] J. Magalhaes, J. M. Aldrighi, and G. R. de Lima, “Uterine volume and menstrual patterns in users of the levonorgestrel-releasing intrauterine system with idiopathic menorrhagia or menorrhagia due to leiomyomas,” *Contraception*, vol. 75, no. 3, pp. 193–198, 2007.
[447] M. J. Thrippleton *et al.*, “Unbiased and efficient estimation of the volume of the fibroid uterus using the Cavalieri method and magnetic resonance imaging,” *Reprod. Sci.*, vol. 22, no. 1, pp. 15–22, 2015.
[448] J. Shwayder and K. Sakhel, “Imaging for Uterine Myomas and Adenomyosis,” *J. Minim. Invasive Gynecol.*, vol. 21, no. 3, pp. 362–376, 2014.
[449] M. L. . Fogata and K. A. Jain, “Degenerating cystic uterine fibroid mimics an ovarian cyst in a pregnant patient,” *J. Ultrasound Med.*, vol. 25, no. 5, pp. 671–674, 2006.
[450] S. Karasick, A. S. Lev-Toaff, and M. E. Toaff, “Imaging of uterine leiomyomas,” *Am. J. Roentgenol.*, vol. 158, no. 4, pp. 799–805, 1992.
[451] O. Baltarowich, A. Kurtz, R. Pennell, L. Needleman, M. Vilaro, and B. Goldberg, “Pitfalls in the sonographic diagnosis of uterine fibroids,” *Am. J. Roentgenol.*, vol. 151, no. 4, pp. 725–728, Oct. 1988.
[452] B. D. Sarkodie, B. O. Botwe, and E. K. Ofori, “Uterine fibroid characteristics and sonographic pattern among Ghanaian females undergoing pelvic ultrasound scan: a study at 3-major centres,” *BMC Womens. Health*, vol. 16, no. 1, p. 10, 2016.
[453] P. L. Williams, S. L. Laifer-Narin, and N. Ragavendra, “US of Abnormal Uterine Bleeding,” *RadioGraphics*, vol. 23, no. 3, pp. 703–718, May 2003.
[454] S. Pasrija, S. S. Trivedi, and M. K. Narula, “Prospective study of saline infusion sonohysterography in evaluation of perimenopausal and postmenopausal women with abnormal uterine bleeding,” *J Obs. Gynaecol Res*, vol. 30, no. 1, pp. 27–33, 2004.
[455] L. Bonnamy, H. Marret, F. Perrotin, G. Body, C. Berger, and J. Lansac, “Sonohysterography: a prospective survey of results and complications in 81 patients,” *Eur J Obs. Gynecol Reprod Biol*, vol. 102, no. 1, pp. 42–47, 2002.
[456] C. Farquhar, A. Ekeroma, S. Furness, and B. Arroll, “A systematic review of transvaginal ultrasonography, sonohysterography and hysteroscopy for the investigation of abnormal uterine bleeding in premenopausal women,” *Acta Obs. Gynecol Scand*, vol. 82, no. 6, pp. 493–504, 2003.
[457] S. Adusumilli *et al.*, “MRI of sonographically indeterminate adnexal masses,” *AJR Am J Roentgenol*, vol. 187, no. 3, pp. 732–740, 2006.
[458] K. W. Griffin, M. R. Ellis, and L. Wilder, “What is the appropriate diagnostic evaluation of fibroids?,” *J. Fam. Pract.*, vol. 54, no. 5, p. 3, 2017.
[459] C. P. Stamatopoulos *et al.*, “Value of Magnetic Resonance Imaging in Diagnosis of Adenomyosis and Myomas of the Uterus,” *J. Minim. Invasive Gynecol.*, vol. 19, no. 5, pp. 620–626, 2012.
[460] E. D. Levens, R. Wesley, A. Premkumar, W. Blocker, and L. K. Nieman, “Magnetic resonance imaging and transvaginal ultrasound for determining fibroid burden: implications for research and clinical care,” *Am. J. Obstet. Gynecol.*, vol. 200, no. 5, pp. 537.e1–7, May 2009.
[461] E. Cicinelli, “Transabdominal Sonohysterography, Transvaginal Sonography, and Hysteroscopy in the Evaluation of Submucous Myomas,” *Obstet. Gynecol.*, vol. 85, no. 1, pp. 42–47, Jan. 1995.

[462] S. S. Singh, “December 1st,” in *Personal Communication*, 2017.
[463] E. Murase, E. S. Siegelman, E. K. Outwater, L. A. Perez-Jaffe, and R. W. Tureck, “Uterine Leiomyomas: Histopathologic Features, MR Imaging Findings, Differential Diagnosis, and Treatment,” *RadioGraphics*, vol. 19, pp. 1179–1197, 1999.
[464] D. L. Berridge and T. C. Winter, “Saline infusion sonohysterography: technique, indications, and imaging findings,” *J Ultrasound Med*, vol. 23, no. 1, pp. 95–97, 2004.
[465] S. Goldstein, “Saline Infusion Sonohysterography,” *Clin. Obstet. Gynecol.*, vol. 39, no. 1, p. 11, 1996.
[466] L. Rogerson, J. Bates, M. Weston, and S. Duffy, “A comparison of outpatient hysteroscopy with saline infusion hysterosonography,” *Bjog*, vol. 109, no. 7, pp. 800–804, 2002.
[467] S. Dessole, M. Farina, G. Rubattu, E. Cosmi, G. Ambrosini, and G. Battista Nardelli, “Side effects and complications of sonohysterosalpingography,” *Fertil Steril*, vol. 80, no. 3, pp. 620–624, 2003.
[468] “ACOG technology assessment in obstetrics and gynecology, number 4, August 2005: hysteroscopy,” *Obs. Gynecol*, vol. 106, no. 2, pp. 439–442, 2005.
[469] “Technology assessment No. 7: Hysteroscopy,” *Obs. Gynecol*, vol. 117, no. 6, pp. 1486–1491, 2011.
[470] “Hysteroscopy. ACOG Technical Bulletin Number 191-April 1994,” *Int J Gynaecol Obs.*, vol. 45, no. 2, pp. 175–180, 1994.
[471] F. W. Jansen, C. B. Vredevoogd, K. van Ulzen, J. Hermans, J. B. Trimbos, and T. C. Trimbos-Kemper, “Complications of hysteroscopy: a prospective, multicenter study,” *Obs. Gynecol*, vol. 96, no. 2, pp. 266–270, 2000.
[472] M. Henri *et al.*, “Contribution of contrast-enhanced ultrasound with Sonovue to describe the microvascularization of uterine fibroid tumors before and after uterine artery embolization,” *Eur. J. Obstet. Gynecol. Reprod. Biol.*, vol. 181, pp. 104–110, 2014.
[473] A. Mas, M. Tarazona, J. Dasi Carrasco, G. Estaca, I. Cristobal, and J. Monleon, “Updated approaches for management of uterine fibroids,” *Int J Womens Heal.*, vol. 9, pp. 607–617, 2017.
[474] G. A. Vilos, “The Management of Uterine Leiomyomas,” *J. Obstet. Gynaecol. Canada*, vol. 37, no. 2, pp. 157–178, 2015.
[475] P. Y. Laberge, A. Murji, G. A. Vilos, C. Allaire, N. Leyland, and S. (Sony) Singh, “No. 389-Medical Management of Symptomatic Uterine Leiomyomas – An Addendum,” *J. Obstet. Gynaecol. Canada*, vol. 41, no. 10, pp. 1521–1524, 2019.
[476] “ACOG practice bulletin. Alternatives to hysterectomy in the management of leiomyomas,” *Obs. Gynecol*, vol. 112, no. 2 Pt 1, pp. 387–400, 2008.
[477] D. L. Clarke-Pearson and E. J. Geller, “Complications of hysterectomy,” *Obs. Gynecol*, vol. 121, no. 3, pp. 654–673, 2013.
[478] L. R. Boyd, A. P. Novetsky, and J. P. Curtin, “Effect of surgical volume on route of hysterectomy and short-term morbidity,” *Obs. Gynecol*, vol. 116, no. 4, pp. 909–915, 2010.
[479] L. A. Learman *et al.*, “A randomized comparison of total or supracervical hysterectomy: surgical complications and clinical outcomes,” *Obs. Gynecol*, vol. 102, no. 3, pp. 453–462, 2003.
[480] C. I. for H. Information, “Inpatient Hospitalizations, Surgeries and Newborn Indicators 2015-2016,” Canadian Institute for Health Information, 2016.
[481] H. Al-Fozan, J. Dufort, M. Kaplow, D. Valenti, and T. Tulandi, “Cost analysis of myomectomy, hysterectomy, and uterine artery embolization,” *Am J Obs. Gynecol*, vol. 187, no. 5, pp. 1401–1404, 2002.
[482] O. Sizzi *et al.*, “Italian multicenter study on complications of laparoscopic myomectomy,” *J. Minim. Invasive Gynecol.*, vol. 14, no. 4, pp. 453–462, 2007.
[483] L. A. Learman *et al.*, “A randomized comparison of total or supracervical hysterectomy: Surgical complications and clinical outcomes,” *Obstet. Gynecol.*, vol. 102, no. 3, pp. 453–462, 2003.

[484] P. Seinera, R. Arisio, A. Decko, C. Farina, and F. Crana, “Laparoscopic myomectomy: indications, surgical technique and complications,” *Hum Reprod*, vol. 12, no. 9, pp. 1927–1930, 1997.
[485] E. A. Stewart, “Uterine Fibroids,” *N. Engl. J. Med.*, vol. 372, no. 17, pp. 1646–1655, 2015.
[486] M. Lemyre, E. Bujold, R. Lathi, L. Bhagan, J. Q. Huang, and C. Nezhat, “Comparison of morbidity associated with laparoscopic myomectomy and hysterectomy for the treatment of uterine leiomyomas,” *J Obs. Gynaecol Can*, vol. 34, no. 1, pp. 57–62, 2012.
[487] M. Shiota, Y. Kotani, M. Umemoto, T. Tobiume, and H. Hoshiai, “Recurrence of uterine myoma after laparoscopic myomectomy: What are the risk factors?,” *Gynecol. Minim. Invasive Ther.*, vol. 1, no. 1, p. 3.
[488] M. P. Radosa *et al.*, “Long-term risk of fibroid recurrence after laparoscopic myomectomy,” *Eur J Obs. Gynecol Reprod Biol*, vol. 180, pp. 35–39, 2014.
[489] L. Fedele, F. Parazzini, L. Luchini, R. Mezzopane, L. Tozzi, and L. Villa, “Recurrence of fibroids after myomectomy: a transvaginal ultrasonographic study,” *Hum Reprod*, vol. 10, no. 7, pp. 1795–1796, 1995.
[490] E. H. Yoo *et al.*, “Predictors of leiomyoma recurrence after laparoscopic myomectomy,” *J Minim Invasive Gynecol*, vol. 14, no. 6, pp. 690–697, 2007.
[491] S. Al-Mahrizi and T. Tulandi, “Treatment of uterine fibroids for abnormal uterine bleeding: myomectomy and uterine artery embolization,” *Best Pr. Res Clin Obs. Gynaecol*, vol. 21, no. 6, pp. 995–1005, 2007.
[492] H. Al-Fozan, J. Dufort, M. Kaplow, D. Valenti, and T. Tulandi, “Cost analysis of myomectomy, hysterectomy, and uterine artery embolization,” *Am. J. Obstet. Gynecol.*, vol. 187, no. 5, pp. 1401–1404, 2002.
[493] Y. Kitamura *et al.*, “Imaging manifestations of complications associated with uterine artery embolization,” *Radiographics*, vol. 25 Suppl 1, pp. S119-32, 2005.
[494] E. A. Stewart, “Clinical practice. Uterine fibroids,” *N Engl J Med*, vol. 372, no. 17, pp. 1646–1655, Apr. 2015.
[495] M. Mara and K. Kubinova, “Embolization of uterine fibroids from the point of view of the gynecologist: pros and cons,” *Int. J. Womens. Health*, vol. 6, pp. 623–629, 2014.
[496] A. Hirst *et al.*, “A multi-centre retrospective cohort study comparing the efficacy, safety and cost-effectiveness of hysterectomy and uterine artery embolisation for the treatment of symptomatic uterine fibroids. The HOPEFUL study,” *Heal. Technol Assess*, vol. 12, no. 5, pp. 1–248, iii, 2008.
[497] M. M. Freed and J. B. Spies, “Uterine artery embolization for fibroids: a review of current outcomes,” *Semin Reprod Med*, vol. 28, no. 3, pp. 235–241, 2010.
[498] E. Zupi, M. Sbracia, D. Marconi, and M. G. Munro, “Myolysis of uterine fibroids: is there a role?,” *Clin Obs. Gynecol*, vol. 49, no. 4, pp. 821–833, 2006.
[499] H. Park, S. W. Yoon, and A. Sokolov, “Scaled signal intensity of uterine fibroids based on T2-weighted MR images: a potential objective method to determine the suitability for magnetic resonance-guided focused ultrasound surgery of uterine fibroids,” *Eur Radiol*, vol. 25, no. 12, pp. 3455–3458, 2015.
[500] W. P. Zhao, J. Y. Chen, and W. Z. Chen, “Effect of biological characteristics of different types of uterine fibroids, as assessed with T2-weighted magnetic resonance imaging, on ultrasound-guided high-intensity focused ultrasound ablation,” *Ultrasound Med Biol*, vol. 41, no. 2, pp. 423–431, 2015.
[501] H. Park, S. W. Yoon, and A. Sokolov, “Scaled signal intensity of uterine fibroids based on T2-weighted MR images: a potential objective method to determine the suitability for magnetic resonance-guided focused ultrasound surgery of uterine fibroids,” *Eur. Radiol.*, vol. 25, no. 12, pp. 3455–3458, 2015.
[502] W.-P. Zhao, J.-Y. Chen, and W.-Z. Chen, “Effect of Biological Characteristics of Different Types of

Uterine Fibroids, as Assessed with T2-Weighted Magnetic Resonance Imaging, on Ultrasound-Guided High-Intensity Focused Ultrasound Ablation," *Ultrasound Med. Biol.*, vol. 41, no. 2, pp. 423–431, Feb. 2015.
[503] A. Napoli *et al.*, "MR Imaging-guided Focused Ultrasound for Treatment of Bone Metastasis.," *Radiographics*, vol. 33, pp. 1555–68, 2013.
[504] A. N. Kurup and M. R. Callstrom, "Ablation of skeletal metastases: Current status," *J. Vasc. Interv. Radiol.*, vol. 21, no. SUPPL. 8, pp. S242–S250, 2010.
[505] N. A. Clark, S. L. Mumford, and J. H. Segars, "Reproductive impact of MRI-guided focused ultrasound surgery for fibroids: a systematic review of the evidence," *Curr Opin Obs. Gynecol*, vol. 26, no. 3, pp. 151–161, 2014.
[506] B. Naoulou and M. C. Tsai, "Efficacy of tranexamic acid in the treatment of idiopathic and non-functional heavy menstrual bleeding: a systematic review.," *Acta Obstet. Gynecol. Scand.*, vol. 91, no. 5, pp. 529–537, May 2012.
[507] A. Lethaby, K. Duckitt, and C. Farquhar, "Non-steroidal anti-inflammatory drugs for heavy menstrual bleeding.," *Cochrane database Syst. Rev.*, no. 1, p. CD000400, Jan. 2013.
[508] G. H. Sayed, M. S. Zakherah, S. A. El-Nashar, and M. M. Shaaban, "A randomized clinical trial of a levonorgestrel-releasing intrauterine system and a low-dose combined oral contraceptive for fibroid-related menorrhagia.," *Int. J. Gynaecol. Obstet.*, vol. 112, no. 2, pp. 126–130, Feb. 2011.
[509] U. S. Sangkomkamhang, P. Lumbiganon, M. Laopaiboon, and B. W. J. Mol, "Progestogens or progestogen-releasing intrauterine systems for uterine fibroids.," *Cochrane database Syst. Rev.*, no. 2, p. CD008994, Feb. 2013.
[510] R. L. Barbieri, "The use of Danazol as a treatment of endometriosis," in *Modern Approaches to Endometriosis*, E. Thomas and J. Rock, Eds. Dordrecht, Netherlands: Springer Science+Business Media, 2012, pp. 239–256.
[511] D. Panidis, D. Vavilis, D. Rousso, K. Stergiopoulos, and A. Kalogeropoulos, "Danazol influences gonadotropin secretion acting at the hypothalamic level.," *Int. J. Gynaecol. Obstet.*, vol. 45, no. 3, pp. 241–246, Jun. 1994.
[512] "ACOG practice bulletin. Surgical alternatives to hysterectomy in the management of leiomyomas. Number 16, May 2000 (replaces educational bulletin number 192, May 1994).," *Int. J. Gynaecol. Obstet.*, vol. 73, no. 3, pp. 285–293, Jun. 2001.
[513] L.-Q. Ke, K. Yang, J. Li, and C.-M. Li, "Danazol for uterine fibroids.," *Cochrane database Syst. Rev.*, no. 3, p. CD007692, Jul. 2009.
[514] H. Sumitani *et al.*, "In situ estrogen synthesized by aromatase P450 in uterine leiomyoma cells promotes cell growth probably via an autocrine/intracrine mechanism.," *Endocrinology*, vol. 141, no. 10, pp. 3852–3861, Oct. 2000.
[515] N. Duhan, S. Madaan, and J. Sen, "Role of the aromatase inhibitor letrozole in the management of uterine leiomyomas in premenopausal women," *Eur. J. Obstet. Gynecol. Reprod. Biol.*, vol. 171, no. 2, pp. 329–332, Dec. 2013.
[516] H. Song, D. Lu, K. Navaratnam, and G. Shi, "Aromatase inhibitors for uterine fibroids.," *Cochrane database Syst. Rev.*, no. 10, p. CD009505, Oct. 2013.
[517] N. Magon, "Gonadotropin releasing hormone agonists: Expanding vistas.," *Indian J. Endocrinol. Metab.*, vol. 15, no. 4, pp. 261–267, Oct. 2011.
[518] A. Lethaby, L. Puscasiu, and B. Vollenhoven, "Preoperative medical therapy before surgery for uterine fibroids.," *Cochrane database Syst. Rev.*, vol. 11, p. CD000547, Nov. 2017.
[519] J. Donnez *et al.*, "Ulipristal acetate versus leuprolide acetate for uterine fibroids.," *N. Engl. J. Med.*, vol. 366, no. 5, pp. 421–432, Feb. 2012.
[520] D. F. Archer *et al.*, "Elagolix for the management of heavy menstrual bleeding associated with uterine fibroids: results from a phase 2a proof-of-concept study.," *Fertil. Steril.*, vol. 108, no. 1,

pp. 152-160.e4, Jul. 2017.
[521] K. Chwalisz, M. C. Perez, D. Demanno, C. Winkel, G. Schubert, and W. Elger, “Selective progesterone receptor modulator development and use in the treatment of leiomyomata and endometriosis.,” *Endocr. Rev.*, vol. 26, no. 3, pp. 423–438, May 2005.
[522] Q. Shen, Y. Hua, W. Jiang, W. Zhang, M. Chen, and X. Zhu, “Effects of mifepristone on uterine leiomyoma in premenopausal women: a meta-analysis.,” *Fertil. Steril.*, vol. 100, no. 6, pp. 1710–1722, Dec. 2013.
[523] I. de Milliano, M. Twisk, J. C. Ket, J. A. Huirne, and W. J. Hehenkamp, “Pre-treatment with GnRHa or ulipristal acetate prior to laparoscopic and laparotomic myomectomy: A systematic review and meta-analysis.,” *PLoS One*, vol. 12, no. 10, p. e0186158, 2017.
[524] J. Donnez, G. E. Courtoy, and M. M. Dolmans, “Fibroid management in premenopausal women,” *Climacteric*, vol. 22, no. 1, pp. 27–33, 2019.
[525] Health Canada, “Health Canada safety review finds possible link between Fibristal and risk of liver injury,” 2019.
[526] J. Donnez *et al.*, “Long-term medical management of uterine fibroids with ulipristal acetate.,” *Fertil. Steril.*, vol. 105, no. 1, pp. 165-173.e4, Jan. 2016.
[527] B. C. J. M. Fauser *et al.*, “Safety after extended repeated use of ulipristal acetate for uterine fibroids.,” *PLoS One*, vol. 12, no. 3, p. e0173523, 2017.
[528] E. J. Chen, J. Novakofski, W. K. Jenkins, and W. D. O’Brien, “Young’s modulus measurements of soft tissues with application to elasticity imaging,” *IEEE Trans. Ultrason. Ferroelectr. Freq. Control*, vol. 43, no. 1, pp. 191–194, Jan. 1996.
[529] F. P. Beer and E. R. Johnston, *Mechanics of Materials*. New York, NY, USA: McGraw-Hill, 1981.
[530] P. H. Mott, J. R. Dorgan, and C. M. Roland, “The bulk modulus and Poisson’s ratio of ‘incompressible’ materials,” *J. Sound Vib.*, vol. 312, no. 4–5, pp. 572–575, May 2008.
[531] Y. K. Mariappan, K. J. Glaser, and R. L. Ehman, “Magnetic resonance elastography: A review,” *Clin. Anat.*, vol. 23, no. 5, pp. 497–511, Jun. 2010.
[532] D. L. Bartel, D. T. Davy, and T. M. Keaveny, “Orthopaedic Biomechanics: Mechanics and Design in Musculoskeletal Systems,” 1st editio., Upper Saddle River, NJ, USA: Pearson Higher Education & Professional Group, 2006.
[533] R. Chaney, K. Demars, and K. Farrag, “Development of an Accelerated Creep Testing Procedure for Geosynthetics, Part II: Analysis,” *Geotech. Test. J.*, vol. 21, no. 1, p. 38, 1998.
[534] P. N. T. Wells and H.-D. Liang, “Medical ultrasound: imaging of soft tissue strain and elasticity,” *J. R. Soc. Interface*, vol. 8, no. 64, pp. 1521–1549, Nov. 2011.
[535] A. Samani, J. Bishop, C. Luginbuhl, and D. B. Plewes, “Measuring the elastic modulus of ex vivo small tissue samples,” *Phys. Med. Biol.*, vol. 48, no. 14, pp. 2183–2198, Jul. 2003.
[536] S. Pereira, A. P. Frick, L. C. Poon, A. Zamprakou, and K. H. Nicolaides, “Successful induction of labor: prediction by preinduction cervical length, angle of progression and cervical elastography,” *Ultrasound Obstet. Gynecol.*, vol. 44, no. 4, pp. 468–475, Oct. 2014.
[537] A. Thomas, S. Kümmel, O. Gemeinhardt, and T. Fischer, “Real-Time Sonoelastography of the Cervix: Tissue Elasticity of the Normal and Abnormal Cervix,” *Acad. Radiol.*, vol. 14, no. 2, pp. 193–200, Feb. 2007.
[538] L. Sun *et al.*, “Is transvaginal elastography useful in pre-operative diagnosis of cervical cancer?,” *Eur. J. Radiol.*, vol. 81, no. 8, pp. e888–e892, Aug. 2012.
[539] F. S. Molina, L. F. Gómez, J. Florido, M. C. Padilla, and K. H. Nicolaides, “Quantification of cervical elastography: a reproducibility study,” *Ultrasound Obstet. Gynecol.*, vol. 39, no. 6, pp. 685–689, Jun. 2012.
[540] A. Fruscalzo, R. Schmitz, W. Klockenbusch, and J. Steinhard, “Reliability of Cervix Elastography in the Late First and Second Trimester of Pregnancy,” *Ultraschall der Medizin - Eur. J. Ultrasound*,

vol. 33, no. 07, pp. E101–E107, May 2012.
[541] A. Fruscalzo *et al.*, “Reliability of quantitative elastography of the uterine cervix in at-term pregnancies,” *J. Perinat. Med.*, vol. 41, no. 4, Jan. 2013.
[542] E. Hernandez-Andrade *et al.*, “Evaluation of cervical stiffness during pregnancy using semiquantitative ultrasound elastography,” *Ultrasound Obstet. Gynecol.*, vol. 41, no. 2, pp. 152–161, Feb. 2013.
[543] L. C. Carlson *et al.*, “Changes in shear wave speed pre- and post-induction of labor: a feasibility study,” *Ultrasound Obstet. Gynecol.*, vol. 46, no. 1, pp. 93–98, Jul. 2015.
[544] M. Swiatkowska-Freund and K. Preis, “Elastography of the uterine cervix: implications for success of induction of labor,” *Ultrasound Obstet. Gynecol.*, vol. 38, no. 1, pp. 52–56, Jul. 2011.
[545] H. S. Hwang, I. S. Sohn, and H. S. Kwon, “Imaging Analysis of Cervical Elastography for Prediction of Successful Induction of Labor at Term,” *J. Ultrasound Med.*, vol. 32, no. 6, pp. 937–946, Jun. 2013.
[546] A. Fruscalzo, A. Londero, C. Fröhlich, M. Meyer-Wittkopf, and R. Schmitz, “Quantitative Elastography of the Cervix for Predicting Labor Induction Success,” *Ultraschall der Medizin - Eur. J. Ultrasound*, vol. 36, no. 01, pp. 65–73, Feb. 2014.
[547] E. Hernandez-Andrade *et al.*, “Cervical strain determined by ultrasound elastography and its association with spontaneous preterm delivery,” *J. Perinat. Med.*, vol. 42, no. 2, Jan. 2014.
[548] K. Köbbing *et al.*, “Quantitative Elastography of the uterine cervix as a predictor of preterm delivery,” *J. Perinatol.*, vol. 34, no. 10, pp. 774–780, Oct. 2014.
[549] R. Lu, Y. Xiao, M. Liu, and D. Shi, “Ultrasound Elastography in the Differential Diagnosis of Benign and Malignant Cervical Lesions,” *J. Ultrasound Med.*, vol. 33, no. 4, pp. 667–671, Apr. 2014.
[550] Y. Xu *et al.*, “Strain elastography imaging for early detection and prediction of tumor response to concurrent chemo-radiotherapy in locally advanced cervical cancer: feasibility study,” *BMC Cancer*, vol. 17, no. 1, p. 427, Dec. 2017.

9 Appendices

9.1.1 Medical Imaging: Current Diagnosis and Characterization of Uterine Fibroids

While an experienced physician may be able to detect UFs and even accurately measure uterus size using bimanual palpation [123], visualization by medical imaging is required to diagnose UFs and to characterize the number, size, and position of UFs in the uterus. In the case of a woman presenting with symptoms characteristic of UFs [1], [2], [12], [341], [342], USI is the primary diagnostic imaging modality due to its availability, affordability, and ease of use [4], [362]. Depending on the size, number, and position of UFs in the uterus, more than 20% of UFs may remain undetected on USI [438]–[440]. As such, other imaging modalities have been applied to UFs including saline infused sonohysterography (SIS), hysteroscopy, and magnetic resonance imaging (MRI).

9.1.1.1 Classifying Uterine Fibroids by Medical Imaging

UFs tumors can be found anywhere in the myometrium [347] and are clinically classified according to position and size on medical imaging [4], [16], [17]. The International Federation of Gynecology (FIGO) classification system is the standard method for classifying UFs and uses a 0 to 8 integer scale to describe position in the uterus (Figure 42) [368]. A FIGO 0 UF is pedunculated into the uterine cavity, while a FIGO 8 UF is pedunculated off the uterine serosa. FIGO 2 through FIGO 7 UFs are scored by their relationship to the endometrium, myometrium and uterine serosa according to Figure 42 [368]. Submucosal UFs (FIGO 0, 1, 2) are the least common types of UFs, accounting for only 5% of UFs [340], [361], but are more likely to cause symptoms, due to their relationship to the endometrium [441], [442]. Intramural UFs (FIGO 3, 4, 5) are the most common types of UFs and are asymptomatic in many cases [340], [360]. Subserosal (FIGO 6, 7) UFs are below the uterine serosa, but project out of the uterus into the abdominal cavity, which can deform the shape of the uterus on medical imaging. Subserosal UFs

are often asymptomatic [361]; however they may become symptomatic if they obstruct adjacent organs or become pedunculated [360].

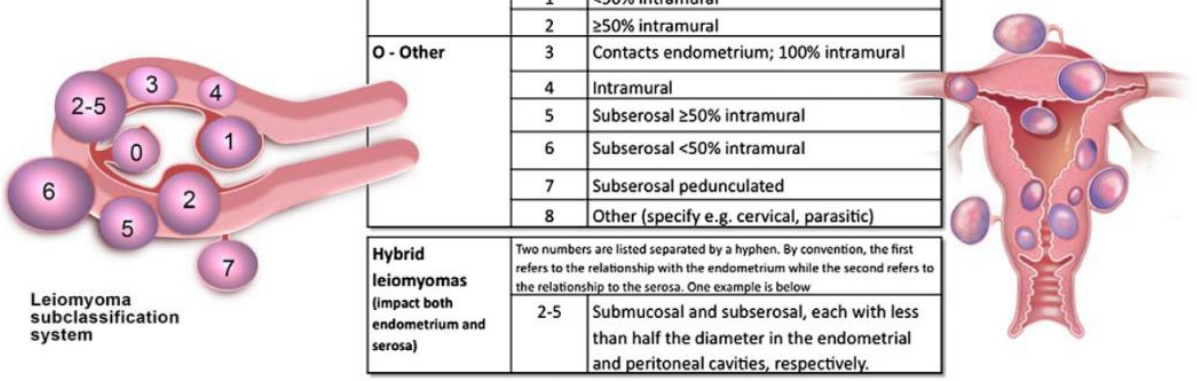

SM - Submucosal	0	Pedunculated intracavitary
	1	<50% intramural
	2	≥50% intramural
O - Other	3	Contacts endometrium; 100% intramural
	4	Intramural
	5	Subserosal ≥50% intramural
	6	Subserosal <50% intramural
	7	Subserosal pedunculated
	8	Other (specify e.g. cervical, parasitic)
Hybrid leiomyomas (impact both endometrium and serosa)	Two numbers are listed separated by a hyphen. By convention, the first refers to the relationship with the endometrium while the second refers to the relationship to the serosa. One example is below	
	2-5	Submucosal and subserosal, each with less than half the diameter in the endometrial and peritoneal cavities, respectively.

Figure 42 International Federation of Gynecology and Obstetrics (FIGO) classification of uterine fibroids by position in the myometrium with respect to the endometrium and serosa, as well as position in the uterus. Adapted with permission from [16], [368]. *© 2011 John Wiley and Sons*

Clinically, UFs are also described by size, where anteroposterior (d_a), transverse (d_t), and longitudinal (d_l) diameters are recorded, though sometimes only the maximum of these three diameters is used as a metric for tracking cases over time [381], [409], [443]. As well, the volume of a UF alone or volume of the uterus as a whole is often recorded [22], [23], [446], [447], [308], [309], [372], [381], [409], [443]–[445], using an ellipsoidal volume calculation ($V = \frac{\pi}{6} d_a d_t d_l$) (Figure 43). While the size and position of UFs in the uterus are important factors [292], they are less useful for differentiating cases that might better respond to less invasive treatments, such as medical therapy.

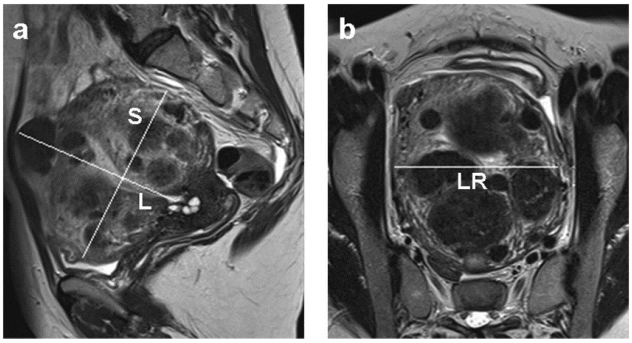

Figure 43 Measuring the volume of a myomatous uterus from MRI in the (a) sagittal and (b) transverse plane, where S is the longitudinal diameter, L is the anteroposterior diameter, and LR is the transverse diameter. Reproduced with permission from [447].

9.1.1.2 Ultrasound Imaging of Uterine Fibroids

USI refers to the use of ultrasonic energy to visualize the tissues in the body. Typically two to three ultrasound pulses are transmitted by the USI probe; as the pulses propagate through the tissue, they are attenuated due to absorption and scattering of the ultrasound energy. The pulses, which have been reflected back and backscattered from tissue and interfaces, are used to build an ultrasound image. UFs on USI are generally visible by irregularity in the uterine contour (76%), enlargement of the uterus (68%), and/or altered echo texture with respect to the myometrium (66%) [440]. The appearance of the UF tumors themselves is dependent on the ratio of fibrous tissue to smooth muscle and on any types of degeneration that are present [362]. On USI, UFs may be isoechoic with the myometrium [360] or have a hyperechoic border surrounding a heterogeneous region containing isoechoic, hyperechoic, and/or hypoechoic foci [360], [362].

Degeneration of UFs can alter echo appearance on USI. Degeneration usually yields a mixed heterogeneous echo pattern in UFs on USI [448]–[450]. Regions of calcification, hyalinization, or higher density tissue can yield hyperechoic foci with shadowing [360], [362], [448], [451], though hyperechoic appearance on USI has also been associated with lipoleiomyoma [360], [448]. Regions of cystic degeneration can appear as heterogeneous and hypo- or anechoic [56], [449], [451]–[453]. Regions of edema, hemorrhage, and necrosis increase heterogeneity on USI [360], [362]. The increased water content associated with these types of degeneration may also yield hypo- or anechoic regions; however, hypo- and anechoic appearances are also attributed to dilated lymphatic or blood vessels [360]. It is not known whether coagulative red degeneration will appear differently to hemorrhagic infarction on USI.

In a sample of 106 premenopausal women, Dueholm et al. [439] found that USI yielded 99% sensitivity and 91% specificity for diagnosing UFs, with pathology as a gold standard. Using a combination of methods as a gold standard (e.g. hysteroscopy, pathology, or “clinical survey”), two independent studies of USI for diagnosing UFs found sensitivity and specificity ranged from 53% to 85%

and 79% to 99%, respectively [438], [454], [455]. Further, a meta-analysis of nine USI studies with substantial heterogeneity expanded these ranges further, finding that sensitivity and specificity of USI for diagnosis of UFs could range from 21%-100% and 53%-100%, respectively [456]. USI is clearly an excellent tool for diagnosis and treatment planning in cases of symptomatic UFs; however, USI is purely a visualization tool and provides no information on potential suitability for less invasive treatment, such as medical therapy.

9.2 Review of Material Properties

9.2.1 Linear Elastic Materials

The mechanical properties of a material are generally derived from a material's response to external loading. In the case of linear elasticity, the stress (σ) applied to a material is defined as the ratio of average force applied to the surface of a material (F) along some axis over the undeformed cross-sectional area (A_0) of the material transverse to the axis of loading (Equation 20).

$$\sigma = \frac{F}{A_0} \tag{20}$$

If the stress applied to a material has a component coplanar with the material's surface, the component of the stress that is coplanar with the material's surface is referred to as shear stress (τ) or simple shear (Figure 44a), while the stress component perpendicular to the material surface is termed normal stress (Figure 45). An element within a material sample may also experience pure shear under axial compression (Figure 44b&c).

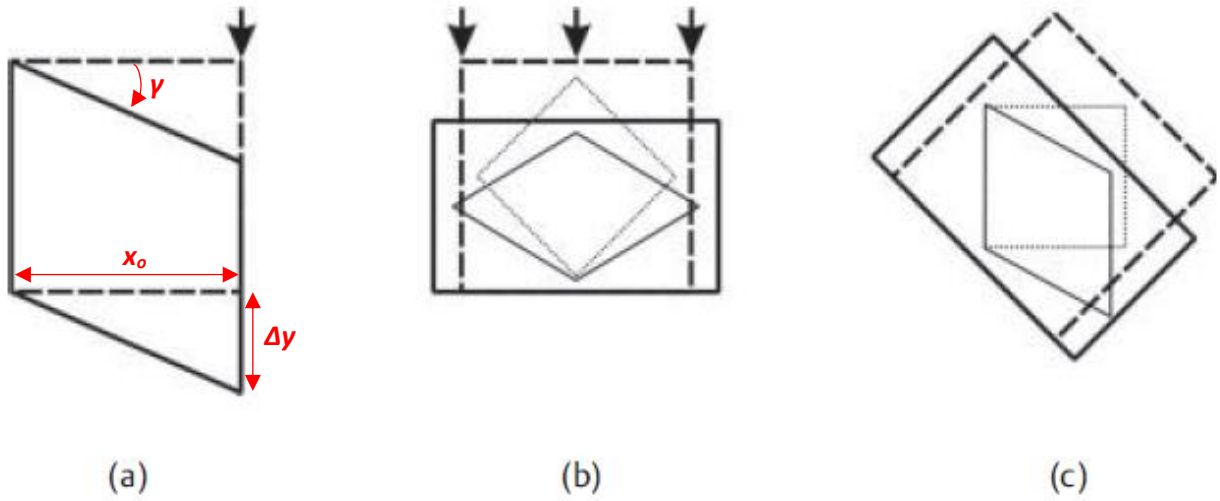

Figure 44 Simple shear caused by a force (black arrow) on an undeformed material cross-section (dotted rectangle) that is coplanar with the materials surface and results in a deformed (solid trapezoid) cross-section (a).The shear strain in the case of simple shear in (a) is the ratio of the deformation along the axis of the shear stress (Δy) over the length of the surface where the stress was applied (x_0). Pure shear is caused by a force (black arrow) distributed across the surface of an undeformed material cross-section (dotted rectangle) and results in axial compression (solid rectangle) of the material cross section (b). While (b) appears to be a case of normal stress, the shearing action of the applied load is revealed by observing the deformation of a diamond element in (b), which has a different shape than the material sample. The pure shear is more

readily visualized by rotating the scenario 45 degrees and observing how the undeformed diamond (finely dotted rectangle) experiences shear and yields a deformed cross section (solid trapezoid), while the overall material sample is subject to a volumetric compression. Reproduced with permission from [47]. *© Georg Thieme Verlag KG*

The strain (ε) that a material experiences along an axis is the ratio of the change in length (i.e. deformation) along that axis (Δx) over the undeformed length of that material along that axis (x_0; Equation 21; Figure 45). On the other hand, shear strain (γ) is the strain caused by shear stress, visualized in (Figure 44a). Shear strain may be defined as the angular deformation of a body (Figure 44a). Alternatively, the tangent of the shear strain may be defined as the ratio of the deformation along the axis of the shear stress (Δy) over the length of the surface to which the stress was applied (x_0) (Equation 22).

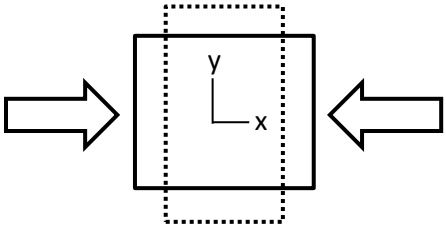

Figure 45 A material subject to strain along an axis (e.g. compression along the x-axis) will respond with some of strain along the perpendicular axis (e.g. expansion along the y-axis), the magnitude of which is determined by the material's Poisson's ratio.

$$\varepsilon_x = \frac{\Delta x}{x_0} \tag{21}$$

$$\tan(\gamma) = \frac{\Delta y}{x_0} \tag{22}$$

Isotropic materials are those which exhibit identical mechanical properties in all directions. When an isotropic material is strained along an axis ($d\varepsilon_x$; e.g. compression along the x-axis), in response it will exhibit strain along the perpendicular axes ($d\varepsilon_y$; $d\varepsilon_z$; e.g. expansion along the z-axis and y-axis), the magnitude and direction of which is determined by the Poisson's ratio (ν) of the material [528] (Equation 23; Figure 45). The Poisson's ratio can range from ν=0 (compressible) to ν=0.5 (incompressible) and most soft tissues are assumed to have 0.45<ν<0.50 [127], [529].

$$\nu = -\frac{d\varepsilon_y}{d\varepsilon_x} = -\frac{d\varepsilon_z}{d\varepsilon_x} \quad (23)$$

Linear elastic materials are those materials which exhibit a linear relationship between stress and strain, independent of time (or frequency). The stress-strain relationship for a linear elastic, isotropic material can then be quantified using one of three inter-related moduli: the Young's modulus (E), the shear modulus (G), or the bulk modulus (K) [127]. The Young's modulus (a.k.a. elastic modulus) for a linear elastic, isotropic material is defined as the ratio of stress to strain (Equation 24) [127]. The shear modulus, or modulus of rigidity, is the ratio of shear stress to shear strain and can also be defined in terms of the Young's modulus and Poisson's ratio for a linear elastic, isotropic material (Equation 25) [127]. The bulk modulus of a linear elastic, isotropic material describes resistance to compression and is defined using the Young's modulus and the Poisson's ratio (Equation 26) [127].

$$E = \frac{\sigma}{\varepsilon} \quad (24)$$

$$G = \frac{\tau}{\tan(\gamma)} = \frac{E}{2(1+\nu)} \quad (25)$$

$$K = \frac{E}{3(1-2\nu)} \quad (26)$$

It should be noted here that, for incompressible materials (ν=0.5) the shear modulus will be equal to 1/3 of the Young's modulus. However, for incompressible materials, the bulk modulus approaches infinity. Experimentally, all materials are compressible and the bulk modulus is finite, meaning that the Poisson's ratio can never truly be 0.5 [530].

9.2.2 Wave Propagation in Soft Tissues

The propagation of waves in soft tissue is related to the mechanical properties of those tissues. The two types of waves most relevant to SWE are longitudinal waves (pressure waves, p-waves) and shear waves (s-waves, transverse waves). Longitudinal waves involve a transfer of pressure and density between tissue elements and particle motion occurs along the axis of wave propagation (Figure 46a). Shear wave propagation involves the transfer of shear force and deformation between tissue elements and particle motion occurs perpendicular to the axis of wave propagation (Figure 46b).

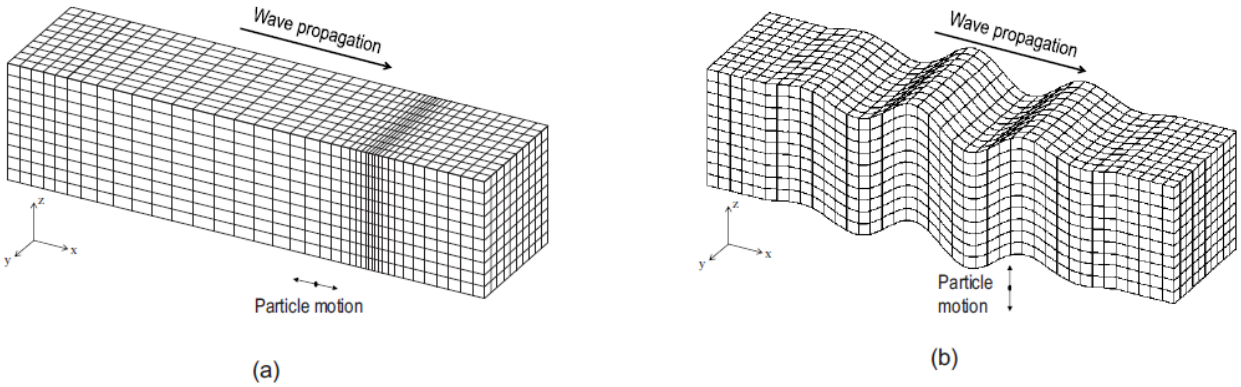

Figure 46 Longitudinal waves involve a transfer of pressure and density between tissue elements and particle motion occurs along the axis of wave propagation (a). Shear waves propagate involve transfers of shear force and deformation between tissue elements and particle motion occurs perpendicular to the axis of wave propagation (b). Reproduced with permission from [47]*. © Georg Thieme Verlag KG*

Ultrasound imaging uses the characteristics of transmitted and received sound (longitudinal) waves, at frequencies above human hearing (20kHz), to visualize the soft tissues in the body. The speed of sound waves (c_l) in soft tissue is a factor of the tissue density (ρ), the bulk modulus (K), and the shear modulus (G). However, in soft tissues K>>G (K~G$x10^6$) so the speed of sound in soft tissues is treated as a function of the bulk modulus and density alone (Equation 27). The speed of sound in soft tissues is approximately 1540m/s [47]. In contrast, SWE relates shear wave velocity (c_s) to the mechanical properties of soft tissues, where the speed of shear waves in soft tissue is a function of the density and

the shear modulus (Equation 28). Shear wave speed in soft tissue generally ranges between 1m/s and 10m/s [47].

$$c_l = \sqrt{\frac{1}{\rho}\left(K + \frac{4}{3}G\right)} \sim \sqrt{\frac{K}{\rho}} \tag{27}$$

$$c_s \sim \sqrt{\frac{G}{\rho}} = \sqrt{\frac{E}{2\rho(1+v)}} \tag{28}$$

From these definitions, it becomes apparent that the mechanical properties of the tissue are in fact the reason that UE is possible. Quasi-static tissue deformation during strain imaging can be visualized using USI. Although SWE employs transient excitation, because K>>G and similarly $c_l > c_s$ ($c_l \sim c_s x 10^3$), USI is still capable of visualizing shear waves propagating in the tissue during SWE. Moreover, the bulk modulus is fairly constant in all soft tissues, with only about 12% variability, while the shear modulus of soft tissue can vary by a factor of 10^5 [47]. This variability of the shear modulus in soft tissue allows for the possibility of much higher contrast between tissues of differing stiffness. However, shear viscosity causes high frequencies shear waves (>kHz) to attenuate rapidly in soft tissue [47], [191]. While higher frequency shear waves are required to yield effective spatial resolution, this rapid attenuation of high frequency waves means that only shallower depths can be imaged [531]. This results in a tradeoff between depth of target and resolution.

9.3 CellScale BioTester Resolution and Noise Floor

The resolution of the CellScale BioTester (CellScale, Waterloo, Canada) calculated for the 13 bit ADC and the 500 gram (4.905 N) load cell. The detectable voltage is +/- 300 mV. The calibration factor is 25 mV/V and 5 V excitation is used, so the system reaches 125 mV at full scale. Thus the percentage of the maximum range being used is $\frac{125mV}{600mV}$ or 20.83%. While the total number of steps available is 2^{13} or 8192 steps, with only 20.83% of the maximum range being used, there are 1706 steps used for digital conversion. The resolution of the system can then be calculated as to be 5.74 mN, as seen in the expression below.

$$Resolution = \frac{Load\ Cell\ Range}{Number\ of\ Steps} = \frac{\pm 4905mN}{1706\ steps} = \frac{9810mN}{1706\ steps} = 5.74mN$$

The noise floor of the CellScale Biotester (CellScale, Waterloo, Canada) was calculated by applying a constant load to the system. Data was acquired for approximately 30 seconds (Figure 47a), the loading bias was removed from the signal (Figure 47b), and the noise floor of the system was calculated, as the root mean square (RMS) error of the bias removed signal, to be 3.45mN.

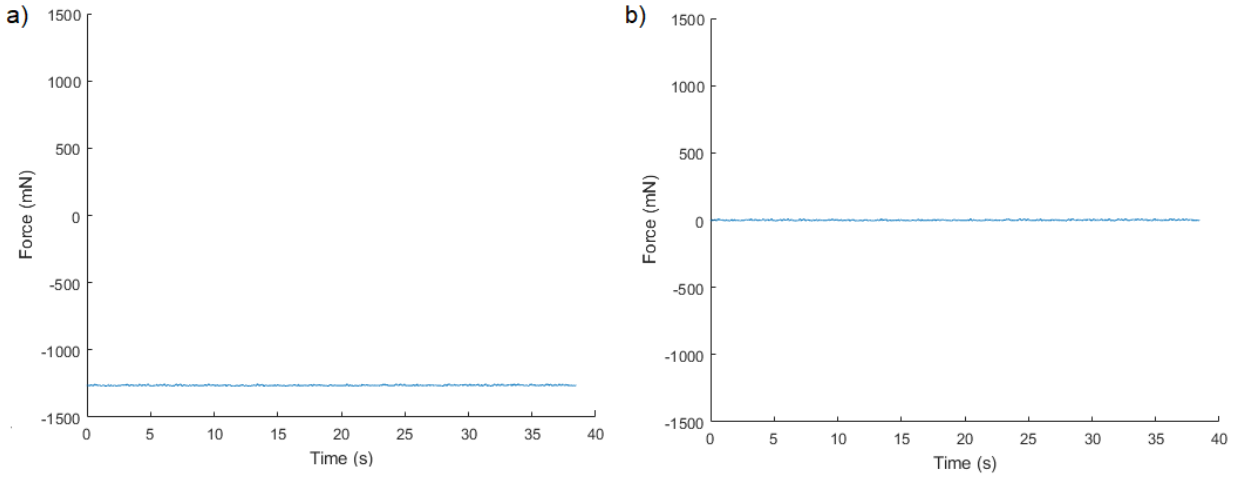

Figure 47 In order to calculate the noise floor of the CellScale Biotester (CellScale, Waterloo, Canada), the system was brought to a constant load and then load data was acquired for approximately 30 seconds (a). The bias from the loading on the signal was removed (b) and the noise floor was calculated as the root mean square error of the bias removed signal.

9.4 University of Ottawa Research Ethics Board Certificate of Approval

Université d'Ottawa
Bureau d'éthique et d'intégrité de la recherche

University of Ottawa
Office of Research Ethics and Integrity

H-08-18-790 - ANN3-790 - Certificat d'approbation éthique renouvelé / Certificate of Ethics Approval Renewed

(English message follows)

Cher/Chère Linda McLean,

Merci d'avoir soumis une demande de renouvellement pour le projet de recherche intitulé «Characterisation of tissue stiffness to improve the diagnosis and management of uterine fibroids».

Veuillez trouver ci-joint le certificat d'approbation éthique renouvelé, valide jusqu'au 08-07-2022.

NOTE: The expiry date of July 8, 2022 was set in accordance with the OHSN-REB ethics certificate approval dates.

Recherche financée : Veuillez faire suivre une copie du certificat renouvelé au Service de gestion de la recherche.

Si vous avez des questions, n'hésitez pas à communiquer avec le Bureau d'éthique à ethique@uottawa.ca ou en composant le 613-562-5387.

Vous pouvez voir votre demande en vous connectant à votre compte eReviews.

Cordialement,

Riana Marcotte
Responsable d'éthique en recherche

Ceci est une réponse automatisée, merci de ne pas répondre à ce courriel.

Dear Linda McLean,

Thank you for submitting a renewal request for your research project titled "Characterisation of tissue stiffness to improve the diagnosis and management of uterine fibroids".

Please find attached the renewed certificate of ethics approval, valid until 08-07-2022.

NOTE: The expiry date of July 8, 2022 was set in accordance with the OHSN-REB ethics certificate approval dates.

Funded research: A reminder that you must provide a copy of this certificate to Research Management Services.

If you have any questions, please contact the Ethics Office at ethics@uottawa.ca or by telephone at 613-562-5387.

You can view your project at any time by logging into eReviews.

Best regards,

Riana Marcotte
Protocol Officer

This is an automated message. Please do not reply directly to this email.

9.5 Telephone Recruitment and Screening Script

Hello.

This is [*Name of Research Team Member*] calling from the Ottawa Hospital. I am conducting a research study that will evaluate the potential for ultrasound to measure tissue stiffness of the uterus. Findings will be used to improve diagnosis and management for fibroids. You are being contacted because you are scheduled for [*hysterectomy or removal of fibroids*]. Participation in this study is voluntary.

Are you interested in hearing more about the study and your involvement as a potential participant?

[*If no, thank the participant for their time and consideration.*]

[*If yes, continue with script*]

The study requires participants to attend [*one or two*] ultrasound imaging sessions at the University of Ottawa prior to your surgery. Each session will take approximately 60 minutes total to complete. We will reimburse you for any costs incurred for parking on site or public transportation.

At the ultrasound imaging session you will have ultrasound scan performed. For this, an ultrasound wand will be inserted into your vagina while you are lying down on you back on an ultrasound table. Stiffness of your uterus and fibroids will be measured using a special ultrasound setting called shear wave elastography. You will be allowed to take a break or stop at any time during the session.

We will also be collecting samples from the tissues removed during your surgery which will be tested in a machine that measures stiffness. The stiffness measured in the ultrasound will be compared to the stiffness measured by the machine. Additional personal health information from

your medical records including your medical history, referring diagnosis, procedures had (if any), and pathology report after surgery will also be collected.

If you are interested in participating we will set up a time that is convenient for you to come to our lab at the University of Ottawa. Upon arrival at the lab you will be met by a member of our research team and be provided with an Informed Consent Form. You will be given as much time as you like to review the consent form and ask any questions or address any concerns you may have. We can also send you a full consent form before your first scheduled session to review at your convenience. After you have reviewed the consent form, we will ask you again if you are still willing to participate in the study. If you still agree then we will get you to sign the Informed Consent form. No data or personal information will be recorded until you have signed the Informed Consent form.

Do you agree to participate in this study knowing that you can withdraw at any point with no consequences to you?

[If yes, schedule a meeting date and thank the participant for their time.]

[If no, thank the participant for their time and consideration.]

9.6 Control and Asymptomatic Fibroid Groups Letter of Information and Informed Consent

Title of Study: Characterization of tissue stiffness to improve the diagnosis and management of uterine fibroids.

Principal Investigator (PI)
Sukhbir S. Singh, MD, FRCSC

Co-Investigators (Co-I)
Vincent della Zazzera, MD, FRCSC
Linda McLean, PT, PHD
Michel Labrosse, PhD, PEng
Teresa Flaxman, PhD
Catorina Czyrnyj, PhD (c)
Sarah Strickland, MD, FRCPC,

Sponsor: The Ottawa Hospital Research Institute

Participation in this study is voluntary. Please read through this Participant Informed Consent Form carefully before you decide if you would like to participate. Ask as many questions as you like. We encourage you to discuss your options with family, friends or your healthcare team.

Why am I being given this form?
You are being asked to participate in this research study because you are a healthy woman, aged at least 18 years old, have regular menstrual cycles, and have no gynecological medical history.

Why is this study being done?
Uterine fibroids are the most common gynecological condition, with prevalence up to 70% in premenopausal women. Up to 50% of women with uterine fibroids experience symptoms such as heavy menstrual cycles, increased abdominal pressure, and infertility.

Currently, transvaginal ultrasound is the standard method for diagnosing uterine fibroids and identifying the number, size and location of the fibroids. However, there are different types of fibroids that cannot be differentiated with ultrasound. Knowledge of a patient's fibroid type can help physicians decide the best treatment. The different fibroid types can be classified according to their stiffness because they range from very hard to very soft. A new transvaginal ultrasound

technology, called shear wave elastography, was developed to measure tissue stiffness but it has not been used clinically in gynecology. The ability to reliably and accurately measure uterine tissue and fibroid stiffness with shear wave elastography is unknown. It is however approved by Health Canada for use and is currently used to screen for breast cancer and liver cirrhosis.

The goal of this study is to evaluate stiffness characteristics of healthy uterine tissue and uterine fibroids. We will also determine if stiffness characteristics can be used to classify the different types of uterine fibroids.

Furthermore, the effect of the following on uterine tissue stiffness is unknown:

- Age
- History of pregnancy
- Use of contraception
- The presence of fibroids on stiffness of the unaffected uterine tissue
- Use of medication specific for management symptoms associated with uterine fibroids

Data from healthy participants will be compared to participants with uterine fibroids to better understand these relationships. Findings from this study will contribute to a future research study to determine if shear wave elastography can improve the diagnosis and monitoring of uterine fibroids such that physicians make more informed medical and surgical management decisions.

What is expected of me?

If you choose to participate you will take part in two ultrasound imaging sessions at the University of Ottawa, spaced 2-3 days apart. Each session will take approximately 60 minutes to complete and will be conducted at a time convenient to you. The ultrasound imaging sessions will involve an ultrasound wand being inserted into your vagina while you are lying on your back on an ultrasound table. Stiffness of your uterus will be measured using several ultrasound settings. The ultrasound procedures will be the same at each session. At the first ultrasound imaging session, you will also be asked to complete a set of questionnaires about your medical history, current symptoms (if any), and quality of life. The questionnaires will take approximately 15 minutes to complete. Some of these questionnaires will be available in English only.

The transvaginal ultrasounds will be performed in a private room at the Motor Function and Movement Laboratory at the University of Ottawa by Physiotherapist, Linda MacLean and/or her student, Catorina Czyrnyj, who have both been trained on the procedure.

We estimate that 90 participants will be enrolled in this study, including 60 healthy volunteers from The Ottawa Hospital and the University of Ottawa.

Will my research data be used in future research?

Your research data will be de-identified and securely stored at the Ottawa Hospital for 10 years. Only de-identified data will be used in future research projects relating to uterine fibroids. All future research conducted with your data will be approved by a Research Ethics Board before it begins.

How long will I be involved in the study?
The entire study will last approximately 2 years. Your participation in the study will be completed once you complete the two ultrasound imaging sessions.

What are the potential risks I may experience?
The risks involved in participating in this study are minimal.
There is a risk of distress from the ultrasound imaging session: a slender transducer of the ultrasound device is inserted into the vagina, thus depicting the pelvic organs. The ultrasound examination through the vagina is not painful; it has no more impact than any gynecological examination. If you have experienced discomfort during a recent gynecological exam, then you should decline to participate in this study. To date, there have been no descriptions of biological effects on women who have been examined by diagnostic ultrasound. The ultrasound imaging session will be performed in private and towels will be draped over the lower half of your body for privacy.

There is also a risk that the questionnaires/scales might be upsetting or distressing as the questions asked can be very personal and uncomfortable. You might not like all of the questions that they are asked. You do not have to complete the questions if you do not want to. The questionnaires will be completed in private, which may minimize the risk of distress.

During the study, the researchers may learn something about you that they did not expect. For example, the imaging may show a suspected abnormality of the uterus. If this occurs, you will be informed and advised to make an appointment with your family doctor for follow-up.

Participation in the ultrasound imaging sessions may be inconvenient because it will involve two sessions that take approximately 60 minutes each to complete.

If you become distressed at any time during the experimental session, you can stop participation at any time and/or you can be referred to an applicable medical professional for help. You can also withdraw from the study at any time.

Can I expect to benefit from participating in this research study?
You will not receive any direct benefit from your participation in this study. Your participation may benefit future patients by allowing researchers to classify uterine fibroids based on their stiffness to improve health management options.

Do I have to participate? What alternatives do I have? If I agree now, can I change my mind and withdraw later?
Your participation in this study is voluntary. The alternative to this study is not to participate. You may decide not to be in this study, or to be in the study now, and then change your mind later.
If you withdraw your consent, the study team will no longer collect your personal health or identifying information for research purposes. Information collected before your withdrawal will be removed from the study.

What compensation will I receive if I am injured or become ill in this study?

In the event of a study-related injury or illness, you will be provided with appropriate medical treatment and care. Financial compensation for lost wages, disability or discomfort due to an injury or illness is not generally available. You are not waiving any of your legal rights by agreeing to participate in this study. The study doctor, the Ottawa Hospital, the University of Ottawa, and The Ottawa Hospital Research Institute still have their legal and professional responsibilities.

Will I be paid for my participation or will there be any additional costs to me?

You will not be paid for your participation. Costs for parking at the University of Ottawa or public transportation costs will be reimbursed, with receipt. There will be no additional costs to you.

How is my personal information being protected?

- If you decide to participate in this study, the investigator(s) and study staff will look at your personal health information and collect only the information they need for this study. "Personal health information" is health information about you that could identify you because it includes information such as your name, address, telephone number, date of birth, and your reported medical history.
- Information that identifies you will be released only if it is required by law.
- All information collected during your participation in this study will be identified with a unique study number (for example participant # AB01), and will not contain information that identifies you.
- With the exception of this consent form, which will contain your name and will be securely brought to The Ottawa Hospital for storage, documents leaving University of Ottawa will only contain the coded study number.
- Documents leaving The Ottawa Hospital will only contain the coded study number.
- Data will be stored under password protection at The Ottawa Hospital and the University of Ottawa.
- A Master List provides the link between your identifying information and the coded study number. This list will only be available to Dr. Singh and his research staff and will not leave The Ottawa Hospital. The Master List and coded study records will be password protected and stored securely.
- For audit purposes only, your original study and medical records may be reviewed under the supervision of Dr. Singh's staff by representatives from:
    - The Ottawa Health Science Network Research Ethics Board (OHSN-REB), the Ottawa Hospital Research Institute, the University of Ottawa Research Ethics Board (UO-REB), and the University of Ottawa.
- You will not be identified in any publications or presentations resulting from this study.
- Research records will be kept for 10 years, as required by the OHSN-REB and the UO-REB.
- At the end of the storage time, all paper records will be shredded and all electronic records will be securely deleted.

A description of this clinical trial will be available on http://www.ClinicalTrials.gov. This Web site will not include information that can identify you. At most, the Web site will include a summary of the results. You can search this Web site at any time.

This research study can be found on the above listed website by using the clinical trial registration number NCT03369600.

Do the investigators have any conflicts of interest?

There are no conflicts of interest to declare related to this study.

Who do I contact if I have any further questions?

If you have any questions about this study, or if you feel that you have experienced a study-related injury or illness, please contact the study staff at (613) 738-8400 ext 81733; MISgyneresearch@toh.ca or any of the investigators listed on the first page of this form.

The Ottawa Health Science Network Research Ethics Board (OHSN-REB) and the University of Ottawa Research Ethics Board (UO-REB) has reviewed the plans for this research study. The Boards consider the ethical aspects of all research studies involving human participants at the Ottawa Hospital and the University of Ottawa. If you have any questions about your rights as a study participant, you may contact the Chairpersons of OHSN-REB at (613)798-5555 ext 16719 or the UO-REB at (613)562-5387.

Consent to Participate in Research

Title of Study: Characterization of tissue stiffness to improve the diagnosis and management of uterine fibroids.

- I understand that I am being asked to participate in a research study that will evaluate tissue stiffness of uterine tissue and fibroids in women.
- This study was explained to me by _____.
- I have read, or someone has read to me, each page of this Participant Informed Consent Form.
- All of my questions have been answered to my satisfaction.
- If I decide later that I would like to withdraw my participation and/or consent from the study, I can do so at any time.
- I voluntarily agree to participate in this study.
- I will be given a copy of this signed Participant Informed Consent Form.

_____	_____	_____
Participant's Printed Name	Participant's Signature	Date

Investigator or Delegate Statement

I have carefully explained the study to the study participant. To the best of my knowledge, the participant understands the nature, demands, risks and benefits involved in taking part in this study.

_____	_____	_____
Investigator's Printed Name	Investigator's Signature	Date

9.7 Symptomatic Fibroid Group Letter of Information and Informed Consent

Title of Study: Characterization of tissue stiffness to improve the diagnosis and management of uterine fibroids.

Principal Investigator (PI)
Sukhbir S. Singh, MD, FRCSC

Co-Investigators (Co-I)
Vincent della Zazzera, MD, FRCSC Linda McLean, PT, PHD Michel Labrosse, PhD, PEng

Teresa Flaxman, PhD Catorina Czyrnyj, PhD Candidate

Sponsor: The Ottawa Hospital Research Institute

Participation in this study is voluntary. Please read through this Participant Informed Consent Form carefully before you decide if you would like to participate. Ask as many questions as you like. We encourage you to discuss your options with family, friends or your healthcare team.

Why am I being given this form?
You are being asked to participate in this research study because you are a woman who is scheduled for surgery for uterine fibroids at The Ottawa Hospital.

Why is this study being done?
Uterine fibroids are the most common gynecological condition, with prevalence up to 70% in premenopausal women. Up to 50% of women with uterine fibroids experience symptoms such as heavy menstrual cycles, increased abdominal pressure, and infertility.

Currently, transvaginal ultrasound is the standard method for diagnosing uterine fibroids and identifying the number, size and location of the fibroids. However, there are different types of fibroids that cannot be differentiated with ultrasound. Knowledge of a patient's fibroid type can help physicians decide the best treatment. The different fibroid types can be classified according to their stiffness because they range from very hard to very soft. A new transvaginal ultrasound technology, called shear wave elastography, was developed to measure tissue stiffness but it has not been used clinically in gynecology. The ability to reliably and accurately measure uterine

tissue and fibroid stiffness with shear wave elastography is unknown. It is however approved by Health Canada for use and is currently used to screen for breast cancer and liver cirrhosis.

The goal of this study is to evaluate stiffness characteristics of healthy uterine tissue and uterine fibroids. We will also determine if stiffness characteristics can be used to classify the different types of uterine fibroids.

Furthermore, the effect of the following on uterine tissue stiffness is unknown:

- Age
- History of pregnancy
- Use of contraception
- The presence of fibroids on stiffness of the unaffected uterine tissue
- Use of medication specific for management symptoms associated with uterine fibroids

Data from participants with uterine fibroids will be compared to participants without uterine fibroids to better understand these relationships. Findings from this study will contribute to a future research study to determine if shear wave elastography can improve the diagnosis and monitoring of uterine fibroids such that physicians make more informed medical and surgical management decisions.

What is expected of me?

If you choose to participate you will take part two ultrasound imaging sessions at the University of Ottawa within two weeks of your planned surgery, spaced 2-3 days apart. Each session will take approximately 60 minutes to complete and will be conducted at a time convenient to you. The ultrasound imaging sessions will involve an ultrasound wand being inserted into your vagina while you are lying on your back on an ultrasound table. Stiffness of your uterus and fibroids will be measured using several ultrasound settings. The ultrasound procedures will be the same at each session. At the first ultrasound imaging session, you will also be asked to complete a set of questionnaires about your medical history, current symptoms, and quality of life. The questionnaires will take approximately 15 minutes to complete. Some of these questionnaires will be available in English only.

If you received a magnetic resonance imaging (MRI) scan of the pelvis within the past 12 months, then your de-identified images will also be used for study purposes.

The transvaginal ultrasounds will be performed in a private room at the Motor Function and Movement Laboratory at the University of Ottawa by Physiotherapist, Linda MacLean and/or her student, Catorina Czyrnyj, who have both been trained on the procedure.

We will also be collecting tissue samples from your uterus and fibroids that were removed during surgery and that would normally have been discarded. These samples will be tested in a machine that measures stiffness. The stiffness measured in the ultrasound will be compared to the stiffness measured by the machine. Additional personal health information from your

medical records including your medical history, referring diagnosis, procedures had (if any), and pathology report after surgery will also be collected.

We estimate that 90 participants will be enrolled in this study, including 30 participants with uterine fibroids from The Ottawa Hospital.

Will my research data be used in future research?

Your research data will be de-identified and securely stored at the Ottawa Hospital for 10 years. Only de-identified data will be used in future research projects relating to uterine fibroids. All future research conducted with your data will be approved by a Research Ethics Board before it begins.

How long will I be involved in the study?

The entire study will last approximately 2 years. Your participation in the study will be completed once you have your standard of care surgery.

Your participation in the study may be stopped for any of the following reasons:

- The study doctor feels it is in your best interest.
- You no longer wish to take part in the study.

What are the potential risks I may experience?

The risks involved in participating in this study are minimal.

There is a risk of distress from the ultrasound imaging session: a slender transducer of the ultrasound device is inserted into the vagina, thus depicting the pelvic organs. The ultrasound examination through the vagina is not painful; it has no more impact than any gynecological examination. If you have experienced discomfort during a recent gynecological exam, then you should decline to participate in this study. To date, there have been no descriptions of biological effects on women who have been examined by diagnostic ultrasound. The ultrasound imaging session will be performed in private and towels will be draped over the lower half of your body for privacy.

There is also a risk that the questionnaires/scales might be upsetting or distressing as the questions asked can be very personal and uncomfortable. You might not like all of the questions that they are asked. You do not have to complete the questions if you do not want to. The questionnaires will be completed in private, which may minimize the risk of distress.

There is a small risk that the tissue samples for mechanical jig testing contains findings that would alter the pathologic diagnosis.

Participation in this study is voluntary. If you become distressed at any time during the sessions, you can stop participation at any time and/or you can be referred to an applicable medical

professional for help. You can also withdraw from the study at any time. Participation in this study will not change your treatment plan and quality of care.

Participation in the ultrasound imaging sessions may be inconvenient because it will involve two sessions that take approximately 60 minutes each to complete.

Can I expect to benefit from participating in this research study?
You will not receive any direct benefit from your participation in this study. Your participation may benefit future patients by allowing researchers to classify uterine fibroids based on their stiffness to improve health management options.

Do I have to participate? What alternatives do I have? If I agree now, can I change my mind and withdraw later?
Your participation in this study is voluntary. The alternative to this study is not to participate. You may decide not to be in this study, or to be in the study now, and then change your mind later without affecting the medical care or other services to which you are entitled or are presently receiving at this institution. Even if you choose not to participate in this study you will still have your standard of care surgery.

If you withdraw your consent, the study team will no longer collect your personal health or identifying information for research purposes. Information collected before your withdrawal will be removed from the study.

What compensation will I receive if I am injured or become ill in this study?

In the event of a study-related injury or illness, you will be provided with appropriate medical treatment and care. Financial compensation for lost wages, disability or discomfort due to an injury or illness is not generally available. You are not waiving any of your legal rights by agreeing to participate in this study. The study doctor, the Ottawa Hospital, the University of Ottawa, and The Ottawa Hospital Research Institute still have their legal and professional responsibilities.

Will I be paid for my participation or will there be any additional costs to me?
You will not be paid for your participation. Costs for parking at the University of Ottawa or public transportation costs will be reimbursed, with receipt. There will be no additional costs to you.

How is my personal information being protected?
- If you decide to participate in this study, the investigator(s) and study staff will look at your personal health information and collect only the information they need for this study. "Personal health information" is health information about you that could identify you because it includes information such as your name, address, telephone number, date of birth, new and existing medical records, or the types, dates and results of various tests and procedures.

- Information that identifies you will be released only if it is required by law.

- All information collected during your participation in this study will be identified with a unique study number (for example participant # AB01), and will not contain information that identifies you.
- With the exception of this consent form, which will contain your name and will be securely brought to The Ottawa Hospital for storage, documents leaving University of Ottawa will only contain the coded study number.
- Documents leaving The Ottawa Hospital will only contain the coded study number.
- Data will be stored under password protection at The Ottawa Hospital and the University of Ottawa.
- Coded tissue samples will be sent to a laboratory at the University of Ottawa Heart Institute for analysis
- A Master List provides the link between your identifying information and the coded study number. This list will only be available to Dr. Singh and his research staff and will not leave The Ottawa Hospital. The Master List and coded study records will be password protected and stored securely.
- For audit purposes only, your original study and medical records may be reviewed under the supervision of Dr. Singh's staff by representatives from:
    - The Ottawa Health Science Network Research Ethics Board (OHSN-REB), the Ottawa Hospital Research Institute, the University of Ottawa Research Ethics Board (UO-REB), and the University of Ottawa.
- You will not be identified in any publications or presentations resulting from this study.
- Research records will be kept for 10 years, as required by the OHSN-REB and the UO-REB.
- At the end of the storage time, all paper records will be shredded and all electronic records will be securely deleted.

A description of this clinical trial will be available on http://www.ClinicalTrials.gov. This Web site will not include information that can identify you. At most, the Web site will include a summary of the results. You can search this Web site at any time.

This research study can be found on the above listed website by using the clinical trial registration number NCT03369600.

Do the investigators have any conflicts of interest?
There are no conflicts of interest to declare related to this study.

Who do I contact if I have any further questions?
If you have any questions about this study, or if you feel that you have experienced a study-related injury or illness, please contact the study staff at (613) 738-8400 ext 81733; MISgyneresearch@toh.ca or any of the investigators listed on the first page of this form.

The Ottawa Health Science Network Research Ethics Board (OHSN-REB) and the University of Ottawa Research Ethics Board (UO-REB) has reviewed the plans for this research study. The Boards consider the ethical aspects of all research studies involving human participants at the Ottawa Hospital and the University of Ottawa. If you have any questions about your rights as a study participant, you may contact the Chairpersons of OHSN-REB at (613)798-5555 ext 16719 or the UO-REB at (613)562-5387.

Consent to Participate in Research

Title of Study: Characterization of tissue stiffness to improve the diagnosis and management of uterine fibroids.

- I understand that I am being asked to participate in a research study that will evaluate tissue stiffness of uterine tissue and fibroids in women.
- This study was explained to me by _____.
- I have read, or someone has read to me, each page of this Participant Informed Consent Form.
- All of my questions have been answered to my satisfaction.
- If I decide later that I would like to withdraw my participation and/or consent from the study, I can do so at any time.
- I voluntarily agree to participate in this study.
- I will be given a copy of this signed Participant Informed Consent Form.

_____	_____	_____
Participant's Printed Name	Participant's Signature	Date

Investigator or Delegate Statement

I have carefully explained the study to the study participant. To the best of my knowledge, the participant understands the nature, demands, risks and benefits involved in taking part in this study.

_____	_____	_____
Investigator's Printed Name	Investigator's Signature	Date

9.8 Uterine Fibroids Symptoms Quality of Life Questionnaire

UTERINE FIBROID SYMPTOM AND HEALTH-RELATED QUALITY OF LIFE QUESTIONNAIRE (UFS-QOL)

Listed below are symptoms experienced by women who have uterine fibroids. Please consider each symptom as it relates to your uterine fibroids or menstrual cycle. Each question asks how much distress you have experienced from each symptom during the previous 3 months.

There are no right or wrong answers. Please be sure to answer every question by checking (✓) the most appropriate box. If a question does not apply to you, please mark "not at all" as a response.

During the previous 3 months, how distressed were you by…	Not at all	A little bit	Some-what	A great deal	A very great deal
1. Heavy bleeding during your menstrual period	☐ 1	☐ 2	☐ 3	☐ 4	☐ 5
2. Passing blood clots during your menstrual period	☐ 1	☐ 2	☐ 3	☐ 4	☐ 5
3. Fluctuation in the duration of your menstrual period compared to your previous cycle	☐ 1	☐ 2	☐ 3	☐ 4	☐ 5
4. Fluctuation in the length of your monthly cycle compared to your previous cycles	☐ 1	☐ 2	☐ 3	☐ 4	☐ 5
5. Feeling tightness or pressure in your pelvic area	☐ 1	☐ 2	☐ 3	☐ 4	☐ 5
6. Frequent urination during the daytime hours	☐ 1	☐ 2	☐ 3	☐ 4	☐ 5
7. Frequent nighttime urination	☐ 1	☐ 2	☐ 3	☐ 4	☐ 5
8. Feeling fatigued	☐ 1	☐ 2	☐ 3	☐ 4	☐ 5

The following questions ask about your feelings and experiences regarding the impact of uterine fibroid symptoms on your life. Please consider each question as it relates to your experiences with uterine fibroids during the previous 3 months.

There are no right or wrong answers. Please be sure to answer every question by checking (✓) the most appropriate box. If the question does not apply to you, please check "none of the time" as your option.

During the previous 3 months, how often have your symptoms related to uterine fibroids...	None of the time	A little of the time	Some of the time	Most of the time	All of the time
9. Made you feel anxious about the unpredictable onset or duration of your periods?	☐ 1	☐ 2	☐ 3	☐ 4	☐ 5
10. Made you anxious about traveling?	☐ 1	☐ 2	☐ 3	☐ 4	☐ 5
11. Interfered with your physical activities?	☐ 1	☐ 2	☐ 3	☐ 4	☐ 5
12. Caused you to feel tired or worn out?	☐ 1	☐ 2	☐ 3	☐ 4	☐ 5
13. Made you decrease the amount of time you spent on exercise or other physical activities?	☐ 1	☐ 2	☐ 3	☐ 4	☐ 5
14. Made you feel as if you are not in control of your life?	☐ 1	☐ 2	☐ 3	☐ 4	☐ 5
15. Made you concerned about soiling underclothes?	☐ 1	☐ 2	☐ 3	☐ 4	☐ 5
16. Made you feel less productive?	☐ 1	☐ 2	☐ 3	☐ 4	☐ 5
17. Caused you to feel drowsy or sleepy during the day?	☐ 1	☐ 2	☐ 3	☐ 4	☐ 5
18. Made you feel self-conscious of weight gain?	☐ 1	☐ 2	☐ 3	☐ 4	☐ 5
19. Made you feel that it was difficult to carry out your usual activities?	☐ 1	☐ 2	☐ 3	☐ 4	☐ 5
20. Interfered with your social activities?	☐ 1	☐ 2	☐ 3	☐ 4	☐ 5
21. Made you feel conscious about the size and appearance of your stomach?	☐ 1	☐ 2	☐ 3	☐ 4	☐ 5
22. Made you concerned about soiling bed linen?	☐ 1	☐ 2	☐ 3	☐ 4	☐ 5

During the previous 3 months, how often have your symptoms related to uterine fibroids...	None of the time	A little of the time	Some of the time	Most of the time	All of the time
23. Made you feel sad, discouraged, or hopeless?	☐ 1	☐ 2	☐ 3	☐ 4	☐ 5
24. Made you feel down hearted and blue?	☐ 1	☐ 2	☐ 3	☐ 4	☐ 5
25. Made you feel wiped out?	☐ 1	☐ 2	☐ 3	☐ 4	☐ 5
26. Caused you to be concerned or worried about your health?	☐ 1	☐ 2	☐ 3	☐ 4	☐ 5
27. Caused you to plan activities more carefully?	☐ 1	☐ 2	☐ 3	☐ 4	☐ 5
28. Made you feel inconvenienced about always carrying extra pads, tampons, and clothing to avoid accidents?	☐ 1	☐ 2	☐ 3	☐ 4	☐ 5
29. Caused you embarrassment?	☐ 1	☐ 2	☐ 3	☐ 4	☐ 5
30. Made you feel uncertain about your future?	☐ 1	☐ 2	☐ 3	☐ 4	☐ 5
31. Made you feel irritable?	☐ 1	☐ 2	☐ 3	☐ 4	☐ 5
32. Made you concerned about soiling outer clothes?	☐ 1	☐ 2	☐ 3	☐ 4	☐ 5
33. Affected the size of clothing you wear during your periods?	☐ 1	☐ 2	☐ 3	☐ 4	☐ 5
34. Made you feel that you are not in control of your health?	☐ 1	☐ 2	☐ 3	☐ 4	☐ 5
35. Made you feel weak as if energy was drained from your body?	☐ 1	☐ 2	☐ 3	☐ 4	☐ 5
36. Diminished your sexual desire?	☐ 1	☐ 2	☐ 3	☐ 4	☐ 5
37. Caused you to avoid sexual relations?	☐ 1	☐ 2	☐ 3	☐ 4	☐ 5

UFS-QoL Scoring Manual

To calculate a symptom score for symptom severity, create a summed score from the items listed below and then use the formula below the table to transform the value. This will provide symptom scores where higher score values are indicative of greater symptom severity or bother and lower scores will indicate minimal symptom severity (high scores = bad).

Scale	Sum Item Values	Lowest and Highest Possible Raw Scores	Possible Raw Score Range
Symptom Severity	Sum 1 – 8	8, 40	32

Transformation for Symptom Severity raw scores ONLY:

$$\text{Transformed Score} = \frac{(\textit{Actual}\text{ raw score} - \textit{lowest}\text{ possible raw score})}{\textit{Possible raw score range}} \times 100$$

For the HRQL subscales (concern, activities, energy/mood, control, self-conscious, and sexual function), create summed scores of the items listed below for each individual subscale. To calculate the HRQL total score, sum the value of each individual subscale (do not sum individual items). Use the formula below the table to transform all values. Higher scores will be indicative of better HRQL (high = good).

Scale	Sum Item Values	Lowest and Highest Possible Raw Scores	Possible Raw Score Range
Concern	9+15+22+28+32	5, 25	20
Activities	10+11+13+19+20+27+29	7, 35	28
Energy/mood	12+17+23+24+25+31+35	7, 35	28
Control	14+16+26+30+34	5, 25	20
Self-conscious	18+21+33	3, 15	12
Sexual function	36+37	2, 10	8
HRQL TOTAL	Sum of 6 Subscale Scores	29, 145	116

Formula for transformation of HRQL raw scores ONLY:

$$\text{Transformed Score} = \frac{(\textit{Highest}\text{ possible score} - \textit{Actual raw score})}{\textit{Possible raw score range}} \times 100$$

Missing Items

For the subscale analyses, if < 50% of the scale items are missing, the scale should be retained with the mean scale score of the items present used to impute a score for the missing items. If ≥ 50% of the items are missing, no scale score should be calculated, the subscale score should be considered missing. If a subscale score is missing, the HRQL total cannot be calculated.

9.9 Menstrual Bleeding Questionnaire

These questions ask for details about your period. Periods can be different from month to month. Please make sure you read all of the options. For this questionnaire, period refers to any bleeding that you have from your vagina, even if it is irregular.

Some of the questions may sound similar. Just read through each question carefully and give your best answer.

You may have other medical problems that could affect your answers. Please try to focus on questions and answers **ONLY** as they relate to your period.

During the past month, did you have ANY bleeding?

Yes..... [ ]

No..... [ ]

If you answered "YES" continue to question 1.
If you answered "NO" skip to question 10.

1. During the past month, how would you describe your periods?

Very Light.....	[ ]0
Light.....	[ ]1
Moderate.....	[ ]2
Heavy.....	[ ]3
Very Heavy.....	[ ]4

Instructions for questions 2, 3, and 4
"High absorbency" sanitary productes means any type of tampon or pad that is NOT a thin pantiliner.

"Soaked" means completely or almost completely stained and filled with blood.

2. On your heaviest day of bleeding during the past month, how many high absorbency sanitary products did you soak (either completely or almost completely)?

0.....	[ ]0
1-4.....	[ ]1
5-8.....	[ ]2
9-12.....	[ ]3
13-16.....	[ ]4
More than 16.....	[ ]5

3. During the past month, how often did you need to wear either an incontinence brief or more than one high absorbency sanitary product (either more than one pad, a pad and a tampon, more than one tampon) at a time to contain your bleeding?

Never.....	[ ]0
1-3 times.....	[ ]1
4-6 times.....	[ ]2
7-10 times.....	[ ]3
11 times or greater.....	[ ]4

4. During the past month, how many times have you had an episode of bleeding that soaked through your "outer" clothes (pants, skirt, dress)?

Never	[ ]0
1-3 times	[ ]1
4-6 times	[ ]2
Greater than 6 times	[ ]3

5. During the past month, how many times did you need to get out of bed in the middle of night (or during sleep hours) to change your sanitary products?

Never	[ ]0
1-3 times	[ ]1
4-6 times	[ ]2
7-10 times	[ ]3
11 times or greater	[ ]4

6. During the past month, how many times did you pass blood clots (clumps of blood)?

Never	[ ]0
1-3 times	[ ]1
4-6 times	[ ]2
Greater than 6 times	[ ]3

7. During the past month, how often did passing blood clots (clumps of blood) stain your clothing?

Never	[ ]0
1-3 times	[ ]1
4-6 times	[ ]2
Greater than 6 times	[ ]3

8. Please fill in the following statement about pain related to your period. During the past month, my period was associated with...

No pain	[ ]0
Slight pain	[ ]1
Moderate pain	[ ]2
Severe pain	[ ]3

9. During the past month, how many weeks did your periods last?

1 week or less out of 4 weeks	[ ]0
More than 1 week, less than 2 weeks out of 4 weeks	[ ]1
More than 2 weeks, less than 3 weeks out of 4 weeks	[ ]2
More than 3 weeks out of 4 weeks	[ ]3

10. During the past month, on how many days do think your work at your job suffered because you were bleeding?

I am currently not working outside of the home	[ ]**
Never, my bleeding does not affect my work	[ ]0
1-3 days	[ ]1
4-8 days	[ ]2
9-12 days	[ ]3
13 days or more	[ ]4

11. During the past month, on how many days did you miss work because you were bleeding?

I am currently not working outside of the home	[ ]**
Never, my bleeding does not affect my work schedule	[ ]0
1-3 days	[ ]1
4-8 days	[ ]2
9-12 days	[ ]3
13 days or more	[ ]4

12. During the past month, on how many days did you avoid family activities (grocery shopping, household chores) when you thought you would be bleeding?

Never	[ ]0
1-3 days	[ ]1
4-8 days	[ ]2
9-12 days	[ ]3
13 days or more	[ ]4

13. During the past month, when would you carry sanitary products (pads, tampons) with you (in your pocket, in your bag)?

Every day, in case I had any bleeding	[ ]2
On the days when I had bleeding and on days when I guessed that I might have bleeding	[ ]1
Only on the days that I had bleeding	[ ]0

14. During the past month, on how many days did you avoid social activities (such as getting together with friends, going shopping for fun, going sight-seeing) when you thought you would be bleeding?

Never	[ ]0
1-3 days	[ ]1
4-8 days	[ ]2
9-12 days	[ ]3
13 days or more	[ ]4

15. During the past month, on how many days did you plan <u>your</u> activities (work, social, or family) based on whether or not there was a bathroom nearby?

Never	[ ]0
1-3 days	[ ]1
4-8 days	[ ]2
9-12 days	[ ]3
13 days or more	[ ]4

16. During the past month, on how many days did you bring extra clothes with you (to work, out shopping) in case you had staining from your period?

Never	[ ]0
1-3 days	[ ]1
4-6 days	[ ]2
Greater than 6 days	[ ]3

17. During the past month, on how many days did you choose what to wear based on whether or not you were bleeding?

Never	[ ]0
1-3 days	[ ]1
4-8 days	[ ]2
9-12 days	[ ]3
13 days or more	[ ]4

18. On a scale of 0-10, with 0 being no concern at all and 10 being extremely concerned, please rate your overall concern about bleeding staining your clothes.

_____

19. During the past month, would you say that your period start date was…

Completely predictable	[ ]0
Somewhat predictable	[ ]1
Not at all predictable	[ ]2

20. During the past month, would you say that your period end date was…

Completely predictable	[ ]0
Somewhat predictable	[ ]1
Not at all predictable	[ ]2

** for women who are not working outside of the home, impute the score given on question number 12

Total Menstrual Bleeding Questionnaire Score is obtained by summing the values obtained on questions 1-20.